UNIVERSITY OF SOUTHAMPTON

FACULTY OF ENGINEERING AND PHYSICAL SCIENCES

School of Electronics and Computer Science

Compressed Sensing-Aided Multi-Dimensional Index Modulation Transceiver Design

by

Siyao Lu

BEng., MSc.(Hons)

Thesis for the degree of Doctor of Philosophy

September 2019

SUPERVISORS: *Dr. Mohammed El-Hajjar and Prof. Lajos Hanzo*

School of Electronics and Computer Science

University of Southampton

Southampton SO17 1BJ

United Kingdom

Dedicated to my beloved father Zhicai Lu, mother Shuzhen Zhai and husband Zhenzhou Wang.

UNIVERSITY OF SOUTHAMPTON

ABSTRACT

FACULTY OF ENGINEERING AND PHYSICAL SCIENCES
School of Electronics and Computer Science

Doctor of Philosophy

COMPRESSED SENSING-AIDED MULTI-DIMENSIONAL INDEX MODULATION TRANSCEIVER DESIGN

by Siyao Lu

In this thesis, we propose a suite of compressed sensing (CS)-aided index modulation (IM) techniques for transmission over frequency-selective fading channels invoked in orthogonal frequency division multiplexing (OFDM) and multiple-input multiple-output (MIMO) arrangements. The design objective is to improve both the performance and the design flexibility by striking flexible trade-offs among the performance, bandwidth efficiency, energy efficiency and complexity.

Specifically, a novel CS-aided frequency-domain IM system is proposed, combining the benefits of space-time shift keying (STSK), OFDM-IM and CS, in order to strike a flexible trade-off between the throughput and bit error rate (BER) performance. The proposed CS-aided frequency-domain IM is termed as CS-OFDM-STSK-IM. Explicitly, the CS-aided signalling strategy is applied to the transmitter for improving the throughput by introducing the concept of virtual domain. Then a pair of reduced-complexity detectors are proposed, which rely on the CS principles. In particular, we derive the discrete-input continuous-output memoryless channel (DCMC) capacity for characterising the achievable performance limit of the CS-OFDM-STSK-IM. Furthermore, in order to attain extra diversity gains at no cost in terms of power or bandwidth, the coordinate interleaving technique is applied. Additionally, for the sake of achieving a near-capacity performance, we conceive a two-stage serially concatenated channel-coded CS-OFDM-STSK-IM scheme employing iterative detection.

To attain an improved BER performance as well as system capacity in comparison to the CS-OFDM-STSK-IM scheme, we propose an improved CS-aided multi-dimensional IM system relying on both frequency- and spatial-domain IM. Explicitly, extra implicit information bits are transmitted by detecting the activated indices of both the TAs and subcarriers, while striking a flexible design trade-off between the throughput and the diversity gain. Furthermore, CS is invoked at both the transmitter and the receiver of our multi-dimensional system for the sake of improving the system's design flexibility, whilst reducing the detector's complexity. We first present the maximum likelihood (ML) detector of the CS-aided multi-dimensional IM system for characterising the lower bound of the system's performance. Specifically, an upper bound is derived for the average bit error probability (ABEP) and it is observed that the theoretical upper bound derived becomes tight when compared to the ML detector simulation curves as the value of SNR increases. Although the ML detector is capable of achieving the optimal performance, its prohibitive computational complexity makes it impractical for our multi-dimensional scheme. Hence we propose a reduced-complexity detector based on CS principles, which imposes only a modest BER degradation compared to the ML detector. We also analyse the computational complexities of both the ML and of the reduced-complexity detectors in different system configurations. We show that the CS-aided reduced-complexity detector is capable of attaining a flexible trade-off between the throughput and the complexity. Furthermore, soft-input soft-output decoders relying on both the optimal ML and on the reduced-complexity detectors are proposed for attaining near-capacity performances, which are analysed with the aid of EXtrinsic Information Transfer (EXIT) charts. Then we characterise the maximum achievable rate of the CS-aided multi-dimensional IM using both the ML and our reduced-complexity detectors by formulating the DCMC capacity and by invoking EXIT charts.

Finally, attracted by the benefits of large-scale multi-user MIMO (LS-MU-MIMO) systems in terms of their high bandwidth efficiency, high energy efficiency and increased reliability, we conceive a novel two-dimensional IM, namely the CS-aided (generalised) space-frequency IM (CS-(G)SFIM) scheme in our LS-MU-MIMO uplink scenarios. Explicitly, extra information bits are conveyed by mapping both to the activated spatial- and frequency-domain indices. More particularly, we employ different transmit antenna (TA) activation patterns for different transmitted symbols instead of using the same active TAs for the whole subcarrier group as proposed in the CS-aided multi-dimensional IM scheme, which improves both the BER performance as well as the diversity gains. For the sake of further increasing the system's achievable rate without sacrificing any bandwidth or energy, CS-aided pre-processing is applied to the frequency-domain IM.

Then we design a CS-aided reduced-complexity multi-user detector, namely the reduced-search-space based iterative matching pursuit (RSS-IMP), which significantly reduces the detection complexity compared to the ML detector. Furthermore, the RSS-IMP detector is capable of significantly reducing the detection complexity, while attaining better performances than both the conventional MU-MIMO-OFDM system and the proposed system using the classical minimum mean square error (MMSE) detector. We also characterise the performances of the CS-(G)SFIM system in the presence of channel estimation errors. Our simulation results show that the CS-(G)SFIM system is more robust to imperfect channel estimation than the conventional MU-MIMO-OFDM system. More importantly, owing to the highly flexible structure of our proposed scheme, improved trade-offs may be struck among the bandwidth efficiency, energy efficiency, BER performance, as well as the computational complexity by beneficially configuring our design, depending on the associated system requirements and channel conditions.

Declaration of Authorship

I, **Siyao Lu** , declare that the thesis entitled **Compressed Sensing-Aided Multi-Dimensional Index Modulation Transceiver Design** and the work presented in the thesis are both my own, and have been generated by me as the result of my own original research. I confirm that:

- this work was done wholly or mainly while in candidature for a research degree at this University;
- where any part of this thesis has previously been submitted for a degree or any other qualification at this University or any other institution, this has been clearly stated;
- where I have consulted the published work of others, this is always clearly attributed;
- where I have quoted from the work of others, the source is always given. With the exception of such quotations, this thesis is entirely my own work;
- I have acknowledged all main sources of help;
- where the thesis is based on work done by myself jointly with others, I have made clear exactly what was done by others and what I have contributed myself;
- parts of this work have been published as shown in the list of publications.

Signed:.....

Date:.....

Acknowledgements

I would like to express my heartfelt gratitude to Prof. Lajos Hanzo and Dr. Mohammed El-Hajjar for their outstanding supervision and support throughout my research. Thank Prof. Lajos Hanzo for not only offering me professional supervision in the academic studies but also teaching me the attitude of "step by step" and "work smartly". Thank Dr. Mohammed El-Hajjar for his unwavering support, invaluable encouragement and most of all his cherished friendship. Without their patient instruction, insightful criticism and expert guidance, my research would not have been done easily. In a word, their guidance, inspiration and encouragement have greatly benefited me not only in work but also in life.

Many thanks to my friends and colleagues and to the entire Southampton Next Generation Wireless group staff, both present and past, for their immense support and contribution to my personal and professional time at Southampton. I am especially grateful to Prof. Lie-Liang Yang, Prof. Sheng Chen, Prof. Robert Maunder, Dr. Soon (Michael) Ng for their invaluable advice and comments. I am also grateful to Dr. Ibrahim Hemadeh, Dr. Dimitrios Alanis, Dr. Panagiotis Botsinis, Dr. Zunaira Babar, Prof. Shaoshi Yang, Dr. Rakshith Rajashekar, Dr. Nguyen Viet Hung, Dr. Chao Xu, Dr. Jiankang Zhang, Mr. Daryus Chandra, Dr. Shruti Gupta, Mr. Katla Satyanarayana, Dr. Yichuan Li, Dr. Tong Bai, Dr. Jingjing Wang, Dr. Fasong Wang, Dr. Chaowen Liu, Dr. Qi Wang, Dr. Xuan Li and Mr. Haochen Liu for the helpful discussions we had and for creating such a wonderful research environment. I would like to express my gratitude to my best friend to-be-Dr. Xiaoyu (Colin) Zhang for his invaluable help.

I would like to express my warmest gratitude to my family, for all their love, encouragement and endless sacrifices that got me here. I dedicate this thesis to my mother Ms. Shuzhen Zhai, to my father Mr. Zhicai Lu, to my mother-in-law Ms. Xi Chen, to my father-in-law Mr. Mingwei Wang and to my super lovely dog, Nemo. This thesis would have not been possible without them. Last but not the least, I would like to greatly thank my husband to-be-Dr. Zhenzhou Wang, for his insightful advice, encouragement, love and accompany.

List of Publications

Journal Papers

1. **S. Lu**, I. A. Hemadeh, M. El-Hajjar and L. Hanzo, "Compressed-Sensing-Aided Space-Time Frequency Index Modulation," IEEE Transactions on Vehicular Technology, vol. 67, no. 7, pp. 6259-6271, July 2018.

2. I. A. Hemadeh, **S. Lu**, M. El-Hajjar and L. Hanzo, "Compressed Sensing-Aided Index Modulation Improves Space-Time Shift Keying Assisted Millimeter-Wave Communications," IEEE Access, vol. 6, pp. 64742-64756, 2018.

3. **S. Lu**, I. A. Hemadeh, M. El-Hajjar and L. Hanzo, "Compressed Sensing-Aided Multi-Dimensional Index Modulation," in IEEE Transactions on Communications, vol. 67, no. 6, pp. 4074-4087, June 2019.

4. **S. Lu**, M. El-Hajjar and L. Hanzo, "Two-Dimensional Index Modulation for the Large-Scale Multi-User MIMO Uplink," in IEEE Transactions on Vehicular Technology, vol. 68, no. 8, pp. 7904-7918, Aug. 2019.

Conference Paper

1. **S. Lu**, I. A. Hemadeh, M. El-Hajjar and L. Hanzo, "An Adaptive Multi-User MIMO Scheme for the Millimeter-Wave Downlink," 2018 IEEE 29th Annual International Symposium on Personal, Indoor and Mobile Radio Communications (PIMRC), Bologna, 2018, pp. 1-5.

Contents

Glossary

4G	Fourth-Generation
5G	Fifth-Generation
ABEP	Average Bit Error Probability
AC	Antenna Combination
APM	Amplitude/Phase Modulated
AWGN	Additive White Gaussian Noise
BER	Bit Error Rate
BPSK	Binary Phase Shift Keying
BS	Base Station
CCs	Convolutional Codes
CP	Cyclic Prefix
CPEP	Conditional Pairwise Error Probability
CS	Compressed Sensing
CSI	Channel State Information
DAC	Distinctive Antenna Combination
DCMC	Discrete-Input Continuous-Output Memoryless Channel
DM	Dispersion Matrix
EXIT	Extrinsic Information Transfer

FEC	Forward Error Correction
FFT	Fast-Fourier-Transform
GSM	Generalised Spatial Modulation
HD	Hard-Decision
IFFT	Inverse Fast Fourier Transform
IM	Index Modulation
LDC	Linear Dispersion Coding
LLRs	Logarithmic-Likelihood Ratios
Log-MAP	Logarithmic Maximum *a posteriori*
MAP	Maximum *a posteriori*
MIMO	Multiple-Input-Multiple-Output
MIP	Mutual Incoherence Property
ML	Maximum Likelihood
MMSE	Minimum Mean-Squared Error
MMV	Multiple Measurement Vector
MU	Multi-User
MUD	Multi-User Detector
OFDM	Orthogonal Frequency Division Multiplexing
PAPR	Peak-to-Average Power Ratio
PE	Pairwise Error
PSK/QAM	Phase Shift Keying/Quadrature Amplitude Modulation
RA	Receive Antenna
RF	Radio Frequency
RSC	Recursive Systematic Convolutional
SD	Soft-Decision

SM	Spatial Modulation
STBC	Space-Time Block Code
SNR	Signal-to-Noise Ratio
STSK	Space-Time Shift Keying
TA	Transmit Antenna
TCM	Trellis-Coded Modulation
UPEP	Unconditional Pairwise Error Probability
V-BLAST	Vertical Bell Labs Layered Space-Time

List of Symbols

General notation

- The superscript ^{T} is used to indicate matrix transpose operation.
- The superscript ^{H} is used to indicate complex conjugate transpose operation.
- The operator $\lfloor \cdot \rfloor$ is used to denote the integer floor operation.
- The operator $(\cdot)^\dagger$ represents the Moore-Penrose pseudo-inverse operation.
- The operator $diag\{\cdot\}$ is used to denote the diagonal structure of a matrix.
- The operator $\| \cdot \|$ denotes the Frobenius norm.
- The operator $\mathbb{C}^{r \times c}$ illustrates the size of a complex-valued matrix, where the size is $(r \times c)$.
- The operator $L(\cdot)$ indicates LLRs of a bit sequence.
- The operator $\mathcal{O}(\cdot)$ denotes the complexity order.
- The operator $\log_2(\cdot)$ denotes the Logarithm to base 2.
- The operator $\arg\min_{x \in \mathcal{S}}\{f(x)\}$ denotes the argument $x_i \in \mathcal{S}$ yielding the minimum.
- The operator $\arg\max_{x \in \mathcal{S}}\{f(x)\}$ denotes the argument $x_i \in \mathcal{S}$ yielding the maximum.
- The operator $p(a|b)$ represents the probability of a given b.
- The operator jac$(\cdot)$ denotes the Jacobian maximum operator.
- The operator $exp(\cdot)$ denotes the exponential function.

General symbols

b	Number of information bits per subcarrier group.
G	Number of subcarrier groups per OFDM frame.
K	Number of active subcarriers per subcarrier group.
N_v	Dimension of the virtual domain per subcarrier group.
N_f	Dimension of the frequency domain per subcarrier group.
N_c	Number of subcarriers per OFDM frame.
$\mathcal{L}$	Size of the constellation symbol.
M	Number of STSK spatial dimensions.
N	Number of receive antennas.
Q	Number of dispersion matrices.
T	Number of STSK time slots.
σ_n^2	Noise variance.

Special symbols

Chapter 2

$\mathbf{X}_g$	Output space-time matrix of the STSK encoder for the g-th subcarrier group, where $g = 1, 2, \ldots, G$.
$\hat{\mathbf{X}}_g$	Coordinated interleaved space-time matrix $\mathbf{X}_g$.
$\bar{\mathbf{X}}_g$	The symbols of the g-th subcarrier group in the virtual domain.
$\mathbf{S}_m^g$	The symbols of the g-th subcarrier group in the virtual domain at the m-th transmit antenna.
$\mathbf{A}$	The measurement matrix.
$\hat{\mathbf{S}}_m^g$	The symbols of the g-th subcarrier group in the frequency domain at the m-th transmit antenna.

$\mathbf{Y}_g$	The received frequency-domain signal of the g-th subcarrier group.
$\mathbf{H}_g$	The block-diagonal frequency-domain channel matrix of the g-th subcarrier group.
$\hat{\mathbf{A}}$	The equivalent CS measurement matrix used for the signals from the M transmit antennas.
$\mathbf{S}_g$	The virtual-domain signal of the g-th subcarrier group transmitted from the M transmit antennas over T time slots.
$\mathbf{W}_g$	The AWGN matrix.
$\mathbf{I}_g$	The block diagonal matrix that illustrates the specific subcarrier indices mapping pattern for the g-th subcarrier group.
$\mathbf{I}_g^m$	The submatrix that represents the subcarrier indices combination mapping pattern at the m-th transmit antenna.
I_c	The library of subcarrier indices combination.
N_{SI}	Number of subcarrier indices combination of the g-th subcarrier group.
$\mathbf{F}_g$	The MMSE filtering matrix for the g-th subcarrier group.
e_g^i	The residual error of the g-th subcarrier group in the i-th detection iteration.
C_{DCMC}	DCMC capacity.

Chapter 3

N_t	Number of transmit antennas.
N_r	Number of receive antennas.
N_{AC}	Number of active transmit antenna combinations for a single subcarrier group.
σ_n^2	Noise variance.
$\mathbf{H}$	The frequency-domain channel matrix for each subcarrier group.

$\bar{\mathbf{I}}_{AC}$	The diagonal-structure matrix that denotes the transmit antennas selection pattern in each subcarrier group
$\mathbf{S}^{FD}$	The transmitted frequency-domain space-time signals of a single subcarrier group.
$\mathbf{S}^{VD}$	The virtual-domain space-time signals of a single subcarrier group.
$\mathbf{X}$	The output of the STSK encoder.
$\bar{\mathcal{I}}_{AC}(\gamma)$	All possible realisations of the active transmit antenna indices for a single subcarrier group, where $\gamma = 1, 2, \ldots, N_{AC}$.
$\mathcal{I}_{SI}(\beta)$	All possible realisations of the active subcarrier indices for a single subcarrier group, where $\beta = 1, 2, \ldots, N_{SI}$.
$N_{q,l}$	Number of all possible realisations of STSK codewords for a single subcarrier group.
$\mathcal{X}_{q,l}(\varphi)$	All possible realisations of STSK codewords for a single subcarrier group, where $\varphi = 1, 2, \ldots, N_{q,l}$.
$\mathcal{O}_{ML}$	Complexity order of the ML detector.
$\bar{\mathbf{S}}$	The equivalent transmitted signal matrix for a single subcarrier group.
$M_{\xi}(\alpha)$	The moment generating function of ξ.
$\bar{\mathbf{H}}$	The equivalent frequency-domain channel matrix.
$\mathbf{\Phi}$	The equivalent index modulation supporting matrix.
ρ_s	The average SNR per symbol.
$L^{\dagger}_{i,e}(u)$	The pre-processed extrinsic LLRs passed from the inner demodulator to the deinterleaver.
$\mathcal{A}$	The empirical transformation coefficient.
γ	Index of combinations of active transmit antennas per subcarrier group.
β	Index of combinations of active subcarrier indices per subcarrier group.

φ	Index of combinations of STSK codewords per subcarrier group.

Chapter 4

U	Number of uplink users.
N_t^a	Number of active transmit antennas.
$\mathbf{b}_{u,g}$	Information sequence of the u-th user for the g-th group.
$\mathbf{b}_{u,g}^1$	Information sequence processed by the Virtual-Domain Frequency Index Selector of the u-th user for the g-th group.
$\mathbf{b}_{u,g}^2$	Information sequence processed by the Spatial-Domain Modulation/Mapping block of the u-th user for the g-th group.
$\mathbf{X}_{u,g}$	Output signal matrix of the Spatial-Domain Modulation/Mapping block of the u-th user for the g-th group.
$\underline{\mathcal{S}}_{u,g}$	Space-frequency matrix of the u-th user for the g-th group before the process of the compressed sensing.
$\mathbf{s}_{u,g}^t$	N_f-dimensional frequency-domain vector from the t-th transmit antenna of the u-th user for the g-th group.
R_t	Transmission rate.
N_{cp}	Number of cyclic prefix.
$\mathbf{H}_i^u$	The diagonal-structure matrix of the complex-valued channel gain for the transmission of a single subcarrier group of the u-th user from the N_t transmit antennas to the i-th receive antenna.
$\mathbf{s}_u$	The frequency-domain symbols sequence of the u-th user transmitted from N_t transmit antennas.
$\mathbf{y}_g$	The received frequency-domain signal sequence of the g-th subcarrier group from U users.
l_g	Index of realisations of AMP symbols for all users of the g-th subcarrier group.

i_g	Index of active subcarriers combinations for all users of the g-th subcarrier group.
j_g	Index of active transmit antennas combinations for all users of the g-th subcarrier group.

Chapter 1

Introduction

1.1 Motivation

With the development of industry and the worldwide deployment of mobile networks, there is a dramatic increase in the number of users who subscribe to wireless systems every year, whilst powerful smart phones and laptops are becoming more and more popular [1]. The fifth-generation (5G) wireless network is expected to support $1,000$ times the capacity, 10 times the data rate and 25 times the average cell throughput compared to the fourth-generation (4G) wireless network [2]. However, the existing modulation techniques based on classic multiple-input multiple-output orthogonal frequency division multiplexing (MIMO-OFDM) fail to satisfy these requirements [3]. This is partly attributable to practical challenges, such as the high peak-to-average power ratio (PAPR), the inter-carrier interference and the inter-antenna interference encountered [4]. Hence, new modulation techniques are required. In this context, the emerging index modulation (IM) techniques [5] attain a high spectral- and energy-efficiency by conveying extra implicit information mapped to the activated subcarrier- and antenna-indices in addition to the classical modulation schemes [6].

In Section 1.2, we commence with a brief review of IM techniques designed for next-generation wireless networks, including the spatial-domain IM techniques of Section 1.2.1, the space-time-domain IM techniques of Section 1.2.2, the frequency-domain IM techniques of Section 1.2.3 and the multi-dimensional IM techniques of Section 1.2.4. Specifically, a brief review of applying IM techniques both to large-scale MIMO and to multi-user scenarios is provided in Section 1.2.5. Additionally, both transmitter-side

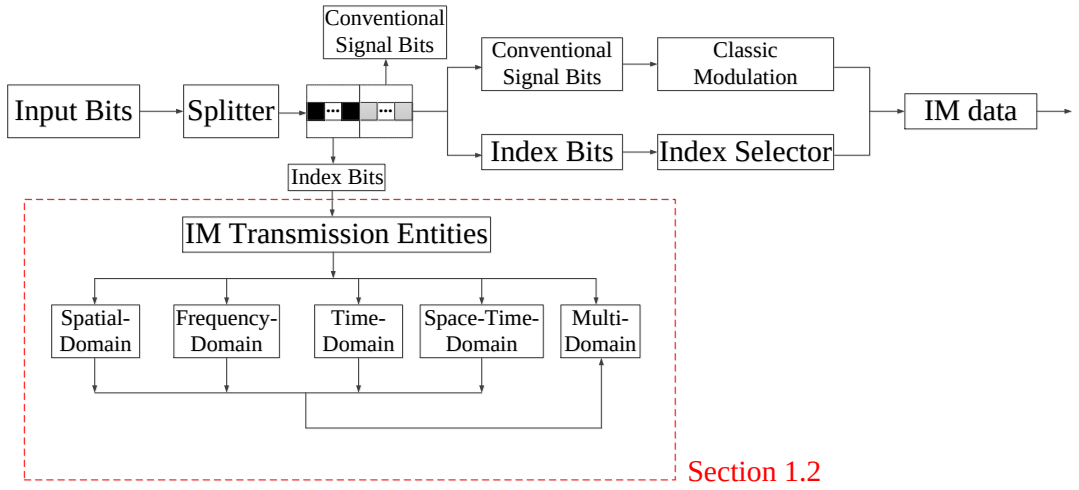

Figure 1.1: The basic transmitter model of IM and the examples of index types.

and receiver-side compressed sensing-aided IM techniques are briefly introduced in Section 1.3. Finally, the novel contributions and the outline of this thesis will be presented in Section 1.4 and in Section 1.5, respectively.

1.2 Index Modulation for Next-Generation Wireless Communications

IM [1, 5–7] has attracted much attention as an emerging modulation concept, since it provides alternative ways of transmitting information in contrast to traditional amplitude/phase/frequency digital modulation schemes. Explicitly, IM modulates signals by altering the on/off status of the transmission entities, such as antennas, subcarriers, time slots or dispersion matrices, where the index of the activated transmission entities is embedded into the transmitted or received signals for carrying additional information with little or even no extra power consumption [7]. The basic transmitter model of IM and the examples of index types are portrayed in Fig. 1.1, where the information sequence is split into index bits and conventional signal bits for realising IM and classic modulation techniques, respectively. Based on Fig. 1.1, in the following sections we will review the main contributions conceived for popular spatial-domain, frequency-domain, space-time-domain and multi-domain IM techniques.

1.2.1 Spatial-domain Index Modulation

The spatial modulation (SM) concept constitutes a novel way of carrying information by the activated indices of the transmit antennas (TAs) in addition to the conventional $\mathcal{L}$-ary signal constellations. This scheme is the most well-known application of the spatial-domain IM concept which relies on the indices of the activated TAs as the transmission entity [8]. The conventional MIMO schemes rely on either spatial multiplexing [9] for increasing the throughput by transmitting different symbols from different TAs, or on spatial diversity [10, 11] for improving the bit error rate (BER) by receiving multiple independently fading copies of symbols from different TAs or receive antennas (RAs). By contrast, in SM both the indices of activated TAs and the classical constellation symbols carry information [1]. In its simplest form SM requires the activation of a single antenna at each time slot. The single-antenna-activation based property allows SM to eliminate the inter-antenna interference and to avoid inter-antenna synchronisation, while achieving a spatial multiplexing gain. However, it has not transmit-diversity gain. It has been demonstrated [12–14] that SM has the potential of striking more attractive design trade-offs than the well-known MIMO techniques, such as the vertical Bell Labs layered space-time (V-BLAST) scheme and Alamouti's space-time block code (STBC) [9, 10]. Hence SM has also been combined with OFDM [15]. Given its benefits [5–8, 16–18], SM may be viewed as a potential candidate for spectrum- and energy-efficient next-generation wireless communication [2].

Inspired by [8] and [20], which introduced the SM and space-shift keying (SSK) schemes, respectively, SM has attracted considerable interests across the wireless community and numerous papers have been published on SM [21, 22, 24–26]. Explicitly, in order to increase the bandwidth efficiency of SM as well as to mitigate the constraints on the number of active TAs, an improved version of SM, referred to as generalised SM (GSM) was proposed [21, 22, 26], where the number of active TAs is no longer limited to one and the same data symbol is transmitted over multiple active TAs. In [27], a closed form expression has been derived for the capacity of GSM and the BER performance of GSM has been analysed for transmission over fading channels. Additionally, low-complexity detection algorithms have been proposed for GSM, while providing near-optimal BER performance [23, 28–31].

To further explore the potential of IM, a great deal of SM variants have been proposed. Explicitly, quadrature SM (QSM) was proposed by Mesleh *et al.* [24] as an enhancement to the conventional SM [8], which applied SM both to the in-phase and quadrature dimensions, hence doubling the number of index bits. Hence QSM has been further

Year	Author(s)	Contribution
2008	Mesleh *et al.* [8]	The concept of SM was refined, where a single out of N_t TAs is activated for transmitting a single modulated $\mathcal{L}$-ary symbol.
2008	Jeganathan *et al.* [19]	Designed an optimal ML detector for SM and the BER performance of SM was analysed.
2009	Jeganathan *et al.* [20]	Proposed the concept of SSK, where simply the TA activation index conveys the source information.
2010	Younis *et al.* [21]	Proposed the concept of GSM, where a single modulated symbol is transmitted from multiple active antennas at each time slot, while requiring only one RF chain.
2012	Wang *et al.* [22]	Proposed another version of GSM, where the same number of RF chains as that of active antennas to transmit multiple independent modulated symbols is required in comparison to [21].
2013	Serafimovski *et al.* [14]	Characterised the performance of SM with an experimental test bed.
2014	Xiao *et al.* [23]	Proposed low-complexity signal detection for GSM.
2015	Mesleh *et al.* [24]	Proposed the concept of QSM, which expands the spatial domain to include both the in-phase and quadrature dimensions for doubling the bandwidth efficiency contributed by the index bits.
2015	Cheng *et al.* [25]	Proposed the concept of ESM, where one or two TAs are activated for transmission at each time slot.
2015	Yang *et al.* [12]	Provided a general survey of the SM design framework as well as of its intrinsic limits.

Table 1.1: Main contributions on spatial-domain IM.

studied in [32–37], including its BER performance analysis [33], its low-complexity detection algorithms [32,36,37], the impact of co-channel interference on the performance of QSM-MIMO [34], its capacity analysis [35] and so on. In order to overcome the limited bandwidth efficiency of SM due to the activation of a single antenna, enhanced SM (ESM) was proposed in [25] for improving the BER performance by transmitting information bits using combinations of several activated TAs and signal constellations. Attracted by its advantages, some follow-up studies have been conducted in [38–40]. Explicitly, the performance of ESM was analysed in [38,40], while new signal designs were conceived for ESM in [39] . The major contributions on spatial-domain IM applications

in single-user scenarios are listed in Table 1.1.

1.2.2 Space-Time-Domain Index Modulation

Space-time-domain IM techniques have been designed for jointly exploiting both the spatial- and time-domains for IM. In this family, space-time shift keying (STSK) [41], Trellis coded spatial modulation (TCSM) [42], space-time block coded spatial modulation (STBC-SM) [43], and differential spatial modulation (DSM) [44] constitute popular representative examples of space-time-domain IM. Explicitly, in order to attain transmit-diversity gains, the concept of STSK was proposed by Sugiura *et al.* [41] in 2010. The STSK scheme constitutes a generalised shift-keying architecture exploiting both the space as well as time dimensions and hence includes the SM and SSK schemes as special cases. Motivated by the idea of Trellis coded modulation (TCM) [45] and SM, the TCSM concept was proposed in [42], where the TAs are partitioned into sub-sets and the spacing between antennas is maximised. Another popular space-time-domain IM scheme so-called STBC-SM was first appeared in [43], as in the classic set-partitioning scheme of TCM [45], which benefits from both SM and STBC [11]. In [44], DSM was introduced, where the first part and the second part of information bits are used for selecting a space-time matrix indicating the antenna activation order and to determine the modulated symbols, respectively. In the following we focus our attention on describing the STSK technique, which has been used in Chapter 2 and Chapter 3 of this thesis.

The STSK design is based on the activation of appropriately indexed space-time dispersion matrices (DMs) [53] within each STSK block duration [41, 46, 54], instead of indexing TAs at each symbol duration as in the SM/SSK scheme of [8, 20], where the STSK scheme has been considered as a combination of linear dispersion coding (LDC) [53] and SM [46]. As a benefit of the high degree of design-freedom attained by appropriately choosing both the number of DMs as well as the size of the modulation scheme and the number of TAs/RAs, the STSK scheme becomes capable of striking a flexible trade-off between the diversity gain and multiplexing gain [54]. To further exploit the potential of STSK, a generalised STSK (GSTSK) scheme was proposed in [46], where the GSTSK scheme introduces an additional multiplexing gain by allowing multiple parallel streams of STSK transmission matrices to be transmitted simultaneously by each STSK transmitter. As a further development, attractive low-complexity STSK detectors [47, 55, 56] and GSTSK detectors [48] have also been proposed.

In order to overcome the frequency-selective fading imposed by the time dispersion associated with the multi-path components' delay in wideband channels, the STSK

Year	Author(s)	Contribution
2010	Sugiura *et al.* [41]	Proposed the concept of STSK, where the STSK scheme is capable of achieving a flexible trade-off between the diversity gain and multiplexing gain.
2011	Sugiura *et al.* [46]	Proposed the concept of GSTSK, where the GSTSK scheme introduces an additional multiplexing gain by allowing multiple parallel streams of STSK transmission matrices to be transmitted simultaneously by each STSK transmitter.
2011	Sugiura *et al.* [47]	Proposed a reduced-complexity near-optimal detection algorithm for coherently-detected STSK (CSTSK) and a concept of differentially-encoded STSK (DSTSK).
2012	Sugiura *et al.* [48]	Proposed a reduced-complexity soft decision-aided detector for both the STSK and GSTSK.
2012	Driusso *et al.* [49]	Proposed STSK-OFDM scheme in order to overcome the frequency-selective fading imposed by the time dispersion associated with the multi-path components delay in wideband channels.
2015	Kadir *et al.* [50]	Provided a survey and tutorial on the subject of STSK multicarrier systems.
2016	Hemadeh *et al.* [51, 52]	Proposed the concept of MS-STSK, which is a further generalised architecture by intrinsically amalgamating the philosophy of both SM and STSK.

Table 1.2: Main contributions on STSK scheme.

scheme was amalgamated with OFDM [49,50,57–59]. Additionally, based on intrinsically amalgamating the philosophy of both SM and STSK, the concept of multi-set STSK (MS-STSK) was proposed in [51] as a further generalised architecture. This MS-STSK scheme introduced an additional degree of design freedom into the system. Hence it was concluded in [51, 52, 60] that the MS-STSK scheme is capable of achieving a higher flexibility in terms of its data rate and its BER than the original STSK scheme of [41]. The major contributions on STSK are listed in Table 1.2.

1.2.3 Frequency-Domain Index Modulation

In this sub-section, we consider IM applied in the frequency domain [61–65]. OFDM [66] has become a ubiquitous digital communications technique as a benefit of its capability

of providing high-rate transmission by splitting the original serial data stream into many low-rate parallel data streams, hence mitigating the inter-symbol interference caused by a dispersive channel [67]. Thanks to the above-mentioned attractive features, OFDM has been widely adopted in standards such as Long-Term Evolution (LTE), IEEE 802.11x wireless local area networks (WLAN) and IEEE 802.16e-WiMAX [66].

As the frequency-domain representative of SM, OFDM relying on IM (OFDM-IM) was proposed in [62], where only a subset of subcarriers is activated to carry the classic modulated symbols. More explicitly, in OFDM-IM, the information is transmitted using both the classical constellation symbols and implicitly also by the indices of the activated subcarriers for conveying additional information bits without consuming extra energy. Owing to its advantages of providing a more flexible trade-off between the bandwidth efficiency and the BER performance, as well as owing to improving the BER performance for low-to-medium throughput, over the conventional OFDM, OFDM-IM has attracted considerable research interests over the past few years. The first frequency-domain IM aided OFDM was referred to as subcarrier IM OFDM (SIM-OFDM) [61]. However, in SIM-OFDM, the number of active subcarriers in each OFDM block is different. Furthermore, in [61] perfect detection was assumed at the receiver, but an incorrect detection of a subcarrier state may lead to the incorrect demodulation of all subsequent modulated symbols. Hence, an enhanced SIM-OFDM (ESIM-OFDM) scheme was proposed in [65] for avoiding the above-mentioned error propagation problem of SIM-OFDM. However, the limitation throughput of the ESIM-OFDM scheme deterred further attempts concerning its practical implementation. The investigations of [65] were carried out independently in [62], where the same scheme was termed as OFDM-IM.

As s further development, the capacity analysis of OFDM-IM was provided in [68], while its BER performance was disseminated in [69]. The selection of the optimal number of active subcarriers was investigated in [70,71], while the BER performance of OFDM-IM systems in the presence of carrier frequency offset was investigated in [72]. In order to improve the BER performance, the authors of [73,74] proposed a subcarrier-interleaving technique for the OFDM-IM scheme. Additionally, in [75] the transmit diversity order of OFDM-IM was improved from unity to two.

A pair of flexible OFDM-IM schemes were proposed in [76]. The first one was termed as OFDM relying on generalised IM (OFDM-GIM) that allows a high number of legitimate subcarrier activation patterns to be used. By contrast, the second one was referred to as OFDM using in-phase/quadrature IM that improves the throughput by applying IM independently to the in-phase/quadrature components of the complex data symbols analogous to the QSM scheme reviewed in Section 1.2.1. Following [76], a

low-complexity maximum likelihood (ML) detector was developed in [77], while further variants of OFDM-IM were disseminated in [78–85]. More specifically, in order to further increase the energy efficiency as well as the diversity gain of OFDM-IM, the authors of [82] proposed a compressed sensing (CS) assisted signalling strategy for OFDM-IM by carting the conventional IM to a high-dimensional virtual domain and then invoking CS for compressing the resultant high-dimensional IM symbols into low-dimensional frequency-domain subcarriers. A low-complexity detector based on the greedy pursuit concept of CS principles was also proposed in [82]. It was demonstrated in [82] that the proposed CS-assisted OFDM-IM system is capable of achieving both a higher bandwidth efficiency as well as an increased energy efficiency over the classical OFDM-IM systems. In order to reduce the practical implementation cost of OFDM-IM, low-complexity suboptimal detection methods were also proposed for OFDM-IM in [86–88]. Owing to the inherent advantages of OFDM-IM, there were some further studies focusing on the application of OFDM-IM to specific communication systems, such as vehicular communication systems [89, 90], underwater acoustic communication systems [91, 92], internet of things (IoT) communications [93] and visible light communications (VLC) [94].

MIMO techniques have become one of the most important next-generation waveform designs due to the continuously increasing demand for higher data rates as well as for improved quality of service (QoS) [2]. The authors of [95–97, 99–107] have further explored the potential of OFDM-IM and have reported promising results compared to conventional MIMO-OFDM schemes. Specifically, a MIMO-OFDM-IM scheme was proposed by Basar in [95] by modifying the single-input single-output OFDM-IM framework to operate for transmission over MIMO-aided frequency-selective fading channels. It was demonstrated [95] that a significant signal-to-noise ratio (SNR) improvement can be obtained by the MIMO-OFDM-IM scheme over classical MIMO-OFDM systems.

In [100], the author has shed light both on the implementation and on the BER performance of a MIMO-OFDM-IM scheme designed for next-generation wireless networks, where both the ML, a near-ML, and a low-complexity minimum mean square error (MMSE) and ordered successive interference cancellation based MMSE detectors was proposed. It was shown [100] that a beneficial trade-off between the BER performance and throughput was provided by the MIMO-OFDM-IM scheme. However, the strong inter-channel interference makes the detection of transmitted data a challenging task. Hence, several low-complexity detectors were proposed in [96, 102, 105] for MIMO-OFDM-IM schemes. As described in Chapter 2 in [97], we proposed a CS-aided OFDM-STSK-IM scheme by amalgamating the advantages of CS, OFDM-IM and

Year	Author(s)	Contribution
2009	Abu-alhiga *et al.* [61]	Proposed the concept of SIM-OFDM, which is the first attempt of the FD-IM for OFDM.
2011	Tsonev *et al.* [65]	Proposed the concept of ESIM-OFDM, which mitigates the error propagation problem of SIM-OFDM in [61].
2013	Basar *et al.* [62]	Proposed the concept of OFDM-IM, which activates a subset of subcarriers to carry the modulated symbols simultaneously.
2014	Wen *et al.* [70]	Proposed the optimal strategy in maximising the EE of OFDM-IM.
2015	Basar [75]	Proposed the concept of coordinate interleaved OFDM-IM (CI-OFDM-IM), where the real and imaginary parts of the data symbols are transmitted over different active subcarriers to achieve an additional diversity gain.
2015	Fan *et al.* [76]	Proposed two generalisation schemes of OFDM-IM, where a higher bandwidth efficiency than that of OFDM-IM is achieved.
2015	Basar *et al.* [95]	Proposed OFDM-IM-MIMO systems, where a flexible trade-off between bandwidth efficiency and BER performance is achieved.
2016	Zhang *et al.* [82]	Proposed a CS-assisted signalling strategy for OFDM-IM systems and an iterative residual check (IRC)-based low-complexity detector.
2017	Zheng *et al.* [96]	Proposed low-complexity detectors for OFDM-IM-MIMO systems in [95].
2017	Mao *et al.* [80, 81]	Proposed the concepts of both dual-mode OFDM-IM (DM-OFDM-IM) and generalised DM-OFDM-IM (GDM-OFDM-IM).
2017	Wen *et al.* [85]	Proposed a novel multiple-mode OFDM-IM (MM-OFDM-IM) scheme for improving the bandwidth efficiency by conveying information through multiple distinguishable modes and their full permutations.
2018	Lu *et al.* [97]	Proposed both uncoded and FEC-coded CS-aided OFDM-STSK-IM schemes, where CS-based low-complexity detector is also provided.
2018	Hemadeh *et al.* [98]	Explored the CS-aided OFDM-STSK-IM scheme of [97] with beamforming technique in mmWave communications.
2019	Zhang *et al.* [84]	Proposed the concept of linear precoding-assisted IM for OFDM (LPIM-OFDM).
2019	Kadir *et al.* [99]	Provided analysis of achievable rate and BER performance, was well as design guidelines for OFDM-STSK-IM schemes.

Table 1.3: Main contributions on frequency-domain IM.

STSK principles for transmission over frequency-selective fading channels, where the CS-assisted subcarrier-index strategy of [82] was exploited in our OFDM-STSK framework for increasing the energy efficiency. First, a ML detector was applied for determining the best-case bound of the system's BER performance. It was demonstrated by our simulation results that the CS-aided OFDM-STSK-IM system is capable of achieving higher SNR gains than the conventional OFDM-STSK system. Then in order to mitigate the potentially excessive complexity of the ML detector, we also proposed a pair of reduced-complexity detectors based on CS principles [108] at the cost of a modest BER degradation. Additionally, in order to achieve a near-capacity performance for the family of MIMO-OFDM-IM systems, forward error correction (FEC) [109] was invoked for our proposed CS-aided OFDM-STSK-IM system, which operated by iteratively exchanging extrinsic information between the associated soft decoders. Following [97] of Chapter 2, we amalgamated the CS-aided OFDM-STSK-IM scheme with beamforming in millimetre-wave (mmWave) communications [98], where the BER performances of both the uncoded and the coded systems were analysed, as well as the capacity was quantified with the aid of extrinsic information transfer (EXIT) charts [110]. More recently, Kadir [99] proposed a SIM-OFDM-aided STSK scheme, where a comprehensive analysis of its BER performance and achievable rate was provided. The major contributions on frequency-domain IM are listed in Table 1.3.

1.2.4 Multi-Dimensional Index Modulation

Motivated by the performance gains that can be potentially realised by exploiting the index bits, multi-dimensional IM techniques have been proposed in [52, 111–117] by indexing multiple transmission entities as seen in Fig. 1.2, such as antennas, subcarriers, time slots and radio frequency (RF) mirrors, simultaneously.

Specifically, a generalised space-frequency IM scheme was proposed in [111] by combining the OFDM-IM concept with the GSM principle and exploiting both the spatial and frequency domains for IM. It has been shown in [111] that the generalised space-frequency IM scheme is capable of providing performance improvements over conventional MIMO-OFDM with the aid of ML detection for lower-order constellations, when a joint space-frequency indexing strategy is applied at the transmitter side. However, it becomes much more challenging to detect both the active TAs, as well as the active subcarrier indices and the classic modulated symbols due to the strong interference imposed both on the OFDM-IM subblock and TAs. Although the ML detector is capable of achieving the optimal performance, its potentially excessive computational complexity

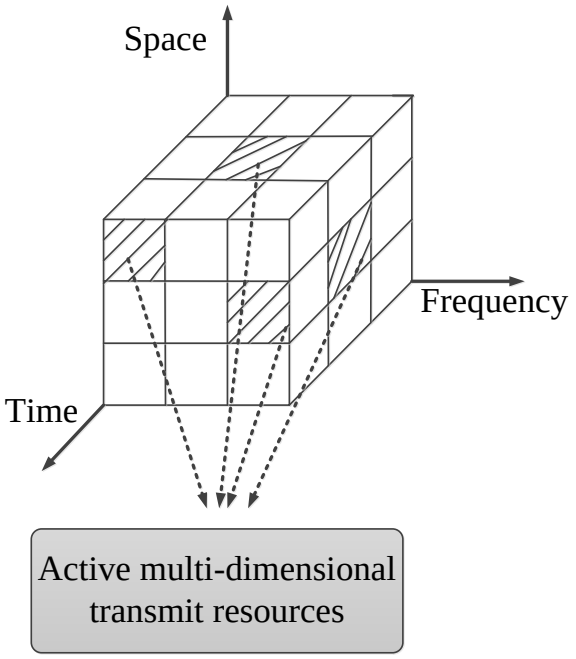

Figure 1.2: An example of multi-dimensional IM by exploring space, time, and frequency resources.

makes it impractical for the generalised space-frequency IM scheme. Hence, it is essential to conceive a low-complexity detector for generalised space-frequency IM schemes, such as that in [111]. In [112], a space-time IM (STIM) scheme was proposed, where both the time slots and TAs are indexed. It was shown that STIM of [112] achieves a better performance than conventional OFDM. Furthermore, a low-complexity detection algorithm based on the classic message passing [118] principle was also proposed in [112] for the detection of high-dimensional STIM signals. In [114], a time-indexed media-based modulation (TI-MBM) arrangement was proposed, where both the time slots and RF mirrors were indexed, and low-complexity algorithms based on the CS principles were proposed. It was shown in [114] that the TI-MBM scheme operating in frequency-selective channels achieves a better BER performance than the conventional media-based modulation (MBM) of [119]. Recently, a space-time media-based modulation (ST-MBM) [113] scheme based on the principles of SSK and MBM was proposed, and its theoretical performance was analysed. The associated computer simulations showed the superior performance of the ST-MBM scheme over the state-of-the-art MIMO based transmission systems.

More specifically, in [117] we proposed a CS-aided multi-dimensional IM scheme relying on both frequency- and spatial-domain IM. Explicitly, in [117], we designed both the optimal ML detector as well as a reduced-complexity so-called simultaneous matching

Year	Author(s)	Contribution
2016	Datta *et al.* [111]	Proposed a generalised space-frequency IM scheme by combining OFDM-IM concept with GSM principle and exploiting both spatial and frequency domains for IM, where a joint space-frequency indexing strategy is applied at the transmitter.
2017	Shamasundar *et al.* [115]	Proposed some IM schemes in which multiple transmission entities are indexed simultaneously. Results showed that improved BER performance is achieved when the number of indexed transmission entities is increased.
2017	Jacob *et al.* [112]	Proposed the concept of STIM, where information bits are conveyed through antenna indexing in the spatial domain, slot indexing in the time domain, and classical constellation symbols.
2017	Shamasundar *et al.* [114]	Proposed the concept of TI-MBM, where both indices of time slots and RF mirror activation patterns are explored.
2019	Yigit and Basar [113]	Proposed concept of ST-MBM, which is based on principles of SSK and MBM.
2019	Lu *et al.* [117]	Proposed a CS-aided multi-dimensional IM scheme relying on both frequency- and spatial-domain IM as an enhancement of [97], where a group-based TA indexing strategy is applied in the spatial domain instead of fixing the antenna indexing for the whole OFDM frame.

Table 1.4: Main contributions on multi-dimensional IM applications.

pursuit (S-MP) detector based on CS principles for the CS-aided multi-dimensional IM scheme. Furthermore, the BER performance and the capacity of CS-aided multi-dimensional IM scheme were analysed. A better performance was achieved compared to the classical MIMO-OFDM and to our system of Chapter 2. The main contributions on multi-dimensional IM applications are listed in Table 1.4.

1.2.5 Application of IM to Large-Scale MIMO and Multi-User Scenarios

The escalating tele-traffic growth outstrips the capacity increase of wireless communications. Hence, the capacity of wireless communications networks has to be increased in order to guarantee the QoS requirements of mobile applications [129]. The concept of

Year	Author(s)	Contribution
2011	Renzo *et al.* [120]	The performances of SSK modulation and GSSK modulation for multi-user MIMO wireless systems in the presence of multiple-access interference were studied and compared.
2011	Serafimovski *et al.* [121]	Proposed a jointly optimum multi-user detector of the SM in the multi-user scenario, for minimising the BER for all users and not suffering from the near-far problem.
2014	Narasimhan *et al.* [122]	Proposed two novel algorithms for detection of large-scale SM-MIMO signals at the BS, where acceptable performance was achieved.
2015	Narasimhan *et al.* [123]	Investigated GSM for large-scale multi-user MIMO communications on the uplink, where the performance was analysed and low-complexity algorithm based on message passing was proposed.
2015	Rodriguez [124]	Designed a CS-based detector that allows the reduction of the signal processing load at the BS particularly pronounced for SM in large-scale MIMO systems, where analytical performance and complexity studies were carried out.
2016	Gao *et al.* [125]	Proposed a large-scale SM-MIMO uplink system with RA selection at the BS for reducing the cost and the power consumption, where both a joint transmission scheme for all users and the CS-based detector were designed.
2016	Zhu *et al.* [126]	Proposed SIM-OFDM for multi-user uplink transmission in MIMO systems, where an iterative detector based on the message passing algorithm was developed.
2017	Hemadeh *et al.* [127]	Proposed a multi-user steered multiset STSK (MU-MS-STSK) scheme for the downlink of mmWave communications, which was combined with beamforming technique to overcome the high attenuation of mmWaves.
2019	Lu *et al.* [128]	Proposed both uncoded and coded CS-aided two-dimensional IM schemes for the multi-user LS-MIMO uplink, where for the sake of attaining improved diversity gains, different TA activation patterns were employed for different transmitted symbols, and a reduced-complexity multi-user detector based on CS principles was also proposed.

Table 1.5: Main contributions on IM techniques in large-scale multi-user scenarios.

large-scale MIMO (LS-MIMO), which is also known as massive MIMO, was proposed by Marzetta [130]. Explicitly, the acronym LS-MIMO refers to the system that applies hundreds of antennas for simultaneously serving dozens of users [131]. Both the theoretical and simulation results of [129,132,133] indicated that a LS-MIMO scheme is capable of significantly improving the bandwidth efficiency, despite reducing the transmit power. Attracted by its appealing bandwidth efficiency vs energy efficiency trade-off, a LS-MIMO scheme has been regarded as a promising technique of next-generation wireless communications systems [3].

SM is also attractive in the context of LS-MIMO systems due to its reduced power consumption and more modest hardware cost. Hence several contributions [120–125, 127,134–155] have reported on the implementation.

In [120–125,134–146], the uplink transmission scenarios were investigated and SM-based solutions were provided. In the uplink scenario, the users are equipped with multiple TAs and the base station (BS) is equipped with tens to hundreds RAs. In most of these studies, the authors have investigated low-complexity detection algorithms by exploiting the sparsity of transmitted vectors of SM and its variants. In [139], a low-complexity MMSE detector based on the nearest neighbour search was proposed, where it was demonstrated by computer simulations that the detector is capable of approaching the interference-free BER performance at a much lower complexity. In [140] and [124], a matching pursuit based CS-aided detector was proposed for LS-MIMO schemes, where the complexity of the SM matching pursuit detector was analysed and it was shown to be a promising candidate for increasing the energy efficiency of SM-LS-MIMO systems. In [125], RA selection was considered at the BS for reducing both the cost and the power consumption. Furthermore, both a joint multi-user transmission scheme as well as a CS-based detector conceived for exploiting the sparsity of the transmitted signals. On the other hand, the authors of [127,147–155] considered downlink transmission scenarios by applying SM and its variants to LS-MIMO systems. These studies were mainly focused on multi-user precoding schemes designed for simultaneously transmitting to different users. In the downlink scenario, a BS equipped with tens to hundreds TAs was used to simultaneously serve different users.

Additionally, the authors of [126, 156] investigated OFDM-IM involved in LS-MIMO systems. Specifically, the authors of [156] investigated multi-user detection aided LS-MIMO-OFDM-IM systems relying on realistic imperfect channel state information (CSI) relying on a low-complexity generalised approximate message passing algorithm conceived for uplink transmission. It was shown in [156] that the LS-MIMO-OFDM-IM system is capable of improving the energy efficiency without sacrificing the bandwidth

efficiency and BER performance compared to its LS-MIMO-OFDM counterpart. Furthermore, the same authors [126] investigated OFDM-IM in a multi-user LS-MIMO uplink scenario and demonstrated that improvements can be obtained in terms of the PAPR, energy efficiency and BER performance compared to classical multi-user OFDM systems.

In Chapter 4, we proposed both uncoded and coded CS-aided (generalised) space-frequency IM (CS-(G)SFIM) schemes for the multi-user LS-MIMO uplink by exploiting both spatial- and frequency-domain IM at the transmitter. The BER analysis and the associated EXIT chart-based capacity results were also provided. These results were also disseminated in [128], which is the first contribution exploring the multi-dimensional IM technique in large-scale multi-user scenarios. To elaborate a little further, in [128] we designed a novel index separation strategy in for achieving a higher design flexibility in comparison to the joint space-frequency indexing strategy of [111,157,158]. Additionally, for the sake of improving the diversity gains, different TA activation patterns have been employed for different transmitted symbols instead of fixing the active TAs for the entire OFDM subcarrier group. Finally, we have also proposed a reduced-complexity detector in [128], which made the CS-(G)SFIM scheme feasible for employment in multi-user LS-MIMO scenarios. The main contributions on IM techniques in large-scale multi-user scenarios are listed in Table 1.5.

1.3 Compressed Sensing for Wireless Communications

In recent years, CS has attracted a great deal of research attention [159–164] as means of reconstructing sparse signals from compressed measurements, since the constitutions of Donoho [108] and Candes *et al.* [165]. In other words, CS is a sampling method connected to transform coding, which converts sparse high-dimensional input signals into significantly lower-dimensional signals, as detailed in [159, 166, 167].

Recently, CS techniques have been invoked for solving numerous wireless communications problems, such as channel estimation [168–171], interference cancellation [172], impulse noise cancellation in OFDM systems [173, 174], direction estimation in mmWave communications [175], spectrum sensing in cognitive radios [176], and symbol detection [177]. In this treatise, we do not dedicate much attention to the mathematical properties of CS, since the interested readers can find the details in [159, 178–184]. Explicitly, in [178], a short summary of CS was presented, while an extended summary can be found in [159]. A tutorial on CS with an emphasis on its mathematical properties and performance guarantee was provided by Forucart and Rauhut [179], but a

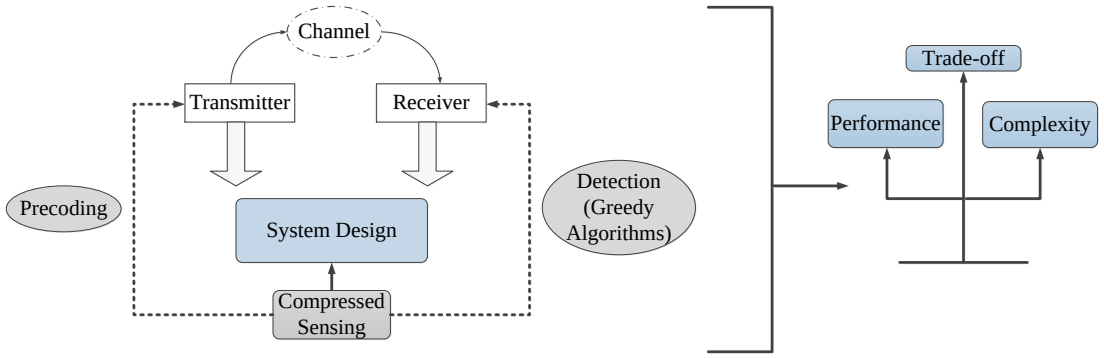

Figure 1.3: The general framework of the CS-aided system design considered in this thesis.

similar approach was also pursued in [180]. Furthermore, Eldar and Kutyniok provided a comprehensive treatment of diverse issues in their book [181], such as sparse recovery algorithms, the associated performance guarantees and CS applications. The CS techniques conceived for wireless networking application were discussed in [182], complemented by [183, 184].

Here, we focus our attention in the context of CS on the IM techniques discussed in Section 1.2. There are three distinct CS sub-problems related to wireless communications [184]: sparse estimation, support identification and sparse detection. Accordingly, we commence with the basic model, where the signal of interest is transmitted over linear channels contaminated by additive white Gaussian noise (AWGN), where the input-output relationship is given by $\mathbf{y} = \mathbf{A}\mathbf{s} + \mathbf{v}$, where $\mathbf{y} \in \mathbb{C}^m$ is the m-length vector of received signals (referred to as measurement vector), $\mathbf{A} \in \mathbb{C}^{m \times n}$ is the measurement matrix, $\mathbf{s} \in \mathbb{C}^n$ is the n-length desired signal vector to be recovered, and $\mathbf{v} \in \mathbb{C}^m$ is the noise vector with a mean of zero and a variance of σ_v^2. In particular, we are primarily interested in the scenario where the desired vector $\mathbf{s}$ is an exactly k-sparse vector, i.e. we have $\|\mathbf{s}\|_0 = k$, where the number k of non-zero elements in $\mathbf{s}$ is far smaller than its dimension n. Hence $\mathbf{s}$ is a compressible vector. In this case, we are interested in detecting the sparse vector $\mathbf{s}$ from its lower-dimensional observations in $\mathbf{y} \in \mathbb{C}^m$ associated with $m \leq n$, whilst ensuring that the target performance of the detection can indeed be achieved. In other words, the basic premise of CS in wireless communications is that the sparse signal vector can be reconstructed from the vector of received signals [183]. More explicitly, we would like to strike a compelling trade-off between the performance attained and the complexity imposed instead of achieving the optimal performance regardless of the complexity , as seen in Fig. 1.3. Specifically, the columns of the measurement matrix $\mathbf{A}$ should be carefully designed to be as uncorrelated as

possible for meeting the mutual incoherence property (MIP)[1] [185], so that the uniqueness of the resultant sparse solution can be guaranteed. In particular, we convert the measurement matrix design problem to the practical design problem associated with a transmit precoding scheme in the following chapters.

Year	Author(s)	Contribution
2007	Tropp *et al.* [186]	Proposed the concept of OMP greedy algorithm.
2009	Needell *et al.* [187]	Proposed the concept of CoSaMP greedy algorithm.
2009	Dai *et al.* [188]	Proposed the concept of SP greedy algorithm.
2009	Blumensath *et al.* [189]	Proposed the concept of IHT iterative algorithm.
2011	Bayati *et al.* [190]	Proposed the concept of AMP iterative algorithm.
2012	Wang *et al.* [191]	Proposed the concept of gOMP greedy algorithm.
2014	Kwon *et al.* [192]	Proposed the concept of MMP greedy algorithm.

Table 1.6: History of iterative greedy algorithms conceived for sparse recovery.

In recent years, a family of iterative greedy algorithms conceived for reducing the complexity has attracted significant research attention as a benefit of its simple geometric interpretation. To elaborate a little further, they were designed for further reducing the computational complexity of the l_1-norm minimisation technique [165]. The authors of [193] proposed the so-called orthogonal matching pursuit (OMP) algorithm, in which the OMP algorithm iteratively updates the results by finding the specific column of $\mathbf{A}$ having the maximum correlation with the current residual. Then a number of variants of the OMP algorithm were proposed, such as the generalised OMP (gOMP) [191], the compressive sampling matching pursuit (CoSaMP) [187], the subspace pursuit (SP) [188] and the multipath matching pursuit (MMP) [192]. These variants have a refined step conceived for improving the recovery performance attained. Additionally, the technique termed as iterative hard thresholding (IHT) was proposed in [189, 194] for further improving the achievable recovery performance. An approximate message passing (AMP) detection algorithm was proposed in [190], whose complexity is comparable to that of the IHT algorithm. In a nutshell, there are two important issues in the design of CS-based wireless communications systems, namely that of mapping the wireless communications problem into an appropriate CS problem and the identification of the most appropriate recovery algorithm. Note that the algorithm should be suitably modified for meeting the

[1]The MIP is defined as the mutual coherence of a matrix is very small [185].

requirements of the specific wireless communications systems. The history of iterative greedy algorithms conceived for sparse recovery is provided in Table 1.6 at a glance.

1.4 Novel Contributions of the Thesis

The thesis is based on three published journal papers [97,98,117] and a submitted journal paper [128]. The novel contributions of this thesis are summarised below.

- **Chapter 2: [97, 98]**

  1. Bearing in mind the advantages of OFDM-STSK, OFDM-IM and CS-OFDM-IM for transmission over frequency-selective fading channels, a novel CS-aided OFDM-STSK scheme relying on frequency-domain IM (CS-aided OFDM-STSK-IM) is proposed, where the coordinate interleaving technique of [75] is exploited for achieving an additional diversity gain, hence improving the performance.
  2. First, the classic ML detector is used for recovering the information bits, which forms the best-case performance bound. We also formulate the Discrete-Input Continuous-Output Memoryless Channel (DCMC) capacity of the system proposed. The novel CS-aided OFDM-STSK-IM scheme is shown to be capable of achieving a better BER performance than the classical OFDM-MIMO scheme.
  3. Then, in order to mitigate the excessive complexity of the optimal ML detector, a pair of reduced-complexity detectors based on CS principles is proposed, which is capable of attaining a considerably lower complexity than the ML detector at the cost of a modest BER degradation.
  4. Furthermore, we also conceive soft-input soft-output decoding for the proposed CS-aided OFDM-STSK-IM system. Explicitly, a two-stage serially concatenated soft-decision based detector is designed for our CS-aided OFDM-STSK-IM scheme, where a pair of inner and outer decoders iteratively exchange their extrinsic information for the sake of achieving near-capacity performance.

- **Chapter 3: [117]**

  1. A novel CS-aided multi-dimensional IM system relying on both frequency-domain and spatial-domain IM for improving the performance by attaining

an improved diversity gain, whilst increasing the system capacity by indexing multiple transmission entities. This scheme is compared both to the classical OFDM-MIMO system and to our previously proposed CS-OFDM-STSK-IM system of Chapter 2. Furthermore, an upper bound of the average bit error probability (ABEP) of the proposed CS-aided multi-dimensional IM system is derived and confirmed by computer simulations. This flexible multi-functional design allows us to strike a flexible trade-off between the performance, the throughput and the complexity, where the different components in the design can be conveniently configured in order to attain our specific design requirements.

2. Then a reduced-complexity so-called simultaneous matching pursuit (S-MP) based detector is proposed for simultaneously detecting multiple measurement vectors by exploiting the powerful CS principles, whilst mitigating the potentially excessive complexity of the ML detector at the cost of a modest performance loss. Explicitly, the S-MP detector is specifically designed for our novel CS-aided multi-dimensional IM system, where the active TAs and active subcarriers are first jointly detected and then they are utilised for reconstructing the space-time symbols.

3. Then powerful CS-aided multi-dimensional soft-input soft-output IM receivers using both the ML detector and the proposed S-MP detector are conceived for iteratively exchanging extrinsic soft information between the constituent decoders in order to achieve a near-capacity performance. More specifically, EXIT charts are used for visually characterising the flow of soft-information between the constituent decoders of our concatenated structure. We also construct EXIT charts for evaluating the maximum achievable rate of the proposed system using both the ML detector and the S-MP detector. Furthermore, the DCMC capacity of the proposed CS-aided multi-dimensional IM scheme is formulated and compared to the maximum achievable rate of the system derived from the EXIT charts.

- **Chapter 4:** [128]

1. A CS-SFIM scheme is proposed for striking an improved performance vs complexity trade-off than the conventional LS-MU-MIMO-OFDM systems. The basic idea of the proposed CS-SFIM scheme is that for each user the information is conveyed by three distinctive parts, namely by the frequency-domain IM, spatial-domain IM representing the TA activation and by the classic Amplitude/Phase Modulation (APM) symbols. Additionally, the new generalised

SM, namely CS-GSFIM, is also invoked for improving the throughput without increasing the number of RF chains compared to the CS-SFIM scheme of Section 4.2.1.2. More particularly, in order to attain improved diversity gain, in contrast to Chapter 3, different TA activation patterns are employed for the different transmitted symbols instead of fixing the active TAs for the entire OFDM subcarrier group as in Chapter 3. We then analyse the ABEP of the proposed CS-GSFIM system using the ML detection and we derive an upper bound of the ABEP. Our numerical results demonstrate that the proposed MU CS-(G)SFIM system attains better BER performance than the conventional MU-MIMO-OFDM system, the MU CS-aided multi-dimensional system using the same TA activation pattern for each subcarrier group shown in Chapter 3, and the MU CS-aided frequency-domain IM shown in Chapter 2 at the same bandwidth efficiency.

2. Then our reduced search-space based iterative matching pursuit (RSS-IMP) detection scheme is proposed for the CS-GSFIM system, which relies on CS principles. The computational complexities are compared for the proposed systems using the ML detector, the MMSE detector and the novel RSS-IMP detector. We demonstrate that the proposed RSS-IMP detector is capable of achieving an improved BER vs complexity trade-off than the conventional MU-MIMO-OFDM system using the ML detector and the proposed systems employing the MMSE detector, despite its significantly reduced complexity. This makes the proposed CS-GSFIM system eminently suitable for LS-MU-MIMO communications.

3. We then proceed by investigating the performances of the proposed CS-(G)SFIM systems in the presence of imperfect channel state information (ICSI). It is demonstrated by our simulation results that the proposed systems are more robust to channel estimation errors than the conventional MU-MIMO-OFDM system.

4. For the sake of attaining a near-capacity performance, we then design specific soft multi-user detectors based on both the ML detector and on the proposed RSS-IMP detector for iteratively exchanging soft information with the FEC decoders. Our FEC-coded numerical results indicate that near-capacity performances can indeed be achieved by the proposed multi-user detectors. Additionally, we investigate the maximum achievable rates of the proposed CS-(G)SFIM system with the aid of EXIT charts.

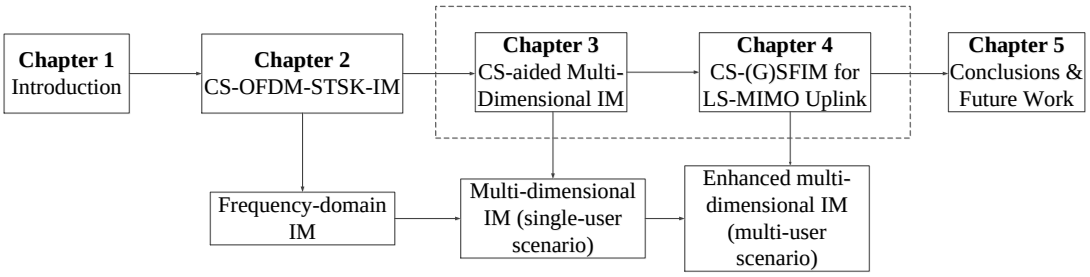

Figure 1.4: Organisation of the thesis.

1.5 Outline of the Thesis

In this thesis, we focus our attention on the multi-dimensional IM design of both single-user and multi-user scenarios, including the employment of a CS-aided indexing strategy at the transmitter, the design of our CS-assisted low-complexity detector and the design of soft decoders. To begin with, let us now highlight the outline of this thesis, which is portrayed in Fig. 1.4.

- **Chapter 2: Compressed Sensing-Aided Frequency-Domain Index Modulation [97, 98]**

  In Chapter 2, we propose a novel CS-aided OFDM-STSK scheme relying on frequency-domain IM. The general background knowledge on STSK, OFDM-IM, and CS-OFDM-IM is reviewed in Section 2.2. The transmitter model of CS-aided OFDM-STSK conceived with frequency-domain IM is introduced in Section 2.3.1. In Section 2.3.2, the optimal ML detector is detailed and then a pair of reduced-complexity detectors based on CS principles is proposed. Additionally, a two-stage serially concatenated soft-decision detector is designed for the CS-aided OFDM-STSK-IM system for the sake of achieving a near-capacity performance. Our performance analysis and simulation results, including the DCMC capacity analysis, BER performances and the computational complexity analysis are discussed in Section 2.4.1, Section 2.4.2, and Section 2.4.3, respectively. Finally, we conclude this chapter in Section 2.5.

- **Chapter 3: Compressed Sensing-Aided Multi-Dimensional Index Modulation [117]**

  In Chapter 3, we conceive a CS-aided multi-dimensional IM scheme by combining the benefits of STSK, OFDM-IM and SM. Explicitly, extra information bits are transmitted through the active indices of both the TAs and subcarriers, whilst striking a flexible design trade-off between the throughput and the diversity gain. In Section 3.2, the system model of the proposed CS-aided multi-dimensional IM

scheme is introduced, including the transmitter model in Section 3.2.1 and the receiver model in Section 3.2.2. Then the hard-decision based ML and the proposed S-MP detectors are introduced in Section 3.3.1, as well as the theoretical BER performance relying on the ML detector is analysed. The soft-decision based ML and S-MP detectors are designed and detailed in Section 3.3.2. In Section 3.4, our performance analysis is discussed, including the trade-off between the BER performance and the computational complexity, the EXIT chart analysis, the DCMC capacity analysis, the analysis of the maximum rates attained with the aid of EXIT charts, as well as the coded BER performance. Finally, we conclude this chapter in Section 3.5.

- **Chapter 4: Multi-Dimensional Index Modulation for the Large-Scale Multi-User MIMO Uplink [128]**

  In Chapter 4, we propose both uncoded and coded CS-aided two-dimensional IM schemes, namely CS-(G)SFIM conceived for the LS-MIMO uplink upon combining the benefits of LS-MIMO, SM, GSM, OFDM-IM and CS for uplink transmission over frequency-selective fading channels. Specifically, compared to the multi-dimensional design of Chapter 3, the CS-(G)SFIM proposed here applies different TA activation patterns for different transmitted symbols instead of fixing the active TAs for each subcarrier block, which increases both the diversity gain and the design flexibility. In Section 4.2.1, the uplink transmission model is detailed by introducing the components of the transmitter, such as the virtual-domain frequency index selector, spatial-domain modulator/mapper, space-frequency index modulator, compressed sensing block and the block assembler. In Section 4.3, both the hard-decision-aided and soft-decision-aided multi-user detectors are designed, including the optimal ML detector and the novel RSS-IMP detector. Additionally, the computational complexity is analysed in Section 4.3.3. Then in Section 4.4 we provide performance results and comparisons between the different systems, where we demonstrate that the proposed CS(G)SFIM scheme is capable of achieving better performances than the systems proposed both in Chapter 2 and Chapter 3 as well as the classical multi-user MIMO-OFDM systems. We also demonstrate that the proposed RSS-IMP detector is capable of making the CS-(G)SFIM system suitable for LS-MIMO scenarios. Finally, we conclude in Section 4.5.

- **Chapter 5: Conclusions and Future Research**

  In Chapter 5, we summarise the main findings of the thesis, provide brief design guidelines and outline a range of suggestions for future research.

Chapter 2

Compressed Sensing-Aided Frequency-Domain Index Modulation

2.1 Introduction

Index modulation (IM)-assisted wireless communications have attracted substantial attention due to their potential of striking an attractive trade-off between bandwidth efficiency and energy efficiency [1,5–7]. Moreover, OFDM-IM proposed in [62], as an attractive frequency-domain IM scheme, has attracted considerable research interest over the past few years owing to its advantages of providing a more flexible trade-off between the bandwidth efficiency and the error probability than conventional OFDM. In order to further increase the energy efficiency of the OFDM-IM system, while potentially increasing its bandwidth efficiency, a compressed sensing (CS)-aided OFDM-IM scheme was proposed in [82]. They can also be conveniently combined with powerful MIMO techniques for meeting the demand for continuously increasing data rates as well as quality of service (QoS) [2]. As a particularly powerful solution, space-time shift keying (STSK) [41, 50] was proposed for extending the concept of the conventional spatial modulation (SM) [8] and space-shift keying (SSK) [195] by exploiting both the spatial and temporal dimensions, in order to provide both substantial transmit-diversity and multiplexing gains.

Basar [95, 100] has explored the potential intrinsically amalgamating OFDM-IM with MIMO systems and reported promising results outperforming MIMO-OFDM schemes.

However, Basar's studies were based on using hard-decision-aided detection at the receiver. Hence Basar's schemes can be substantially improved by invoking powerful forward error correction (FEC) coding schemes [109] upon incorporating redundancy into the transmitted information, especially, when soft-decision-aided detection is used at the receiver. Hence, a plethora of powerful channel coding techniques have been proposed since 1950s, such as Hamming codes [196], Convolutional Codes (CCs) [197], turbo codes [198] as well as diverse other channel coding techniques presented in [199]. In 1974, a potent decoding technique known as the Maximum A Posteriori (MAP) algorithm was conceived for attaining the minimum bit error ratio (BER) in the context of CC [200]. As another powerful concept, concatenated codes were proposed [201] by Forney as early as 1966. The turbo principle of [198] was also extended to block codes exchanging extrinsic soft information similar to Berrou's original turbo codes relying on CCs [202]. Explicitly, in [198], parallel concatenation of two Recursive Systematic Convolutional (RSC) codes was applied by Berrou and Glavieux, where the soft-decision detector iteratively exchanged extrinsic information between the decoders for the sake of achieving an infinitesimally low BER at near-capacity SNRs. As a further advance, Extrinsic Information Transfer (EXIT) charts were introduced in [203] and [204], which constitute a powerful semi-analytical tool for investigating the convergence behaviour of soft-decision-aided FEC-coded systems as well as for evaluating their achievable rate.

In this chapter, inspired by the benefits of the above-mentioned OFDM-STSK, OFDM-IM, CS and FEC coding schemes, we propose a novel CS-aided frequency-domain index modulation scheme, namely the CS-OFDM-STSK-IM arrangement shown in Fig. 2.1, where the information bits are mapped to and transmitted through the spatial-, time- and frequency dimensions for striking a flexible trade-off between the energy efficiency, bandwidth efficiency, BER performance and complexity. Both uncoded and FEC-coded schemes are proposed as well as investigated in this chapter. Against this background, the novel contributions of this chapter can be summarised as follows:

- By amalgamating the advantages of OFDM-STSK, OFDM-IM and CS-based OFDM-IM designed for communicating over frequency-selective fading channels, we propose a new CS-aided OFDM-STSK arrangement relying on frequency-domain index modulation, where coordinate interleaving is invoked for achieving an additional diversity gain, hence improving the performance. Initially, the optimal but potentially excessive-complexity ML detector is used for recovering the information bits, which forms the best-case bound on the system's performance. Compared

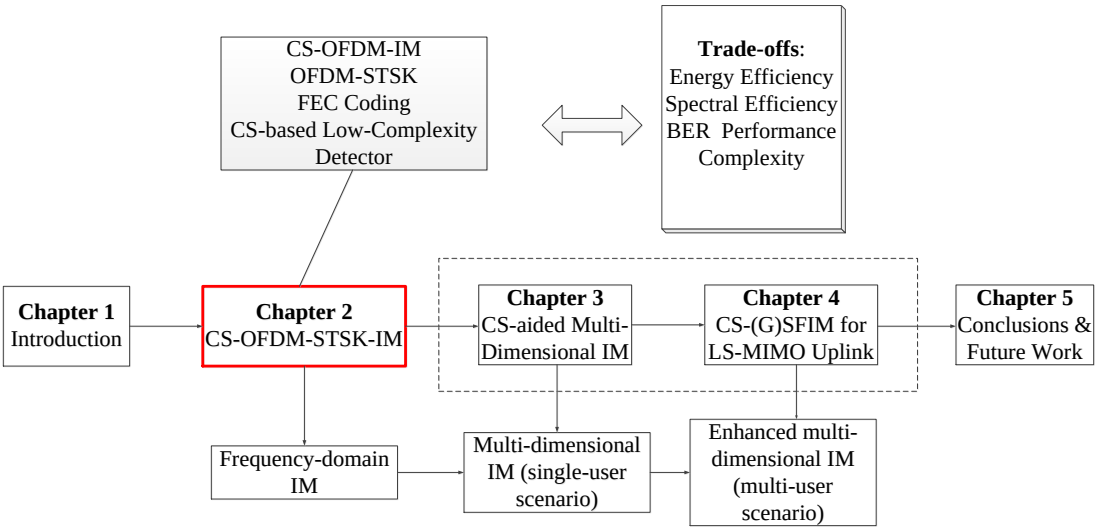

Figure 2.1: Interconnection of Chapter 2 with the rest of the thesis.

to the classical OFDM-STSK relying on the ML detector at the receiver, the proposed system exhibits about 8.1 dB SNR-gain at the BER of 10^{-5} compared to conventional OFDM-STSK.

- Then, to mitigate the excessive complexity of the ML detector, we propose a pair of reduced-complexity detection algorithms, which impose a considerably lower complexity than the ML detector at the cost of a modest BER degradation.

- We also conceive a soft-input soft-output decoder for the proposed CS-aided OFDM-STSK-IM system. This is the first CS-aided OFDM-STSK-IM system relying on soft-decoding-aided channel coding in the open literature. Explicitly, a two-stage serially concatenated soft-decision detector is applied to the proposed CS-aided OFDM-STSK-IM system, where a pair of inner and outer decoders iteratively exchange their extrinsic information in order to achieve a near-capacity performance.

The rest of the chapter is organised as follows. In Section 2.2, we briefly provide the required background knowledge on the STSK, OFDM-IM and CS-OFDM-IM schemes, respectively. In Section 2.3.1, we first outline the transmitter model of our proposed CS-aided OFDM-STSK-IM scheme. Then the detection algorithms are detailed in Section 2.3.2, including the hard-decision-based optimal ML detector, a pair of new hard-decision-based reduced-complexity detectors and powerful soft-decision-based detectors. Our performance analysis and simulation results are provided in Section 2.4. Finally, we conclude this chapter in Section 2.5.

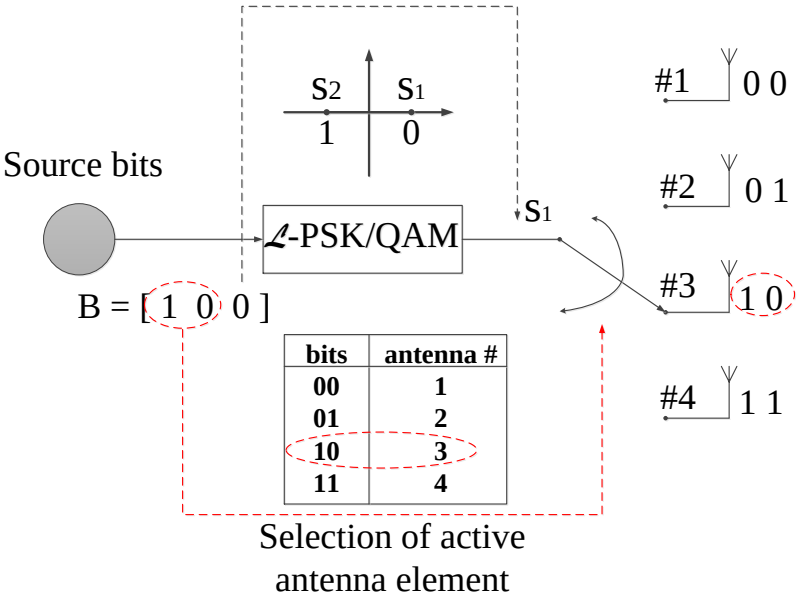

Figure 2.2: The schematic of SM transmitter, while having an example of $\mathcal{L} = 2$ and $M = 4$.

2.2 Background

In this section, we commence by briefly portraying STSK as one of the most sophisticated space-time-domain IM techniques, followed by OFDM-IM and OFDM-IM using CS, as detailed in Section 2.2.1, Section 2.2.2 and Section 2.2.3, respectively.

2.2.1 Review of STSK

As introduced in Section 1.2.1, the so-called SM/SSK scheme [8,19,20] is based on a novel modulation technique relying on activating one out of a total of M transmit antenna (TA) elements during each symbol interval. Since the STSK scheme is inspired by and partly based on the SM/SSK concept, it is useful to briefly introduce the principle of the SM/SSK scheme. Explicitly, in conventional SM scheme, it is assumed that $B = \log_2(\mathcal{L}) + \log_2(M)$ source bits are transmitted during each channel use, where $\log_2(\mathcal{L})$ source bits are mapped to the classic $\mathcal{L}$-PSK/QAM symbol and $\log_2(M)$ source bits are conveyed by the activation of one out of M TA elements. Then the SM modulated signals $\mathbf{S}_{l,m} \in \mathbb{C}^{M\times 1}$ are expressed as [8]

$$\mathbf{S}_{l,m} = [\underbrace{0,\cdots,0}_{m-1}, \overbrace{s_l}^{m^{th}position}, \underbrace{0,\cdots,0}_{M-m}]^T, \tag{2.1}$$

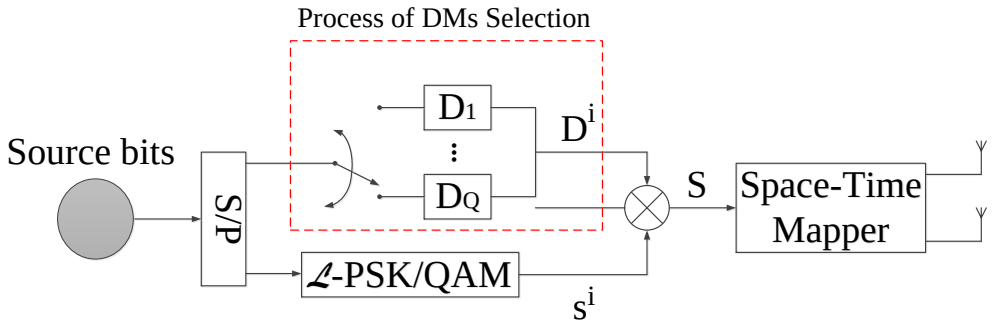

Figure 2.3: The schematic of STSK transmitter.

where s_l represents the classic PSK/QAM symbols modulated based on the $\log_2(\mathcal{L})$ source bits, and the integer $m = \log_2(M)$ represents the TA index bits. Note that according to [20], the SSK scheme can be regarded as a special case of the SM, where only the spatial domain is exploited to convey information. In order to expound further, we portray the schematic of the SM transmitter in Fig. 2.2 by considering the example of $\mathcal{L} = 2$ and $M = 4$. Then $B = 3$ source bits are split into one bit used for generating a BPSK-modulated symbol and two bits are employed for activating the TA element. This process is shown in Fig. 2.2. More explicitly, observe in Fig. 2.2 that if the source bits are "[100]", then the third TA is activated, while the the constellation point s_1 shown in Fig. 2.2 is chosen as the transmitted symbol, and so on. Specifically, in the SSK scheme, the activated TA element only transmits a symbol of $s_1 = 1$, which can be considered to be a special $\mathcal{L} = 1$ instantiation of the SM scheme.

Based the above example, the source information of the SM/SSK scheme is directly assigned to the TAs, where only the spatial domain is exploited for the conventional modulation scheme, hence no transmit diversity gain is achieved upon activating a single TA. To be specific, the STSK philosophy is based on the activation of Q number of space-time dispersion matrices (DMs) [53] within each STSK block duration [41, 46, 54], instead of indexing the TAs within each symbol duration, as in the SM/SSK scheme of [8, 19, 20]. The STSK encoder is specified by the parameter $(M, N, T, Q, \mathcal{L})$, where M and N represent the number of TAs and receive antennas (RAs), respectively, Q is the number of dispersion matrices and $\mathcal{L}$ represents the size of the classic constellation. More specifically, the schematic of the STSK transmitter proposed in [41, 54] is depicted in Fig. 2.3, where the transmitter assigns $\log_2 \mathcal{L}$ bits to a single $\mathcal{L}$-PSK/QAM symbol, while $\log_2 Q$ bits are assigned to select a single one out of a total number of Q DMs $\mathbf{D}_q$ $(q = 1, \cdots, Q)$. Then the modulated symbol s^i is dispersed into both the spatial and temporal dimensions by the activated DM $\mathbf{D}^i$, so that the STSK transmission matrix

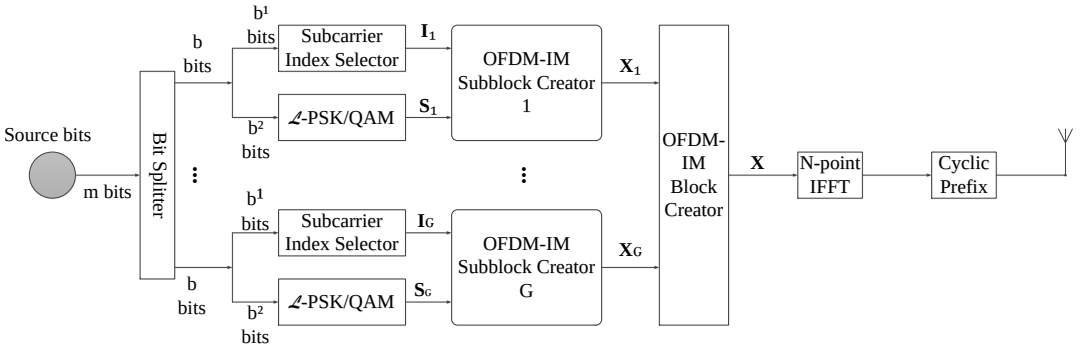

Figure 2.4: The block diagram of the OFDM-IM transmitter [62], which is an example of Fig. 1.1.

seen in Fig. 2.3 is given by $\mathbf{S} = s^i \cdot \mathbf{D}^i$. Therefore, the STSK scheme may be considered to constitute a combination of linear dispersion coding (LDC) [53] and SM [46]. As a benefit of the high degree of design-freedom by appropriately choosing both the number of DMs, the size of the classic modulation alphabet, and the number of TAs/RAs, the STSK scheme becomes capable of striking a flexible trade-off between the diversity gain and multiplexing gain [54].

2.2.2 Review of OFDM-IM

OFDM-IM is a multi-carrier transmission scheme that has been inspired by beneficially transplanting the concept of SM from the spatial to the frequency domain [62, 95]. In the OFDM-IM scheme, the source information is carried by two parts, the classical constellation symbols and subcarrier index pattern selection, where only a subset of the available subcarriers is activated for transmitting the classic constellation symbols, while the remaining subcarriers are idle. The block diagram of the OFDM-IM transmitter is given in Fig. 2.4, where a total of m source bits enter the OFDM-IM transmitter for the transmission of each OFDM frame, while considering an OFDM system having a total of N_c available subcarriers. The m source bits are first split into G groups, each containing $b = m/G$ bits, where each group of b bits is mapped to an OFDM sub-block[1] of subcarrier-length $N_f = N_c/G$. Then, for each OFDM sub-block, only K out of N_f subcarriers are activated based on the first $b^1 = \lfloor \log_2 \binom{N_f}{k} \rfloor$ bits of the incoming b-bit sequence. According to [62], the selection procedure of the active subcarriers per OFDM sub-block can be implemented by using two different mapping techniques,

[1]In OFDM, N_c may assume very large values, such as 128, 256, 512 or 1024 and if the subcarrier index selector is applied directly to N_c, there could be a huge number of possible combinations for active subcarrier indices, which makes the selection of active indices an almost impossible task. As a result, the subcarriers are partitioned into G smaller sub-blocks to perform subcarrier index selection.

either using a simple look-up table that specifies the active indices corresponding to the incoming bits, or the technique that is based on combinatorial number theory for a large number of information bits b^1, as detailed in [62]. Note that we use the look-up table based technique in this chapter, which will be detailed in Section 2.3. Additionally, the remaining $b^2 = K \log_2 \mathcal{L}$ bits of the incoming b-bit sequence are mapped to the classical $\mathcal{L}$-PSK/QAM modulation for determining the data symbols that modulate the activated subcarriers. Hence the total number of bits transmitted per OFDM-IM frame is given by

$$m = b \times G = \left(\lfloor \log_2 \binom{N_f}{K} \rfloor + K \log_2 \mathcal{L} \right) \times G. \tag{2.2}$$

As shown in Fig. 2.4, for the first OFDM sub-block, the resultant matrices of $\mathbf{I}_1$ and $\mathbf{S}_1$ represent the selected indices and constellation symbols, respectively, where $\mathbf{I}_1$ has the size of $(N_f \times K)$ and $\mathbf{S}_1$ has the size of $(K \times 1)$. Then the OFDM-IM sub-block creator of Fig. 2.4 assembles the sub-blocks $\mathbf{X}_g \in \mathbb{C}^{N_f \times 1} = \mathbf{I}_g \mathbf{S}_g$ for $g = 1, 2, \ldots, G$. Then, the OFDM-IM block creator shown in Fig. 2.4 collects these sub-blocks and forms an OFDM-IM frame $\mathbf{X} \in \mathbb{C}^{N_f \times 1}$. Finally, inverse Fast Fourier transform (IFFT) and cyclic prefix (CP) insertion are performed for the transmission of the signals through the wireless channel, as in classical OFDM systems.

2.2.3 Review of CS-OFDM-IM

As introduced in Section 1.3, CS has attracted considerable research attention, especially in the context of recovering sparse signals. In this section, we introduce the CS technique in the context of the OFDM-IM transmitter of Section 2.2.2. The CS technique was first applied to the family of OFDM-IM systems in [82], where the CS-assisted subcarrier indexing strategy was implemented by carting the conventional OFDM-IM to a high-dimensional virtual domain, and then the virtual-domain signals were compressed into low-dimensional signals in the frequency domain. In this way, both the bandwidth efficiency and energy efficiency became higher than the conventional OFDM-IM. To expound a little further, the block diagram of the CS-OFDM-IM transmitter is portrayed in Fig. 2.5 based on [82]. Similar to the conventional OFDM-IM of Fig. 2.4, the source information is first split into G groups each containing b bits, where part of the b bits are used to generate constellation symbols, while the remaining part is applied to selecting active subcarriers for transmitting the constellation symbols. Specifically, the active subcarrier indices seen in Fig. 2.5 are selected in a N_v-dimensional virtual domain,

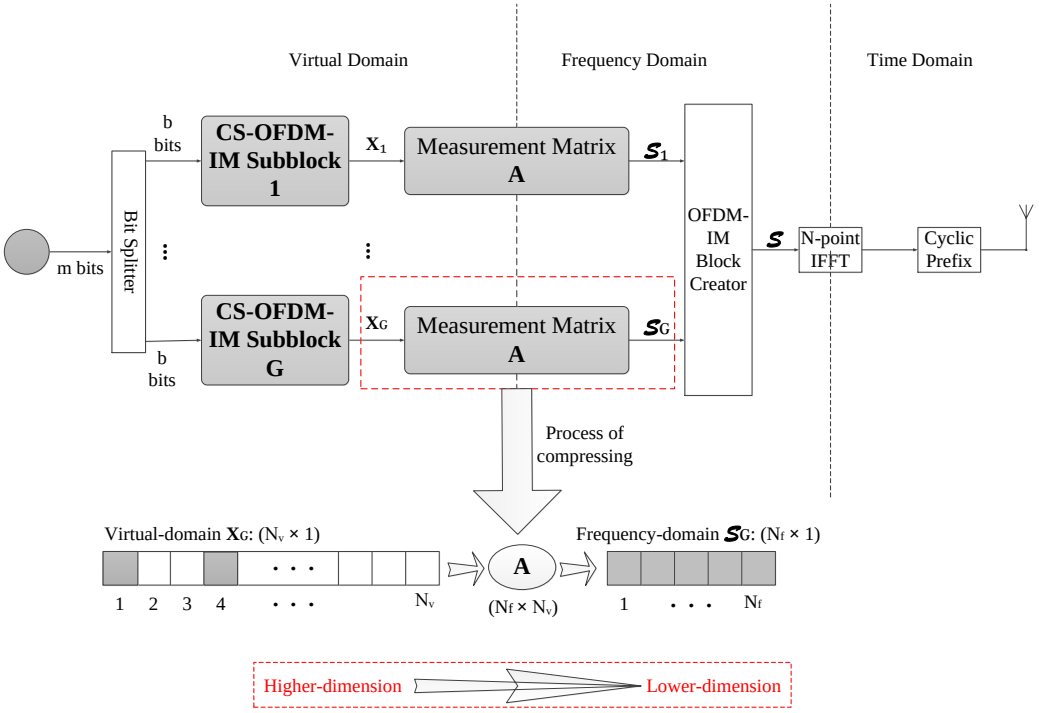

Figure 2.5: The block diagram of the CS-OFDM-IM transmitter [82], which was developed from Fig. 2.4.

where we have $(N_v > N_f)$. Hence the total number of bits transmitted per CS-OFDM-IM frame is given by

$$m = b \times G = \left(\lfloor \log_2 \binom{N_v}{K} \rfloor + K \log_2 \mathcal{L} \right) \times G. \tag{2.3}$$

Explicitly, by comparing Eq. (2.2) and Eq. (2.3) we observe that more data bits can be transmitted by the CS-OFDM-IM scheme than by the classical OFDM-IM scheme reviewed in Fig. 2.4, when we fixed the values of N_f, K, $\mathcal{L}$. Let us briefly consider the example of $N_v = 32$, $N_f = 8$, $K = 2$ and $\mathcal{L} = 2$, where we have 1 bit-per-channel-use and 1.5 bits-per-channel-use for the conventional OFDM-IM and the CS-OFDM-IM, respectively, when we carry out the calculations in Eq. (2.3). Hence we conclude that the CS-assisted indexing strategy is capable of transmitting more bits at no extra cost in terms of either power or bandwidth.

As shown in Fig. 2.5, a CS measurement matrix $\mathbf{A} \in \mathbb{C}^{N_f \times N_v}$ is applied for compressing the high-dimensional g-th CS-OFDM-IM sub-block signal $\mathbf{X}_g \in \mathbb{C}^{N_v \times 1}$ in the virtual domain into a low-dimensional frequency-domain signal $\mathcal{S}_g \in \mathbb{C}^{N_f \times 1}$. This process may be expressed as

$$\mathcal{S}_g = \mathbf{A} \cdot \mathbf{X}_g. \tag{2.4}$$

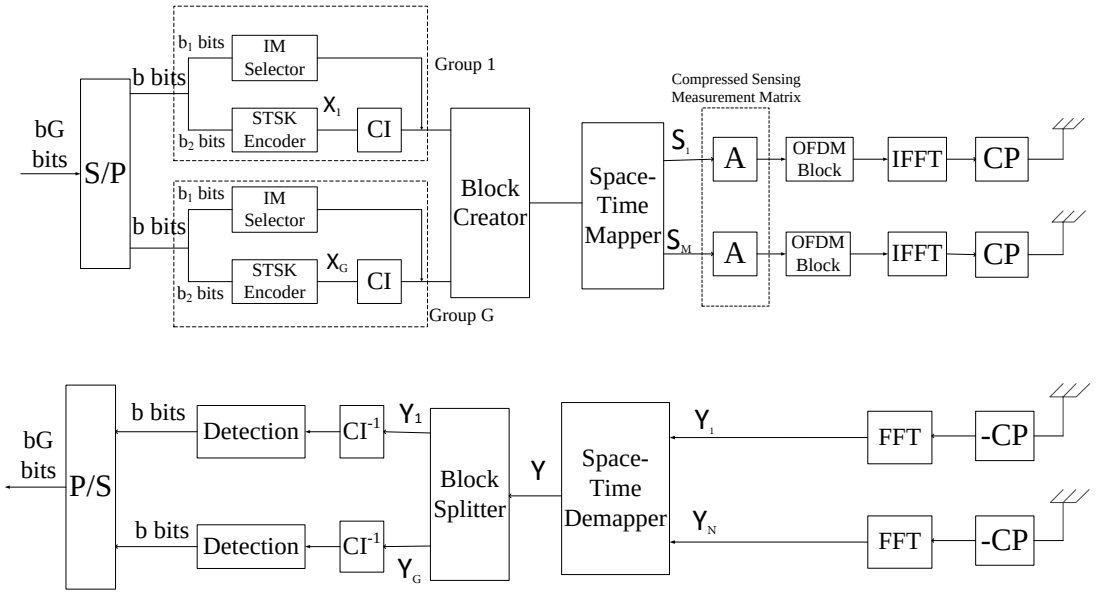

Figure 2.6: The transceiver architecture of the proposed CS-OFDM-STSK-IM system, which was developed from both Fig. 2.3 and Fig. 2.5. The STSK encoder of the architecture follows the principle reviewed in Fig. 2.3.

Additionally, the illustration of Eq. (2.4) is shown in Fig. 2.5. Then, the OFDM-IM block creator of Fig. 2.5 collects the compressed frequency-domain signals from the G sub-blocks, followed by the IFFT and CP insertion. More specifically, Eq. (2.4) represents the classical mathematical modelling of CS [108], whose detection performance at the receiver is determined by the specific characteristics of the measurement matrix $\mathbf{A}$ [184]. The particular design principles of the measurement matrix are comprehensively detailed in [167, 185, 205, 206].

2.3 Proposed System Model

The block diagram of our proposed scheme is shown in Fig. 2.6, where bG number of information bits are divided into G parallel groups with b number of information bits processed in each group, as shown in Fig. 2.6. For each group of b bits, b_1 bits are mapped to the IM selector, which chooses K active indices out of N_v available indices. The remaining b_2 bits are used for generating K STSK codewords, and then these K codewords are coordinate-interleaved for providing an additional diversity gain to improve the BER performance. In Fig. 2.6, the K coordinate-interleaved codewords are then mapped to the active indices according to the IM selector, while the inactive indices are set to zero. Then the block creator collects all codewords from G groups in parallel

and forms a frame, which is mapped to the spatial- and time-domain by the space-time mapper followed by OFDM modulation and then transmission.

In the system proposed in Fig. 2.6, we consider OFDM modulation with N_c subcarriers, which are equally divided into G subcarrier groups for performing index selection and each group contains $N_f = N_c/G$ subcarriers in the frequency domain. In each subcarrier group, K number of indices are active out of N_v available subcarrier indices in the virtual domain. Hence the information bits are divided into G groups at the input of the transmitter as shown in Fig. 2.6. The details of the transmitter and receiver models are discussed in the following sections.

2.3.1 Transmitter Model

As illustrated in Fig. 2.6, bG data bits are split into G groups of length b bits and then the corresponding b bits are processed in each group of the transmitter by the STSK encoder and the IM selector. As introduced in Section 2.2.1, the STSK encoder specified by the parameter (M, N, T, Q, L) generates space-time codewords from the information bits by activating a single dispersion matrix out of Q dispersion matrices and combined with the L-ary modulated symbols for transmission over T time slots. As shown in Fig. 2.6, b_2 data bits are processed by the STSK encoder in each group, where we have $b_2 = K \times \log_2(QL)$. In the g-th group, the STSK codewords are represented by $\mathbf{X}_g[i]$, where $g = 1, 2, \ldots G$ and $i = 1, 2, \ldots K$.

In order to further increase the diversity gain and improve the system's performance, the coordinate interleaving (CI) technique of [75] is invoked for each group after the STSK encoder, as illustrated in Fig. 2.6. Specifically, coordinate interleaving is applied to the STSK codewords $\mathbf{X}_g[i] \in \mathbb{C}^{M\times T}$ where $i = 1, 2 \ldots K$ in the g-th group and K is an even number because the interleaving takes place between a pair of codewords. According to the coordinate interleaving, the real and imaginary parts of the complex data symbols are transmitted over different active indices of the system. The output signal after coordinate interleaving blocks is represented by $\hat{\mathbf{X}}_g \in \mathbb{C}^{KM\times T}$ and contains

K STSK codewords, which can be expressed as

$$\hat{\mathbf{X}}_g = \begin{bmatrix} \mathcal{R}\{\mathbf{X}_g[1]\} + j\mathcal{I}\{\mathbf{X}_g[2]\} \\ \mathcal{R}\{\mathbf{X}_g[2]\} + j\mathcal{I}\{\mathbf{X}_g[1]\} \\ \vdots \\ \mathcal{R}\{\mathbf{X}_g[K-1]\} + j\mathcal{I}\{\mathbf{X}_g[K]\} \\ \mathcal{R}\{\mathbf{X}_g[K]\} + j\mathcal{I}\{\mathbf{X}_g[K-1]\} \end{bmatrix}, \tag{2.5}$$

where $\mathcal{R}[\,]$ and $\mathcal{I}[\,]$ represent the real and imaginary parts of the complex-valued symbol respectively, and the real part of the codeword after the coordinate interleaving block of Fig. 2.6 at the first active index comes from the real part of the first STSK codeword. By contrast, the imaginary part of the codeword after the coordinate interleaving block of Fig. 2.6 at the first active index comes from the imaginary part of the second STSK codeword and so on, for each of active indices.

The coordinate-interleaved space-time codewords $\hat{\mathbf{X}}_g[i]$ in each subcarrier group are then mapped to K active subcarrier indices chosen from the N_v available indices according to the OFDM-IM principle introduced in Section 2.2.2, and each space-time matrix is applied to an active index. The remaining $b_1 = \lfloor \log_2 C(N_v, K) \rfloor$ data bits in each group are used to select K out of N_v available indices by the IM selector, and only the selected active indices are allocated the space-time codewords. $C(N_v, K)$ represents the number of possible combinations upon choosing K out of N_v and the notation $\lfloor\,\rfloor$ represents the floor operation. The remaining $(N_v - K)$ indices are inactive and set to zero. Additionally, the index selection procedure can be performed by referring to a look-up table [1], where the information bits are conveyed by the corresponding combinations of active indices. A look-up table example is provided in Table 2.1 for $b_1 = 2$, $K = 2$ and $N_v = 4$. For example, according to the look-up Table 2.1, if the information bits of the IM selector are [0 0], the first and second indices out of the 4 available indices should be active indices, while the other two indices should be set to zero as shown in the table, and so on.

In the IM selector of Fig. 2.6, we consider a virtual domain rather than the frequency domain, where the number of the indices N_v available in the virtual domain is higher than the number of subcarriers N_f in the frequency domain of each group as reviewed in Fig. 2.5. With the aid of this virtual domain, the proposed system becomes capable

Bits	Indices	Blocks
[0 0]	$\{1, 2\}$	$[\mathbf{x}_1\, \mathbf{x}_2\, \mathbf{0}\, \mathbf{0}]$
[0 1]	$\{2, 3\}$	$[\mathbf{0}\, \mathbf{x}_1\, \mathbf{x}_2\, \mathbf{0}]$
[1 0]	$\{3, 4\}$	$[\mathbf{0}\, \mathbf{0}\, \mathbf{x}_1\, \mathbf{x}_2]$
[1 1]	$\{1, 4\}$	$[\mathbf{x}_1\, \mathbf{0}\, \mathbf{0}\, \mathbf{x}_2]$

Table 2.1: A look-up table example for $K = 2$ and $N_v = 4$

of transmitting more information within the fixed bandwidth at no cost in terms of power. For example, there are $N_c = 128$ subcarriers partitioned into $G = 16$ subcarrier groups with $N_f = 8$ subcarriers in each group and the STSK encoder specified by $(2, 2, 2, 2, 2)$ is applied. For each group of the conventional OFDM-STSK-IM [2] having $K = 2$ active subcarriers, $b_2 = 2 \times \log_2(2 \times 2) = 4$ bits are used for encoding $2^4 = 16$ STSK codewords and $b_1 = \lfloor \log_2 C(8, 2) \rfloor = 4$ bits for selecting 2 active subcarriers out of 8 available subcarriers in each group, since we have $2^4 = 16$ legitimate combinations. Hence a total of $b = 8$ bits are transmitted through each subcarrier group. By contrast, the proposed CS-aided OFDM-STSK-IM system introduces the virtual domain having N_v number of subcarriers for the IM selector, where the length of N_v in the virtual domain is designed much higher than that of N_f in the frequency domain. Explicitly, $N_v = 15$ is assumed here, then $b_1 = \lfloor \log_2 C(15, 2) \rfloor = 6$ bits are used for selecting $2^6 = 64$ legitimate combinations relying on 2 active indices out of 15 available indices in the virtual domain. Quantitatively, $b_2 = 2 \times \log_2(2 \times 2) = 4$ bits are used for the $2^4 = 16$ STSK codewords of Fig. 2.6, yielding a total of $b = 10$ bits transmitted through each subcarrier group. Hence, the proposed CS-aided system transmits more information than the conventional OFDM-STSK-IM scheme within the same bandwidth at no extra power consumption.

After the allocation of active indices in each group, the symbols in the g-th group can be expressed as $\overline{\mathbf{X}}_g = [x_g(1)\, x_g(2)\, \ldots\, x_g(N_v)]$ in the virtual domain. The mapping of the STSK codewords to N_v parallel available indices is illustrated in Fig. 2.7 as a 3D structure, where the x-axis, y-axis and z-axis represent the time slots, the available frequency indices in the virtual domain and the transmit antennas, respectively. Additionally, N_v space-time matrices having $(M \times T)$ elements are allocated in parallel slices. The slices which correspond to the active indices are set to the coordinate-interleaved space-time codewords and the other slices are set to zero.

[2] The conventional OFDM-STSK-IM is the OFDM-IM technique without applying the CS.

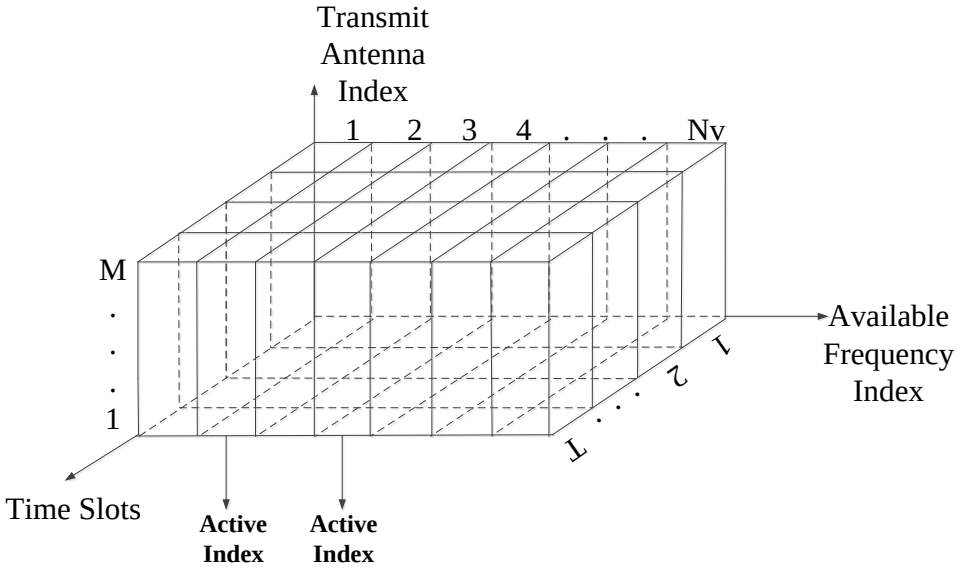

Figure 2.7: The OFDM-STSK frame in the virtual domain for one subcarrier group with N_v available indices, which indicates the space-time frame of each subcarrier group before the Block Creator shown in Fig. 2.6.

The block creator of Fig. 2.6 concatenates G groups of codewords into a single frame and then the space-time symbols $\overline{\mathbf{X}} = [\overline{\mathbf{X}}_0\, \overline{\mathbf{X}}_1\, \ldots\, \overline{\mathbf{X}}_G]$ in the virtual domain are mapped to M transmit antennas over T time slots by the space-time mapper. With the aid of the space-time mapper of Fig. 2.6, we generate the transmit symbol vectors from M transmit antennas over T time slots, which can be written as $[\mathbf{S}_1\, \mathbf{S}_2\, \ldots\, \mathbf{S}_M]$ over one time slot, and the symbols at the m-th transmit antenna $\mathbf{S}_m \in \mathbb{C}^{GN_v \times 1}$ can be also expressed as $\mathbf{S}_m = [\mathbf{S}_m^1\, \mathbf{S}_m^2\, \ldots\, \mathbf{S}_m^G]$, where $\mathbf{S}_m^g \in \mathbb{C}^{N_v \times 1}$ represents the symbols of the g-th group at the m-th transmit antenna.

In order to map the symbols in the virtual domain to the frequency domain for constructing the OFDM symbols, the measurement matrix $\mathbf{A} \in \mathbb{C}^{N_f \times N_v}$ is applied to compress the N_v-dimensional signal $\mathbf{S}_m^g$ in the virtual domain into the N_f-dimensional signal $\hat{\mathbf{S}}_m^g$ in the frequency domain and this procedure is shown as

$$\hat{\mathbf{S}}_m^g = \mathbf{A}\mathbf{S}_m^g, \tag{2.6}$$

where $\hat{\mathbf{S}}_m^g \in \mathbb{C}^{N_f \times 1}$ and Eq. (2.6) represents the classic mathematical model of CS [108]. However, there are no widely configured design principles for the CS measurement matrix $\mathbf{A}$. According to [108, 184], the CS measurement matrix dominantly influences the receiver's symbol recovery performance. In order to make the recovery efficient,

the columns of the matrix $\mathbf{A}$ should be as uncorrelated as possible, so that the matrix preserves more energy of the input signal $\mathbf{S}_m^g$, where the mutual coherence of the measurement matrix $\mathbf{A}$ is designed to be lower than $1/(2K-1)$.

As illustrated in Fig.2.6, the OFDM symbols in the frequency domain are obtained after the above procedures, and then the N_c-point IFFT is applied to the frequency-domain symbols at each transmit antenna, yielding the time-domain symbols $[\overline{\mathbf{S}}_1\,\overline{\mathbf{S}}_2\,\ldots\,\overline{\mathbf{S}}_M]$. Finally, the CP of length N_{cp}, which has to be longer than the channel's delay spread, is concatenated at the front of the time-domain symbols for eliminating the effects of the inter-symbol-interference over multi-path fading channels. Then, the resultant signals are transmitted simultaneously from the M transmit antennas over the wireless channel.

2.3.2 Detection of the Proposed System

The signal glanced from the transmit antennas is assumed to be transmitted over a L_{ch}-tap frequency-selective channel and the channel state information (CSI) is assumed to be perfectly known at the receiver.

Using the channel model $h_{m,n}(n_c)$, which represents the time-domain channel at the n_c-th subcarrier between the m-th transmit antenna as well as the n-th receive antenna and following the CP removal and FFT operation at the space-time demapper, the signal $\mathbf{Y}[n_c] \in \mathbb{C}^{N\times T}$ received at the n_c-th subcarrier ($n_c = 0, 1, \ldots, N_c-1$) over N receive antennas can be expressed as

$$\mathbf{Y}[n_c] = \mathbf{H}[n_c]\hat{\mathbf{S}}[n_c] + \mathbf{W}[n_c], \tag{2.7}$$

where $\mathbf{H}[n_c] \in \mathbb{C}^{N\times M}$ is the frequency-domain channel matrix at the n_c-th subcarrier, $\hat{\mathbf{S}}[n_c] \in \mathbb{C}^{M\times T}$ is the compressed symbols at the n_c-th subcarrier transmitted from M transmit antennas over T time slots, and $\mathbf{W}[n_c] \in \mathbb{C}^{N\times T}$ represents the additive white Gaussian noise (AWGN) following the distribution $\mathcal{CN}(0, \sigma_n^2)$, where σ_n^2 represents the noise variance.

The received signal $\mathbf{Y} \in \mathbb{C}^{N_cN\times T} = \left[\mathbf{Y}^T[0]\,\mathbf{Y}^T[1]\,\cdots\,\mathbf{Y}^T[N_c-1]\right]^T$ based on Eq. (2.7) is then passed through the block splitter and the received symbols in G groups are detected separately as shown in Fig. 2.6. Then the received signal $\mathbf{Y}_g \in \mathbb{C}^{N_fN\times T}$ in the g-th group before detection can be obtained from Eq. (2.7), which is expressed further as:

$$\mathbf{Y}_g = \mathbf{H}_g\hat{\mathbf{A}}\mathbf{S}_g + \mathbf{W}_g, \tag{2.8}$$

where $\mathbf{H}_g \in \mathbb{C}^{N_f N \times N_f M}$ represents the block-diagonal channel matrix of the whole g-th block, $\hat{\mathbf{A}} \in \mathbb{C}^{N_f M \times N_v M}$ is the equivalent CS measurement matrix used for the signals glanced from the M transmit antennas, and $\mathbf{S}_g \in \mathbb{C}^{N_v M \times T}$ contains the information transmitted from the M transmit antennas over T time slots in the virtual domain. Additionally, $\mathbf{W}_g \in \mathbb{C}^{N_f N \times T}$ is the AWGN matrix, which obeys the distribution $\mathcal{CN}(0, \sigma_n^2)$.

For the analysis of different types of detectors, Eq. (2.8) can be expanded specifically for N_f consecutive subcarriers of block g as:

$$\begin{bmatrix} \mathbf{Y}_g^1 \\ \mathbf{Y}_g^2 \\ \vdots \\ \mathbf{Y}_g^{n_f} \\ \vdots \\ \mathbf{Y}_g^{N_f} \end{bmatrix} = \begin{bmatrix} \mathbf{H}_g^1 & \mathbf{0} & \dots & \mathbf{0} \\ \mathbf{0} & \mathbf{H}_g^2 & \dots & \mathbf{0} \\ \vdots & \vdots & \ddots & \vdots \\ \mathbf{0} & \mathbf{0} & \dots & \mathbf{H}_g^{N_f} \end{bmatrix} \begin{bmatrix} \hat{\mathbf{A}}_1 \\ \hat{\mathbf{A}}_2 \\ \vdots \\ \hat{\mathbf{A}}_{n_f} \\ \vdots \\ \hat{\mathbf{A}}_{N_f} \end{bmatrix} \mathbf{I}_g \hat{\mathbf{X}}_g + \mathbf{W}_g, \tag{2.9}$$

where $\mathbf{Y}_g^{n_f} \in \mathbb{C}^{N \times T}$ represents the space-time codeword received at the n_f-th subcarrier in group g. Each channel matrix element $\mathbf{H}_g^{n_f}$ has the size of $(N \times M)$, and the submatrix $\hat{\mathbf{A}}_{n_f} \in \mathbb{C}^{M \times M N_v}$ in the equivalent CS measurement matrix is derived from the n_f-th row of the measurement matrix $\mathbf{A}$ and can be specifically expanded as:

$$\hat{\mathbf{A}}_{n_f} = \begin{bmatrix} \mathbf{A}_{n_f} & \mathbf{0} & \dots & \mathbf{0} \\ \mathbf{0} & \mathbf{A}_{n_f} & \dots & \mathbf{0} \\ \vdots & \vdots & \ddots & \vdots \\ \mathbf{0} & \mathbf{0} & \dots & \mathbf{A}_{n_f} \end{bmatrix}, \tag{2.10}$$

where $\mathbf{A}_{n_f}$ has the size of $(1 \times N_v)$ and represents the n_f-th row-vector of the measurement matrix $\mathbf{A}$. In addition, $\hat{\mathbf{X}}_g \in \mathbb{C}^{KM \times T}$ in Eq. (2.9) represents the coordinate-interleaved signal at the K active indices received from the M transmit antennas over

T time slots in Eq. (2.5), and $\mathbf{I}_g \in \mathbb{C}^{N_v M \times KM}$ is a block-diagonal matrix of the form

$$\mathbf{I}_g = \begin{bmatrix} \mathbf{I}_g^1 & \mathbf{0} & \dots & \mathbf{0} \\ \mathbf{0} & \mathbf{I}_g^2 & \dots & \mathbf{0} \\ \vdots & \vdots & \ddots & \vdots \\ \mathbf{0} & \mathbf{0} & \dots & \mathbf{I}_g^M \end{bmatrix}, \tag{2.11}$$

which illustrates the specific mapping pattern of selecting K active indices out of N_v available indices in the virtual domain for M transmit antennas. In Eq. (2.11) each submatrix $\mathbf{I}_g^m \in \mathbb{C}^{N_v \times K}$ represents the index combination mapping pattern at the m-th transmit antenna, and the N_v rows in $\mathbf{I}_g^m$ represent the N_v available frequency indices shown in Fig. 2.7, while the K columns in matrix $\mathbf{I}_g^m$ represent the K selected active indices. Additionally, we assume that the index mapping pattern is the same for the M transmit antennas, where $\mathbf{I}_g^1 = \mathbf{I}_g^2 = \cdots = \mathbf{I}_g^M$ in Eq. (2.11). For example, let us assume that there are 2 transmit antennas, where the first and second indices are selected as active indices out of the 4 available indices in the virtual domain. Then the mapping matrix for 2 transmit antennas is shown as:

$$\mathbf{I}_g = \begin{bmatrix} \mathbf{I}_g^1 & \mathbf{0} \\ \mathbf{0} & \mathbf{I}_g^2 \end{bmatrix} = \begin{bmatrix} 1 & 0 & \vdots & 0 & 0 \\ 0 & 1 & \vdots & 0 & 0 \\ 0 & 0 & \vdots & 0 & 0 \\ 0 & 0 & \vdots & 0 & 0 \\ \dots & \dots & \dots & \dots & \dots \\ 0 & 0 & \vdots & 1 & 0 \\ 0 & 0 & \vdots & 0 & 1 \\ 0 & 0 & \vdots & 0 & 0 \\ 0 & 0 & \vdots & 0 & 0 \end{bmatrix}. \tag{2.12}$$

In the following, we will first describe the ML detection followed by our proposed reduced-complexity algorithm conceived for reducing the excessive complexity of the ML detector without unduly eroding the performance.

2.3.2.1 Maximum Likelihood Detection

In our proposed system model of Eq. (2.9), we should identify the matrix required for detecting the information bits used in the index selector of Fig. 2.6 and also to detect the information bits used for constructing the STSK codewords for all active indices.

Using the matrix given in Eq. (2.9), the ML detection of the proposed CS-aided OFDM-STSK-IM for each block g is performed in the detection block of Fig. 2.6, which is formulated as

$$< \hat{q}, \hat{l}, \hat{I}_c >= \arg \min_{q,l,I_c \in \mathcal{I}_c} \|\mathbf{Y}_g - \mathbf{H}_g \hat{\mathbf{A}} I_c \hat{\mathbf{X}}_{g,q,l}\|^2, \tag{2.13}$$

where $\mathcal{I}_c$ represents the index-combination library, which contains all possible index combinations in the transmitter look-up table and $\hat{\mathbf{X}}_{g,q,l}$ represents the K coordinate-interleaved space-time codewords in the g-th group. The total decoding complexity order of the ML detection given in Eq. (2.13) for one subcarrier group is $\mathcal{O}(N_{SI}(Q\mathcal{L})^K)$, which is considerably higher than that of classical OFDM-STSK, whose complexity order of one subcarrier group is $\mathcal{O}(N_f Q\mathcal{L})$. Therefore, we employ a reduced-complexity detector in our system for reducing the complexity of the ML detection of Eq. (2.13).

2.3.2.2 Reduced-Complexity Detection

We propose a pair of reduced-complexity detection techniques, which strike a trade-off between the performance and the complexity as detailed below.

The initialisation stages are the same for both reduced-complexity techniques described as follows:

1. During the first stage, G independent and successive minimum mean square error (MMSE) detection are performed relying on Eq. (2.8) using the following MMSE filtering matrix:

$$\mathbf{F}_g = \left[(\mathbf{H}_g)^H \mathbf{H}_g + \frac{1}{\rho} \mathbf{I}_{MN_f} \right]^{-1} (\mathbf{H}_g)^H, \tag{2.14}$$

where ρ is the average signal-to-noise ratio (SNR) per symbol and $\mathbf{H}_g$ of Eq. (2.8), represents the equivalent channel matrix for the g-th group. Following the left-multiplication of $\mathbf{Y}_g$ of Eq. (2.8) with the MMSE filtering matrix $\mathbf{F}_g$ of Eq. (2.14), the MMSE detection is performed as

$$\hat{\mathbf{S}}_g = \mathbf{F}_g \mathbf{H}_g \hat{\mathbf{A}} \mathbf{S}_g + \mathbf{F}_g \mathbf{W}_g = \hat{\mathbf{A}} \mathbf{S}_g + \hat{\mathbf{W}}_g, \tag{2.15}$$

where $\hat{\mathbf{S}}_g \in \mathbb{C}^{MN_f \times T}$ is the estimate of the transmitted CS-processed signal and $\hat{\mathbf{W}}_g \in \mathbb{C}^{MN_f \times T}$ is the noise matrix after MMSE channel equalisation.

2. Secondly, in order to get rough estimates of the space-time codewords in the virtual domain, the Hermitian transpose $\hat{\mathbf{A}}^H$ of the equivalent measurement matrix $\hat{\mathbf{A}}$ is multiplied by $\hat{\mathbf{S}}_g$ in Eq. (2.15), which is shown as

$$\tilde{\mathbf{S}}_g = \hat{\mathbf{A}}^H \hat{\mathbf{A}} \mathbf{S}_g + \tilde{\mathbf{W}}_g, \tag{2.16}$$

where $(\hat{\mathbf{A}}^H \hat{\mathbf{A}}) \in \mathbb{C}^{MN_v \times MN_v}$ is a square matrix and $\tilde{\mathbf{W}}_g = \hat{\mathbf{A}}^H \hat{\mathbf{W}}_g$ is an AWGN noise matrix.

3. Then, the estimated signal $\tilde{\mathbf{S}}_g \in \mathbb{C}^{MN_v \times T}$ of Eq. (2.16) is rearranged into N_v consecutive space-time codewords, which have the same structure as shown in Fig. 2.7 and the rearranged signal is represented by $\bar{\mathbf{S}}_g = [\bar{\mathbf{S}}_g^1 \, \bar{\mathbf{S}}_g^2 \, \ldots \, \bar{\mathbf{S}}_g^{N_v}]^T$, where each $\bar{\mathbf{S}}_g^{n_v} \in \mathbb{C}^{M \times T}$ is the estimated space-time codeword of the index n_v for group g in the OFDM-STSK frame shown in Fig. 2.7. Then the magnitudes of N_v consecutive space-time codewords obtained from $\bar{\mathbf{S}}_g$ are calculated as $[|\bar{\mathbf{S}}_g^1|^2 \, |\bar{\mathbf{S}}_g^2|^2 \, \ldots \, |\bar{\mathbf{S}}_g^{N_v}|^2]$. Because of the 'sparsification' of $\mathbf{S}_g$ in Eq. (2.8), there are K nonzero codewords at the active indices shown in Fig. 2.7 complemented by $(N_v - K)$ zero codewords at the inactive subcarrier indices. As a result, the N_v magnitudes provided should have K values, which are higher than the other $(N_v - K)$ values [3]. After calculating and ordering the magnitudes, the specific subcarrier index having the highest magnitude may have a high probability to be one of the K active indices and the index with the lowest magnitude may have a high probability to be one of the $(N_v - K)$ inactive indices.

Again, the above initialisation procedures are the same for the two reduced-complexity techniques and in the following we explain how the two techniques operate, following the above initialisation stages.

Reduced-Complexity Detection Algorithm 1: According to the calculated magnitudes at N_v consecutive subcarriers in the virtual domain, the subcarrier index having the highest magnitude among $[|\bar{\mathbf{S}}_g^1|^2 \; |\bar{\mathbf{S}}_g^2|^2 \; \ldots \; |\bar{\mathbf{S}}_g^{N_v}|^2]$ is selected by the detector as the first active subcarrier candidate [4]. Then ML detection is employed depending on the specific candidate selected. For example, if the first candidate n_v^1 is selected, then ML

[3] This is not true at very low SNRs, when the noise variance is high.

[4] The candidate in reduced-complexity techniques represents the subcarrier index which is selected according to the magnitudes calculated and ordered in the virtual domain.

detection is performed for each block g which is formulated as

$$< \hat{q}, \hat{l}, \hat{I}_{n_v^1} >= \arg \min_{q,l,I_{n_v^1}} \|\mathbf{Y}_g - \mathbf{H}_g \hat{\mathbf{A}} I_{n_v^1} \hat{\mathbf{X}}_{g,q,l}\|^2, \tag{2.17}$$

where $I_{n_v^1}$ represents a specific part of the index-combination library $\mathcal{I}_c$ in Eq. (2.13), which contains all possible index combinations with the index of the n_v^1 candidate in the transmitter look-up table and $\hat{\mathbf{X}}_{g,q,l}$ represents the coordinate-interleaved space-time codewords in the g-th group. Similarly, the subcarrier index n_v^2 having the second highest magnitude is selected as the second candidate and ML detection is performed as

$$< \hat{q}, \hat{l}, \hat{I}_{n_v^2} >= \arg \min_{q,l,I_{n_v^2}} \|\mathbf{Y}_g - \mathbf{H}_g \hat{\mathbf{A}} I_{n_v^2} \hat{\mathbf{X}}_{g,q,l}\|^2, \tag{2.18}$$

where $I_{n_v^2}$ contains all possible index combinations with the indices of n_v^1 and n_v^2 candidates in the transmitter look-up table, and so on for the rest of the selected candidates. Therefore, the detection with N_v candidates can exploit all possible index combinations in the transmitter look-up table and the performance merges with that of the ML detector of Eq. (2.13), whilst having the same complexity order.

Therefore, the complexity order of the reduced-complexity Algorithm 1 depends on the number $\hat{N}_{SI}$ of index combinations processed from the look-up table provided at the transmitter, until the process is terminated. Then the generalised complexity order of Algorithm 1 is expressed as $\mathcal{O}(\hat{N}_{SI}(Q\mathcal{L})^K)$. If all index candidates are selected at the detector, then we have $\hat{N}_{SI} = N_{SI}$, where N_{SI} represents the number of all index combinations provided by the transmitter and the complexity order of Algorithm 1 is exactly the same as that of ML detection. However, it is not necessary to process all index candidates to maintain the performance. Hence $\hat{N}_{SI}$ is typically lower than the number of all possible combinations N_{SI}, where the complexity order $\mathcal{O}(\hat{N}_{SI}(Q\mathcal{L})^K)$ is lower than the complexity order $\mathcal{O}(N_{SI}(Q\mathcal{L})^K)$ of the ML detector.

Reduced-Complexity Detection Algorithm 2: With the benefit of CS, we propose an orthogonal matching pursuit (OMP)-like detection algorithm to make a locally optimal decision at each iteration, which is one of the most popular greedy algorithms [186].

- In the first iteration, the index having the highest magnitude among $[|\bar{\mathbf{S}}_g^1|^2\ |\bar{\mathbf{S}}_g^2|^2\ \ldots\ |\bar{\mathbf{S}}_g^{N_v}|^2]$ is selected as one candidate and represented by $\hat{n}_a^1$. With reference to the index combination table within the IM selector of the transmitter in Fig. 2.6, all combinations containing the selected index $\hat{n}_a^1$ will be processed in

the first iteration and C_1 number of index combinations are assumed during the first iteration. Considering Table 2.1 as an example and assuming $\hat{n}_a^1 = 1$, the first index has the highest probability to be one of the 2 active indices and the combinations with the first index in Table 2.1 will be processed during the first iteration, where the index combinations $\{1, 2\}$ and $\{1, 4\}$ that both contain the first index are selected.

- Then in order to make our analysis comprehensive, the estimated signal $\hat{\mathbf{S}}_g$ after channel equalisation in Eq. (2.15) is expanded as

$$\hat{\mathbf{S}}_g = \hat{\mathbf{A}}\mathbf{I}_g\hat{\mathbf{X}}_g + \hat{\mathbf{W}}_g = \hat{\mathbf{A}}_g\hat{\mathbf{X}}_g + \hat{\mathbf{W}}_g, \tag{2.19}$$

where the matrix $\mathbf{I}_g$ explained in Eq. (2.11) illustrates the specific index combination of selecting K active indices out of N_v available indices in the virtual domain for M transmit antennas. Additionally, according to the principle of the OMP algorithm, the process of $\hat{\mathbf{A}}_g = \hat{\mathbf{A}}\mathbf{I}_g$ creates an over-determined scenario for the proposed detection system [186]. In this scenario, the simple least squares solution can be employed to recover the index combination used at the transmitter by using the pseudo-inverse operator. The pseudo-inverse operator $\hat{\mathbf{A}}_g^+$ of $\hat{\mathbf{A}}_g$ in Eq. (2.19) is denoted as

$$\hat{\mathbf{A}}_g^+ = (\hat{\mathbf{A}}_g^H\hat{\mathbf{A}}_g)^{-1}\hat{\mathbf{A}}_g^H, \tag{2.20}$$

which is multiplied with $\hat{\mathbf{S}}_g$ in Eq. (2.19) and $\hat{\mathbf{A}}_g^+\hat{\mathbf{A}}_g = I_{KM} + \mathbf{e}$ is obtained to recover the transmitted signal $\hat{\mathbf{X}}_g$ in the g-th block, where $\mathbf{e}$ is the error matrix owing to the mismatch of the index combinations. Hence the estimated signal $\hat{\hat{\mathbf{X}}}_g$ can be written in the general format of:

$$\hat{\hat{\mathbf{X}}}_g = \hat{\mathbf{X}}_g + \mathbf{e} + \hat{\hat{\mathbf{W}}}_g. \tag{2.21}$$

In the first iteration, there are C_1 number of index combinations containing the selected index $\hat{n}_a^1$. Hence C_1 pseudo-inverse operators are generated and multiplied with $\hat{\mathbf{S}}_g$ in Eq. (2.19).

- After obtaining the estimated codewords $\hat{\hat{\mathbf{X}}}_g$ in Eq. (2.21) at the K active indices in group g, the ML detection is applied to Eq. (2.21) for detecting the STSK codewords, index-by-index as follows:

$$\hat{x}_g(k, \hat{q}, \hat{l}) = \arg\min_{q,l} \|\hat{\hat{X}}_g(k) - x(q, l)\|^2, \tag{2.22}$$

where q and l are the dispersion matrix index and the symbol constellation index, respectively. Furthermore, $\hat{q}$ and $\hat{l}$ are the corresponding estimated indices, and $\hat{x}_g(k, \hat{q}, \hat{l})$ represents the estimated STSK codeword associated with $\hat{q}$ dispersion matrices and a constellation size of $\hat{l}$ at the k-th active index, $k = 1, 2, \ldots, K$.

- In the above stages of the first iteration, we can obtain C_1 estimated signal matrices, where each matrix contains K space-time codewords over T time slots. In order to optimise the C_1 estimated results in the first iteration, the best fit result can be found by evaluating $< \arg\min \|\hat{\mathbf{S}}_g - \hat{\mathbf{A}}\hat{\mathbf{I}}_g^{c_1}\hat{\mathbf{x}}_g^{c_1}\|^2 >$ to get the specific index mapping matrix and the STSK codeword, which can minimise the difference between the received signal and the estimated signal, where $c_1 = 1, 2, \ldots, C_1$, and $\hat{\mathbf{I}}_g^{c_1}$ is the mapping matrix for the c_1-th processed index combination in the first iteration and $\hat{\mathbf{x}}_g^{c_1}$ illustrates the estimated coordinate-interleaved space-time codewords at the K active indices over T time slots in group g for the c_1-th processed index combination in the iteration considered. Then the optimised result $\hat{\mathbf{S}}_g^1$ obtained during the first iteration contains the information of the best-fit index selection pattern. Finally, the information bits detected for constructing space-time codewords are obtained.

  The signals $[\hat{\mathbf{S}}_g^1\, \hat{\mathbf{S}}_g^2\, \hat{\mathbf{S}}_g^3\, \ldots]$ optimised for all iterations can be obtained by repeating the above stages for the rest of the iterations.

  In fact, it is unnecessary to invoke all iterations as a benefit of applying the pseudo-inverse shown in Eq. (2.21), since the potential error matrix $\mathbf{e}$ in Eq. (2.21) becomes $\mathbf{0}$ if the correct index combination is detected. As a result, an error threshold e_{th} can be set up to terminate the process of iterations for reducing the computational complexity. The potential residual error e_g^i after the i-th iteration becomes:

$$e_g^i = \|\mathbf{Y}_g - \mathbf{H}_g\hat{A}\hat{\mathbf{S}}_g^i\|^2. \tag{2.23}$$

  If the error e_g^i in the i-th iteration is lower than or equal to the threshold error e_{th}, then the process can be terminated and the correct index modulation bits and STSK information bits can be detected in the g-th group.

The complexity order of the reduced-complexity detection Algorithm 2 depends on the number of index combinations $\tilde{N}_{SI}$ processed from the look-up table provided at the transmitter, until the process is terminated. Then the generalised complexity order of Algorithm 2 is expressed as $\mathcal{O}(\tilde{N}_{SI}Q\mathcal{L}K)$, where $\tilde{N}_{SI}$ is typically lower than the number of all possible combinations N_{SI}. Additionally, the maximum complexity order of Algorithm 2 is $\mathcal{O}(N_{SI}Q\mathcal{L}K)$, which is still lower than the complexity order $\mathcal{O}(N_{SI}(Q\mathcal{L})^K)$

of the ML detector. Compared to the generalised complexity order $\mathcal{O}(\hat{N}_{SI}(Q\mathcal{L})^K)$ of Algorithm 1 having $\hat{N}_{SI} = \tilde{N}_{SI}$, the complexity order of Algorithm 2 is lower than that of the first algorithm.

2.3.2.3 Soft-Decision Detection

In this section, we extend the proposed hard-decision receiver to soft-decision detection. To elaborate further, the block diagram of a two-stage serially concatenated RSC-coded

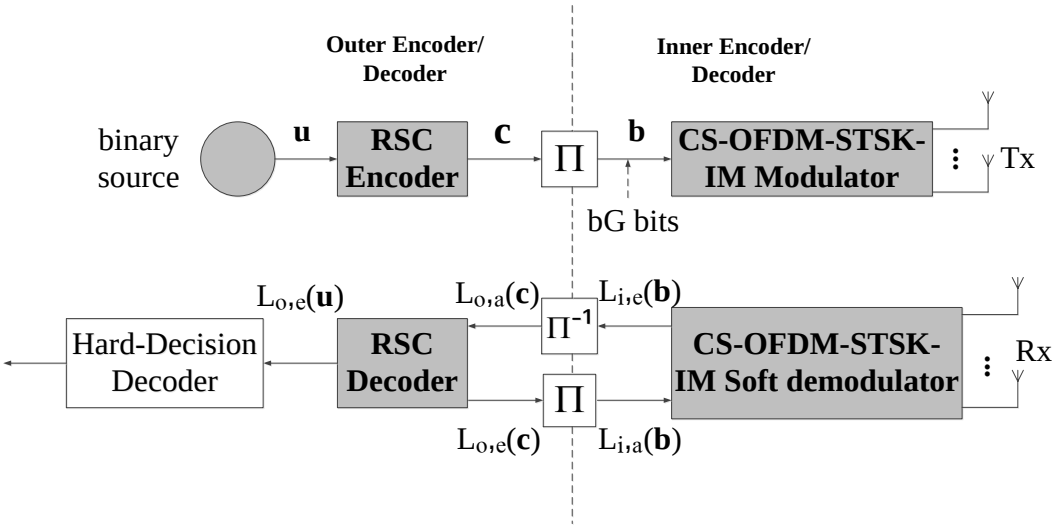

Figure 2.8: Block diagram of a two-stage serially concatenated RSC-coded CS-OFDM-STSK-IM system.

CS-OFDM-STSK-IM system employing iterative detection inspired by [207] is portrayed in Fig. 2.8. As shown in Fig. 2.8, the binary source stream $\mathbf{u}$ is convolutionally encoded by the RSC code, generating the binary stream $\mathbf{c}$ and then the sequence $\mathbf{c}$ is interleaved by a random bit interleaver Π [208]. Then the interleaved stream $\mathbf{b}$ is modulated by the CS-OFDM-STSK-IM scheme of Fig. 2.8. The resultant set of symbols are then mapped to the TAs and then transmitted over the wireless channel. At the receiver of Fig. 2.8, the CS-OFDM-STSK-IM soft demodulator and the RSC decoder iteratively exchange their soft-information in the form of Logarithmic-Likelihood Ratios (LLRs) [209], where $L(\cdot)$ in Fig. 2.8 denotes the LLRs of the bits concerned, the subscript i represents the CS-OFDM-STSK-IM soft demodulator, also regarded as the inner "decoder", and o represents the RSC decoder, also regarded as the outer "decoder" [110]. Furthermore, the subscripts a and e used in Fig. 2.8 refer to the extrinsic and *a priori* LLRs of the

bits, respectively [202]. Specifically, during each inner-outer decoding iteration [5] the CS-OFDM-STSK-IM soft demodulator's extrinsic output LLRs $L_{i,e}(\mathbf{b})$ are deinterleaved by a soft-bit random deinterleaver for generating the soft bits $L_{o,a}(\mathbf{c})$, which are then passed to the RSC decoder as *a priori* LLRs in order to obtain the extrinsic LLRs $L_{o,e}(\mathbf{c})$ for all the channel-coded bits. The extrinsic LLRs $L_{o,e}(\mathbf{c})$ are calculated by invoking the Logarithmic Maximum *a posteriori* (Log-MAP) algorithm [209,210], where the extrinsic LLRs are then interleaved and fed back to the CS-OFDM-STSK-IM soft demodulator as *a priori* LLRs. During the final iteration, only the LLRs $L_{o,e}(\mathbf{u})$ representing the original uncoded bits $\mathbf{u}$ are required, which are then passed to the hard-decision decoder of Fig. 2.8 for determining the estimated binary source.

According to the conditional probability of the soft demapper of STSK systems in [41], the conditional probability $p(\mathbf{Y}_g|\hat{\mathbf{S}}_g)$ of the received signal block $\mathbf{Y}_g$ obtained from the equivalent system model represented in Eq. (2.8) can be expressed as:

$$\begin{aligned} p(\mathbf{Y}_g|\hat{\mathbf{S}}_g) &= \frac{1}{(\pi N_0)^{NT}} \exp\left(-\frac{\|\mathbf{Y}_g - \mathbf{H}_g\hat{\mathbf{A}}I_g\hat{\mathbf{X}}_g\|^2}{N_0}\right) \\ &= \frac{1}{(\pi N_0)^{NT}} \exp\left(-\frac{\|\mathbf{Y}_g - \mathbf{H}_g\hat{\mathbf{S}}_g\|^2}{N_0}\right), \end{aligned} \tag{2.24}$$

where $\hat{\mathbf{X}}_g$ represents the K number of coordinate interleaved space-time codewords in the g-th block and $\hat{\mathbf{S}}_g$ denotes the compressed symbols in the g-th block. The received signal block $\mathbf{Y}_g$ carries B channel-coded bits in the g-th block for both the index selector and the STSK encoder illustrated in Fig. 2.6. The channel-coded bit sequence in the g-th block can be represented as $\mathbf{b}_g = [b_1, b_2, \ldots, b_B]$ and the resultant extrinsic LLR value of bit b_i $(i = 1, \ldots, B)$ can be expressed as:

$$\begin{aligned} L_{i,e}(b_i) &= \ln \frac{\sum_{\hat{\mathbf{S}}_g \in (\hat{S}_g)_1^i} p(\mathbf{Y}_g|\hat{\mathbf{S}}_g) \exp\left[\sum_{j\neq i} b_j L_{i,a}(b_j)\right]}{\sum_{\hat{\mathbf{S}}_g \in (\hat{S}_g)_0^i} p(\mathbf{Y}_g|\hat{\mathbf{S}}_g) \exp\left[\sum_{j\neq i} b_j L_{i,a}(b_j)\right]} \\ &= \ln \frac{\sum_{\hat{\mathbf{S}}_g \in (\hat{S}_g)_1^i} \exp\left[-\|\mathbf{Y}_g - \mathbf{H}_g\hat{\mathbf{S}}_g\|^2/N_0 + \sum_{j\neq i} b_j L_{i,a}(b_j)\right]}{\sum_{\hat{\mathbf{S}}_g \in (\hat{S}_g)_0^i} \exp\left[-\|\mathbf{Y}_g - \mathbf{H}_g\hat{\mathbf{S}}_g\|^2/N_0 + \sum_{j\neq i} b_j L_{i,a}(b_j)\right]}, \end{aligned} \tag{2.25}$$

$(\hat{S}_g)_0^i$ and $(\hat{S}_g)_1^i$ in Eq. (2.25) represent the sub-set of the space-time-frequency codewords, satisfying $(\hat{S}_g)_0^i \equiv \{\hat{\mathbf{S}}_g \in \hat{S} : b_i = 0\}$ and $(\hat{S}_g)_1^i \equiv \{\hat{\mathbf{S}}_g \in \hat{S} : b_i = 1\}$, respectively. Furthermore, $L_{i,a}(.)$ in Eq. (2.25) represents the *a priori* LLR as the feedback from the RSC decoder to the soft decoder of the proposed system. In order to avoid numerical overflow and to simplify the soft-detection, the Jacobian logarithm of [211] is employed

[5] To avoid confusion with the iteration in the Reduced-Complexity Algorithm 2, we will refer to this as inner-outer iteration and we use the abbreviation IO-Iter.

for computing Eq. (2.25) as:

$$\begin{aligned} & L_{i,e}(b_i) \\ =& \mathrm{jac}_{\hat{\mathbf{S}}_g \in (\hat{S}_g)_1^i} \left(-\|\mathbf{Y}_g - \mathbf{H}_g \hat{\mathbf{S}}_g\|^2 / N_0 + \sum_{j \neq i} b_j L_{i,a}(b_j) \right) - \\ & \mathrm{jac}_{\hat{\mathbf{S}}_g \in (\hat{S}_g)_0^i} \left(-\|\mathbf{Y}_g - \mathbf{H}_g \hat{\mathbf{S}}_g\|^2 / N_0 + \sum_{j \neq i} b_j L_{i,a}(b_j) \right). \end{aligned} \tag{2.26}$$

2.4 Performance Analysis and Simulation Results

In this section, the performance of the proposed CS-aided OFDM-STSK-IM system considered for transmission over frequency-selective fading channels is characterised. The system parameters used in this section are shown in Table 2.2 and Table 2.3. In all simulations, we assume perfect CSI knowledge at the receiver. The comparisons between the classical OFDM-STSK, conventional OFDM-STSK-IM, and the CS-aided OFDM-STSK-IM are presented at the same transmission data rates. The BER performances of these schemes are evaluated by Monte Carlo simulations. We first analyse the system's capacity in Section 2.4.1. Then we proceed to characterise the BER performance of the proposed CS-aided OFDM-STSK-IM system in Section 2.4.2. In Section 2.4.3, we compare the computational complexity of the different detectors of this chapter.

Parameters	**Values**
Multi-carrier System	OFDM
Number of subcarriers, N_c	128
Length of Cyclic Prefix, N_{cp}	16
Number of subcarrier groups, G	16 (change in Fig. 2.9)
Number of subcarriers/group, N_f	8 (change in Fig. 2.9)
Number of available indices/group, N_v	16 (change in Fig. 2.9)
Number of active indices/group, K	2 (or 4) (change in Fig. 2.9)
Channel Specification	COST207-TU12 Rayleigh Fading
Number of transmit antennas , M	2 (change in Fig. 2.14)
Number of receive antennas, N	2
Number of time slots, T	2 (change in Fig. 2.14)

Table 2.2: System parameters in the simulations of Chapter 2.

2.4.1 DCMC Capacity Analysis

The discrete-input continuous-output memoryless channel (DCMC) capacity of our CS-aided OFDM-STSK-IM system is first developed on a per block basis in order to include both the K activated codewords as well as the implicit index of each block and then it is divided by the number of frequency-domain subcarriers in order to determine the capacity per subcarrier. The DCMC capacity of our CS-aided OFDM-STSK-IM scheme using $\mathcal{L}$-PSK/QAM signalling can be formulated as [212]

$$C_{DCMC} = \frac{1}{N_f} \max_{\{p(\mathbf{S})\}_{\forall q,l,I}} \sum \int_{-\infty}^{+\infty} \cdots \int_{-\infty}^{+\infty} p\left(\mathbf{Y}_g|\mathbf{S}\right) p\left(\mathbf{S}\right) \cdot \log_2 \left[\frac{p\left(\mathbf{Y}_g|\mathbf{S}\right)}{\sum_{\forall \mathbf{S} \in \mathcal{S}} p\left(\mathbf{Y}_g|\mathbf{S}'\right) p\left(\mathbf{S}'\right)} \right] d\mathbf{Y}_g, \tag{2.27}$$

which is maximised when the transmitted realisations per subcarrier group $p\left(\mathbf{S}\right)$ are equiprobable, given that $p\left(\mathbf{Y}_g|\mathbf{S}\right)$ is the conditional probability of receiving $\mathbf{Y}_g$, when $\mathbf{S} = \left(\mathbf{S}\right)_{q,l}$ is transmitted.

Now, based on the conditional probability given by $p\left(\mathbf{Y}_g|\mathbf{S}\right)$, the DCMC capacity can be further simplified to [212]

$$C_{DCMC} = \frac{b}{N_f} - \frac{1}{2^b \cdot N_f} \times \sum_{q,l,I} E\left[\log_2 \left\{ \sum_{q',l',I'} \exp\left(\overline{\psi}\right) \right\} \right], \tag{2.28}$$

where the intrinsic metric of the exponent $\overline{\psi}$ denoting the difference between two symbols may be expressed as

$$\overline{\psi} = \frac{-\left\| \left(\mathbf{H}_g \cdot \hat{\mathbf{A}} \right) \cdot \left(\mathbf{S} - \mathbf{S}' \right) + \boldsymbol{n_g} \right\|^2 + \left\| \boldsymbol{n_g} \right\|^2}{N_0}, \tag{2.29}$$

with $\mathbf{S}'$ being the transmitted realisation $\left[\left(\mathbf{S}\right)_{q',l',I'} \right]$.

The maximum number of bits transmitted over the N_c sub-carriers can be expressed as

$$R = C_{DCMC} \times N_c. \tag{2.30}$$

The DCMC capacity curves of several CS-aided OFDM-STSK-IM systems associated with different design specifications are depicted in Fig. 2.9. Furthermore, we included in Fig. 2.9 several OFDM-STSK-IM systems using no CS, where no CS matrix is applied under the constraint of $N_f = N_v$, hence we disregard the concept of virtual-domain to

Systems	STSK $(M, N, T, Q, \mathcal{L})$	N_f	N_v	K
System 1	$(2, 2, 2, 2,$ BPSK$)$	8	16	1
System 2 (no CS)	$(2, 2, 2, 2,$ 4QAM$)$	8	8	1
System 3	$(2, 2, 2, 2,$ BPSK$)$	8	16	2
System 4 (no CS)	$(2, 2, 2, 4,$ BPSK$)$	8	8	2
System 5	$(2, 2, 2, 2,$ BPSK$)$	8	32	2
System 6 (no CS)	$(2, 2, 2, 2,$ 8QAM$)$	8	8	2

Table 2.3: System parameters of Fig. 2.9.

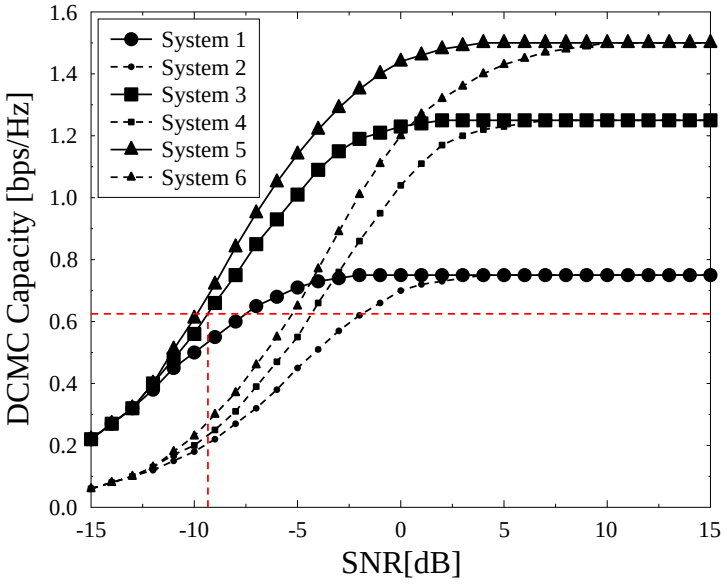

Figure 2.9: DCMC capacity of several CS-aided OFDM-STSK-IM schemes with different configurations by adjusting different parameters, where the configurations are shown in Table 2.3. Additionally, the capacity line of the half-rate RSC-coded System 3 is marked by the dashed line.

frequency-domain conversion[6]. Observe in Fig. 2.9 that the capacity curves tend towards their maximum attainable normalised rate, as the SNR value increases. Furthermore, beneficial design flexibility can be achieved by appropriately adjusting the different parameters, such as the parameters of the STSK encoder, as well as the values of N_f, N_v and K as shown in Table 2.3, in order to meet the system's capacity requirement. To determine the total number of bits conveyed per frequency-domain block, the normalised

[6]We included the capacity plots of the OFDM-STSK-IM system using no CS for showing the impact of employing CS on its achievable capacity limit.

achievable rate of each curve should be multiplied by its corresponding N_f value. It is also shown in Fig. 2.9 that our CS-aided OFDM-STSK-IM system is capable of achieving a higher capacity than that operating without CS.

2.4.2 BER Performances

In Fig. 2.10, we compare the BER performance of the classical OFDM-STSK, conventional OFDM-STSK-IM, and the proposed CS-aided OFDM-STSK-IM schemes, where all these systems use ML detection and have the same transmission rate of 1.1111 bits/s/Hz [7] for the sake of fair comparison. In order to keep the same transmission data

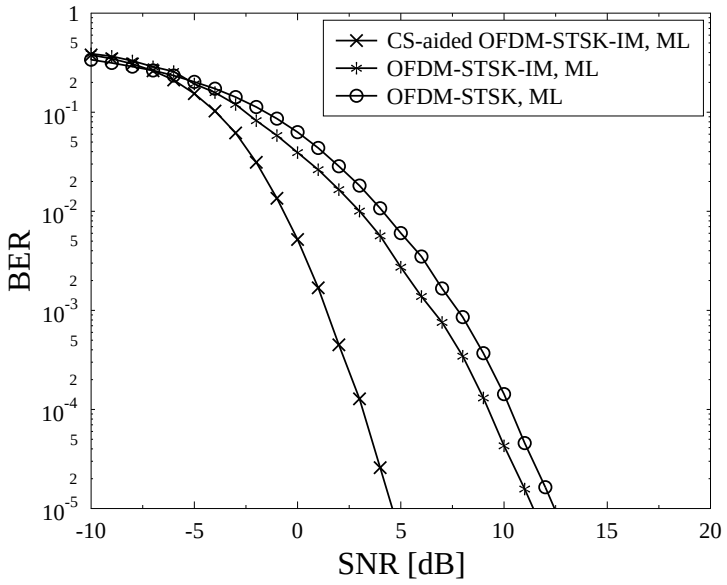

Figure 2.10: BER performances of classical OFDM-STSK, conventional OFDM-STSK-IM, and CS-aided OFDM-STSK-IM by employing ML detection with the same transmission rate of 1.1111 bits/s/Hz. All other parameters were summarised in Table 2.2.

rate, the three schemes apply the STSK encoders specified as STSK $(2, 2, 2, 2, 2)$, STSK $(2, 2, 2, 4, 2)$, and STSK $(2, 2, 2, 2, 2)$, respectively, which contains 2 bits, 3 bits, and 2 bits per space-time codeword separately and each subcarrier group can transmit 10 data bits from 2 transmit antennas over 2 time slots across 8 subcarriers. Additionally, only 80 out of 128 subcarriers are applied by the classical OFDM-STSK scheme for keeping the same transmission rate of 1.1111 bits/s/Hz. As seen from Fig. 2.10, at a BER value of 10^{-5}, the conventional OFDM-STSK-IM scheme operating without

[7] The transmission rate o here is calculated by $\frac{bG}{(N_c+N_{cp})}$ bits/s/Hz.

CS requires about 1.25 dB lower SNR than the classical OFDM-STSK system, and the proposed CS-aided system achieves approximately 7.92 dB and 6.67 dB lower SNR than the classical OFDM-STSK system and the conventional OFDM-STSK-IM system, respectively. We can observe that the proposed CS-aided system significantly outperforms both the classical OFDM-STSK and the conventional OFDM-STSK-IM. When considering these three systems characterised in Fig. 2.10, the complexity order of the proposed CS-aided system is $\mathcal{O}(64 \times (2 \times 2)^2) = \mathcal{O}(1024)$, which is the same as the complexity order of $\mathcal{O}(16 \times (2 \times 4)^2) = \mathcal{O}(1024)$ of the conventional OFDM-STSK-IM system, while the complexity order of the classical OFDM-STSK scheme is $\mathcal{O}(8 \times (2 \times 2)) = \mathcal{O}(32)$. Because of the considerably higher complexity of the proposed system, the proposed reduced-complexity detectors are applied in the simulation results shown in Fig. 2.11 and Fig. 2.12.

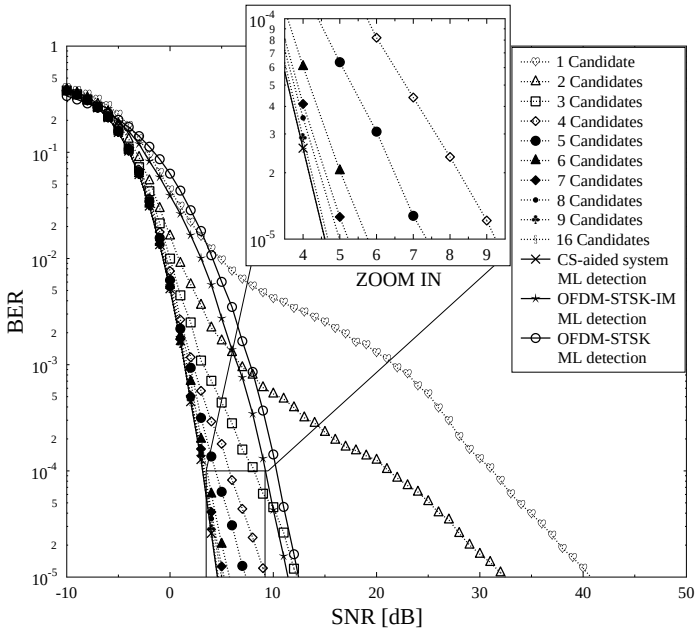

Figure 2.11: BER performances of all schemes of Fig. 2.10 applying both ML detection and the reduced-complexity detection Algorithm 1 with the same transmission rate of 1.1111 bits/s/Hz. All other parameters were summarised in Table 2.2.

In Fig. 2.11, we apply the proposed reduced-complexity detection Algorithm 1 to the CS-aided scheme and compare the BER performance attained to that of the CS-aided scheme using ML detection, as shown in Fig. 2.10. We have portrayed the BER performances of the CS-aided OFDM-STSK-IM system employing the reduced-complexity detector using 1 to 16 number of candidates, as well as the other two schemes shown in Fig. 2.10. For

the sake of fair comparison, again, all figures have the same transmission rate of 1.1111 bits/s/Hz, the same bandwidth and use coordinate interleaving to increase the diversity gain. The reduced-complexity detector characterised in Fig. 2.11 is capable of achieving a considerably lower complexity while choosing adequate number of candidates than the same system using the ML detector. According to the simulation results of the schemes exploiting different number of candidates in Fig. 2.11, the systems using 1 candidate, 2 candidates and 3 candidates have worse performances than these of the three schemes shown in Fig. 2.10. We can observe from Fig. 2.11 that the system using 4 candidates achieves about 2 dB better performance than that of the conventional IM system at a BER of 10^{-5}, while the system with 5 candidates can achieve about 1.95 dB better performance than the system using 4 candidates, as well as the system with 6 candidates achieves about 1.55 dB better performance than using 5 candidates. Then it is shown in Fig. 2.11 that the systems exploiting over 7 candidates in the reduced-complexity system has performance that approaches the performance of the ML detection. In addition, the detector using 16 candidates attains identical performance as the ML detector, as well as the complexity order. Hence, in the case of Fig. 2.11, using 4 to 5 candidates is enough to maintain a better performance than that of the classical OFDM-STSK-IM system shown in Fig. 2.11 with considerably lower complexity.

In order to further reduce the complexity of the detector, the reduced-complexity detection Algorithm 2 is proposed and simulation results under the same transmission data rate of 1.1111 bits/s/Hz are shown in Fig. 2.12. Again, the three schemes applying the ML detection in Fig. 2.10 are also shown in Fig. 2.12 for sake of convenient comparison. In Fig. 2.12, only performances of Algorithm 2 with 1 candidate and 16 candidates are illustrated in the figure. The system applying only one candidate has the worst performance and the system applying 16 candidates which can exploit all possible subcarrier index combinations from the look-up table of the transmitter has the best performance of the proposed reduced-complexity detection Algorithm 2. The best case of the Algorithm 2 achieves about 2.6 dB worse performance than that of the ML detection, while the complexity order $O(512)$ of the best case is considerably lower than that of the ML detection which is $O(1024)$. Hence, there is a trade-off between the complexity and the BER performance while selecting schemes.

In Fig. 2.13 and Fig. 2.14 higher transmission rates are investigated. The schemes in Fig. 2.13 use $K = 2$ active indices out of $N_v = 16$ available indices in each group of the virtual domain, $N_f = 8$ subcarriers in each group of the frequency domain and the STSK scheme is specified by $(2, 2, 2, 2, 4)$. The transmission rate is 1.3333 bits/s/Hz. The performance of the ML detector, of the reduced-complexity Algorithm 1 applying

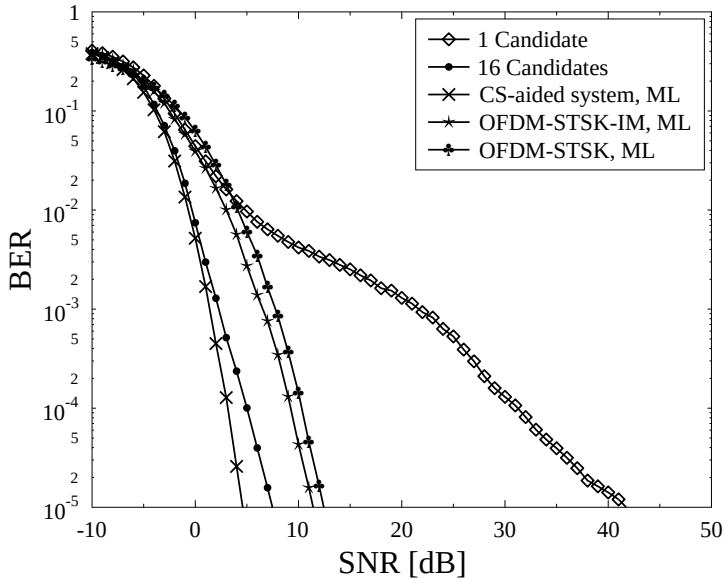

Figure 2.12: BER performances of all schemes of Fig. 2.10 applying both ML detection and the reduced-complexity detection Algorithm 2 with the same transmission rate of 1.1111 bits/s/Hz. All other parameters were summarised in Table 2.2.

4 candidates and the reduced-complexity Algorithm 2 applying 16 candidates are compared in Fig. 2.13. It is shown in Fig. 2.13 that the performance of Algorithm 2 applying 16 candidates is about 0.25 dB and 1 dB lower than that of Algorithm 1 and that of the ML detector, respectively. More quantitatively, Algorithm 1 has 0.75 dB performance loss compared to the ML detector at a BER value of 10^{-5}. We conclude that using 4 candidates in Algorithm 1 is sufficient for the system in Fig. 2.13 to attain a better performance, despite having a lower decoding complexity. Additionally, in order to further reduce the complexity, Algorithm 2 applying 16 candidates can be invoked by the proposed system for striking a performance vs complexity trade-off.

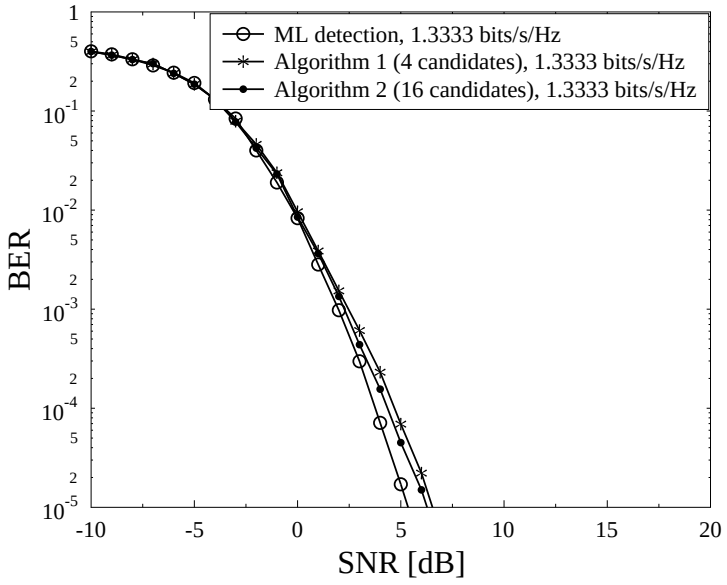

Figure 2.13: BER performances of three schemes applying ML detection, reduced-complexity detection Algorithm 1 with 4 candidates and reduced-complexity detection Algorithm 2 with 16 candidates at the same transmission rate of 1.3333 bits/s/Hz. All other parameters were summarised in Table 2.2.

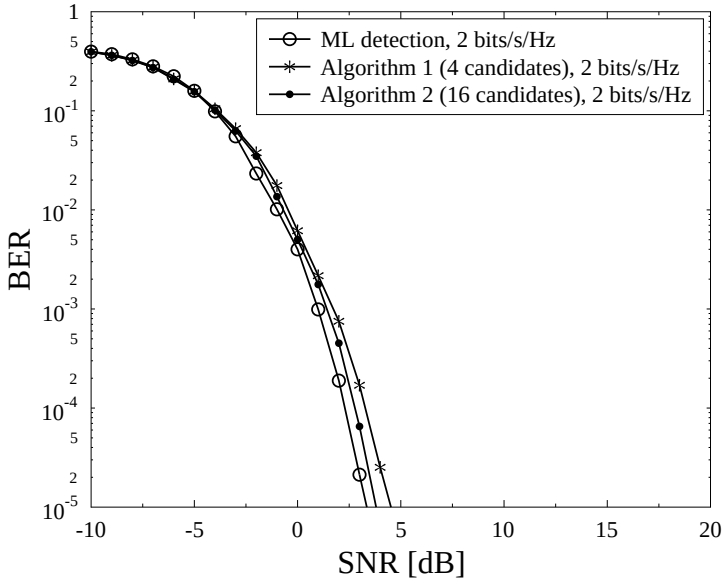

Figure 2.14: BER performances of three schemes applying ML detection, reduced-complexity detection Algorithm 1 with 4 candidates and reduced-complexity detection Algorithm 2 with 16 candidates at the same transmission rate of 2 bits/s/Hz. All other parameters were summarised in Table 2.2.

Similarly, the system of Fig. 2.14 activates $K = 4$ indices out of $N_v = 16$ available indices in each group in the virtual domain and the STSK $(4, 2, 4, 2, 2)$ encoder is applied, which has a transmission rate of 2 bits/s/Hz. It is shown in Fig. 2.14 that Algorithm 1 applying 4 candidates achieves about 1 dB lower performance than the ML detector. Algorithm 2 applying 16 candidates has only 0.5 dB lower performance compared to that of the ML detector. In conclusion, similar trends are valid for both Fig. 2.13 and Fig. 2.14.

In Fig. 2.15, we present simulation results for the proposed CS-aided system under both perfect and imperfect CSI at the transmission rate of 1.1111 bits/s/Hz in order to characterise the effects of imperfect channel estimation on the BER performance. At the receiver, the error of channel estimation is assumed to be complex Gaussian distributed with a mean of zero and a variance of δ_h^2 [213]. In Fig. 2.15, we show the resultant BER performances for $\delta_h^2 = 0.1$, 0.3 and 1.0, where $\delta_h^2 = 1.0$ indicates the scenario of SNR = 0 dB. Compared to the proposed system under perfect CSI, the system relying on realistic imperfect channel estimation shows an evident performance loss. Additionally, it is shown in Fig. 2.15 that there is a higher BER performance degradation upon increasing the power of the channel estimation error.

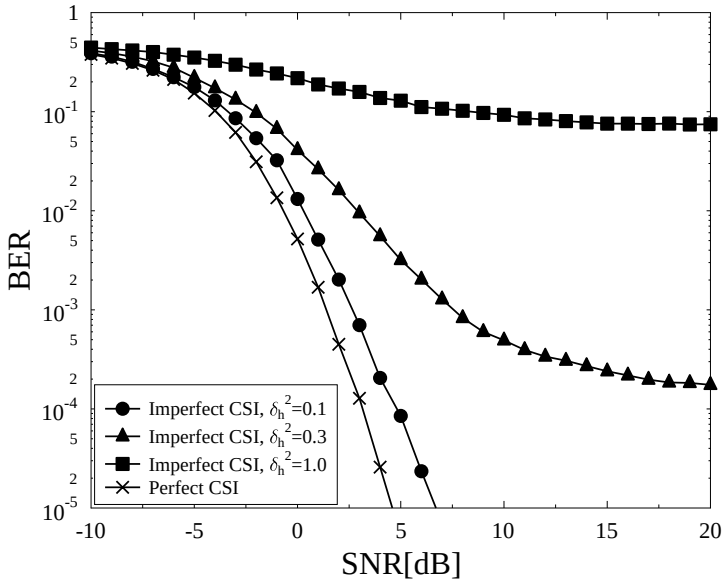

Figure 2.15: BER performances of the proposed CS-aided OFDM-STSK-IM system presented in Fig. 2.10 applying ML detection under the imperfect CSI at the transmission rate of 1.1111 bits/s/Hz. All other parameters were summarised in Table 2.2.

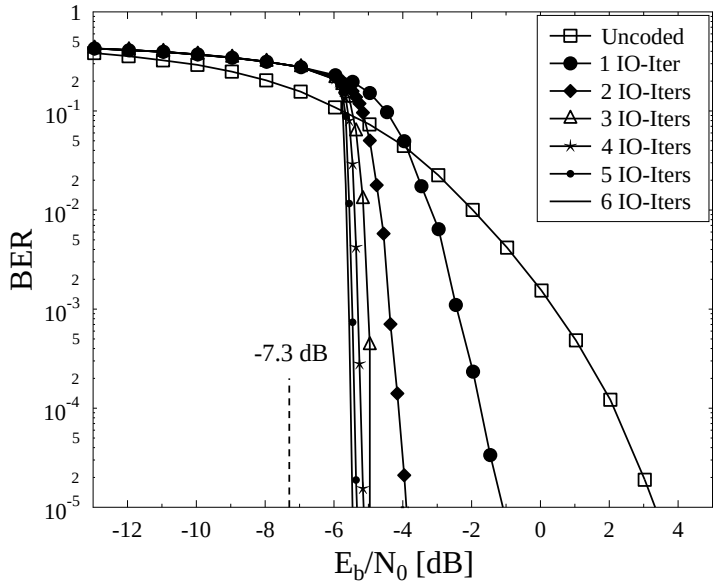

Figure 2.16: BER performances of the 1/2-rate, RSC-coded CS-aided OFDM-STSK-IM scheme presented in Fig. 2.10, while using an interleaver depth of 320, 000 bits. 6 inner-outer detection iterations are applied. Here, IO-Iter is the abbreviation of inner-outer iteration. All other parameters were summarised in Table 2.2.

Fig. 2.16 shows the attainable performance of the 1/2-rate RSC-coded proposed CS-aided OFDM-STSK-IM system of Fig. 2.10 employing an interleaver depth of 320, 000 bits, while using a gradually increasing number of IO decoding iterations of 1 to 6. Here, we use the soft-input soft-output decoder of Eq. (2.26). It is shown in Fig. 2.16 that there is an evident performance improvement when increasing the number of IO decoding iterations. Additionally, the system attains an infinitesimally low BER at around $E_b/N_0 = -5.5$ dB when using 6 IO decoding iterations. In particular, the capacity line at $Eb/N0 = -7.3$ dB of the 1/2-rate RSC-coded CS-aided OFDM-STSK-IM scheme is obtained by Fig. 2.9, which is marked in Fig. 2.16 as well. As seen in Fig. 2.16 that the infinitesimally low BER using 6 IO decoding iterations is only about 1.8 dB away from the system's capacity line.

2.4.3 Computational Complexity Analysis

In Table 2.4, the averaged complexity orders of the schemes characterised in Fig. 2.10-2.14 using the ML detector, the reduced-complexity Algorithm 1 and Algorithm 2 of Section 2.3.2.2 are provided.

Transmission Rate	**ML Detector**	**Algorithm 1**					**Algorithm 2**	
		1 Candidate	**2 Candidates**	**3 Candidates**	**4 Candidates**	**16 Candidates**	**1 Candidate**	**16 Candidates**
1.1111 bits/s/Hz (Fig. 2.10)	$\mathcal{O}(1024)$	$\mathcal{O}(1.7 \times 10^2)$	$\mathcal{O}(3.2 \times 10^2)$	$\mathcal{O}(4.3 \times 10^2)$	$\mathcal{O}(6.1 \times 10^2)$	$\mathcal{O}(1024)$	$\mathcal{O}(84)$	$\mathcal{O}(512)$
1.3333 bits/s/Hz (Fig. 2.13)	$\mathcal{O}(4096)$	$\mathcal{O}(7.3 \times 10^2)$	$\mathcal{O}(1.4 \times 10^3)$	$\mathcal{O}(1.8 \times 10^3)$	$\mathcal{O}(2.6 \times 10^3)$	$\mathcal{O}(4096)$	$\mathcal{O}(1.8 \times 10^2)$	$\mathcal{O}(1024)$
2 bits/s/Hz (Fig. 2.14)	$\mathcal{O}(2.6 \times 10^5)$	$\mathcal{O}(4.3 \times 10^4)$	$\mathcal{O}(8.1 \times 10^4)$	$\mathcal{O}(1.1 \times 10^5)$	$\mathcal{O}(1.6 \times 10^5)$	$\mathcal{O}(2.6 \times 10^5)$	$\mathcal{O}(2.7 \times 10^3)$	$\mathcal{O}(1.6 \times 10^4)$

Table 2.4: Averaged complexity orders of schemes presented in Fig. 2.10, Fig. 2.13, and Fig. 2.14

Combining the BER performances and the averaged complexity orders of these schemes, it can be concluded that we can strike a flexible performance vs detection complexity trade-off by appropriately adjusting the maximum number of candidates exploited. The specific choice of Algorithm 1/Algorithm 2 also depends on the trade-off between the BER performance and complexity order.

Fig. 2.17 illustrates the detection complexity imposed by detecting each group of symbols, when both the ML and the proposed pair of reduced-complexity detectors are employed. Here, the averaged complexity orders in Fig 2.17 are obtained by simulations and can fully illustrate the detection complexity of the proposed reduced-complexity schemes shown in Fig. 2.11 and Fig. 2.12. In Fig. 2.17, the reduced-complexity detector 1 employing $I_n = 1, \ldots, 9$ and N_v candidates is considered for the proposed scheme. It can be readily shown in Fig. 2.17 that the detection complexity of the proposed reduced-complexity detector 1 can be significantly reduced depending on the number of candidates exploited in the proposed system, especially when the number of candidates is set to under 5 candidates. Considering both the BER performance in Fig. 2.11 and

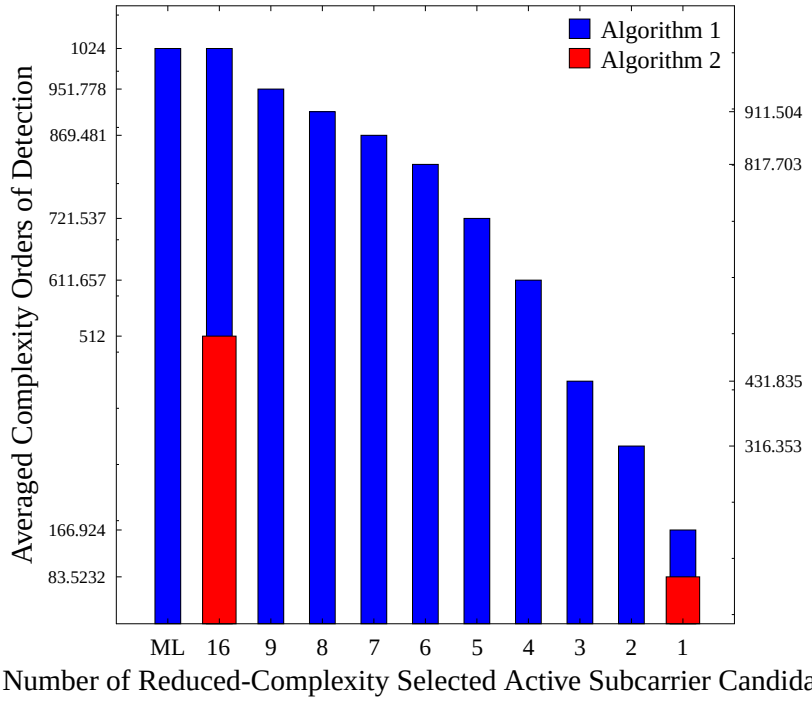

Figure 2.17: Averaged complexity orders with different number of reduced-complexity selected active subcarrier candidates applied for both Algorithm 1 shown in Fig. 2.11 and Algorithm 2 shown in Fig. 2.12.

the detection complexity in Fig. 2.17, we can conclude that the detection complexity can be further reduced by limiting the maximum number of candidates at the cost of some performance loss. For example, the averaged complexity of the scheme applying 4 candidates is almost 0.6 times that of ML detector at the cost of about 4.67 dB performance loss. Similarly, the averaged complexity of the scheme with 5 candidates is 0.7 times that of ML detector at the cost of only 2.72 dB loss. Meanwhile, the averaged complexity orders of the proposed reduced-complexity detector 2 using 1 iteration and 16 iterations are compared in Fig. 2.17. It is obvious in Fig. 2.17 that the averaged complexity order of the detector 2 exploiting all index combinations is half that of the ML detector as well as that of the detector 1 employing 16 candidates at the cost of only 2.92 dB performance loss than ML detection.

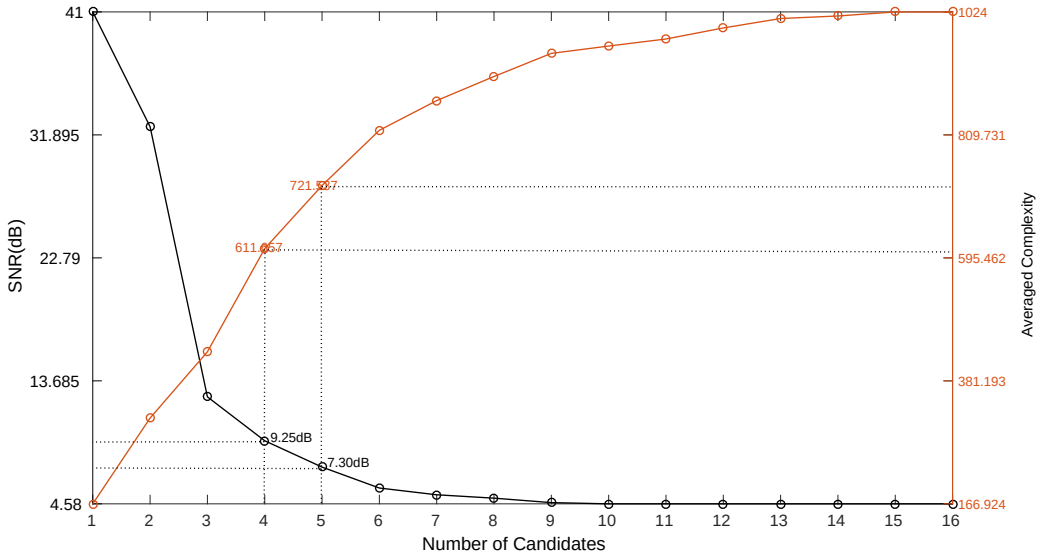

Figure 2.18: The required SNR and averaged complexity orders required to attain a BER value of 10^{-5} for the proposed CS-aided OFDM-STSK-IM decoding Algorithm 1 shown in Fig. 2.11.

In order to further illustrate the BER performance vs complexity trade-off of the different schemes shown in Fig. 2.11, Fig. 2.18 shows the SNR required and the average complexity order required for attaining a BER of 10^{-5} for the CS-aided OFDM-STSK-IM system employing decoding Algorithm 1. As shown in Fig. 2.18, employing more candidates results in a reduced SNR required for attaining a BER of 10^{-5}. Furthermore, no performance improvement is attained employing beyond more than 9 candidates. Fig. 2.18 also shows the average complexity order of the decoder when employing different number of candidates. It becomes clear that using more candidates results in a higher complexity order. According to Fig. 2.12 and Fig. 2.18, Algorithm 2 applying 16 candidates has a similar performance to that of Algorithm 1 applying 5 candidates, but

Algorithm 2 has a lower average complexity order. As a result, for the proposed CS-aided OFDM-STSK-IM scheme employing reduced-complexity detectors, we can strike a flexible performance vs detection complexity trade-off by appropriately adjusting the maximum number of candidates exploited. Finally, the choice of employing Algorithm 1 or Algorithm 2 also depends on the BER performance vs complexity trade-off.

2.5 Chapter Conclusions

In this chapter, we proposed a novel CS-OFDM-STSK-IM scheme relying on a pair of CS-aided reduced-complexity detectors designed for transmission over Rayleigh fading channels. The information bits are transmitted using the space, time and frequency dimensions for improving both the bandwidth efficiency as well as the BER performance. In our simulations, the proposed CS-OFDM-STSK-IM system employing the ML detector of Section 2.3.2.1 has the best BER performance, as seen in Fig. 2.11. Quantitatively, it has a 7.92 dB better performance than the classical OFDM-STSK system at the complexity order of $\mathcal{O}(1 \times 10^3)$. Then, in order to reduce the complexity of the ML detector, a pair of reduced-complexity detectors based on the CS principles were proposed in Section 2.3.2.2. Specifically, we can control the complexity by appropriately adjusting the maximum number of candidates employed by the system at the cost of some performance loss as demonstrated by the simulation results in Fig. 2.17 and Fig. 2.18 of Section 2.4.3. Observe in Figs. 2.12 - 2.14 that the reduced-complexity Algorithm 1 using 4 candidates has a similar BER performance as that of Algorithm 2 using 16 candidates. Additionally, according to Table 2.4, the pair of reduced-complexity algorithms of Section 2.3.2.2 have similar complexity orders, while having lower transmission rates of 1.1111 bits/s/Hz and 1.3333 bits/s/Hz, while Algorithm 2 imposes a reduced complexity at a higher transmission rate of 2 bits/s/Hz. In particular, we summarised the trade-offs among bandwidth efficiency, BER performance and complexity for the CS-OFDM-STSK-IM scheme in Table 2.5, when employing the ML detector of Section 2.3.2.1 and the pair of reduced-complexity detectors of Section 2.3.2.2.

Furthermore, for the sake of achieving a near-capacity performance, a 1/2-rate RSC code was applied to the proposed scheme and iterative decoding exchanging soft extrinsic information between the CS-OFDM-STSK-IM soft decoder and the RSC decoder was employed in Section 2.3.2.3. Observe in Fig. 2.16 that the system attains an infinitesimally low BER at around $E_b/N_0 = -5.5\,dB$, when using 6 inner-outer decoding iterations.

Schemes		**Fig. 2.10**	**Fig. 2.13**	**Fig. 2.14**
$\mathbf{R_t}$**(bits/s/Hz)**		1.1111	1.3333	2
Scenario		-	Increased $\mathcal{L}$	Increased M, T, K
SNR at BER=10^{-5}	ML	4.375 dB	5.25 dB	3.75 dB
	Algorithm 1 (4 candidates)	9.25 dB	6.5 dB	4.75 dB
	Algorithm 2 (16 candidates)	7.5 dB	6.25 dB	4.25 dB
Complexity	ML	$\mathcal{O}(1 \times 10^3)$	$\mathcal{O}(4.1 \times 10^3)$	$\mathcal{O}(2.6 \times 10^5)$
	Algorithm 1 (4 candidates)	$\mathcal{O}(6.1 \times 10^2)$	$\mathcal{O}(2.6 \times 10^3)$	$\mathcal{O}(1.6 \times 10^5)$
	Algorithm 2 (16 candidates)	$\mathcal{O}(5.1 \times 10^2)$	$\mathcal{O}(1 \times 10^3)$	$\mathcal{O}(1.6 \times 10^4)$

Table 2.5: Summary of the CS-OFDM-STSK-IM scheme, employing the system parameters of Table 2.2, where both the ML detector and the reduced-complexity detectors are applied.

This chapter focused on the design of CS-aided frequency-domain IM of OFDM-STSK systems. The simulation results demonstrated that the proposed CS-OFDM-STSK-IM system is capable of achieving better performance than the conventional OFDM-MIMO scheme both in terms of its achievable transmission rate and BER. It is worth mentioning that exploring the spatial-domain IM strategy in conjunction with the CS-OFDM-STSK-IM system is appealing. Therefore, in the following chapter, CS-aided multi-dimensional IM systems will be investigated.

Chapter 3

Compressed Sensing-Aided Multi-Dimensional Index Modulation

3.1 Introduction

In Chapter 2, we investigated CS-aided OFDM-STSK-IM systems, where only frequency-domain IM was invoked at the transmitter. Hence, in this chapter, we propose a CS-aided multi-dimensional IM scheme relying on both frequency- and spatial-domain IM techniques as shown in Fig. 3.1, which is capable of attaining better BER performance as well as higher capacity by indexing multiple transmission entities, when compared to both the classical OFDM-MIMO system and the CS-OFDM-STSK-IM system of Chapter 2. However, it becomes significantly more challenging to detect both the active TAs, as well as the active subcarrier indices and modulated symbols due to the strong interference imposed both on the OFDM-IM sub-blocks and on the TAs. Although the ML detector is capable of achieving optimal performance, its prohibitive computational complexity makes it impractical for the multi-dimensional scheme. Hence, it is essential to conceive reduced-complexity detection. Additionally, we only designed a soft-decision-based decoder using the high-complexity ML detector in Chapter 2. Hence, it is necessary to design a soft-decision-based decoder relying on new reduced-complexity detectors for achieving a near-capacity performance in this chapter.

Several multi-dimensional IM systems relying on both frequency- and spatial-domain IM were proposed in the literature [111, 157], where these studies use a joint space-frequency indexing strategy. In this chapter, a separate spatial-domain and frequency-domain indexing strategy is invoked, which allows configuring the different components

to satisfy specific design requirements.

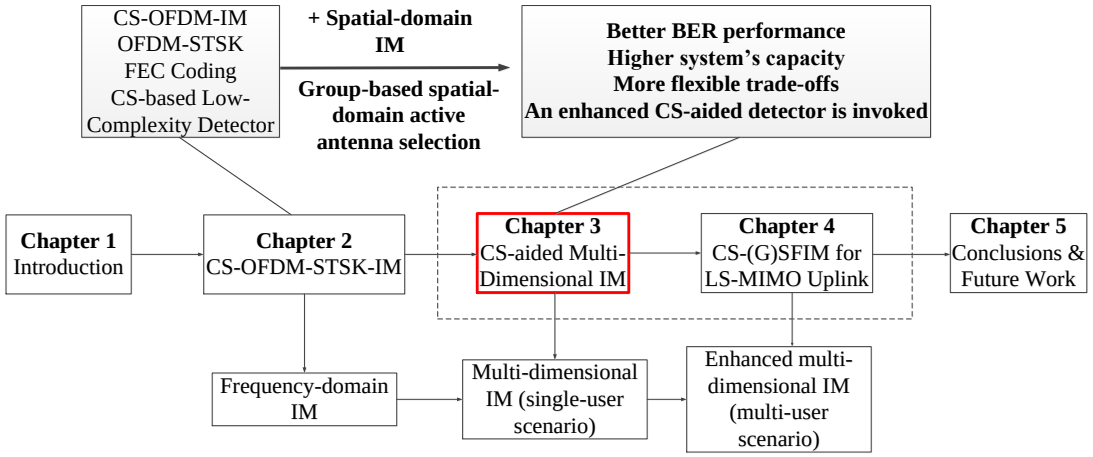

Figure 3.1: Interconnection of Chapter 3 with the rest of the thesis.

Against the above background, the contributions of this chapter are summarised as follows:

- We propose a CS-aided multi-dimensional IM system relying on both frequency-domain and spatial-domain IM for improving the performance by attaining an improved diversity gain, whilst increasing the system capacity by indexing multiple transmission entities. This scheme will be compared both to the classical OFDM-MIMO system and to our previously proposed CS-OFDM-STSK-IM system of Chapter 2. More explicitly, compared to the classical OFDM-STSK system and to the CS-OFDM-STSK-IM system of Chapter 2 relying on the ML detector, the proposed system exhibits SNR-gains of about 8.75 dB and 4.3 dB at the BER of 10^{-5}, respectively. Furthermore, an upper bound of the average bit error probability (ABEP) of the proposed CS-aided multi-dimensional IM system has also been derived and confirmed by computer simulations. The proposed multi-functional design is quite flexible, allowing us to strike a flexible trade-off between the performance, the achievable rate and the complexity, where the different components can be conveniently configured in order to satisfy specific design requirements.

- A reduced-complexity so-called simultaneous matching pursuit (S-MP) based detector is proposed for detecting multiple measurement vectors (MMV) at the same time by exploiting the powerful CS principles, whilst mitigating the excessive complexity of the ML detector at the cost of a modest performance loss. Explicitly, the proposed S-MP detector is specifically designed for our CS-aided multi-dimensional IM system, where the active TAs and active subcarriers are first jointly detected and then they are utilised for reconstructing the space-time symbols.

- Then the CS-aided multi-dimensional soft-input soft-output IM receivers using both the ML detector and the proposed S-MP detector are conceived for iteratively exchanging extrinsic soft information between the constituent decoders in order to achieve a near-capacity performance. More specifically, EXIT charts are used for visually characterising the flow of soft-information between the constituent decoders of our concatenated structure. We also construct EXIT charts for evaluating the maximum achievable rate of the proposed system using both the ML detector and the S-MP detector. Furthermore, the DCMC capacity of the proposed CS-aided multi-dimensional IM scheme is formulated and compared to the maximum achievable rate of the system derived from the EXIT charts.

The rest of the chapter is organised as follows. In Section 3.2, the system model of CS-aided multi-dimensional IM is introduced, including the models of both the transmitter and the receiver. Then in Section 3.3.1 both the hard-decision based ML detector and the CS-based reduced-complexity detector are introduced. Furthermore, soft-decision based detectors relying both on the ML and on the reduced-complexity detectors of Section 3.3.1 are conceived in Section 3.3.2. Our simulation results, EXIT chart analysis and system capacity estimates are provided in Section 3.4. Finally, we conclude the chapter in Section 3.5.

3.2 System Model

In this section, we introduce the transceiver architecture of the proposed CS-aided multi-dimensional IM system relying on N_t TAs and N_r receive antennas (RAs), which is illustrated in Fig. 3.2. Explicitly, in contrast to our CS-aided frequency-domain IM scheme of Fig. 2.6, the spatial-domain IM is amalgamated with frequency-domain IM in our CS-aided multi-dimensional IM scheme of Fig. 3.2. Hence a powerful detector is required for detecting not only the space-time symbols and the activated subcarriers, but also the activated TAs. Similarly to the CS-aided frequency-domain IM scheme of Fig. 2.6 detailed in Section 2.3.1, we consider an OFDM scheme having N_c subcarriers, which are then equally partitioned into G subcarrier groups, where each contains $N_f = N_c/G$ subcarriers in the frequency-domain.

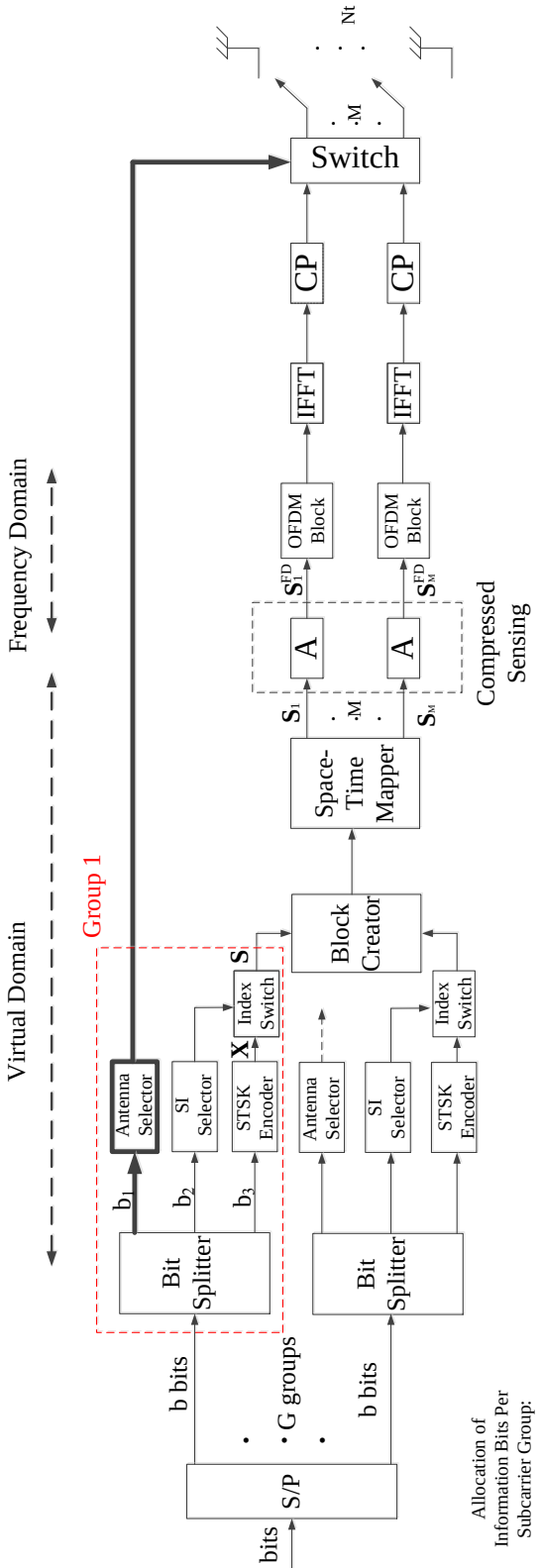

Figure 3.2: The proposed multi-dimensional IM aided transceiver architecture. It was developed from Fig. 2.6, where the Antenna Selector block is introduced to the CS-aided frequency-domain IM system of Fig. 2.6 and is marked using bold lines.

In this chapter, we focus on the transmission and detection of a single group instead of G groups, because each subcarrier group has the same procedures, as shown in Fig. 3.2. The transmitter model is introduced in Section 3.2.1, followed by the receiver model in Section 3.2.2.

3.2.1 Transmitter

The transmitter model of the new CS-aided multi-dimensional IM system is shown in Fig. 3.2, which is developed from Fig. 2.6 by conceiving the spatial-domain IM with frequency-domain IM at the transmitter. Based on the CS-aided frequency-domain IM scheme of Fig. 2.6 detailed in Section 2.3.1, the information bits of Fig. 3.2 are partitioned into G groups each containing b bits. Then each group of b bits are split into smaller segments of b_1, b_2 and b_3 bits, where the first b_1 bits are mapped to the Antenna Selector of Fig. 3.2, while the remaining b_2 and b_3 bits are processed by the Subcarrier Index (SI) Selector and the STSK Encoder, respectively. In other words, the information bits in the proposed system are conveyed not only by the classic PSK/QAM constellation symbols, but also by the indices of both the subcarriers and of the TAs.

In the following subsections, the information flow through the Antenna Selector, the Subcarrier Index Selector, the STSK Encoder and the transmitter model portrayed in Fig. 3.2 will be illustrated, respectively.

3.2.1.1 Antenna Selector

The b_1 bits are processed by the Antenna Selector of Fig. 3.2, which selects M TAs out of the N_t available TAs, while obtaining N_{AC} Antenna Combinations (ACs) in total[1]. Compared to the SM scheme of Fig. 2.2, a specific combination of TAs out of N_{AC} ACs is activated during each transmission block in the proposed system instead of simply activating a single TA. Inspired by the concept of the Distinctive Antenna Combination (DAC) scheme proposed in [52], we assign M unique TAs to each AC in order to avoid the correlation caused by sharing the same TA element among different ACs [52]. Additionally, the specific AC selected for transmitting symbols in each subcarrier group depends on the $b_1 = \lfloor \log_2 (N_{AC}) \rfloor$ information bits controlling the Antenna Selector in Fig. 3.2. Specifically, a look-up table example of the Antenna Selector is provided in Table 3.1 for $M = 2$, $N_t = 4$ and $N_{AC} = 2$. In this example, when the first incoming

[1]The CS-aided frequency-domain IM scheme of Fig. 2.6 becomes a special case of our new CS-aided multi-dimensional IM scheme of Fig. 3.2 if we have $M = N_t$, and the new resultant system can transmit more data bits by applying $M < N_t$ without affecting the performance.

b_1	Indices	Allocation
[0]	$\{1, 2\}$	$[TA^1\ TA^2\ 0\ 0]$
[1]	$\{3, 4\}$	$[0\ 0\ TA^3\ TA^4]$

Table 3.1: A look-up table example for the Antenna Selector in Fig. 3.2 with $M = 2$ and $N_t = 4$.

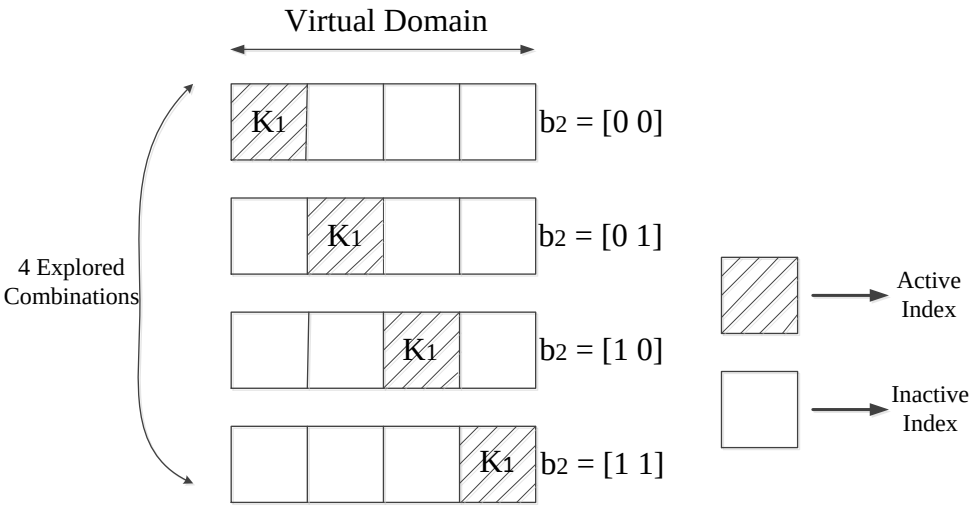

Figure 3.3: The selection procedure of the SI Selector in Fig. 3.2 for $K = 1$ and $N_v = 4$.

bit is $b_1 = [0]$, then the first and second TAs, namely TA^1 and TA^2 will be selected as unique ACs for transmitting symbols in a specific subcarrier block, while the other two TAs remain inactive. Similarly, if the first incoming bit is $b_1 = [1]$, then the third and fourth TAs denoted by TA^3 and TA^4 are activated for the transmission of classic PSK/QAM symbols.

3.2.1.2 Space-Frequency Transmitter Model

Then the second incoming sequence of b_2 bits is applied to the SI Selector in Fig. 3.2. Similarly to the IM Selector of Fig. 2.6, in each subcarrier block only K subcarriers are activated out of the N_v available subcarriers in the virtual domain and their specific selection is determined by the information bits b_2, where a look-up table example of the IM Selector's operation was provided in Table 2.1. More particularly, in order to expound a little further, the selection procedure of the SI Selector of Fig. 3.2 is illustrated in Fig. 3.3 selecting $K = 1$ active subcarriers out of the $N_v = 4$ available subcarriers in

each subcarrier group, where the shaded square represents the active subcarriers, while the blank square indicates the inactive subcarriers. Explicitly, in this example the first subcarrier is activated according to the incoming bits $b_2 = [0\,0]$, while the second, the third and the fourth subcarriers are selected for $b_2 = [0\,1]$, $b_2 = [1\,0]$ and $b_2 = [1\,1]$, respectively. In each subcarrier group, the selected active subcarrier combination is fed into the Index Switch of Fig. 3.2 for allocating K space-time symbols generated by the STSK Encoder to the activated subcarriers.

According to the STSK Encoder of Fig. 2.6 detailed in Section 2.3.1, a total of $b_3 = K\log_2(Q\mathcal{L})$ bits are fed into the STSK Encoder to generate K STSK codewords $\{\mathbf{X}[1], \ldots, \mathbf{X}[i], \ldots, \mathbf{X}[K]\}$, spreading the information both over M TAs and over T time slots in each subcarrier group, where each space-time codeword $\mathbf{X}[i] \in \mathbb{C}^{M\times T}$ is generated by spreading a conventional $\mathcal{L}$-ary constellation symbol over one out of Q DMs. According to the specific SI combination of each subcarrier group gleaned from the Index Switch of Fig. 3.2, the K STSK symbols[2] generated by the STSK Encoder are mapped to the K active subcarriers selected, while the inactive subcarriers are set to zero, which results in the space-time symbol $\mathbf{S}$ in Fig. 3.2.

Upon considering $b_2 = [0\,0]$ of the example shown in Fig. 3.3, the space-time symbol generated after the active subcarrier allocation becomes $\mathbf{S} = \{\mathbf{X}[1]\,\mathbf{0}\,\mathbf{0}\,\mathbf{0}\}$, where Fig. 3.4 was developed from Fig. 2.7 for further illustrating the space-time structure of $\mathbf{S}$. More particularly, Fig. 3.4 also portrays how the measurement matrix A compresses the symbols of dimension $N_v = 4$ observed in the virtual domain into the symbols of dimension $N_f = 2$ in the frequency-domain per subcarrier group. According to both Fig. 2.6 and Fig. 3.2, there are G space-time structures similar to $\mathbf{S}$ shown in Fig. 3.4 for G subcarrier groups, which are then assembled by the Block Creator of Fig. 3.2 for constructing a space-time super frame. Then the space-time symbol $\mathbf{S}$ per subcarrier group[3] is mapped to M transmit antenna elements during T time slots by the Space-Time Mapper of Fig. 2.6 as well as of Fig. 3.2 and M symbol sequences $\{\mathbf{s}_1, \ldots, \mathbf{s}_M\}$ are obtained at the M transmit antenna elements during a single time slot, as illustrated in Fig. 3.4.

Observe in Fig. 3.2 and Fig. 3.4 that the measurement matrix $\mathbf{A}$ of size $(N_f \times N_v)$ is applied to the space-time mapped vectors for compressing the N_v-dimensional vectors $\mathbf{s}_m$ $(m = 1, 2, \ldots, M)$ of the virtual domain into the N_f-dimensional vectors $\mathbf{s}_m^{FD}$ $(m = 1, 2, \ldots, M)$ of the frequency-domain, where M OFDM symbols are constructed,

[2]Note that the number of STSK codewords generated by the STSK Encoder is the same as the number of active subcarriers in each subcarrier group for allocating K STSK codewords to K active subcarriers selected by the SI Selector of Fig. 3.2.

[3]Note that all processes in the following text only refer to a single subcarrier group instead of the entire frame, since all of them are processed identically.

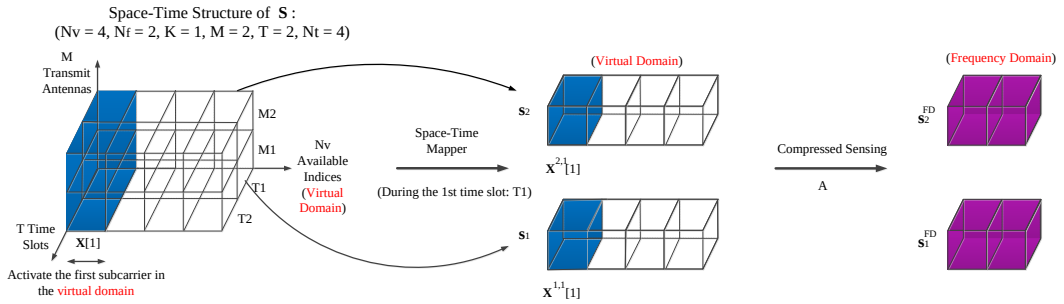

Figure 3.4: Illustration of the structure for the frame symbol $\mathbf{S}$ per subcarrier group shown in Fig. 3.2, the process of the Space-Time Mapper in the virtual domain and the process of CS technique in the frequency-domain, while having $M = 2$ TAs, $T = 2$ time slots, $K = 1$ active subcarrier out of $N_v = 4$ available indices in the virtual domain and $N_f = 2$ subcarriers per subcarrier group in the frequency-domain. Additionally, the example given in Fig. 3.3 is applied and we have $b_2 = [0\,0]$.

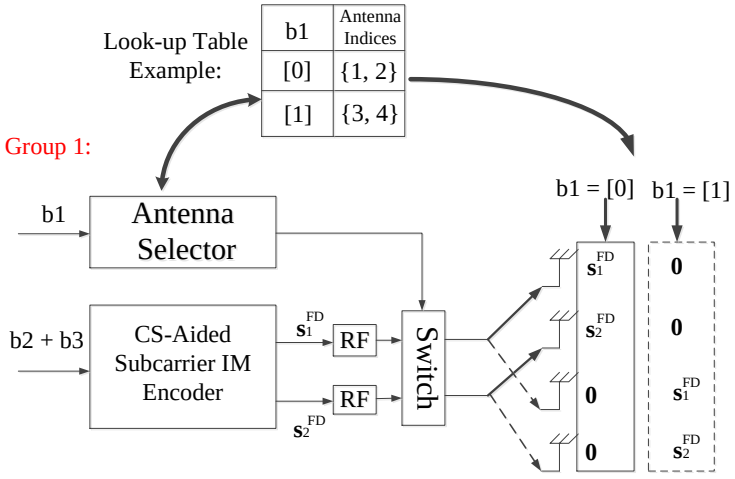

Figure 3.5: The process of selecting active TAs with the example of $M = 2$ and $N_t = 4$.

while hosting G groups of N_f-dimensional vectors. Based on Eqs. (2.4) and (2.6), the frequency-domain vector $\mathbf{s}_m^{FD}$ at the output of the CS block of Fig. 3.2 is calculated by

$$\mathbf{s}_m^{FD} = \mathbf{A}\mathbf{s}_m. \tag{3.1}$$

In contrast to the process after the CS block of Fig. 2.6, the frequency-domain symbol vectors $\mathbf{s}_m^{FD}$ $(m = 1, 2, \ldots, M)$ of Fig. 3.4 per group at the M transmit antenna elements are transmitted over a specific activated TA combination out of N_{AC} available combinations obtained by the Antenna Selector of Fig. 3.2 detailed in Section 3.2.1.1.

More particularly, Fig. 3.5 further illustrates the TA selection scheme with the aid of the look-up table example of Table. 3.1. More explicitly, as shown in Fig. 3.5, the frequency-domain symbol vectors $\mathbf{s}_1^{FD}$ and $\mathbf{s}_2^{FD}$ in each subcarrier group during a single time slot are transmitted over the first and second activated TAs if the incoming data bit is $b_1 = [0]$ and the other two TAs are inactive. The third and the fourth activated TAs are used for transmitting $\mathbf{s}_1^{FD}$ and $\mathbf{s}_2^{FD}$, if the incoming data bit is $b_1 = [1]$.

3.2.2 Receiver

We consider a $(N_r \times N_t)$-MIMO system, where N_r is the number of RAs as shown in Fig. 3.2. At the receiver side, the signals of the G groups received from N_r RAs during T time slots are subjected to the FFT for detecting the frequency-domain output symbols. The frequency-domain channel matrix is $\mathbf{H}_\alpha \in \mathbb{C}^{N_r \times N_t}$ for $\alpha = 1, \ldots, N_f$. As shown in Fig. 3.2, the Space-Time Demapper collects the G groups frequency-domain symbols from N_r RAs over T time slots, and the space-time demapped symbols are split into G groups by the Block Splitter of Fig. 3.2. The symbols received by each subcarrier group are represented by $\mathbf{Y} = \{\mathbf{Y}[1]^T, \ldots, \mathbf{Y}[\alpha]^T, \ldots, \mathbf{Y}[N_f]^T\}^T$ $(\alpha = 1, \ldots, N_f)$, as shown in Fig. 3.2, where $\mathbf{Y} \in \mathbb{C}^{N_r N_f \times T}$ and $\mathbf{Y}[\alpha] \in \mathbb{C}^{N_r \times T}$ characterise the space-time structure and the space-time symbol received at the α-th subcarrier of each subcarrier group, respectively.

Then the signals $\mathbf{Y}[\alpha] \in \mathbb{C}^{N_r \times T}$ $(\alpha = 1, \ldots, N_f)$ received during T time slots of each subcarrier group can be modelled as

$$\mathbf{Y}[\alpha] = \mathbf{H}_\alpha \mathbf{I}_{AC} \mathbf{S}^{FD}[\alpha] + \mathbf{W}[\alpha], \tag{3.2}$$

where the $\mathbf{S}^{FD}[\alpha] \in \mathbb{C}^{M \times T}$ denotes space-time symbols at N_f frequency-domain subcarriers transmitted from M transmit antenna elements over T time slots, and $\mathbf{W}[\alpha] \in \mathbb{C}^{N_r \times T}$ represents the AWGN obeying the distribution of $\mathcal{CN}(0, \sigma_n^2)$ and σ_n^2 is the noise variance. Furthermore, when we compare Eq. (2.7) of the CS-aided frequency-domain IM scheme obeying the transceiver architecture of Fig. 2.6 and Eq. (3.2) of our new CS-aided multi-dimensional IM scheme shown in Fig. 3.2, we observe that $\mathbf{I}_{AC}$ is invoked in the signal model for selecting the activated TAs. Specifically, $\mathbf{I}_{AC} \in \mathbb{C}^{N_t \times M}$ in Eq. (3.2) denotes the $(N_t \times M)$-element submatrix, which explicitly describes the selection pattern of active TAs for each subcarrier group at the transmitter. More specifically, taking the example shown in Fig. 3.5 and Table 3.1 associated with $M = 2$ and $N_t = 4$, the (4×2)-element submatrix $\mathbf{I}_{AC}$ activating the first and second TAs out of the 4 available TAs is generated, as shown in Fig. 3.6. Then after constructing the space-time symbols for

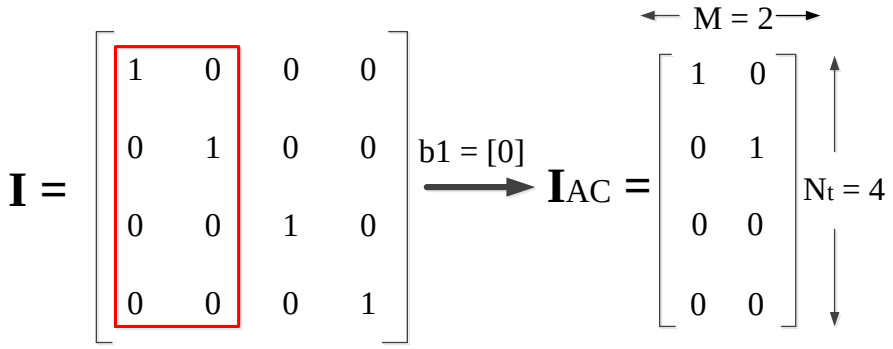

Figure 3.6: The illustration of TA-selection submatrix, where it takes $M = 2$ and $N_t = 4$ as an example.

each subcarrier group by the Space-Time Demapper, the received signals are detected group-by-group as described in the following section.

3.3 Detection Techniques

In the proposed CS-aided multi-dimensional IM system, the receiver has to detect the information bits conveyed by the STSK codewords at the active subcarriers plus the bits mapped to the active subcarrier indices, as well as the bits mapped to the active TAs, as shown in Fig. 3.2. Again, we consider both hard-decision ML detection and our reduced-complexity Simultaneous Matching Pursuit (S-MP) detection, later followed by soft-decision detection.

As shown in Fig. 3.2, the received signal $\mathbf{Y}$ contains N_f space-time symbols at the N_f subcarriers in the frequency-domain of each subcarrier group. According to the received signal model $\mathbf{Y}[\alpha] \in \mathbb{C}^{N_r \times T}$ $(\alpha = 1, \ldots, N_f)$ shown in Eq. (3.2), we can rewrite $\mathbf{Y} \in \mathbb{C}^{N_r N_f \times T}$ as

$$\mathbf{Y} = \mathbf{H}\bar{\mathbf{I}}_{AC}\mathbf{S}^{FD} + \mathbf{W}, \tag{3.3}$$

where $\mathbf{W} \in \mathbb{C}^{N_r N_f \times T}$ denotes the AWGN matrix of the N_f subcarriers, and the channel matrix $\mathbf{H}$ associated with transmitting N_f space-time signals in each subcarrier group,

which has a diagonal structure of size $(N_r N_f \times N_t N_f)$ and can be expanded as

$$\mathbf{H} = \begin{bmatrix} \mathbf{H}_1 & \mathbf{0} & \dots & \mathbf{0} \\ \mathbf{0} & \mathbf{H}_2 & \dots & \mathbf{0} \\ \vdots & \vdots & \ddots & \vdots \\ \mathbf{0} & \mathbf{0} & \dots & \mathbf{H}_{N_f} \end{bmatrix}. \tag{3.4}$$

Similarly, $\bar{\mathbf{I}}_{AC} \in \mathbb{C}^{N_t N_f \times M N_f}$ denotes the TA selection pattern of N_f subcarriers in each subcarrier group, which has the diagonal structure of

$$\bar{\mathbf{I}}_{AC} = \begin{bmatrix} \mathbf{I}_{AC} & \mathbf{0} & \dots & \mathbf{0} \\ \mathbf{0} & \mathbf{I}_{AC} & \dots & \mathbf{0} \\ \vdots & \vdots & \ddots & \vdots \\ \mathbf{0} & \mathbf{0} & \dots & \mathbf{I}_{AC} \end{bmatrix}. \tag{3.5}$$

Additionally, $\mathbf{S}^{FD} \in \mathbb{C}^{M N_f \times T}$ represents the frequency-domain space-time signals of the N_f subcarriers transmitted from M TAs over T time slots, which are obtained after the SI modulation and CS, as shown in Fig. 3.2 and Fig. 3.4. In order to make the analysis more comprehensive, the transmitted space-time signals $\mathbf{S}^{FD} \in \mathbb{C}^{M N_f \times T}$ in Eq. (3.3) are represented as

$$\mathbf{S}^{FD} = \bar{\mathbf{A}} \mathbf{S}^{VD} = \bar{\mathbf{A}} \mathbf{I}_{SI} \mathbf{X}, \tag{3.6}$$

where $\bar{\mathbf{A}} \in \mathbb{C}^{M N_f \times M N_v}$ is the equivalent measurement matrix $\mathbf{A}$ shown in Eq. (3.1) invoked for compressing the M virtual-domain vectors, and $\mathbf{S}^{VD} \in \mathbb{C}^{M N_v \times T}$ denotes the virtual-domain space-time symbols, as shown in Fig. 3.2. Then $\mathbf{S}^{VD}$ is expanded as $\mathbf{S}^{VD} = \mathbf{I}_{SI} \mathbf{X}$, where $\mathbf{X} \in \mathbb{C}^{MK \times T}$ represents K STSK codewords generated by the STSK Encoder of Fig. 3.2. Additionally, the K STSK codewords $\mathbf{X} \in \mathbb{C}^{MK \times T}$ are also illustrated in Fig. 3.4, where $K = 1$ is considered and the shaded $\mathbf{X}[1]$ specifically illustrates the structure of $\mathbf{X} \in \mathbb{C}^{MK \times T}$. Additionally, $\mathbf{I}_{SI} \in \mathbb{C}^{M N_v \times MK}$ illustrates the specific SI selection pattern of each subcarrier group while selecting K active subcarriers out of N_v available subcarriers in the virtual domain. If we consider the example provided in Fig. 3.3 and Fig. 3.4 using $K = 1$, $N_v = 4$ and $M = 2$, then the (8×2)-element

submatrix $\mathbf{I}_{SI}$ for $b_2 = [0\,0]$ is written as

$$\mathbf{I}_{SI} = \begin{bmatrix} 1 & \vdots & 0 \\ 0 & \vdots & 0 \\ 0 & \vdots & 0 \\ 0 & \vdots & 0 \\ \dots & \dots & \dots \\ 0 & \vdots & 1 \\ 0 & \vdots & 0 \\ 0 & \vdots & 0 \\ 0 & \vdots & 0 \end{bmatrix}, \tag{3.7}$$

where the first index is activated out of the 4 available subcarrier indices in the virtual domain.

According to Eq. (3.3) - Eq. (3.7), the received signal model for each subcarrier group can be finally expressed as

$$\mathbf{Y} = \mathbf{H}\bar{\mathbf{I}}_{AC}\bar{\mathbf{A}}\mathbf{I}_{SI}\mathbf{X} + \mathbf{W}, \tag{3.8}$$

where $\bar{\mathbf{I}}_{AC}$ contains the TAs selection information and $\mathbf{I}_{SI}$ includes the SI selection information for the subcarrier group. Based on the received signal model of Eq. (3.8), hard-decision decoding is discussed in Section 3.3.1, while soft-decision decoding is described in Section 3.3.2.

3.3.1 Hard-Decision Detection

In this section, the hard-decision based ML detector and the reduced-complexity detector of the proposed CS-aided multi-dimensional system are proposed and an upper bound of the ABEP of the proposed system is also derived. The computational complexity of the two detectors is also compared. We assume perfect channel knowledge at the receiver.

3.3.1.1 Maximum Likelihood Detection

At the receiver, the ML detector makes a joint decision on the active TA indices, the active subcarrier indices and the constellation points at the corresponding active subcarrier indices by exploring all possible realisations of each subcarrier group. According to the system model in Eq. (3.8), $\bar{\mathbf{I}}_{AC}$ represents the specific realisation of the active TA indices out of the N_{AC} possible realisations in each subcarrier group and we use $\bar{\mathcal{I}}_{AC}(\gamma)$

($\gamma = 1, 2, \ldots, N_{AC}$) to denote the realisation of the active TA indices. Similarly, $\mathbf{I}_{SI}$ in Eq. (3.8) represents the specific realisation of the active subcarrier indices in the virtual domain of each subcarrier group and we use $\mathcal{I}_{SI}(\beta)$ ($\beta = 1, 2, \ldots, N_{SI}$) to denote all possible realisations of the active subcarrier indices. Additionally, there are $N_{q,l} = (Q\mathcal{L})^K$ realisations of $\mathbf{X}$, which represents K STSK codewords in Eq. (3.8) and we apply $\mathcal{X}_{q,l}(\varphi)$ ($\varphi = 1, 2, \ldots, N_{q,l}$) to indicate all realisations of the K STSK codewords in the proposed system model. Then the ML detector of each subcarrier group is formulated as:

$$< \hat{\gamma}, \hat{\beta}, \hat{\varphi} >= \arg \min_{\gamma,\beta,\varphi} \|\mathbf{Y} - \mathbf{H}\bar{\mathcal{I}}_{AC}(\gamma)\bar{\mathbf{A}}\mathcal{I}_{SI}(\beta)\mathcal{X}_{q,l}(\varphi)\|^2, \tag{3.9}$$

where $\hat{\gamma}$, $\hat{\beta}$ and $\hat{\varphi}$ represent the estimates of the active TAs realisation index, the active subcarriers realisation index and the index of the realisation for K STSK codewords in each subcarrier group, respectively.

At the receiver, the ML detector carries out a full search for exploring all possible realisations, while having a complexity order of $\mathcal{O}[N_{AC}N_{SI}(Q\mathcal{L})^K]$ per subcarrier group. More particularly, in contrast to the complexity order $\mathcal{O}[N_{SI}(Q\mathcal{L})^K]$ of the ML detector of Eq. (2.13) obeying the architecture of Fig. 2.6, we observe that the detection of our CS-aided multi-dimensional IM scheme of Fig. 3.2 becomes more complicated due to the application of spatial-domain IM. More precisely, the total computational complexity of the ML detector of Eq. (3.9) can be expressed as $\mathcal{O}_{ML}\Big[(N_rN_tMN_f^3 + N_rM^2N_f^2N_v + N_rN_fM^2N_vK + N_rN_fMKT)N_{AC}N_{SI}(Q\mathcal{L})^K\Big]$, which may become excessive in practice for larger values of Q and $\mathcal{L}$, for a higher-dimensional virtual domain, and for larger number of TAs. Therefore, a reduced-complexity detection algorithm will be proposed in Section 3.3.1.3.

3.3.1.2 Average BEP Analysis of ML Detection

For the sake of improved clarity, we rewrite the per-subcarrier-group received signal model of Eq. (3.8) as

$$\mathbf{Y} = \mathbf{H}\bar{\mathbf{S}} + \mathbf{W}, \tag{3.10}$$

where $\bar{\mathbf{S}} \in \mathbb{C}^{N_tN_f \times T}$ is the equivalent data matrix which has $(N_{AC}N_{SI}(Q\mathcal{L})^K)$ possible realisations. Additionally, it is sufficient to determine the overall system performance by exploring the Pairwise Error (PE) events for a single subcarrier group, because the PE events of different subcarrier groups are the same [214]. If the matrix $\bar{\mathbf{S}}$ is transmitted and it is erroneously detected as $\hat{\bar{\mathbf{S}}}$, the receiver may make decision errors concerning either the active TAs, or the active SI and the STSK codewords per subcarrier group.

Then the Conditional Pairwise Error Probability (CPEP) of the system model given in Eq. (3.10) is expressed as [214]

$$P(\bar{\mathbf{S}} \to \widehat{\bar{\mathbf{S}}}|\mathbf{H}) = Q\left(\sqrt{\frac{\|\mathbf{H}(\bar{\mathbf{S}} - \widehat{\bar{\mathbf{S}}})\|^2}{2\sigma_n^2}}\right). \tag{3.11}$$

Let $\mathbf{D}_{\bar{\mathbf{S}}} = \bar{\mathbf{S}} - \widehat{\bar{\mathbf{S}}}$ denote the difference matrix between $\bar{\mathbf{S}}$ and $\widehat{\bar{\mathbf{S}}}$. Applying $\mathbf{D}_{\bar{\mathbf{S}}}$ to Eq. (3.11), we have

$$P(\bar{\mathbf{S}} \to \widehat{\bar{\mathbf{S}}}|\mathbf{H}) = Q\left(\sqrt{\frac{\|\mathbf{H}\mathbf{D}_{\bar{\mathbf{S}}}\|^2}{2\sigma_n^2}}\right) = \frac{1}{\pi}\int_0^{\pi/2} \exp\left(\xi\alpha\right) d\theta, \tag{3.12}$$

where we have $\xi = \|\mathbf{H}\mathbf{D}_{\bar{\mathbf{S}}}\|^2 = \sum_{i=1}^{N_f}\sum_{r=1}^{N_r} (\mathbf{H}_i)_r \mathbf{D}_{\bar{\mathbf{S}}_i}\mathbf{D}_{\bar{\mathbf{S}}_i}^H (\mathbf{H}_i)_r^H$, $\alpha = -\frac{1}{4\sigma_n^2 \sin^2\theta}$ and $(\mathbf{H}_i)_r$ $(i = 1, 2, \ldots, N_f$ and $r = 1, 2, \ldots, N_r)$ is used for denoting the r-th row of the i-th channel matrix given in Eq. (3.4).

Then the computation of the Unconditional Pairwise Error Probability (UPEP) $P(\bar{\mathbf{S}} \to \widehat{\bar{\mathbf{S}}})$ is obtained by taking the expectation relative to all possible channel realisations, while integrating the CPEP in Eq. (3.12) over the probability density function (pdf) of ξ and yielding

$$P(\bar{\mathbf{S}} \to \widehat{\bar{\mathbf{S}}}) = \mathbb{E}_{\mathbf{H}}\{P(\bar{\mathbf{S}} \to \widehat{\bar{\mathbf{S}}}|\mathbf{H})\} = \frac{1}{\pi}\int_0^{\pi/2} M_\xi(\alpha) d\theta, \tag{3.13}$$

where $M_\xi(\alpha)$ represents the moment generating function of ξ and we have [214]

$$M_\xi(\alpha) = \prod_{i=1}^{N_f}\left(\frac{1}{\det\left(\mathbf{I}_{N_t} - \alpha\mathbb{E}\{(\mathbf{H}_i)_r^H(\mathbf{H}_i)_r\}\mathbf{D}_{\bar{\mathbf{S}}_i}\mathbf{D}_{\bar{\mathbf{S}}_i}^H\right)}\right)^{N_r} = \prod_{i=1}^{N_f}\left(\frac{1}{1 - \alpha\|\mathbf{D}_{\bar{\mathbf{S}}_i}\|^2}\right)^{N_r}. \tag{3.14}$$

Upon substituting Eq. (3.14) into Eq. (3.13), the UPEP is finally obtained as

$$P(\bar{\mathbf{S}} \to \widehat{\bar{\mathbf{S}}}) = \frac{1}{\pi}\int_0^{\pi/2}\prod_{i=1}^{N_f}\left(\frac{\sin^2\theta}{\sin^2\theta + \frac{\|\mathbf{D}_{\bar{\mathbf{S}}_i}\|^2}{4\sigma_n^2}}\right)^{N_r} d\theta. \tag{3.15}$$

After obtaining the UPEP in Eq. (3.15), an upper bound on the ABEP based on union bounding can be obtained by

$$P_B \leq \frac{1}{bN\left(\bar{\mathbf{S}}\right)}\sum_{\bar{\mathbf{S}}}\sum_{\widehat{\bar{\mathbf{S}}}} P(\bar{\mathbf{S}} \to \widehat{\bar{\mathbf{S}}}) d(\bar{\mathbf{S}}, \widehat{\bar{\mathbf{S}}}), \tag{3.16}$$

where b is the number of information bits carried by each subcarrier group, $N\left(\bar{\mathbf{S}}\right) = N_{AC}N_{SI}(Q\mathcal{L})^K$ denotes the total number of possible realisations of $\bar{\mathbf{S}}$ per subcarrier group and $d(\bar{\mathbf{S}}, \hat{\bar{\mathbf{S}}})$ is used for representing the number of bit errors involved in the PE event of $(\bar{\mathbf{S}} \to \hat{\bar{\mathbf{S}}})$.

3.3.1.3 Reduced-Complexity Detection

In order to reduce the search-space of the ML detector of Eq. (3.9), in this section we propose a reduced-complexity detector. According to the received signal model $\mathbf{Y}$ of Eq. (3.8), there are three search items to be detected, namely the active TAs, the active subcarriers and the STSK codewords allocated to the active subcarriers, and for the sake of further analysis, we rewrite Eq. (3.8) as

$$\begin{aligned}\mathbf{Y} &= \mathbf{H}\bar{\mathbf{I}}_{AC}\bar{\mathbf{A}}\mathbf{I}_{SI}\mathbf{X} + \mathbf{W} = \mathbf{H}\bar{\mathbf{S}} + \mathbf{W} \\ &= \bar{\mathbf{H}}\mathbf{S}^{VD} + \mathbf{W} \qquad (3.17) \\ &= \mathbf{\Phi}\mathbf{X} + \mathbf{W}, \qquad (3.18)\end{aligned}$$

where by definition we have $\bar{\mathbf{S}} \in \mathbb{C}^{N_t N_f \times T} = \bar{\mathbf{I}}_{AC}\mathbf{S}^{FD}$ for denoting the equivalent data matrix that has $N_{AC} \cdot N_{SI} \cdot (Q\mathcal{L})^K$ possible realisations, $\bar{\mathbf{H}} \in \mathbb{C}^{N_r N_f \times M N_v} = \mathbf{H}\bar{\mathbf{I}}_{AC}\bar{\mathbf{A}}$ is used for representing the equivalent channel matrix that has N_{AC} possible realisations and $\mathbf{\Phi} \in \mathbb{C}^{N_r N_f \times MK}$ for denoting the equivalent matrix which indicates having $N_{AC} \cdot N_{SI}$ possible joint support identifications, including the active TAs and active subcarriers. In terms of the sparsity characteristics of $\bar{\mathbf{S}}$ in Eq. (3.10) and $\mathbf{S}^{VD}$ in Eq. (3.17), the detector can be designed according to the CS principles [184].

Specifically, we use the matrix $\mathbf{Y} \in \mathbb{C}^{N_r N_f \times T}$ in Eq. (3.10) to explicitly represent the N_f frequency-domain signals received from N_r RAs over T time slots and each column of $\mathbf{Y}$ can be regarded as a measurement vector according to the CS principles, where the joint support identification $\mathbf{\Phi}$ in our scenario is shared by T measurement vectors from $\mathbf{Y}$, which is a manifestation of the MMV problem of CS principles [215]. Various recovery algorithms have been proposed for the MMV scenario, while in this work we propose a S-MP algorithm inspired by the classic Subspace Pursuit (SP) algorithm of [188] which is one of the popular greedy algorithms and it is used to solve the Single Measurement Vector (SMV) problem of [188].

The proposed S-MP procedure is described in **Algorithm 1**, where the T measurement vectors of $\mathbf{Y}$ received are detected simultaneously in order to improve the performance. More specifically, the main differences between the proposed S-MP algorithm and the

Algorithm 1 Reduced-Complexity S-MP Detection

Inputs: $\mathbf{Y}$, $\mathbf{H}$, $\bar{\mathbf{A}}$, hard threshold $\mathcal{T}_\varepsilon$

Outputs: $\hat{\mathbf{\Phi}} = (\bar{\mathcal{I}}_{AC}, \mathcal{I}_{SI})$; $\hat{\mathbf{X}} = \left[\hat{\mathbf{X}}[1]^T\, \hat{\mathbf{X}}[2]^T \ldots \hat{\mathbf{X}}[K]^T\right]^T$.

1: $n = 0$; { Iteration index initialisation }
2: $J = N_{SI}$; { Size of fixed-size subspace }
3: **for** $\alpha = 1 \cdots N_f$ **do**
4: $\quad \mathbf{Y}[\alpha] = \mathbf{H}_\alpha \bar{\mathbf{S}}[\alpha] + \mathbf{W}[\alpha]$; { See Eq. (3.2) and Eq. (3.10) }
5: $\quad \hat{\bar{\mathbf{S}}}[\alpha] = \left((\mathbf{H}_\alpha)^H \mathbf{H}_\alpha + \frac{1}{\rho_s}\mathbf{I}_{N_t}\right)^{-1} \mathbf{H}_\alpha^H \cdot \mathbf{Y}[\alpha]$; { MMSE rough estimation for the α-th subcarrier, where ρ_s indicates the average SNR per symbol. }
6: $\quad \Omega_{AC}^{\alpha} = \arg\max_{t=1\cdots N_{AC}} \|(\hat{\bar{\mathbf{S}}}[\alpha])_t\|^2$; { Obtain the index of the space-time matrix having the highest magnitude, where $(\hat{\bar{\mathbf{S}}}[\alpha])_t \in \mathbb{C}^{M\times T}$ }
7: **end for**
8: **Select the active TAs index Ω_{AC}, which is the most frequent index among Ω_{AC}^{α} $(\alpha = 1, 2, \ldots, N_f)$;**
9: $n = n + 1$; {Update the iteration index}
10: **for** $j = 1 \cdots J$ **do**
11: $\quad \hat{\mathbf{X}}_j^n = (\mathbf{\Phi}_j^n)^\dagger \cdot \mathbf{Y}$; { Least squares operation based on Eq. (3.18) and the identification candidate $\mathbf{\Phi}_j^n$ in the n-th iteration }
12: $\quad \mathbf{R}_j^n = \mathbf{Y} - \mathbf{\Phi}_j^n \hat{\mathbf{X}}_j^n$; { Check the residual }
13: **end for**
14: $\mathbf{\Phi}^n = \arg\min_{j=1\cdots J} \|\mathbf{R}_j^n\|^2$; { Find the support identification of the best candidate of the n-th iteration }
15: **if** $\|\mathbf{Y} - \mathbf{\Phi}^n \hat{\mathbf{X}}^n\|^2 \leq \mathcal{T}_\varepsilon$ **then**
16: $\quad \hat{\mathbf{\Phi}} = \mathbf{\Phi}^n$; { The final refined **joint support identification** }
17: $\quad$ **quit**
18: **else**
19: $\quad$ **if** $\|\mathbf{Y} - \mathbf{\Phi}^n \hat{\mathbf{X}}^n\|^2 > \mathcal{T}_\varepsilon$ **then**
20: $\quad\quad$ **Jump to 8 and select the index having the second largest magnitude for starting the 2^{nd} iteration;**
21: $\quad$ **end if**
22: **end if**

classical SP algorithm lie in two aspects: **1)** The proposed S-MP algorithm is specifically designed for solving the MMV problem in our scenario and it is invoked for jointly detecting both the active TAs in the space domain and the active subcarriers in the virtual domain in our case as described in **Algorithm 1**, for achieving an improved performance. By contrast, the classical SP algorithm is only suitable for single-domain sparsity; **2)** The most significant difference between the proposed S-MP and the classical SP algorithms lies in their specific approach invoked for generating the subspace during each iteration. In the classical SP algorithm, a fixed-size estimated subspace is maintained and refined during each iteration. On the other hand, in the proposed S-MP algorithm, during each iteration the algorithm exploits an N_{SI}-size subspace represented as $\mathbf{\Phi}_j^n$ $(j = 1, 2, \ldots, N_{SI})$, including the estimated active TA support identifications and the N_{SI} possible active subcarrier support identifications, where the tested joint support

identification resulting in the least residual errors is selected as the most reliable candidate during the iteration and then it is evaluated by comparing it to the hard threshold $\mathcal{T}_\varepsilon$ for terminating the iterations.

Based on the reduced-complexity S-MP procedure introduced in **Algorithm 1**, the maximum number of iterations is $n = N_{AC}$, where $N_{AC}N_{SI}$ possible joint realisations will be explored and the complexity order per subcarrier group is given by $\mathcal{O}(N_{AC}N_{SI}+Q\mathcal{L}K)$. Furthermore, most of the computational requirements of the proposed S-MP algorithm are imposed by the least squares operations carried out within the iterations. Therefore, the exact computational complexity of the proposed S-MP algorithm having $n = N_{AC}$ iterations is $\mathcal{O}_{S-MP} = [(MKN_rN_f(2MK+T))\,N_{AC}N_{SI} + KQ\mathcal{L}(MT)]$. Specifically, compared to the computational complexity of the ML detector of Section 3.3.1.1, the proposed S-MP algorithm significantly reduces the influence of having large K, Q, or $\mathcal{L}$ values in the proposed system.

3.3.2 Soft-Decision Detection

Having introduced the hard-decision based ML detection and S-MP detection in Section 3.3, we now introduce soft-decision based detection. As illustrated in Fig. 3.7, analogously to the soft-decision based detector of Fig. 2.8, we employ a two-stage concatenated CS-aided multi-dimensional IM system for achieving a near-capacity performance. Specifically, the channel encoder of Fig. 3.7 encodes the input bits by applying a RSC code for generating the coded bit sequence $\mathbf{c}$ and the interleaver Π is used for generating the interleaved stream $\mathbf{u}$ to avoid the influence of bursty channel errors by dispersing them. Then the interleaved bit sequence $\mathbf{u}$ of each subcarrier group is conveyed by the proposed CS-aided multi-dimensional IM modulator described in Section 3.2.1. At the receiver of Fig. 3.7, the soft-input soft-output decoder iteratively exchanges soft extrinsic information in the form of LLRs [216] with the RSC decoder. To be specific, the demodulator's extrinsic output LLRs $L_{i,e}(\mathbf{u})$ are deinterleaved by a soft-bit deinterleaver to generate $L_{o,a}(\mathbf{c})$, which is the input of the outer RSC decoder in the form of *a priori* LLRs. Then the extrinsic LLRs $L_{o,e}(\mathbf{c})$ of all the channel-coded bits of each subcarrier group are calculated by the Logarithmic Maximum *a posteriori* (Log-MAP) algorithm [199, 217], where the extrinsic information $L_{o,e}(\mathbf{c})$ calculated is then fed back to the demodulator as the *a priori* information $L_{i,a}(\mathbf{u})$ after the interleaver of Fig. 3.7. Then the improved extrinsic LLRs are calculated by the demodulator and further Inner-Outer (IO) iterations are employed.

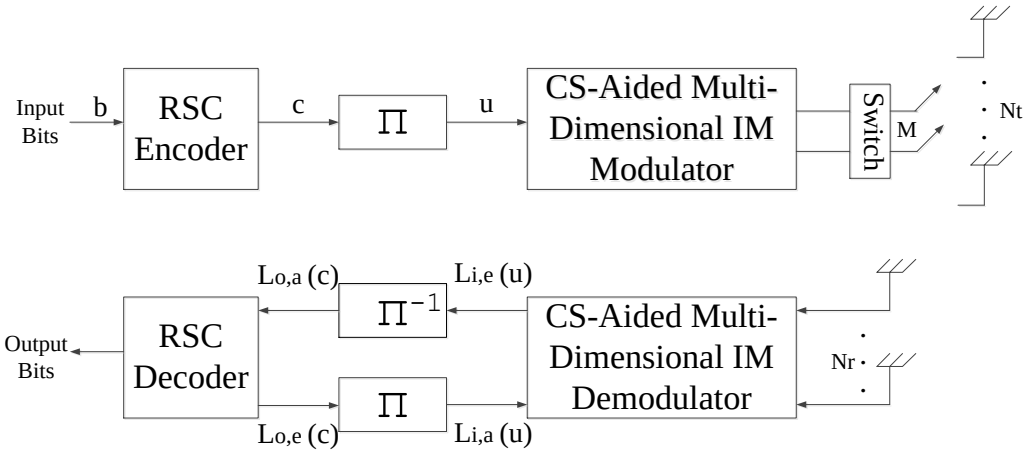

Figure 3.7: The receiver architecture of the soft-decision assisted CS-aided multidimensional IM scheme, which was developed from Fig. 2.8.

3.3.2.1 ML-based Soft-Decision Detection

According to the equivalent system model of Eq. (3.8) and the calculation of the conditional probability of Eq. (2.24), the conditional probability $p(\mathbf{Y}|\mathcal{X}_{\gamma,\beta,\varphi})$ of receiving the group signal $\mathbf{Y}$ is given by

$$p(\mathbf{Y}|\mathcal{X}_{\gamma,\beta,\varphi}) = \frac{1}{(\pi N_0)^{NT}} \exp\left(- \frac{\|\mathbf{Y} - \mathbf{H}\bar{\mathcal{I}}_{AC}(\gamma)\bar{\mathbf{A}}\mathcal{I}_{SI}(\beta)\mathcal{X}_{q,l}(\varphi)\|^2}{N_0} \right), \tag{3.19}$$

where $\mathcal{X}_{\gamma,\beta,\varphi}$ represents STSK codewords at the β-th realisation of active subcarriers, which are transmitted through the φ-th realisation of active TAs, and N_0 is the noise power, where we have $\sigma_n^2 = N_0/2$ with $N_0/2$ representing the double-sided noise power spectral density. The equivalent received signal $\mathbf{Y}$ per subcarrier group carries B channel-coded bits $\mathbf{u} = [u_1, u_2, \ldots, u_B]$ and the extrinsic LLR of bit u_l $(l = 1, 2 \ldots, B)$ is expressed by Eq. (3.20) [203].

$$\begin{aligned} L_{i,e}(u_l) &= \ln \frac{\sum_{\mathcal{X}_{\gamma,\beta,\varphi} \in \mathcal{X}_1^l} p(\mathbf{Y}|\mathcal{X}_{\gamma,\beta,\varphi}) \exp\left[\sum_{j \neq l} u_j L_{i,a}(u_j)\right]}{\sum_{\mathcal{X}_{\gamma,\beta,\varphi} \in \mathcal{X}_0^l} p(\mathbf{Y}|\mathcal{X}_{\gamma,\beta,\varphi}) \exp\left[\sum_{j \neq l} b_j L_{i,a}(b_j)\right]} \\ &= \ln \frac{\sum_{\mathcal{X}_{\gamma,\beta,\varphi} \in \mathcal{X}_1^l} \exp\left[-\|\mathbf{Y} - \mathbf{H}\bar{\mathcal{I}}_{AC}(\gamma)\bar{\mathbf{A}}\mathcal{I}_{SI}(\beta)\mathcal{X}_{q,l}(\varphi)\|^2/N_0 + \sum_{j \neq l} u_j L_{i,a}(u_j)\right]}{\sum_{\mathcal{X}_{\gamma,\beta,\varphi} \in \mathcal{X}_0^l} \exp\left[-\|\mathbf{Y} - \mathbf{H}\bar{\mathcal{I}}_{AC}(\gamma)\bar{\mathbf{A}}\mathcal{I}_{SI}(\beta)\mathcal{X}_{q,l}(\varphi)\|^2/N_0 + \sum_{j \neq l} u_j L_{i,a}(u_j)\right]}. \end{aligned} \tag{3.20}$$

In Eq. (3.20), $\mathcal{X}_1^l$ and $\mathcal{X}_0^l$ represent a subset of the legitimate equivalent signal $\mathcal{X}$ corresponding to bit u_l when $u_l = 1$ and $u_l = 0$, respectively, yielding $\mathcal{X}_1^l \equiv \{\mathcal{X}_{\gamma,\beta,\varphi} \in \mathcal{X} : u_l = 1\}$ and $\mathcal{X}_0^l \equiv \{\mathcal{X}_{\gamma,\beta,\varphi} \in \mathcal{X} : u_l = 0\}$. Additionally, $L_{i,a}(\cdot)$ in Eq. (3.20) represents the a

priori information based on the feedback from the RSC decoder to the proposed modulator. Furthermore, the Approximate Log-MAP (Approx-Log-MAP) algorithm based on the Jacobian maximum operation [110] is implemented for the sake of simplifying the soft-decisions and the algorithm is given by [199, 202],

$$L_{i,e}(u_l) = \text{jac}_{\mathcal{X}_{\gamma,\beta,\varphi}\in\mathcal{X}_1^l}\left(\lambda_{\gamma,\beta,\varphi}\right) - \text{jac}_{\mathcal{X}_{\gamma,\beta,\varphi}\in\mathcal{X}_0^l}\left(\lambda_{\gamma,\beta,\varphi}\right), \tag{3.21}$$

where $\text{jac}(\cdot)$ denotes the Jacobian maximum operation [110] and the intrinsic metric of $\lambda_{\gamma,\beta,\varphi}$ is expressed as

$$\lambda_{\gamma,\beta,\varphi} = \Big(- \|\mathbf{Y} - \mathbf{H}\bar{\mathcal{I}}_{AC}(\gamma)\bar{\mathbf{A}}\mathcal{I}_{SI}(\beta)\mathcal{X}_{q,l}(\varphi)\|^2/N_0 + \sum_{j\neq l} u_j L_{i,a}(u_j)\Big). \tag{3.22}$$

3.3.2.2 S-MP-based Soft-Decision Detection

In order to reduce the computational complexity of the soft decoder, soft-decision based reduced-complexity S-MP detection is invoked. To be specific, the equivalent received signal $\mathbf{Y}$ per subcarrier group carries in total of B channel-coded bits, where the first B_1 channel-coded bits $\mathbf{u}^1 = [u_1^1, u_2^1, \ldots, u_{B_1}^1]$ are invoked for selecting the joint realisations of active TAs and active subcarriers, e.g. $B_1 = \log_2(N_{AC}) + \log_2(N_{SI})$, and the remaining B_2 channel-coded bits $\mathbf{u}^2 = [u_1^2, u_2^2, \ldots, u_{B_2}^2]$ are used for encoding K STSK codewords, where $B_2 = K\log_2(Q\mathcal{L})$. Then at the first step of the S-MP-based soft-detection, the joint realisations of active TAs and active subcarriers are detected by applying our CS technique. Explicitly, based on the estimation of the joint identification support presented in **Algorithm 1**, the extrinsic LLR of bit u_l^1 $(l = 1, 2, \ldots, B_1)$ expressed with the aid of the Jacobian maximum operation is given by [203, 209]

$$L_{i,e}(u_l^1) = \text{jac}_{\mathbf{\Phi}_{\gamma,\beta}\in\mathbf{\Phi}_1^l}(\lambda_{\gamma,\beta}) - \text{jac}_{\mathbf{\Phi}_{\gamma,\beta}\in\mathbf{\Phi}_0^l}(\lambda_{\gamma,\beta}), \tag{3.23}$$

where the intrinsic metric of $\lambda_{\gamma,\beta}$ is represented as

$$\lambda_{\gamma,\beta} = \Big(- \|\mathbf{Y} - \mathbf{\Phi}_{\gamma,\beta}\mathbf{\Phi}_{\gamma,\beta}^{\dagger}\mathbf{Y}\|^2/N_0 + \sum_{j\neq l} u_j L_{i,a}(u_j)\Big). \tag{3.24}$$

Then, first hard decisions can be made based on the LLRs of $L_e(u_l^1)$ for B_1 channel-coded bits to obtain the joint realisation $\hat{\mathbf{\Phi}}$ of the active TAs and active subcarriers. At the second step of the soft-decision based S-MP algorithm, the extrinsic LLR of bit u_l^2

$(l = 1, 2, \ldots, B_2)$ is expressed by employing the Jacobian maximum operation as

$$L_{i,e}(u_l^2) = \text{jac}_{\mathcal{X}_{q,l} \in \mathcal{X}_1^l}(\lambda_{q,l,k}) - \text{jac}_{\mathcal{X}_{q,l} \in \mathcal{X}_0^l}(\lambda_{q,l,k}), \tag{3.25}$$

where the intrinsic metric of $\lambda_{q,l,k}$ is given by

$$\lambda_{q,l,k} = \Big(- \|\hat{\mathbf{X}}(k) - \mathcal{X}_{q,l}\|^2 / N_0 + \sum_{j \neq l} u_j L_{i,a}(u_j) \Big), \tag{3.26}$$

and the estimated STSK codewords $\hat{\mathbf{X}}(k)$ $(k = 1, \ldots, K)$ seen in Eq. (3.26) are obtained based on the result of the first step according to $\hat{\mathbf{X}}(k) = (\hat{\mathbf{\Phi}}^{\dagger}\mathbf{Y})_k$.

Parameters	**Values**
Multi-carrier System	OFDM
Number of subcarriers, N_c	128
Length of cyclic prefix, N_{cp}	16
Channel Specification	COST207-TU12 Rayleigh Fading
FEC coding in Figs. 3.12 - 3.14, 3.16 - 3.17	1/2-rate RSC$(2, 1, 5)$
Depth of interleaver in Figs. 3.12 - 3.14, 3.16 - 3.17	$192,000$ bits
Number of subcarrier groups, G	16 (change in Fig. 3.15)
Number of frequency-domain subcarriers/group, N_f	8 (change in Fig. 3.15)
Number of virtual-domain indices/group, N_v	16 (change in Fig. 3.11, Fig. 3.15, and Table 3.4)
Number of active indices/group, K	2
Number of available transmit antennas, N_t	8 or 2 (change in Fig. 3.8, Fig. 3.15)
STSK $(M, N, T, Q, \mathcal{L})$	$(2, 2, 2, 2, 2)$ (change in Fig. 3.8, Fig. 3.9, Fig. 3.10, and Table 3.3)

Table 3.2: System parameters in the simulations of Chapter 3.

3.4 Performance Analysis

In this section, the performance of the proposed CS-aided multi-dimensional IM system considered for transmission over Rayleigh fading channels is characterised by simulations. Specifically, both the performance and the computational complexity of the CS-aided frequency-domain IM scheme[4] of Fig. 2.6 are compared to our CS-aided multi-dimensional IM scheme of Fig. 3.2. In all simulations, we assume perfect CSI knowledge at the receiver. The BER performances of the schemes are evaluated by Monte-Carlo simulations. We summarise the system parameters of this section in Table 3.2.

3.4.1 Hard-Decision Performances and Computational Complexity Comparison

In Fig. 3.8, we investigate the BER performances of the proposed CS-aided multi-dimensional IM system of Fig. 3.2 using both the ML detector of Section 3.3.1.1 and the proposed S-MP detector of Section 3.3.1.3 associated with $N_t = 8, N_v = 16$ and STSK$(2, 2, 2, 2, 2)$, the CS-aided frequency-domain IM system of Fig. 2.6 using the ML detector in conjunction with $N_t = 2, N_v = 16$ and STSK$(2, 2, 2, 2, 4)$ and the classical OFDM-STSK system applying the ML detector, where 96 out of 128 subcarriers are used for transmitting STSK$(2, 2, 2, 2, 2)$ symbols, at the same transmission rate of about $R_t = 1.3333$ bits/s/Hz. Furthermore, the theoretical bounds of Eq. (3.16) have been added to Fig. 3.8, where it is observed that the upper bound derived becomes very tight upon increasing the SNR values for the proposed CS-aided multi-dimensional IM system. According to the BER performances of these four schemes explored in Fig. 3.8, we conclude that an improved performance can be achieved, when the number of indexed transmission entities is increased. Specifically, for 1.3333 bits/s/Hz, the proposed CS-aided multi-dimensional system of Fig. 3.2 using the ML detector associated with a complexity order of $\mathcal{O}_{ML}(8.52 \times 10^6)$ achieves about 4.3 dB and 9.65 dB better performances than the CS-aided frequency-domain IM system of Fig. 2.6 at the complexity order of $\mathcal{O}_{ML}(5.9 \times 10^6)$ and the classical OFDM-STSK system, respectively, at the BER value of 10^{-5}. Additionally, the proposed CS-aided multi-dimensional IM system using the proposed S-MP detector having a complexity order of $\mathcal{O}_{S-MP}(1.64 \times 10^5)$ exhibits about 4.3 dB worse performance than its ML counterpart and achieves similar performance as the CS-aided frequency-domain IM scheme of Fig. 2.6, but about 4.6 dB better performance than the classical OFDM-STSK system using ML detector, again

[4]In order to have a fair comparison, the coordinate interleaving of Fig. 2.6 detailed in Eq. (2.5) is not applied here.

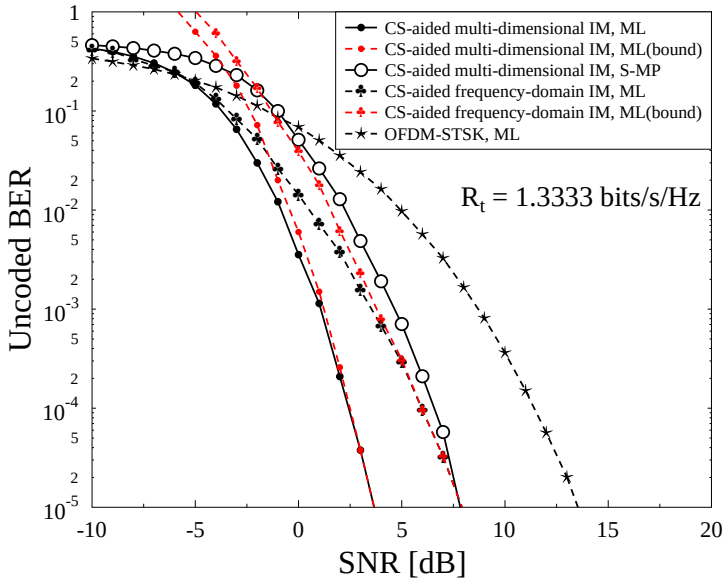

Figure 3.8: BER performances of the proposed CS-aided multi-dimensional IM scheme using both the ML detector and the S-MP detector, the CS-aided frequency-domain IM scheme of Fig. 2.6 using the ML detector and the classical OFDM-STSK system using the ML detector, at the same transmission rate of $R_t = 1.3333$ bits/s/Hz. All other system parameters were summarised in Table 3.2.

at the BER value of 10^{-5}. Hence the performance of the proposed system applying the S-MP detector approaches that of its ML counterpart upon increasing the SNR, while achieving a similar BER performance as the CS-aided frequency-domain IM scheme of Fig. 2.6, despite imposing a significantly lower computational complexity.

Similarly, in Fig. 3.9, we show the BER performances of the proposed CS-aided multi-dimensional IM system of Fig. 3.2 using both the ML detector and the S-MP detector associated $N_t = 16, N_v = 16$ and STSK$(2, 2, 2, 4, 4)$, the CS-aided frequency-domain IM system of Fig. 2.6 using the ML detector in conjunction with $N_t = 2, N_v = 16$ and STSK$(2, 2, 2, 8, 4)$ and the classical OFDM-STSK system applying the ML detector, where 128 subcarriers are used for transmitting STSK$(2, 2, 2, 2, 2)$ symbols, at a higher transmission rate of about $R_t = 1.89$ bits/s/Hz. Observe in Fig. 3.9 that the CS-aided multidimensional IM scheme of Fig. 3.2 using the ML detector associated with a complexity order of $\mathcal{O}_{ML}(5.7\times10^9)$ achieves about 3.4 dB and 9.7 dB better performance than the CS-aided frequency-domain IM system of Fig. 2.6 having a complexity order of $\mathcal{O}_{ML}(9.5 \times 10^8)$ and the classical OFDM-STSK system, respectively, at the BER value of 10^{-5}. Additionally, the proposed CS-aided multi-dimensional IM system using the

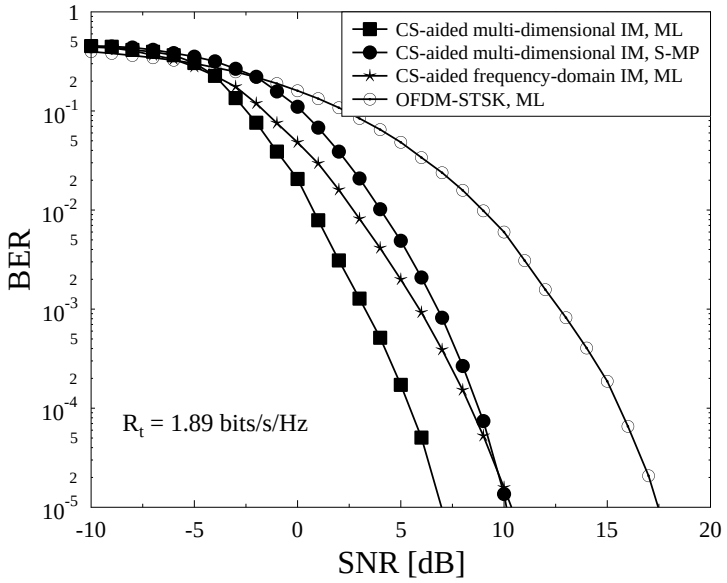

Figure 3.9: BER performances of the proposed CS-aided multi-dimensional IM system using both the ML detector and the S-MP detector, the CS-aided frequency-domain IM scheme of Fig. 2.6 using the ML detector and the classical OFDM-STSK system using the ML detector, at the same transmission rate of $R_t = 1.89$ bits/s/Hz. All other system parameters were summarised in Table 3.2.

proposed S-MP detector associated with a complexity order of $\mathcal{O}_{S-MP}(3.3 \times 10^5)$ has about 3 dB worse performance than its ML counterpart, but about 0.4 dB and 6 dB better performances than the CS-aided frequency-domain IM scheme of Fig. 2.6 having a complexity order of $\mathcal{O}_{ML}(9.5 \times 10^8)$ and the classical OFDM-STSK system using the ML detector, respectively, again at the BER value of 10^{-5}.

In Fig. 3.10, the BER performances of the proposed CS-aided multi-dimensional IM systems using both the ML and the S-MP detectors are presented, while having varying values of $(Q\mathcal{L})$. Note that upon varying the values of $(Q\mathcal{L})$ we can readily control both the SE, as well as influence the BER performance and the complexity orders, while fixing the remaining parameters. As seen in Fig. 3.10, the BER performance of the system having $(Q\mathcal{L}) = 4$ achieves about 1.6 dB and 3.4 dB better performances than that of the system having $(Q\mathcal{L}) = 8$ and $(Q\mathcal{L}) = 16$, respectively, while using the ML detector, at the BER value of 10^{-5}.

Furthermore, in Fig. 3.11, the BER performances of the CS-aided multi-dimensional IM systems using both the ML and the S-MP detectors are presented, while having different virtual-domain sizes N_v. It is shown in Fig. 3.11 that the BER performance

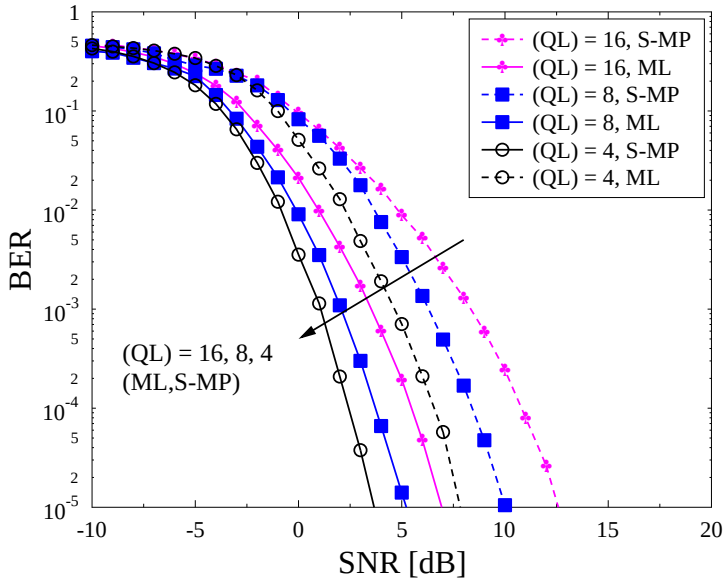

Figure 3.10: BER performances of the CS-aided multi-dimensional IM schemes using both the ML detector and the S-MP detector with the varying values of $(Q\mathcal{L})$. All other system parameters were summarised in Table 3.2.

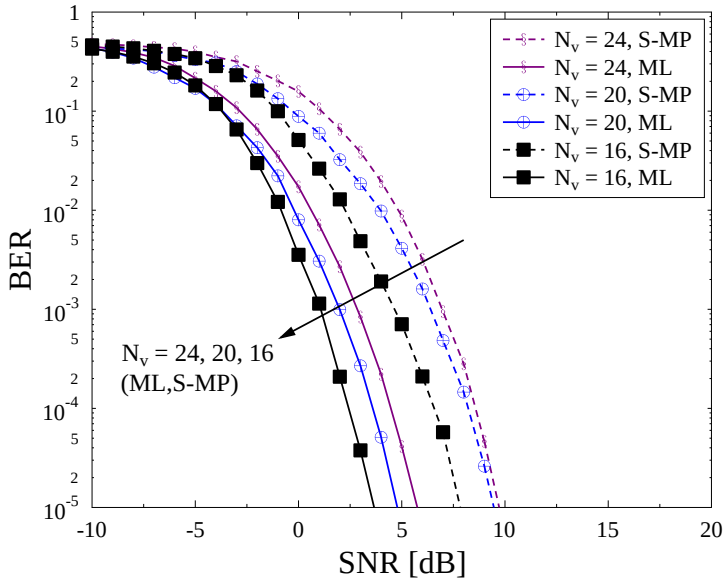

Figure 3.11: BER performances of the CS-aided multi-dimensional IM schemes using both the ML detector and the S-MP detector with the varying values of virtual-domain N_v. All other system parameters were summarised in Table 3.2.

$(Q\mathcal{L})$	Complexities of CS-aided Multi-Dimensional IM Schemes with $N_v = 16, N_f = 8, K = 2, N_t = 8$, STSK$(2, 2, 2, Q, \mathcal{L})$ and varying $(Q\mathcal{L})$	
	ML (Sec. 3.3.1.1)	S-MP (Sec. 3.3.1.3)
4	8.52×10^6	1.64×10^5
8	3.41×10^7	1.64×10^5
16	1.36×10^8	1.64×10^5

Table 3.3: Comparison between the computational complexities (in number of operations) per subcarrier group of the ML detector and the proposed S-MP detector, while having different values of $(Q\mathcal{L})$.

N_v	Complexities of CS-aided Multi-Dimensional IM Schemes with $N_f = 8, K = 2, N_t = 8$, STSK$(2, 2, 2, 2, 2)$ and varying N_v	
	ML (Sec. 3.3.1.1)	S-MP (Sec. 3.3.1.3)
16	8.52×10^6	1.64×10^5
20	2.4×10^8	3.23×10^5
24	5.22×10^8	6.55×10^5

Table 3.4: Comparison between the computational complexities (in number of operations) per subcarrier group of the ML detector and the proposed S-MP detector, while having different dimensions of N_v.

of the system having $N_v = 16$ achieves about 1.2 dB and 2.1 dB better performances in comparison to that of the system having $N_v = 20$ and $N_v = 24$, respectively, while using the ML detector, at the BER value of 10^{-5}.

In order to further illustrate the trade-off between the BER performance and the complexity, we characterise the complexities of the systems shown in both Fig. 3.10 and Fig. 3.11. Observe in Fig. 3.10, Fig. 3.11, Table 3.3 and Table 3.4 that the proposed S-MP detector is capable of reducing the computational complexity of the ML detector at the cost of a modest performance loss. More specifically, the S-MP detector is capable of eliminating the influence of having varying $(Q\mathcal{L})$ values on the computational complexity compared to the ML detector. Additionally, the S-MP detector imposes a gradually increased complexity upon increasing the dimension of N_v, where the increased N_v results

in an increased number of active subcarrier realisations as well as rendering the transmitted signal more sparse. Hence, there is a clear performance versus computational complexity trade-off for the CS-aided multi-dimensional IM system.

3.4.2 EXIT Chart Analysis

The exchange of extrinsic information in the proposed system of Fig. 3.7 can be visualised by plotting the EXIT characteristics of the inner demodulator and the outer RSC decoder [203,218]. The EXIT curves presented in this section correspond to the system employing a 1/2-rate RSC code having a constraint length of 5, denoted as RSC$(2, 1, 5)$, where the code using the generator polynomials of $(53, 75)$.

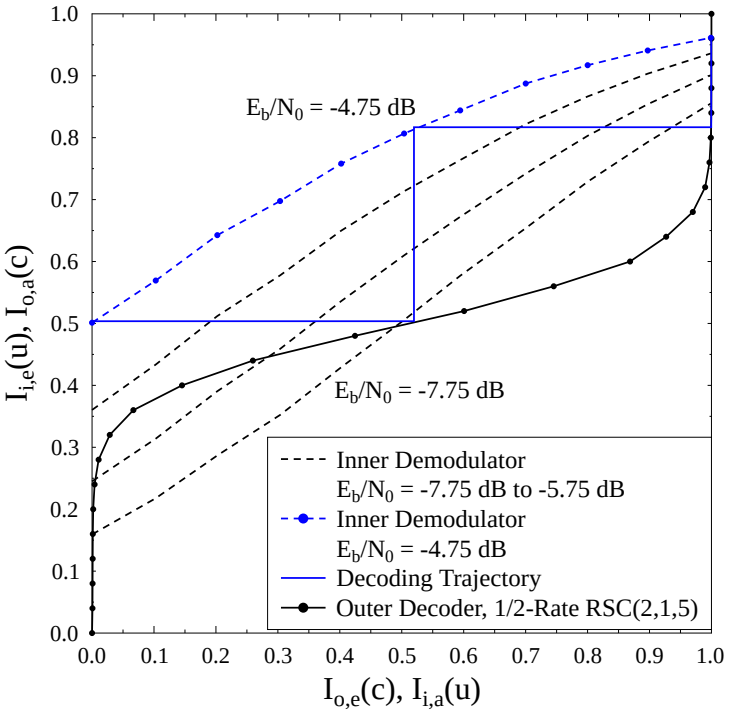

Figure 3.12: The EXIT charts of the proposed CS-aided multi-dimensional IM system presented in Fig. 3.8 relying on the ML-based soft-detection. A decoding trajectory is shown between the outer decoder's EXIT curve and the inner demodulator's EXIT curve at $E_b/N_0 = -3.75$ dB, while using a 1/2-rate RSC$(2, 1, 5)$ with an interleaver depth of $192,000$ bits. All other system parameters were summarised in Table 3.2.

Fig. 3.12 shows the EXIT curves of the proposed CS-aided multi-dimensional IM scheme's inner demodulator for E_b/N_0 values spanning from -7.75 dB to -4.75 dB with a step size of 1.0 dB, while using ML-based soft-detection. The system is characterised by $N_f = 8$, $K = 2$, $N_v = 16$, $N_t = 8$ and STSK$(2, 2, 2, 2, 2)$, while employing a 1/2-rate RSC$(2, 1, 5)$ code relying on an interleaver depth of $192,000$ bits. Additionally, Fig. 3.12 portrays the EXIT chart of the 1/2-rate RSC$(2, 1, 5)$ outer decoder. The Monte-Carlo simulation-based decoding trajectory is recorded at $E_b/N_0 = -4.75$ dB between the inner demodulator and the outer decoder in Fig. 3.12, where the steps seen in the figure indicate the actual extrinsic mutual information transfer between them. According to the open-tunnel shown between the inner curve at $E_b/N_0 = -4.75$ dB and the outer curve, the iterative decoding process is expected to converge at around $E_b/N_0 = -4.75$ dB and at least $I_{IO} = 3$ iterations are required for reaching the mutual information point $(1.0, 1.0)$. Hence, the system is expected to produce an infinitesimally low BER at about $E_b/N_0 = -4.75$ dB.

Fig. 3.13 shows the EXIT curves of the proposed CS-aided multi-dimensional IM system's inner demodulator for E_b/N_0 values at 1.25 dB and at 2.25 dB, while using S-MP-based soft-detection. Observe in Fig. 3.13 that the inner demodulator's EXIT curve shows a decreasing trend upon increasing $I_{i,a}(u)$. The reason for this behaviour is that the u-length output data stream of the proposed CS-aided multi-dimensional IM demodulator using S-MP-based soft-detection is not Gaussian distributed and the LLRs of the u-length data stream denoted by $L_{i,e}(u)$ do not satisfy the consistency condition defined in [218] because of reducing the search space of the detector, although the calculation of $L_{i,e}(u)$ is based on the assumption that the u-length data stream is Gaussian distributed. A trivial solution to this problem is to try and find the probability distribution of the u-length output stream and compute $L_{i,e}(u)$ by using the actual probability density function (pdf). However, it is not straightforward to find a mathematical formula to model the pdf of the u-length data stream. Fortunately, however it is possible to compute the LLRs according to the histogram of the demodulated u-length data stream, computing the histogram for every received group is a complex and time-consuming process.

An empirical transformation of the $L_{i,e}(u)$ LLR values has been investigated for correcting the relationship between the LLRs and the corresponding probabilities to satisfy the consistency condition in [218], as proposed in [219]. This empirical transformation is referred to as LLR postprocessing and it can be expressed as

$$L_{i,e}^{\dagger}(u) = \frac{L_{i,e}(u)}{\mathcal{A}}, \tag{3.27}$$

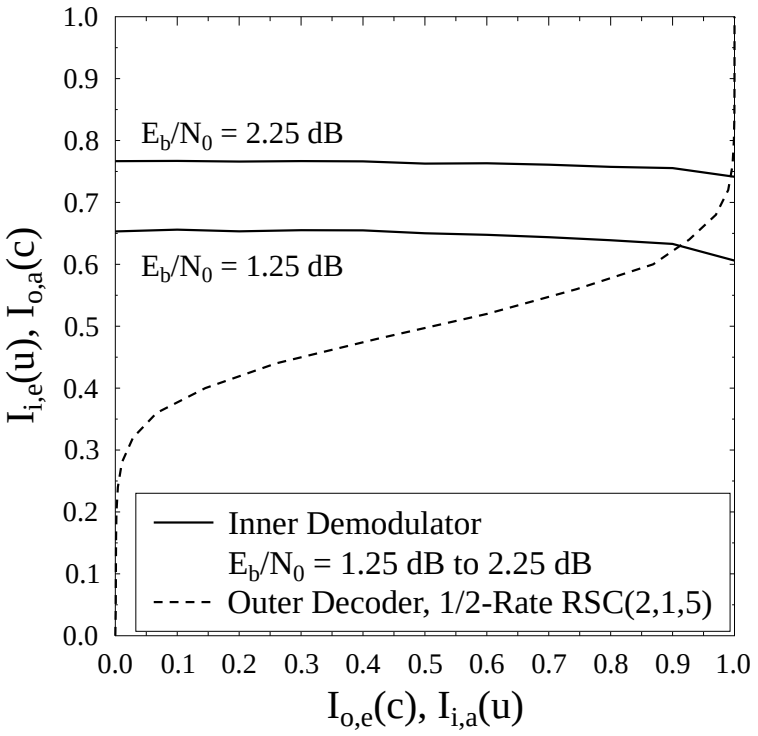

Figure 3.13: The EXIT charts of the proposed CS-aided multi-dimensional IM system presented in Fig. 3.8 relying on the S-MP-based soft-detection without LLR postprocessing. Additionally, the EXIT curve of the 1/2-rate RSC$(2, 1, 5)$ outer decoder with an interleaver depth of $192,000$ bits is shown in the figure. All other system parameters were summarised in Table 3.2.

where $L^{\dagger}_{i,e}(u)$ represents the processed extrinsic LLRs passed from the inner demodulator to the deinterleaver of Fig. 3.7, which satisfies the consistency condition in [218], and $\mathcal{A}$ represents the empirical transformation coefficient, where we have $\mathcal{A} = 8.0$ specifically for our scenario and it is obtained with the aid of simulations.

Fig. 3.14 shows the EXIT charts of the proposed CS-aided multi-dimensional IM system relying on the S-MP-based soft-detection relying on the LLR postprocessing of Eq. (3.27), which is associated with the configuration: $N_f = 8$, $K = 2$, $N_v = 16$, $N_t = 8$ and STSK$(2, 2, 2, 2, 2)$. The EXIT curves of the inner demapper using S-MP-based soft-detection recorded for the E_b/N_0 values spanning from 1.25 dB to 3.25 dB with a step size of 1.0 dB are shown in Fig. 3.14. As shown in Fig. 3.14, the inner demodulator's EXIT charts are shifted upwards upon increasing E_b/N_0 value. Additionally, the decoding trajectories at $E_b/N_0 = 2.25$ dB and $E_b/N_0 = 3.25$ dB between the inner demodulator and the 1/2-rate RSC$(2, 1, 5)$ outer decoder are recorded in Fig. 3.14, where the iterative

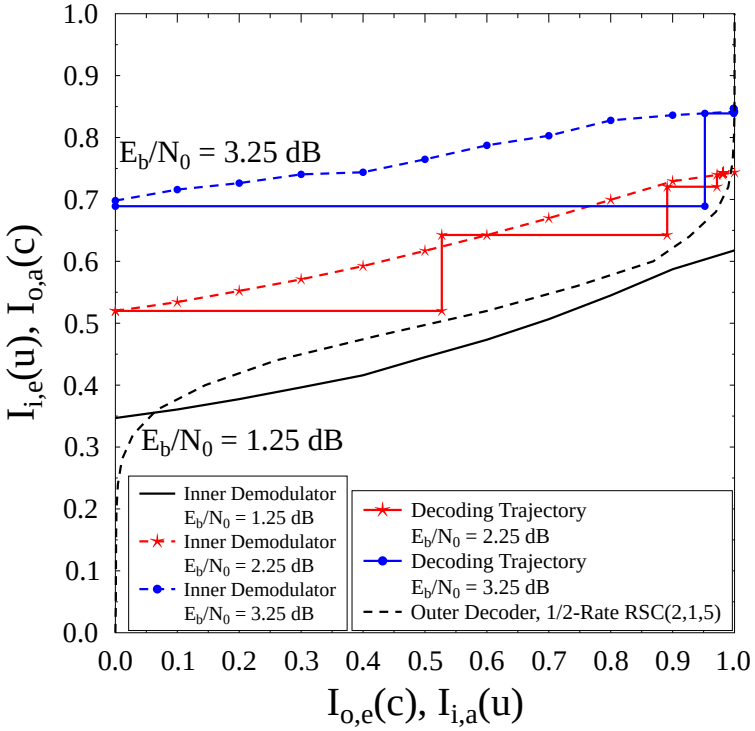

Figure 3.14: The EXIT charts of the system presented in Fig. 3.13 with LLR postprocessing. The decoding trajectories are shown between the outer decoder's EXIT curve and the inner demodulator's EXIT curves at $E_b/N_0 = 2.25$ dB and $E_b/N_0 = 3.25$ dB, while using a 1/2-rate RSC$(2, 1, 5)$ with an interleaver depth of $192,000$ bits. All other system parameters were summarised in Table 3.2.

decoding process is expected to converge around $E_b/N_0 = 3.25$ dB and at least $I_{IO} = 3$ iterations are required for approaching the mutual information point $(1.0, 1.0)$.

3.4.3 Capacity Analysis

In this section, we formulate the DCMC capacity [220] of the proposed CS-aided multi-dimensional IM system using the full-search based ML detector presented in Section 3.3.1.1. Then the powerful tool of EXIT charts is utilised for determining the maximum achievable rate of the proposed system using both the ML detector introduced in Section 3.3.1.1 and the S-MP detector presented in Section 3.3.1.3.

3.4.3.1 Discrete-Input Continuous-Output Memoryless Channel Capacity Analysis

The DCMC capacity of the proposed CS-aided multi-dimensional IM scheme is first developed for each subcarrier group, where N_{AC} is the number of the active TAs combinations, N_{SI} is that of the active subcarriers combinations and K activated STSK codewords are included in each subcarrier group. Then the DCMC capacity per group developed is divided by N_f, namely by the number of frequency-domain subcarriers for determining the capacity per subcarrier. Based on the equivalent received signal model of Eq. (3.10), the DCMC capacity of the proposed scheme can be expressed as [220]

$$C_{DCMC}(SNR) = \max_{p(\bar{\mathbf{S}}^i)|_{i=1}^{I}} \frac{1}{N_f} \sum_{i=1}^{I} \int p(\mathbf{Y}|\bar{\mathbf{S}}^i) p(\bar{\mathbf{S}}^i) \cdot \log_2 \frac{p(\mathbf{Y}|\bar{\mathbf{S}}^i)}{\sum_{j=1}^{I} p(\mathbf{Y}|\bar{\mathbf{S}}^j) p(\bar{\mathbf{S}}^j)} d\mathbf{Y}, \quad (3.28)$$

where $I = N_{AC} N_{SI} (Q\mathcal{L})^K$ denotes the total number of realisations for each subcarrier group including the active TAs, active subcarriers and K STSK codewords at the activated subcarriers. The DCMC capacity of Eq. (3.28) is maximised, when these realisations per subcarrier group are equiprobable, where we have $\{p(\bar{\mathbf{S}}^i) = \frac{1}{I}\}_{i=1}^{I}$. Furthermore, the conditional probability $p(\mathbf{Y}|\bar{\mathbf{S}}^i)$ of receiving $\mathbf{Y}$ given that the group-signal $\bar{\mathbf{S}}^i$ is transmitted over fading channels is determined by the probability density function of the noise, which is formulated as:

$$p(\mathbf{Y}|\bar{\mathbf{S}}^i) = \frac{1}{(\pi N_0)^{N_r N_f}} \exp\left(-\frac{\|\mathbf{Y} - \mathbf{H}\bar{\mathbf{S}}^i\|^2}{N_0} \right). \quad (3.29)$$

Based on Eq. (3.29), the DCMC capacity of Eq. (3.28) may be further simplified as

$$\begin{aligned} C_{DCMC}(SNR) &= \frac{1}{IN_f} \sum_{i=1}^{I} \mathbb{E}\left\{ \log_2 \left[\frac{I \cdot p(\mathbf{Y}|\bar{\mathbf{S}}^i)}{\sum_{j=1}^{I} p(\mathbf{Y}|\bar{\mathbf{S}}^j)} \right] \right\} \\ &= R - \frac{1}{IN_f} \sum_{i=1}^{I} \mathbb{E}\left\{ \log_2 \left[\sum_{j=1}^{I} \exp(\Psi_{i,j}) \right] \right\}, \end{aligned} \quad (3.30)$$

where we have $\Psi_{i,j} = \frac{-\|\mathbf{H}(\bar{\mathbf{S}}^i - \bar{\mathbf{S}}^j) + \mathbf{W}\|^2 + \|\mathbf{W}\|^2}{N_0}$, while the system's achievable rate is given by $R = \frac{\log_2 I}{N_f}$, which is expected to be achieved by the DCMC capacity of $C_{DCMC}(SNR)$ upon increasing the SNR values.

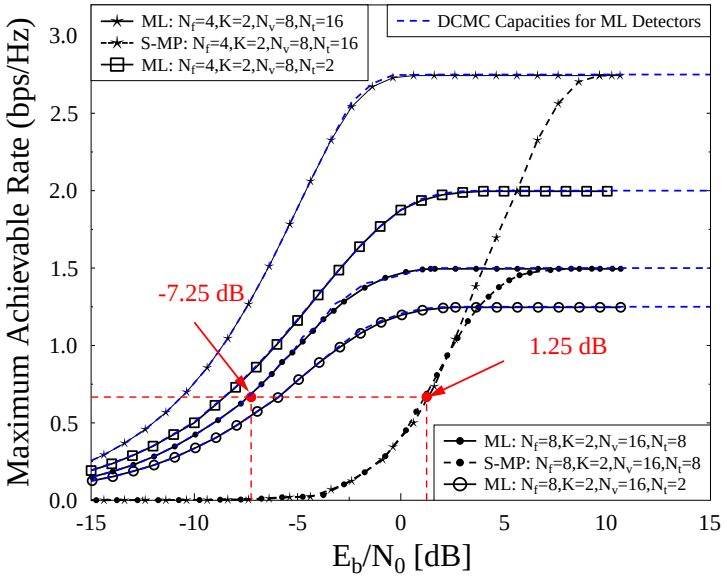

Figure 3.15: Maximum achievable rates of the proposed CS-aided multi-dimensional IM schemes associated with different configurations, while using the ML detector and the S-MP detector.

3.4.3.2 The Maximum Achievable Rate Using the EXIT Charts Tool

The EXIT charts can be utilised for determining the maximum achievable rate of the system at a given E_b/N_0 value [204]. Fig. 3.15 shows the maximum attainable rates of several proposed CS-aided multi-dimensional IM schemes associated with different configurations, while using both ML-based and S-MP-based detectors. As shown in Fig. 3.15, the maximum achievable rate of the system tends to increase, when either the number of TAs N_t or the number of ACs N_{AC} increases. More specifically, it is shown in the figure that the maximum achievable rate of the CS-aided frequency-domain IM scheme of Fig. 2.6 having $N_t = M$ is lower than that of our CS-aided multi-dimensional IM scheme of Fig. 3.2. The DCMC capacity curves evaluated based on Eq. (3.30) are also portrayed in the figure. Observe in Fig. 3.15 that the maximum achievable rate of the proposed system evaluated from the EXIT chart closely matches the DCMC capacity curves. Additionally, it is shown in Fig. 3.15 that the maximum achievable rate curves of the proposed systems using S-MP detection is lower than that of ML detection due to the reduced search space. Specifically, the maximum rates of the proposed systems presented in Fig. 3.8 after employing a half-rate RSC decoder relying both on Eq. (3.21) and Eq. (3.23) are shown at $E_b/N_0 = -7.25$ dB and $E_b/N_0 = 1.25$ dB, respectively.

3.4.4 Coded BER Performance

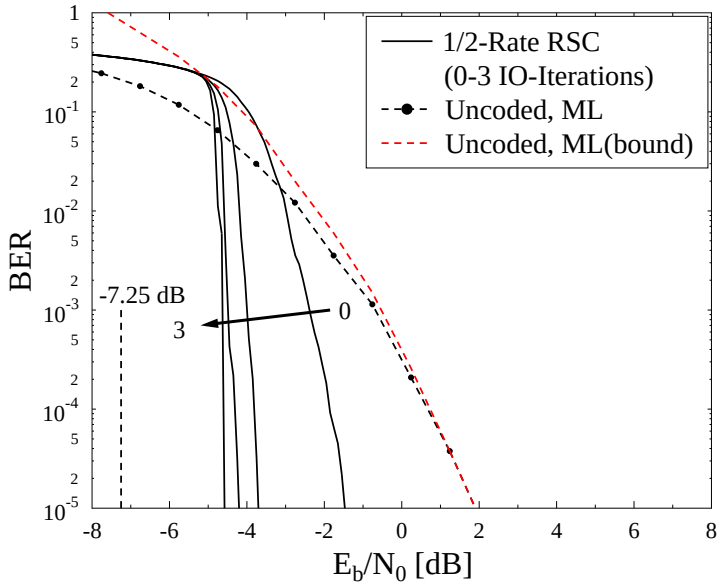

Figure 3.16: BER performances of the 1/2-rate RSC$(2, 1, 5)$-coded ML-based soft-detection system of Fig. 3.7, while using $I_{IO} = 0$ to 3 iterations.

In this section, we show the coded BER performances of the proposed systems for the following configurations: STSK$(2, 2, 2, 2, 2)$, $N_f = 8$, $K = 2$, $N_v = 16$ and $N_t = 8$, while using ML-based soft-detection and S-MP-based soft-detection, where the configurations used are the same as those in Fig. 3.12 and Fig. 3.14. A 1/2-rate RSC$(2, 1, 5)$ encoder having an interleaver depth of $192,000$ bits is employed in both systems.

Fig. 3.16 shows the attainable BER performance of the 1/2-rate RSC$(2, 1, 5)$-coded system of Fig. 3.7, while using an interleaver depth of $196,000$ bits and $I_{IO} = 0$ to 3 iterations. The BER performance of the uncoded system is also shown in the figure. Observe in Fig. 3.16 that there is an evident performance improvement, when increasing the number of iterations. As shown in Fig. 3.16, the system attains an infinitesimally low BER at around $E_b/N_0 = -4.75$ dB, which matches the EXIT chart prediction seen in Fig. 3.12 and is within about 2.5 dB of the maximum achievable rate obtained using EXIT charts and shown in Fig. 3.15.

Fig. 3.17 shows the BER performances of the 1/2-rate RSC$(2, 1, 5)$-coded CS-aided multi-dimensional IM system using the S-MP-based soft-detection of Fig. 3.7, while employing an interleaver depth of $196,000$ bits and $I_{IO} = 0$ to 3 iterations. The BER

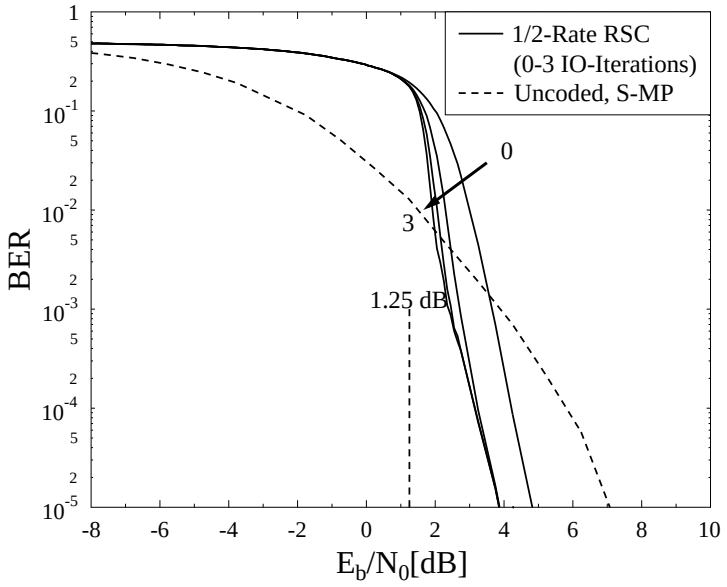

Figure 3.17: BER performances of the 1/2-rate RSC$(2, 1, 5)$-coded S-MP-based soft-detection system of Fig. 3.7, while using $I_{IO} = 0$ to 3 iterations.

performance of the uncoded system is also shown in the figure. Note that the simulation results shown in Fig. 3.17 are obtained after the LLR postprocessing described in Eq. (3.27) of Section 3.4.2. Observe in Fig. 3.17 that there is an evident performance improvement, upon increasing the number of iterations. As shown in Fig 3.17, the system has no substantial performance gain beyond $E_b/N_0 = 3.25$ dB, which matches the EXIT chart prediction seen in Fig. 3.14, which is within about 2.0 dB from the maximum achievable rate obtained using EXIT charts and shown in Fig. 3.15.

3.5 Chapter Conclusions

In this chapter, we proposed a novel CS-aided multi-dimensional IM scheme, which strikes flexible trade-offs among the achievable rate and the achievable performance vs the detector's complexity. Specifically, a CS-based reduced complexity detector of Section 3.3.1.3 was invoked for imposing a reduced computational complexity at a modest performance degradation, which makes the proposed multi-dimensional system eminently suitable for realistic scenarios, because the optimal ML detector is excessively complex.

	Fig. 3.8			**Fig. 3.9**		
$\mathbf{R_t}$	1.33 bits/s/Hz			1.89 bits/s/Hz		
Scenario	-			Increased N_t and $(Q\mathcal{L})$		
Schemes	Chapter 3 (ML)	Chapter 3 (S-MP)	Chapter 2 (ML)	Chapter 3 (ML)	Chapter 3 (S-MP)	Chapter 2 (ML)
SNR (at BER=10^{-5})	3.6 dB	7.9 dB	7.9 dB	7 dB	10 dB	10.4 dB
Complexity	$\mathcal{O}(8.52 \times 10^6)$	$\mathcal{O}(1.64 \times 10^5)$	$\mathcal{O}(5.9 \times 10^6)$	$\mathcal{O}(5.7 \times 10^9)$	$\mathcal{O}(3.3 \times 10^5)$	$\mathcal{O}(9.5 \times 10^8)$

Table 3.5: Summary of the CS-aided multi-dimensional IM scheme, employing the system parameters of Table 3.2, where both the ML and S-MP detectors are applied.

As observed in Fig. 3.8 and Fig. 3.9, at the same transmission rate of $R_t = 1.3333$ bits/s/Hz and $R_t = 1.89$ bits/s/Hz, the proposed CS-aided multi-dimensional IM system of Fig. 3.2 employing the ML detector of Eq. (3.9) exhibited a better performance than the CS-aided frequency-domain IM scheme of Fig. 2.6 employing the ML detector of Eq. (2.13) and the classical OFDM-STSK system. Then in Section 3.3.1.3 the reduced-complexity S-MP detector was proposed, which exhibited a modest BER degradation in Fig. 3.8 and Fig. 3.9.

Explicitly, observe from Table 3.5 providing a summary of Fig. 3.8 and Fig. 3.9 that the reduced-complexity S-MP detector of Section 3.3.1.3 is capable of approaching the ML detector's BER performance at about 2% the ML detector's complexity at the transmission rate of 1.33 bits/s/Hz of Fig. 3.8 and at about 0.00006 times the ML detector's complexity at the higher transmission rate of 1.89 bits/s/Hz of Fig. 3.9. Additionally, the S-MP detector of Section 3.3.1.3 is also capable of achieving similar or even better performance than the CS-aided frequency-domain IM scheme of Fig. 2.6 at a significantly lower complexity. In Table 3.6, a summary of the trade-offs between the BER performance, the complexity and the achievable rate was presented based on Fig. 3.10 and Fig. 3.11, where we can conclude that the proposed CS-aided multi-dimensional IM system of Fig. 3.2 is capable of striking flexible trade-offs by appropriately configuring the system parameters.

	Fig. 3.10						**Fig. 3.11**					
Scenario	Impact of varying $(Q\mathcal{L})$						Impact of varying N_v					
Schemes	$(Q\mathcal{L}) = 16, R_t = 1.78$ bit-s/s/Hz		$(Q\mathcal{L}) = 8, R_t = 1.56$ bits/s/Hz		$(Q\mathcal{L}) = 4, R_t = 1.33$ bits/s/Hz		$N_v = 24, R_t = 1.56$ bit-s/s/Hz		$N_v = 20, R_t = 1.44$ bit-s/s/Hz		$N_v = 16, R_t = 1.33$ bit-s/s/Hz	
	ML	S-MP	ML	S-MP	ML	S-MP	ML	S-MP	ML	S-MP	ML	S-MP
SNR (10^{-5})	7 dB	12.5 dB	5.2 dB	10 dB	3.6 dB	7.9 dB	5.7 dB	9.6 dB	4.8 dB	9 dB	3.6 dB	7.9 dB
Complexity	$\mathcal{O}(1.36\times 10^8)$	$\mathcal{O}(1.64\times 10^5)$	$\mathcal{O}(3.41\times 10^7)$	$\mathcal{O}(1.64\times 10^5)$	$\mathcal{O}(8.52\times 10^6)$	$\mathcal{O}(1.64\times 10^5)$	$\mathcal{O}(5.22\times 10^8)$	$\mathcal{O}(6.55\times 10^5)$	$\mathcal{O}(2.4\times 10^8)$	$\mathcal{O}(3.23\times 10^5)$	$\mathcal{O}(8.52\times 10^6)$	$\mathcal{O}(1.64\times 10^5)$

Table 3.6: Summary of the CS-aided multi-dimensional IM scheme, varying the system parameters $(Q\mathcal{L})$ and N_v, where all other parameters were summarised in Table 3.2, both the ML and S-MP detectors are applied.

Furthermore, the CS-aided multi-dimensional IM soft-input soft-output decoders were conceived in Fig. 3.7 in order to achieve a near-capacity performance. More specifically, in Figs. 3.12 - 3.14 EXIT charts were used not only for visually characterising the flow of soft-information between the constituent decoders of our concatenated structure seen in Fig. 3.7, but also for evaluating the maximum achievable rate of the proposed system. Observe from Fig. 3.15 that the proposed CS-aided multi-dimensional IM system of Fig. 3.2 imposed a higher maximum rate than the CS-aided frequency-domain IM system of Fig. 2.6. More specifically, the high design flexibility of the proposed scheme can be exploited by beneficially configuring the different components in the design, where the design flexibility makes the proposed scheme suitable for adaptive scenarios.

This chapter focused on the design of CS-aided multi-dimensional IM systems relying both on frequency-domain and on spatial-domain IM operating in a single-user scenario. The simulation results demonstrated that the proposed CS-aided multi-dimensional IM system of Fig. 3.2 is capable of achieving better performances than the CS-aided frequency-domain IM system of Fig. 2.6 both in terms of achievable transmission rate and BER. It is worth mentioning that exploring the multi-dimensional IM strategy in large-scale multi-user scenarios is of high promise in the context of next-generation communications. Hence in the following chapter, a two-dimensional IM system will be investigated in large-scale multi-user scenarios.

Chapter 4

Multi-Dimensional Index Modulation for the Large-Scale Multi-User MIMO Uplink

4.1 Introduction

In Chapter 2, the CS-aided OFDM-STSK-IM scheme was shown to provide better BER performance than the conventional OFDM-MIMO scheme in addition to striking flexible bandwidth efficiency and complexity trade-off. In order to attain a further improved performance, the CS-aided multi-dimensional IM scheme was proposed in Chapter 3 by invoking both frequency- and spatial-domain IM for our OFDM-STSK scheme. Furthermore, large-scale multi-user MIMO (LS-MU-MIMO) systems relying on tens to hundreds of antennas have been shown to constitute a promising candidate for next generation wireless systems as a benefit of their high bandwidth efficiency, increased reliability, and energy efficiency [132, 133]. To elaborate further, IM schemes relying on frequency-domain/spatial-domain have been designed for LS-MU-MIMO systems in [120, 121, 126, 147, 148, 156, 221], where a better performance was achieved for the same bandwidth efficiency than that of conventional MU-MIMO solutions. Specifically, OFDM-IM designed for the LS-MU-MIMO uplink and downlink was proposed in [221], where the proposed schemes exhibited improved bandwidth efficiency vs BER performance trade-off, while also reducing the PAPR of the classical MU-MIMO-OFDM system. Hence applying the multi-dimensional IM strategy in LS-MU-MIMO systems is promising. However, one of the most challenging tasks in LS-MU-MIMO systems is the design of reliable, low-complexity multi-user detectors (MUDs) for employment at the base station (BS).

In this chapter, we propose both uncoded and FEC-coded CS-assisted two-dimensional IM for the LS-MU-MIMO uplink seen in Fig. 4.1, in order to combine the benefits of LS-MU-MIMO, SM, GSM, OFDM-IM and CS for uplink transmission over frequency-selective fading channels, where we refer to the proposed system as CS-assisted (generalised) space-frequency IM (CS-(G)SFIM) invoked for the LS-MU-MIMO uplink. Additionally, in order to improve the diversity in contrast to Chapter 3, different TA activation patterns are employed for different transmitted symbols instead of using the same active TAs for each subcarrier group proposed. Then a reduced-complexity detector is designed for providing an attractive BER vs complexity trade-off, where the reduced complexity of the detector makes the employment of our CS-(G)SFIM system realistic in LS-MU scenarios.

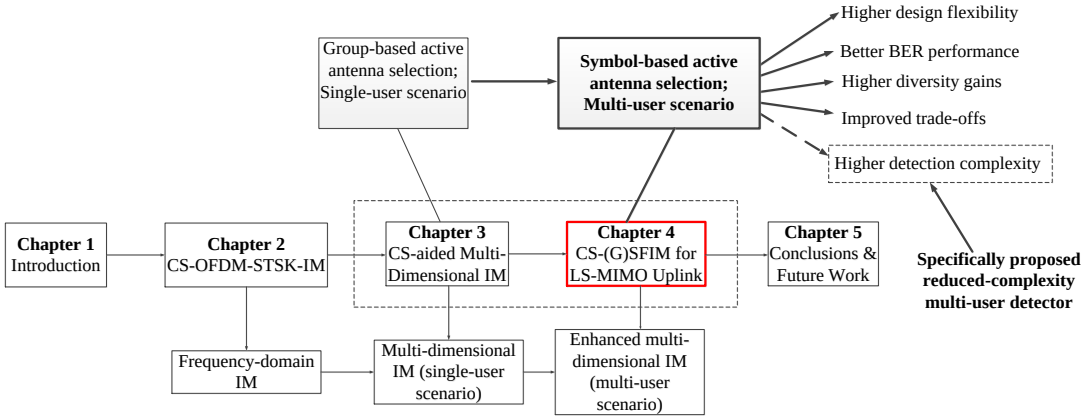

Figure 4.1: Interconnection of Chapter 4 with the rest of the thesis.

Against the above background, the contributions of this chapter are summarised as follows:

- In Section 4.2.1 a CS-SFIM scheme is proposed for striking a better performance vs complexity trade-off than the conventional LS-MU-MIMO-OFDM systems. The basic idea of the proposed CS-SFIM scheme is that for each user, the information is conveyed by three parts, namely by the frequency-domain IM, the spatial-domain IM representing the TA activation and by the classic Amplitude/Phase Modulation (APM) symbols. Explicitly, the conventional frequency-domain IM is implemented in a high-dimensional virtual domain and the appropriately activated TAs are allocated to the active subcarriers of the virtual domain and then the resultant high-dimensional sub-block is compressed into a low-dimensional space-frequency sub-block with the aid of CS. Additionally, the new generalised SM of Section 4.2.1.2, namely CS-GSFIM, is also invoked for improving the throughput

without increasing the number of RF chains compared to the CS-SFIM scheme of Section 4.2.1.2. More particularly, in order to increase the diversity gain attained, in contrast to Chapter 3, we employ different TA activation patterns for the different transmitted symbols instead of fixing the active TAs for the whole OFDM subcarrier group shown. We then analyse the ABEP of the proposed CS-GSFIM system using the ML detection and we derive an upper bound of the ABEP in Section 4.3.1.2. Our numerical results of Section 4.4 demonstrate that the proposed MU CS-(G)SFIM system attains better BER performance than the conventional MU-MIMO-OFDM system, the MU CS-aided multi-dimensional system using the same TA activation pattern for each subcarrier group shown in Chapter 3, and the MU CS-aided frequency-domain IM shown in Chapter 2 at the same transmission rate.

- Then in Section 4.3.2 our reduced search-space based iterative matching pursuit (RSS-IMP) detection is proposed for the CS-GSFIM system, which relies on CS principles. The computational complexities are compared for the proposed systems using the ML detector, MMSE detector and the novel RSS-IMP detector in Section 4.3.3. We demonstrate that the proposed RSS-IMP detector is capable of achieving a better BER vs complexity trade-off than the conventional MU-MIMO-OFDM system using the ML detector and the proposed systems using the MMSE detector, despite its significantly reduced complexity. This makes the proposed CS-GSFIM system eminently suitable for LS-MU-MIMO communications.

- In Section 4.4 we then proceed by investigating the performances of the proposed CS-(G)SFIM systems in the presence of imperfect channel state information (ICSI). It is demonstrated by our simulation results that the proposed systems are more robust to channel estimation errors than the conventional MU-MIMO-OFDM system.

- For the sake of attaining a near-capacity performance, in Section 4.3.1.3 and Section 4.3.2 we then design specific soft MUDs based on both the ML detector and on the proposed RSS-IMP detector for iteratively exchanging soft information with the FEC decoders. Our FEC-coded numerical results of Section 4.4.3 indicate that near-capacity performances can indeed be achieved by the proposed MUDs. Additionally, in Section 4.4.2 we investigate the maximum achievable rates of the proposed CS-(G)SFIM system with the aid of EXIT charts.

The remainder of this chapter is organised as follows. Section 4.2 describes our system model. In particular, Section 4.2.1 introduces the uplink transmission process of the

proposed system and Section 4.3 describes both the ML detector as well as the proposed RSS-IMP detector designed for both hard-decision (HD) and soft-decision (SD) detection. Additionally, the average complexity orders of the different MUDs are provided in Section 4.3. In Section 4.4, our simulation results are presented, including both the uncoded and coded BER performances as well as the capacity analysis. Finally, the chapter is concluded in Section 4.5.

4.2 System Model

In this section, we introduce the proposed large-scale multi-user CS-GSFIM architecture supporting U uplink users, as shown in Fig. 4.2, where each user is equipped with N_t TAs for simultaneously communicating with a BS having N_r RAs, where N_r is on the order of tens to hundreds. The transmitter of our CS-GSFIM scheme at the user terminal is illustrated in Fig. 4.3, where both CS-aided frequency-domain IM and spatial-domain IM techniques are designed for each user in order to improve the uplink throughput vs energy efficiency.

More particularly, in order to increase the diversity gain attained as well as to improve the performance, in contrast to the CS-aided multi-dimensional IM scheme of Fig. 3.2, the spatial-domain IM of our new CS-GSFIM scheme of Fig. 4.3 is designed by employing different active TAs combinations for the different transmitted APM symbols instead of fixing the active TAs for the whole OFDM subcarrier group shown. Additionally, the shared antenna combination is invoked in our new CS-GSFIM scheme of Fig. 4.3 for improving the throughput, while the distinctive antenna combination (DAC) was employed in the CS-aided multi-dimensional IM scheme of Fig. 3.2, as shown in Table 3.1 and Fig. 3.5.

More explicitly, our spatial-domain IM of Fig. 4.3 includes both conventional SM and GSM, where N_t^a out of N_t TAs are activated for transmitting the modulated uplink symbols. We have $N_t^a = 1$ if CS-SFIM-OFDM is applied, and $1 < N_t^a \leq N_t$ for CS-GSFIM-OFDM. The specific procedures of the proposed CS-(G)SFIM systems are detailed in the following subsections. Specifically, in Section 4.2.1, first we introduce the proposed large-scale multi-user CS-(G)SFIM uplink and then focus our attention on the associated MUDs in Section 4.3.

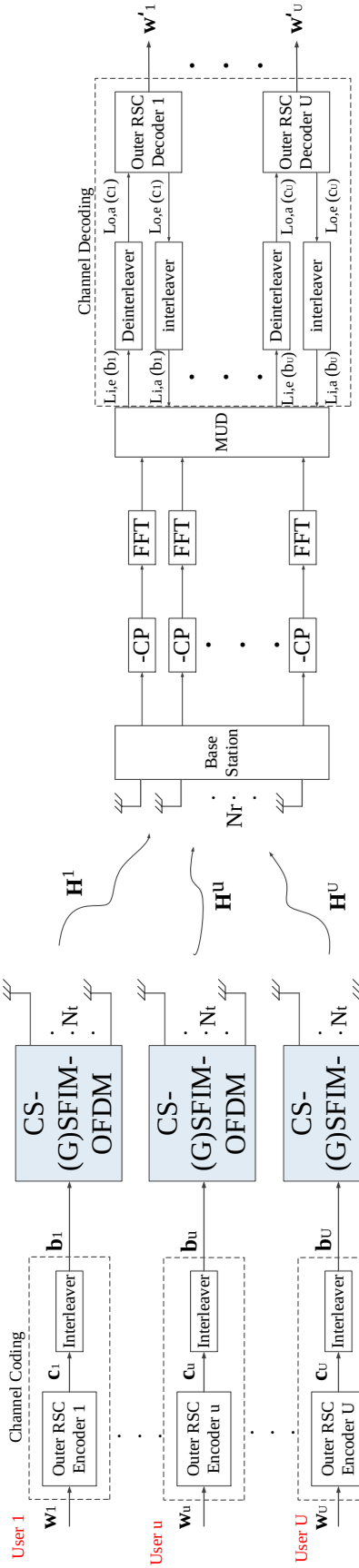

Figure 4.2: The proposed coded CS-(G)SFIM system's transceiver architecture that was developed from Fig. 3.2, where the BS is equipped with N_r RAs to serve U uplink users and each user is equipped with N_t TAs. In the proposed system, both the RSC encoder and the RSC decoder are applied in order to improve the performance of the MUD.

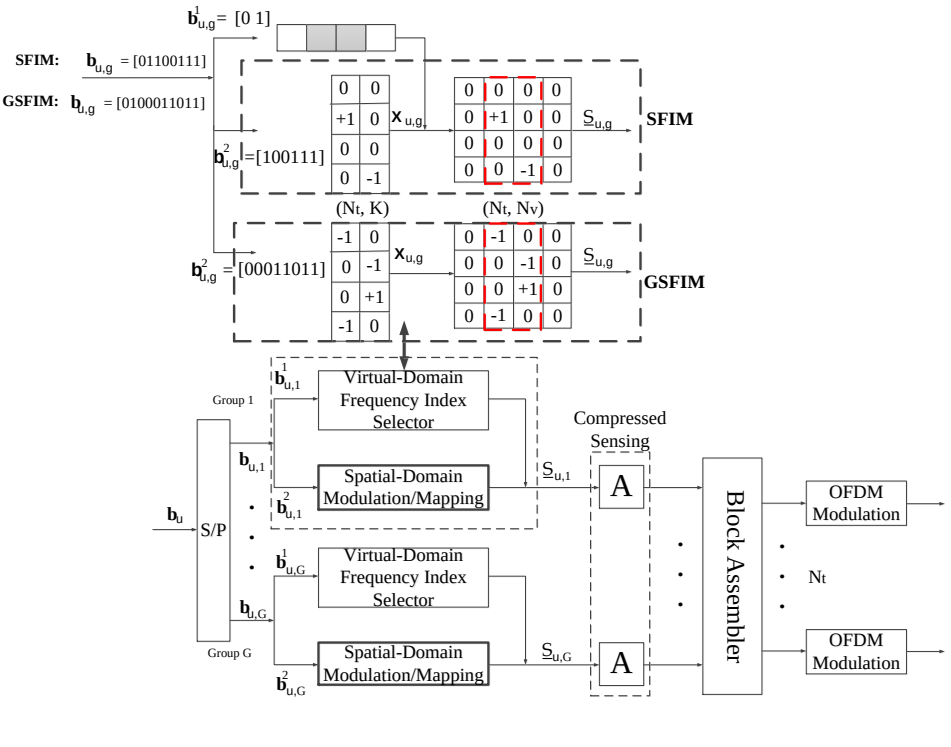

-1

Figure 4.3: The transmitter of the novel CS-GSFIM scheme of Fig. 4.2 at the user terminal, which was developed both from the CS-aided frequency-domain IM scheme of Fig. 2.6 and from the CS-aided multi-dimensional IM scheme of Fig. 3.2. The enhanced block is marked using bold lines.

4.2.1 Uplink Transmission

In the block diagram of the proposed large-scale multi-user CS-(G)SFIM system seen in Fig. 4.2, there are U uplink users communicating with a BS and the CS-(G)SFIM-OFDM techniques advocated are exploited for each user. As shown in Fig. 4.3, the information sequence $\mathbf{b_u}$[1] of the u-th uplink user is split into G subcarrier groups for implementing the CS-(G)SFIM-OFDM technique, where all the G subcarrier groups have the same process as seen in Fig. 4.3, but the frequency index selection, the TA selection and the transmitted APM symbols may vary among the different subcarrier groups. As shown in Fig. 4.3, in the g-th subcarrier group of the u-th user, the information sequence $\mathbf{b}_{u,g}$ is split into $\mathbf{b}^1_{u,g}$ and $\mathbf{b}^2_{u,g}$, which are conveyed by the Virtual-Domain Frequency Index Selector block and the Spatial-Domain Modulation/Mapping block, respectively.

[1]For an uncoded scenario, the information sequence $\mathbf{b_u}$ represents the source information, and for the coded scenario, $\mathbf{b_u}$ represents the RSC coded information sequence.

Input Bits	Antenna Indices	APM Symbols	Allocations
[000000]	1, 1	−1, −1	[−1 0 0 0]; [−1 0 0 0]
[010001]	1, 2	−1, +1	[−1 0 0 0]; [0 + 1 0 0]
[100111]	2, 4	+1, −1	[0 + 1 0 0]; [0 0 0 − 1]
[110100]	2, 1	+1, +1	[0 + 1 0 0]; [+1 0 0 0]
[001000]	3, 1	−1, −1	[0 0 − 1 0]; [−1 0 0 0]
[011011]	3, 4	−1, +1	[0 0 − 1 0]; [0 0 0 + 1]
[101100]	4, 1	+1, −1	[0 0 0 + 1]; [−1 0 0 0]
[111110]	4, 3	+1, +1	[0 0 0 + 1]; [0 0 + 1 0]

Table 4.1: A look-up table example of SM/Mapping for $N_t = 4$, $N_t^a = 1$, $\mathcal{L} = 2$ and $K = 2$, where there are 64 combinations in total and we use 8 out of the total combinations as an example.

4.2.1.1 Virtual-Domain Frequency Index Selector

The bit sequence $\mathbf{b}_{u,g}^1$ of length $\lfloor \log_2 C(N_v, K) \rfloor$ is forwarded to the Virtual-Domain Frequency Index Selector of Fig. 4.3. Similarly to the IM Selector of Fig. 2.6 and the SI Selector of Fig. 3.2, K active subcarriers are selected out of the N_v available subcarriers by the Virtual-Domain Index Selector of Fig. 4.3, and the specific selection procedure is determined by the incoming bits $\mathbf{b}_{u,g}^1$, where we can refer to the look-up table example of Table 2.1, the subcarrier index selection example of Fig. 3.3 detailed both in Section 2.3.1 as well as in Section 3.2.1.2. More explicitly, as shown in Fig. 4.3, the Virtual-Domain Index Selector is illustrated based on the look-up table example of Table 2.1, where the incoming information sequence is assumed to be $\mathbf{b}_{u,g}^1 = [0\,1]$, while the second and the third subcarriers, which are shaded in Fig. 4.3, are activated accordingly.

4.2.1.2 Spatial-Domain Modulation/Mapping

For each subcarrier group, the information sequence $\mathbf{b}_{u,g}^2$ is fed into the Spatial-Domain Modulation/Mapping block of Fig. 4.3. In this section, both the SM/Mapping having $N_t^a = 1$ and the GSM/Mapping having $1 < N_t^a \leq N_t$ are explicitly explained as follows.

SM/Mapping ($N_t^a = 1$) In a given channel use of the SM scheme, the information bits are divided into two parts, where $\lfloor \log_2 C(N_t, 1) \rfloor$ bits are used for activating one out of N_t TAs and $\log_2 \mathcal{L}$ bits are mapped to an $\mathcal{L}$-ary classic APM

symbol. In the architecture illustrated in Fig. 4.3, we have K active subcarriers in each subcarrier group, which indicates that the Spatial-Domain Modulation/Mapping block of Fig. 4.3 maps K $\mathcal{L}$-ary APM symbols in each subcarrier block to the corresponding active TAs for transmission. Hence, the information sequence $\mathbf{b}^2_{u,g}$ in the g-th subcarrier block of the u-th user has the length of $(K\log_2\mathcal{L} + K\lfloor\log_2 C(N_t,1)\rfloor)$ bits, which combines both $(K\log_2\mathcal{L})$ bits for modulating K $\mathcal{L}$-ary APM symbols and $K\lfloor\log_2 C(N_t,1)\rfloor$ bits for selecting the active TAs in order to transmit K APM symbols. As shown in Table 4.1, we apply $K=2$ activated BPSK symbols and each BPSK symbol will be transmitted through $N_t^a = 1$ active TA out of $N_t = 4$ available TAs, where $(K\log_2\mathcal{L} + K\lfloor\log_2 C(N_t,1)\rfloor) = (2\times\log_2 2 + 2\times\lfloor\log_2 4\rfloor) = 6$ bits are mapped to each subcarrier block. More explicitly, if $\mathbf{b}^2_{u,g} = [100111]$, then both the second and the fourth TAs are activated for transmitting the BPSK symbol $(+1)$ and the BPSK symbol (-1), respectively, whilst resulting in the allocation blocks $[0\ +1\ 0\ 0]$ and $[0\ 0\ 0\ -1]$, as seen in Table 4.1. Specifically, in contrast to the indexing strategy of the Antenna Selector of Fig. 3.2 applying the same active TAs combination for symbols in the same subcarrier group, the Spatial-Domain Modulation of Fig. 4.3 is capable of carrying more information bits. Following the process of SM/Mapping, the signal matrix $\mathbf{X}_{u,g} \in \mathbb{C}^{N_t\times K}$ is obtained, which is also illustrated in Fig. 4.3.

GSM/Mapping ($1 < N_t^a \leq N_t$) In order to further increase the bandwidth efficiency of the proposed system, GSM is utilised in the architecture seen in Fig. 4.3, where $1 < N_t^a \leq N_t$ out of N_t TAs are activated in our scenario. Explicitly, the information sequence $\mathbf{b}^2_{u,g}$ in the g-th subcarrier block of the u-th user has the length of $(N_t^a K\log_2\mathcal{L} + K\lfloor\log_2 C(N_t,N_t^a)\rfloor)$ bits, which combines both $(N_t^a K\log_2\mathcal{L})$ bits for modulating $(N_t^a\cdot K)$ $\mathcal{L}$-ary APM symbols and $K\lfloor\log_2 C(N_t,N_t^a)\rfloor$ bits for selecting multiple active TAs for different symbols. Assuming that we have $K=2, N_t^a=2, N_t=4$ and $\mathcal{L}=2$, the information sequence $\mathbf{b}^2_{u,g}$ has the length of $(2\times 2\log_2 2 + 2\times\lfloor\log_2 C(4,2)\rfloor) = 8$ bits. More explicitly, if the incoming information sequence is $\mathbf{b}^2_{u,g} = [00011011]$, as seen in the example illustrated in Fig. 4.3, then the first and fourth TAs are activated for transmitting the BPSK symbols (-1) and (-1), while the second and third TAs are activated for transmitting the BPSK symbols (-1) and $(+1)$, when having $K=2$. Compared to the information sequence associated with $N_t^a = 1$, more information can be transmitted due to the increased number of active TAs.

4.2.1.3 Space-Frequency Index Modulation

According to the specific active subcarrier selection regime of the Virtual-Domain Frequency Index Selector introduced in Section 4.2.1.1 and the output matrix $\mathbf{X}_{u,g} \in \mathbb{C}^{N_t \times K}$ of the Spatial-Domain Modulation/Mapping illustrated in Section 4.2.1.2, the space-frequency matrix $\underline{\mathcal{S}}_{u,g} \in \mathbb{C}^{N_t \times N_v}$ is obtained by allocating the column vectors of the spatial-domain matrix $\mathbf{X}_{u,g}$ to the active subcarriers selected. Explicitly, as shown in the SFIM example illustrated in Fig. 4.3, the BPSK symbol $(+1)$ is transmitted through the second TA and the BPSK symbol (-1) is transmitted through the fourth TA based on the look-up table of Table. 4.1, resulting in a two-column spatial-domain matrix $\mathbf{X}_{u,g} = \{[0\ +1\ 0\ 0]^T, [0\ 0\ 0\ -1]^T\}$. The two column-vectors of $\mathbf{X}_{u,g}$ seen in Fig. 4.3 are then allocated both to the second and to the third subcarriers in the virtual domain, while the rest of the subcarriers remain idle for all TAs, where the space-frequency matrix $\underline{\mathcal{S}}_{u,g}$ of each subcarrier group is generated, as illustrated in Fig. 4.3. Additionally, in the GSFIM example shown in Fig. 4.3, the space-frequency matrix $\underline{\mathcal{S}}_{u,g}$ related to each subcarrier group is obtained by allocating the two-column spatial-domain matrix $\mathbf{X}_{u,g} = \{[-1\ 0\ 0\ -1]^T, [0\ -1\ +1\ 0]^T\}$ to the activated subcarriers accordingly, where it is seen that our new CS-GSFIM scheme is capable of not only carrying more information bits than the CS-aided multi-dimensional scheme of Fig. 3.2 relying on the same TAs combination for the whole subcarrier group, but also provides higher design flexibility by applying different active TAs to different APM symbols. In general, the space-frequency matrix $\underline{\mathcal{S}}_{u,g}$ for each subcarrier block has a sparsity level of $N_t^a \cdot K$, where there are K active subcarriers per space-frequency block and there are N_t^a active TAs for transmitting the signals at each active subcarrier, which results in $N_t^a \cdot K$ non-zero elements in the space-frequency matrix $\underline{\mathcal{S}}_{u,g}$.

4.2.1.4 Compressed Sensing and the Block Assembler

There are G space-frequency matrices $\underline{\mathcal{S}}_{u,g}$ $(g = 1, 2, \ldots G)$ for the u-th user, where G represents the number of subcarrier blocks per OFDM frame. Similarly to the CS block of both Fig. 2.6 and Fig. 3.2 and as detailed in both Eq. (2.6) and Eq. (3.1), for each subcarrier block of the u-th user, the CS measurement matrix $\mathbf{A} \in \mathbb{C}^{N_f \times N_v}$ is employed for compressing the N_v-dimensional vector $\underline{\mathcal{S}}_{u,g}^t$ from the t-th TA in the virtual domain into an N_f-dimensional vector $\mathbf{s}_{u,g}^t$ from the t-th TA in the frequency domain, which can be expressed as

$$\mathbf{s}_{u,g}^t = \mathbf{A}\underline{\mathcal{S}}_{u,g}^t, \tag{4.1}$$

where $t = 1, 2, \ldots, N_t$ and we can express the frequency-domain signals arriving from the N_t TAs in the g-th subcarrier block of the u-th user as $\mathbf{S}_{u,g} \in \mathbb{C}^{N_t \times N_f}$. Then, the Block Assembler collects G frequency-domain signals $\mathbf{S}_{u,g}$ to create a space-frequency super frame $\mathbf{S}_u \in \mathbb{C}^{N_t \times N_c}$, which contains N_t OFDM symbols for transmission from N_t TAs and can be expanded as $\mathbf{S}_u = [\mathbf{S}_{u,1}, \mathbf{S}_{u,2}, \ldots, \mathbf{S}_{u,G}]$. Afterwards, IFFT is applied to the OFDM symbol at each TA for obtaining the time-domain symbol, followed by concatenating the usual CP. Then, as shown in Fig. 4.2, the resultant time-domain signals of the u-th user are simultaneously transmitted from the N_t TAs over the wireless channel.

Considering the uplink transmission of U users as seen in Fig. 4.2, the system's overall achievable rate based on the above discussions is expressed as [97]

$$R_t = \begin{cases} U \frac{G(K \log_2 \mathcal{L} + K \log_2 N_t + \lfloor \log_2 C(N_v, K) \rfloor)}{N_c + N_{cp}} \text{bits/s/Hz} \\ \qquad\qquad\qquad\qquad (\text{if } N_t^a = 1) \\ U \frac{G(N_t^a K \log_2 \mathcal{L} + K \lfloor \log_2 C(N_t, N_t^a) \rfloor + \lfloor \log_2 C(N_v, K) \rfloor)}{N_c + N_{cp}} \text{bits/s/Hz} \\ \qquad\qquad\qquad\qquad (\text{if } 1 < N_t^a \leq N_t). \end{cases}$$

4.3 Multi-User Detection

Let $\mathbf{H}^u \in \mathbb{C}^{N_r \times N_t}$ $(u = 1, 2, \ldots, U)$ denote the MIMO channel matrix of the u-th user, where $\mathbf{H}_i^u[n] \in \mathbb{C}^{1 \times N_t}$ ($i = 1, 2, \ldots, N_r$ and $n = 1, 2, \ldots, N_c$) denotes the complex channel gain of the n-th subcarrier spanning from the N_t TAs of the u-th user to the i-th RA. Assuming perfect synchronisation, the signal $\mathbf{y}_i^u[n]$ received from the u-th user at the i-th RA after the CP removal and FFT-based demodulation is given by

$$\mathbf{y}_i^u[n] = \mathbf{H}_i^u[n]\mathbf{S}_u[n] + \mathbf{v}_i^u[n], \tag{4.2}$$

where $n = 1, 2, \ldots, N_c$ denotes the index of the transmitted frequency-domain subcarriers of the u-th user, $\mathbf{S}_u[n] \in \mathbb{C}^{N_t \times 1}$ denotes the frequency-domain symbols received at the n-th subcarrier from the N_t TAs and $\mathbf{v}_i^u[n]$ is the Gaussian noise with zero mean and variance of σ_n^2.

After collecting the received frequency-domain symbols $\mathbf{y}_i^u[n]$ $(n = 1, 2, \ldots, N_c)$ at the N_c subcarriers, we can express the signal $\mathbf{y}_i^u \in \mathbb{C}^{N_c \times 1}$ received by the i-th RA from the u-th user as

$$\mathbf{y}_i^u = \mathbf{H}_i^u \mathbf{s}_u + \mathbf{v}_i^u, \tag{4.3}$$

where $\mathbf{H}_i^u \in \mathbb{C}^{N_c \times (N_t N_c)} = diag\{\mathbf{H}_i^u[n]\}$ $(n = 1, 2, \ldots, N_c)$ denotes the diagonal-structure of the complex-valued channel gain matrix for the transmission of N_c frequency-domain subcarriers of the u-th user from the N_t TAs to the i-th RA, $\mathbf{s}_u \in \mathbb{C}^{(N_t N_c)\times 1} = [(\mathbf{S}_u[1])^T\,(\mathbf{S}_u[2])^T\,\ldots\,(\mathbf{S}_u[N_c])^T]^T$ represents the N_c-length frequency-domain symbols of the u-th user transmitted from the N_t TAs, while having $(N_t^a \cdot K \cdot G)$ non-zero elements, and $\mathbf{v}_i^u \in \mathbb{C}^{N_c \times 1}$ denotes the Gaussian noise vector, which obeys the distribution of $\mathcal{CN}(0, \sigma_n^2)$.

When all users simultaneously transmit their own signals from the N_t TAs, the frequency-domain signal $\mathbf{y}_i \in \mathbb{C}^{N_c \times 1}$ received at the i-th RA is expressed as

$$\mathbf{y}_i = \sum_{u=1}^{U} \mathbf{y}_i^u = \mathbf{H}_i \mathbf{s} + \mathbf{v}_i, \tag{4.4}$$

where $\mathbf{H}_i = [\mathbf{H}_i^1\,\mathbf{H}_i^2\,\ldots\,\mathbf{H}_i^U]$, $\mathbf{s} \in \mathbb{C}^{(N_t N_c U)\times 1} = [(\mathbf{s}_1)^T\,(\mathbf{s}_2)^T\,\ldots\,(\mathbf{s}_U)^T]^T$, and $\mathbf{v}_i$ is the Gaussian noise matrix.

Stacking the received signal $\mathbf{y}_i$ in Eq. (4.4) over the N_r RAs at the BS, we can express the received signal $\mathbf{y} \in \mathbb{C}^{(N_r N_c)\times 1}$ as

$$\mathbf{y} = \mathbf{H}\mathbf{s} + \mathbf{v}, \tag{4.5}$$

where $\mathbf{y} = [\mathbf{y}_1^T\,\mathbf{y}_2^T\,\ldots\,\mathbf{y}_{N_r}^T]^T$, $\mathbf{H} \in \mathbb{C}^{(N_r N_c)\times(N_t N_c U)} = [\mathbf{H}_1^T\,\mathbf{H}_2^T\,\ldots\,\mathbf{H}_{N_r}^T]^T$ and $\mathbf{v} \in \mathbb{C}^{(N_r N_c)\times 1} = [\mathbf{v}_1^T\,\mathbf{v}_2^T\,\ldots\,\mathbf{v}_{N_r}^T]^T$.

For the sake of analysis, the frequency-domain received signal $\mathbf{y}$ in Eq. (4.5) can be split into G subcarrier groups and the signal $\mathbf{y}_g \in \mathbb{C}^{(N_r N_f)\times 1}$ of the g-th subcarrier group of the U users received from the N_t TAs over the N_r RAs at the BS can be represented by

$$\mathbf{y}_g = \mathbf{H}_g \mathbf{s}_g + \mathbf{v}_g, \tag{4.6}$$

where $\mathbf{s}_g \in \mathbb{C}^{(N_t N_f U)\times 1}$ denotes the signals transmitted to the U users of the g-th subcarrier group from the N_t TAs, $\mathbf{v}_g \in \mathbb{C}^{N_r N_f \times 1}$ is the Gaussian noise vector. The equivalent channel matrix $\mathbf{H}_g \in \mathbb{C}^{(N_r N_f)\times(N_t N_f U)}$ associated with transmitting the signals of U users in the g-th subcarrier group from the N_t TAs over the N_r RAs can be expanded as

$$\mathbf{H}_g = \begin{bmatrix} \mathbf{H}_{1,g}^1 & \mathbf{H}_{1,g}^2 & \cdots & \mathbf{H}_{1,g}^U \\ \mathbf{H}_{2,g}^1 & \mathbf{H}_{2,g}^2 & \cdots & \mathbf{H}_{2,g}^U \\ \vdots & \vdots & \ddots & \vdots \\ \mathbf{H}_{N_r,g}^1 & \mathbf{H}_{N_r,g}^2 & \cdots & \mathbf{H}_{N_r,g}^U \end{bmatrix}, \tag{4.7}$$

where the element matrix $\mathbf{H}_{i,g}^{u} \in \mathbb{C}^{N_f \times (N_t N_f)}$ in Eq. (4.7) represents the complex channel at the i-th RA of the u-th user received from the N_t TAs, which can be written as

$$\mathbf{H}_{i,g}^{u} = \begin{bmatrix} \mathbf{H}_{i,g}^{u}[1] & \mathbf{0} & \cdots & \mathbf{0} \\ \mathbf{0} & \mathbf{H}_{i,g}^{u}[2] & \cdots & \mathbf{0} \\ \vdots & \vdots & \ddots & \vdots \\ \mathbf{0} & \mathbf{0} & \cdots & \mathbf{H}_{i,g}^{u}[N_f] \end{bmatrix}. \tag{4.8}$$

In Eq. (4.8), we use $\mathbf{H}_{i,g}^{u}[n] \in \mathbb{C}^{1 \times N_t}$ $(n = 1, 2, \ldots, N_f)$ to represent the complex channel gain for the n-th frequency-domain subcarrier in the g-th subcarrier group of the u-th user spanning from the N_t TAs to the i-th RA.

Explicitly, based on the process of the proposed CS-(G)SFIM-OFDM scheme of Fig. 4.3, the signals $\mathbf{s}_g$ in Eq. (4.6) transmitted to the g-th group can be expressed as

$$\mathbf{s}_g = \bar{\mathbf{A}} \mathbf{I}_{SI}^{g} \mathbf{I}_{AC}^{g} \mathbf{x}_L^{g}, \tag{4.9}$$

where $\bar{\mathbf{A}} \in \mathbb{C}^{(N_t N_f U) \times (N_t N_v U)}$ denotes the group-equivalent[2] CS measurement matrix of $\mathbf{A}$ in Eq. (4.1), $\mathbf{I}_{SI}^{g} \in \mathbb{C}^{(N_t N_v U) \times (N_t K U)}$ is the group-equivalent representation of the subcarrier indexing pattern, $\mathbf{I}_{AC}^{g} \in \mathbb{C}^{(N_t K U) \times (K N_t^a U)}$ represents the group-equivalent TA indexing for U users in the g-th subcarrier group and we have the generalised expression of Eq. (4.9), since $1 \leq N_t^a \leq N_t$. Furthermore, $\mathbf{x}_L^{g} \in \mathbb{C}^{K N_t^a U \times 1}$ in Eq. (4.9) indicates the vector containing $K N_t^a U$ transmitted APM symbols in the g-th subcarrier group for U users, where we have $1 \leq N_t^a \leq N_t$. Then Eq. (4.6) can be written as

$$\mathbf{y}_g = \mathbf{H}_g \bar{\mathbf{A}} \mathbf{I}_{SI}^{g} \mathbf{I}_{AC}^{g} \mathbf{x}_L^{g} + \mathbf{v}_g = \mathbf{H}_g \bar{\mathbf{A}} \mathbf{I}_g \mathbf{x}_L^{g} + \mathbf{v}_g, \tag{4.10}$$

where $\mathbf{I}_g \in \mathbb{C}^{(N_t N_v U) \times (K N_t^a U)} = \mathbf{I}_{SI}^{g} \mathbf{I}_{AC}^{g}$ is the equivalent supporting matrix containing the information of the active TAs and the active subcarriers of U users in the g-th subcarrier group.

In the following, we will detail both the hard-decision (HD) and the soft-decision (SD) based ML MUDs, which are then followed by the portrayal of both the HD and the SD based reduced-complexity RSS-IMP MUDs.

[2] We use a large-dimension matrix $\bar{\mathbf{A}}$ derived from $\mathbf{A}$ to represent the measurement matrix for compressing signals of U users transmitted from N_t TAs, where we call this large-dimension matrix "group-equivalent" matrix.

4.3.1 Maximum Likelihood Multi-User Detector

In this section, we introduce both the HD-aided and the SD-aided ML MUDs proposed for the uncoded and coded CS-(G)SFIM system, respectively.

4.3.1.1 HD-aided ML Multi-User Detection

For the uncoded scenario of the proposed system illustrated in Fig. 4.2, information sequences $\mathbf{w}_u$ $(u = 1, 2, \ldots, U)$ at the transmitter is processed directly on a group-by-group by the CS-(G)SFIM-OFDM encoder shown in Fig. 4.2 and Fig. 4.3. Then, the signal received at the BS is detected by our MUD of Fig. 4.2. Note that for the sake of simplicity, we only introduce the HD-aided ML algorithm for the g-th subcarrier group here, which can be generalised to the entire OFDM symbol.

Let us assume that $< l_g, i_g, j_g >$ corresponds to the specific input information in the g-th subcarrier group for U users of the proposed system shown in Fig. 4.2. Explicitly, $(\mathbf{x}_L^g)_{l_g}$ denotes the l_g-th realisation of the KN_t^aU APM symbols for $l_g = 1, 2, \ldots, \mathcal{L}^{KN_t^aU}$, $(\mathbf{I}_{SI}^g)_{i_g}$ represents the i_g-th indexing pattern of the active subcarriers of the U users, given that $i_g = 1, 2, \ldots, N_{SI}^U$, and $(\mathbf{I}_{AC}^g)_{j_g}$ is used to denote the j_g-th active TAs selection pattern for KU active subcarriers of U users in the g-th subcarrier group for $j_g = 1, 2, \ldots, (N_{AC}^K)^U$. Additionally, we use $< \hat{l}_g, \hat{i}_g, \hat{j}_g >$ to represent the estimate of the corresponding input information. Then the HD-aided optimal ML detector of Eq. (4.5) and Eq. (4.10) is expressed as

$$\begin{aligned} &< \hat{l}_g, \hat{i}_g, \hat{j}_g > \\ &= \arg \min_{l_g, i_g, j_g} \|\mathbf{y}_g - \mathbf{H}_g \bar{\mathbf{A}} (\mathbf{I}_{SI}^g)_{i_g} (\mathbf{I}_{AC}^g)_{j_g} (\mathbf{x}_L^g)_{l_g}\|^2 \\ &= \arg \min_{l_g, i_g, j_g} \|\mathbf{y}_g - \mathbf{H}_g \bar{\mathbf{A}} \bar{\mathbf{s}}_g\|^2, \end{aligned} \tag{4.11}$$

where we use $\bar{\mathbf{s}}_g = (\mathbf{I}_{SI}^g)_{i_g} (\mathbf{I}_{AC}^g)_{j_g} (\mathbf{X}_L^g)_{l_g}$ to denote the search space of the g-th subcarrier group and the ML detector achieves the optimal detection performance in uncoded scenarios.

4.3.1.2 Average BEP Analysis

Here, we derive the ABEP of the proposed multi-user scenario using ML detection for a single subcarrier group, since all subcarrier groups have the same PE event. Considering the system model of the g-th subcarrier group given in Eq. (4.6), if $\mathbf{s}_g$ is transmitted but

erroneously detected as $\hat{\mathbf{s}}_g \in \mathbb{C}^{(N_t N_f U)\times 1}$, given the channel matrix $\mathbf{H}_g$ in the frequency-domain, then the conditional pairwise error probability (CPEP) is expressed as [222]

$$P(\mathbf{s}_g \to \hat{\mathbf{s}}_g | \mathbf{H}_g) = Q\left(\sqrt{\frac{\|\mathbf{H}_g(\mathbf{s}_g - \hat{\mathbf{s}}_g)\|^2}{2\sigma_n^2}}\right). \tag{4.12}$$

Then Eq. (4.12) can be rewritten by using the alternative form of the Q-function as

$$P(\mathbf{s}_g \to \hat{\mathbf{s}}_g | \mathbf{H}_g) = \frac{1}{\pi}\int_0^{\pi/2} \exp\left(-\frac{\xi_d}{4\sigma_n^2 \sin^2\theta}\right) d\theta, \tag{4.13}$$

where we define

$$\xi_d = \|\mathbf{H}_g(\mathbf{s}_g - \hat{\mathbf{s}}_g)\|^2 \tag{4.14}$$

$$= \sum_{j=1}^{mU} \|\mathbf{H}_g^j(\mathbf{s}_g^j - \hat{\mathbf{s}}_g^j)\|^2 \tag{4.15}$$

$$= \sum_{j=1}^{mU}\sum_{i=1}^{N_r} (\mathbf{H}_g^j)_i(\mathbf{s}_g^j - \hat{\mathbf{s}}_g^j)(\mathbf{s}_g^j - \hat{\mathbf{s}}_g^j)^H (\mathbf{H}_g^j)_i^H, \tag{4.16}$$

and $(\mathbf{H}_g^j)_i \in \mathbb{C}^{1\times N_t}$ is the i-th row element of $\mathbf{H}_g^j \in \mathbb{C}^{N_r \times N_t}$. Then the moment generating function (MGF) [223] of ξ_d defined in Eq. (4.14) can be obtained according to the quadratic form of ξ_d provided in Eq. (4.16) as

$$M_{\xi_d}(t) = \prod_{j=1}^{mU} \frac{1}{\left(1 - t\|\mathbf{s}_g^j - \hat{\mathbf{s}}_g^j\|^2\right)^{N_r}}. \tag{4.17}$$

Finally, integrating the CPEP given in Eq. (4.13) over the probability density function of ξ_d and using the MGF $M_{\xi_d}(t)$ given in Eq. (4.17), the unconditional pairwise error probability (UPEP) is obtained as

$$P(\mathbf{s}_g \to \hat{\mathbf{s}}_g) = \frac{1}{\pi}\int_0^{\pi/2} \prod_{j=1}^{mU} \left(\frac{\sin^2\theta}{\sin^2\theta + \frac{\|\mathbf{s}_g^j - \hat{\mathbf{s}}_g^j\|^2}{4\sigma_n^2}}\right)^{N_r} d\theta. \tag{4.18}$$

After obtaining the UPEP in Eq. (4.18), an upper bound of the ABEP based on the union bound can be obtained by [222]

$$P_B \leq \frac{1}{bN(\mathbf{s}_g)} \sum_{\mathbf{s}_g}\sum_{\hat{\mathbf{s}}_g} P(\mathbf{s}_g \to \hat{\mathbf{s}}_g) d\left[P(\mathbf{s}_g, \hat{\mathbf{s}}_g)\right], \tag{4.19}$$

where b is the number of information bits transmitted by he U users in the uplink within each subcarrier group, $N(\mathbf{s}_g)$ is the total number of legitimate realisations of $\mathbf{s}_g$

for U users per subcarrier group and $d\left[P(\mathbf{s}_g, \hat{\mathbf{s}}_g)\right]$ is used for representing the number of erroneous bits for the PE event of $(\mathbf{s}_g \rightarrow \hat{\mathbf{s}}_g)$.

4.3.1.3 SD-aided Multi-User Detection

Having presented the HD-aided ML detector of the proposed CS-(G)SFIM systems, we present the SD-aided iterative detection technique based on the classic Logarithmic Maximum *a posteriori* (Log-MAP) algorithm [211]. As illustrated in Fig. 4.2, there are U two-stage serially concatenated systems, which incorporate the MUD and U half-rate RSC decoders. The MUD and each RSC decoder are connected by an interleaver and deinterleaver pair, as shown in Fig. 4.2. Specifically, the received complex-valued signal $\mathbf{y}$ in Eq. (4.5) is demapped by the MUD shown in Fig. 4.2 to its LLR representations for the channel-coded bits of each of the U users. The MUD's extrinsic output LLRs $L_{M,e}$ of the u-th user are deinterleaved by the soft-bit deinterleaver of Fig. 4.2 for generating the *a priori* LLRs $L_{R,a}$ entered into the RSC decoder in order to calculate the extrinsic LLRs $L_{R,e}$ based on the Log-MAP algorithm [211] for all channel-coded symbols of the u-th user. As seen in Fig. 4.2, $L_{R,e}$ is then appropriately reordered as $L_{M,a}$ by the soft-bit interleaver and fed back to the MUD as the *a priori* information for providing improved extrinsic LLRs. The improved extrinsic LLRs are then passed to the RSC decoder and then back to the MUD for further inner-outer (IO) iterations.

Using the received signal model of Eq. (4.5), the conditional probability of receiving the signal $\mathbf{y}$ given the full search-space $\bar{\mathbf{s}}$ while exploring all realisations of the CS-(G)SFIM for U users can be expressed as

$$p(\mathbf{y}|\bar{\mathbf{s}}) = \frac{1}{(\pi N_0)^{N_r U}} \exp\left(-\frac{\|\mathbf{y} - \mathbf{H}\bar{\mathbf{s}}\|^2}{N_0}\right). \tag{4.20}$$

According to the uplink transmission of the U users discussed in Section 4.2.1, the received signal $\mathbf{y}$ of Eq. (4.5) carries $\mathbf{b} = [\mathbf{b}_1\, \mathbf{b}_2\, \ldots\, \mathbf{b}_u\, \ldots\, \mathbf{b}_U]$ channel-coded bits, as seen in Fig. 4.2, where each user carries B channel coded bits and we use $b_u(i)$ $(i = 1, 2, \ldots, B)$ to represent the u-th user's channel-coded bits. Then the extrinsic LLR value of $b_u(i) \in \mathbf{b}_u$ can be expressed as

$$\begin{aligned} L_{M,e}\left[b_u(i)\right] &= \ln\left(\frac{p(b_u(i)=1|\mathbf{y})}{p(b_u(i)=0|\mathbf{y})}\right) \\ &= \ln\left(\frac{\sum_{\bar{\mathbf{s}}\in\bar{\mathbf{s}}_1^{b_u(i)}} \exp\left(\Phi_{l,i,j}\right)}{\sum_{\bar{\mathbf{s}}\in\bar{\mathbf{s}}_0^{b_u(i)}} \exp\left(\Phi_{l,i,j}\right)}\right), \end{aligned} \tag{4.21}$$

where $\bar{\mathbf{s}}_1^{b_u(i)}$ and $\bar{\mathbf{s}}_0^{b_u(i)}$ are the subsets of $\bar{\mathbf{s}}$ satisfying $\bar{\mathbf{s}}_1^{b_u(i)} \triangleq \{\bar{\mathbf{s}}_{l,i,j} \in \bar{\mathbf{s}} : b_u(i) = 1\}$ and $\bar{\mathbf{s}}_0^{b_u(i)} \triangleq \{\bar{\mathbf{s}}_{l,i,j} \in \bar{\mathbf{s}} : b_u(i) = 0\}$, respectively. Additionally, the *a posteriori* symbol probability $\Phi_{l,i,j}$ in Eq. (4.21) is expressed by

$$\Phi_{l,i,j} \triangleq -\frac{\|\mathbf{y} - \mathbf{H}\bar{\mathbf{s}}\|^2}{N_0} + \sum_{j \neq i} b_u(j) L_{M,a}\left[b_u(j)\right]. \tag{4.22}$$

In order to avoid numerical overflow, the Jacobian logarithm of [211] is applied for simplifying the SD-aided detection of Eq. (4.21) as

$$L_{M,e}\left[b_u(i)\right] = \mathrm{jac}_{\bar{\mathbf{s}} \in \bar{\mathbf{s}}_1^{b_u(i)}}(\Phi_{l,i,j}) - \mathrm{jac}_{\bar{\mathbf{s}} \in \bar{\mathbf{s}}_0^{b_u(i)}}(\Phi_{l,i,j}). \tag{4.23}$$

4.3.2 RSS-IMP Multi-User Detector

The ML detector introduced in Section 4.3.1 achieves the optimal detection performance due to the full search-space detection, where all possible combinations of the APM symbols, the active TAs and the active subcarriers of all users are explored. However, the detection complexity of the ML detector discussed in Section 4.3.1 may become excessive in practice, for example in our LS-MU-MIMO scenarios. Hence, we propose an RSS-IMP multi-user detector in this section, which iteratively reduces the detector's search space and splits the detection process into several sub-operations with the aid of CS principles. We introduce the reduced-complexity detector in this section based on the received group-equivalent signal $\mathbf{y}_g$ in Eq. (4.6) and Eq. (4.10), which contains all information in the g-th subcarrier group from all users, where we can re-express Eq. (4.10) as

$$\mathbf{y}_g = \bar{\mathbf{H}}_g \bar{\mathbf{s}}_g + \mathbf{v}_g, \tag{4.24}$$

where $\bar{\mathbf{H}}_g \in \mathbb{C}^{(N_r N_f) \times (N_t N_v U)} = \mathbf{H}_g \bar{\mathbf{A}}$ is the equivalent channel matrix of all users in the g-th subcarrier group and $\bar{\mathbf{s}}_g \in \mathbb{C}^{(N_t N_v U) \times 1}$ is the transmitted group-equivalent signal covering all the U users' information received from the active TAs, the active subcarriers and the APM symbols.

Specifically, in the CS-(G)SFIM scheme illustrated in Fig. 4.3, the transmitted group-equivalent signal $\bar{\mathbf{s}}_g$ has an intrinsic sparsity level of $(KN_t^a U)$, where only $KN_t^a U$ elements in $\bar{\mathbf{s}}_g$ are non-zero. Additionally, Eq. (4.24) reveals its over-determined nature (*e.g.* having $N_r N_f > N_t N_v U$) due to the large number of RAs at the BS and hence the CS-based sparse detection algorithm [184] can be applied to the detector according to CS principles [108].

In Eq. (4.24), the group-equivalent channel matrix $\bar{\mathbf{H}}_g$ fulfils the mutual incoherence property (MIP) [108] requirement for guaranteeing a good detection performance according to CS principles, so that $\bar{\mathbf{H}}_g$ can be regarded as a group-equivalent measurement matrix in our following discussions and $\bar{\mathbf{s}}_g$ is a sparse signal, which will be detected with the aid of CS.

Based on the classic greedy algorithm's philosophy and on the iterative algorithm of [184], the proposed RSS-IMP detector searches through multiple promising candidates during each iteration and the number of promising candidates increases with the number of iterations. Then the proposed RSS-IMP detector makes a decision concerning the best candidate at the end of the process. More specifically, the proposed RSS-IMP detector intrinsically amalgamates the classical greedy algorithm and the iterative algorithm for tackling the detection challenge of the proposed CS-(G)SFIM system operating in LS-MU-MIMO scenarios. Explicitly, the proposed RSS-IMP detector is composed of three steps, namely the application of conventional linear detection for initially generating rough estimates and mitigating the MU interference, followed by the iterative detection technique of [184] and the final decision based on minimising the residual error vector, as detailed in the following.

- Step 1:
  The linear minimum mean square error (LMMSE) detector is applied to the received signal $\mathbf{y}_g$ of Eq. (4.24) both for mitigating the MU interference, and for generating a rough estimate $\hat{\mathbf{s}}_g \in \mathbb{C}^{(N_t N_v U)\times 1}$ of the transmitted sparse signal $\bar{\mathbf{s}}_g$ of Eq. (4.24), which can be expressed as

$$\hat{\mathbf{s}}_g = \left(\bar{\mathbf{H}}_g^H \bar{\mathbf{H}}_g + \frac{1}{\gamma}\mathbf{I}_{(N_t N_v U)}\right)^{-1} \bar{\mathbf{H}}_g^H \mathbf{y}_g, \tag{4.25}$$

  where $\hat{\mathbf{s}}_g$ is the estimated signal of the g-th subcarrier group of the U users, containing the information of the active TAs, of the active subcarriers and of the APM symbols. Furthermore, $\gamma = E\|\bar{\mathbf{H}}_g \bar{\mathbf{s}}_g\|_2^2 / E\|\mathbf{v}_g\|_2^2$ is the average SNR per symbol. Additionally, the estimated signal $\hat{\mathbf{s}}_g$ can be split into U vectors in parallel, which can be reformulated as a matrix $\left[\hat{\mathbf{s}}_g^1 \ldots \hat{\mathbf{s}}_g^u \ldots \hat{\mathbf{s}}_g^U\right]^T$ of size $(U \times N_t N_v)$, where $\hat{\mathbf{s}}_g^u \in \mathbb{C}^{N_t N_v \times 1}$ $(u = 1, 2, \ldots, U)$ is the LMMSE estimated signal of the u-th user. There should be KN_t^a active elements in $\hat{\mathbf{s}}_g^u$. According to the indexing strategy illustrated in Eq. (4.9) and Eq. (4.10), the estimated signal $\hat{\mathbf{s}}_g^u$ for the u-th user can be expressed as

$$\hat{\mathbf{s}}_g^u = \mathbf{I}_g^u \mathbf{x}_L^{g,u} + \hat{\mathbf{v}}_g^u, \tag{4.26}$$

where $\mathbf{I}_g^u \in \mathbb{C}^{N_t N_v \times K N_t^a} = \mathbf{I}_{SI}^{g,u} \mathbf{I}_{AC}^{g,u}$ represents the joint support matrix containing the activation patterns of the active TAs $\mathbf{I}_{AC}^{g,u} \in \mathbb{C}^{N_t N_v \times N_t K}$ and the active subcarriers $\mathbf{I}_{SI}^{g,u} \in \mathbb{C}^{N_t K \times K N_t^a}$ for the u-th user in the g-th subcarrier group, $\mathbf{x}_L^{g,u} \in \mathbb{C}^{K N_t^a \times 1}$ represents the APM symbols vector of the u-th user and finally $\hat{\mathbf{v}}_g^u \in \mathbb{C}^{N_t N_v \times 1}$ is the linear-processed Gaussian noise vector.

Then we calculate the magnitudes of $(N_t N_v)$ elements in $\hat{\mathbf{s}}_g^u$ and rearrange these magnitudes in a descending order, where the ordered magnitudes of the U users can be expressed as

$$\begin{bmatrix} \|\hat{\mathbf{s}}_g^1(i_1^1)\|^2 > \|\hat{\mathbf{s}}_g^1(i_2^1)\|^2 > \cdots > \|\hat{\mathbf{s}}_g^1(i_{N_t N_v}^1)\|^2 \\ \vdots \\ \|\hat{\mathbf{s}}_g^u(i_1^u)\|^2 > \|\hat{\mathbf{s}}_g^u(i_2^u)\|^2 > \cdots > \|\hat{\mathbf{s}}_g^u(i_{N_t N_v}^u)\|^2 \\ \vdots \\ \underbrace{\|\hat{\mathbf{s}}_g^U(i_1^U)\|^2}_{1^{st}Iteration} > \underbrace{\|\hat{\mathbf{s}}_g^U(i_2^U)\|^2}_{2^{nd}Iteration} > \underbrace{\cdots}_{\cdots} > \underbrace{\|\hat{\mathbf{s}}_g^U(i_{N_t N_v}^U)\|^2}_{(N_t N_v)^{th}Iteration} \end{bmatrix}, \tag{4.27}$$

where for example, $\|\hat{\mathbf{s}}_g^u(i_1^u)\|^2$ is the highest magnitude of the u-th user and hence the i_1^u-th element $\hat{\mathbf{s}}_g^u(i_1^u)$ in $\hat{\mathbf{s}}_g^u$ has the highest probability to be one of the $K N_t^a$ active elements. In addition, we use N^u to indicate the total number of joint realisations[3] in each subcarrier group of the u-th user, while selecting $K N_t^a$ active elements out of $(N_t N_v)$ transmitted elements, where we have $N^u = N_{SI} N_{AC}^K$. Explicitly, a set of realisations Z_u^1 of the u-th user is selected during the 1^{st} iteration and we have $Z_u^1 < N^u$, where the resultant sets of realisations $\left[Z_1^1\ Z_2^1\ \ldots\ Z_U^1\right]$ of the U users during the 1^{st} iteration will be employed in the second step.

- Step 2:
  In the second step, we carry out the proposed iterative detection based on the greedy algorithm for detecting both the indices of the active TAs, as well as the indices of the active subcarriers and the corresponding APM symbols of all users.

  During the first iteration of the u-th user, there are Z_u^1 realisations of the joint-support matrix $\mathbf{I}_g^u$ in Eq. (4.26) and we refer to these Z_u^1 realisations as the joint-support matrix candidates in the first iteration of the u-th user. Then the joint-support matrix candidates in the first iteration derived for the u-th user are expressed as

$$\{\mathbf{I}_g^u\}_1 = \{\mathbf{I}_{g,1}^u, \mathbf{I}_{g,2}^u, \cdots, \mathbf{I}_{g,Z_u^1}^u\}. \tag{4.28}$$

[3]Note that each realisation is a joint combination of the active TAs and the active subcarriers per subcarrier group for the u-th user, and we have $N^u < C_{N_t N_v}^{K N_t^a}$.

Specifically, based on the estimated signal of Eq. (4.26), we can obtain the estimated signal $\hat{\mathbf{y}}_g^u \in \mathbb{C}^{N_r N_f \times 1}$ received from the u-th user, which is expressed as

$$\hat{\mathbf{y}}_g^u = \mathbf{\Omega}_g^u \mathbf{x}_L^{g,u} + \hat{\bar{\mathbf{v}}}_g^u, \tag{4.29}$$

where we define $\mathbf{\Omega}_g^u \in \mathbb{C}^{(N_r N_f)\times(KN_t^a)} = \mathbf{H}_g^u \bar{\mathbf{A}}^u \mathbf{I}_g^u$ as a group-equivalent matrix, while $\hat{\bar{\mathbf{v}}}_g^u \in \mathbb{C}^{N_r N_f \times 1}$ represents the Gaussian noise vector. According to the candidate set generated during the first iteration listed in Eq. (4.28), the Z_u^1 group-equivalent matrix candidates in the first iteration can be represented as $\{\mathbf{\Omega}_{g,1}^u, \mathbf{\Omega}_{g,2}^u, \cdots, \mathbf{\Omega}_{g,Z_u^1}^u\}$. Additionally, the system of Eq. (4.29) is referred to as an over-determined scenario, since $N_r N_f > KN_t^a$ and hence the pseudo-inverse process can be exploited for detecting the transmitted signals. Then the pseudo-inverse process of the i-th group-equivalent matrix candidate $\mathbf{\Omega}_{g,i}^u$ $(i = 1, 2, \ldots, Z_u^1)$ is expressed as

$$(\mathbf{\Omega}_{g,i}^u)^\dagger = \left((\mathbf{\Omega}_{g,i}^u)^H \mathbf{\Omega}_{g,i}^u \right)^{-1} (\mathbf{\Omega}_{g,i}^u)^H. \tag{4.30}$$

Upon substituting Eq. (4.30) into Eq. (4.29), the estimated signal $\hat{\mathbf{x}}_{L,i}^{g,u} \in \mathbb{C}^{KN_t^a \times 1}$ is obtained as

$$\begin{aligned} \hat{\mathbf{x}}_{L,i}^{g,u} &= (\mathbf{\Omega}_{g,i}^u)^\dagger (\mathbf{\Omega}_g^u \mathbf{x}_L^{g,u} + \hat{\bar{\mathbf{v}}}_g^u) \\ &= \mathbf{x}_L^{g,u} + \bar{\mathbf{v}}_g^u + \mathbf{r}_{g,i}^u, \end{aligned} \tag{4.31}$$

where the linearly processed Gaussian noise vector $\bar{\mathbf{v}}_g^u$ still remains Gaussian distributed, and $\mathbf{r}_{g,i}^u$ is the residual error vector due to the mismatch[4] of the matrix candidate $\mathbf{\Omega}_{g,i}^u$ and the correct matrix $\mathbf{\Omega}_g^u$.

Then the symbol-by-symbol optimal ML algorithm is applied to the estimated $\hat{\mathbf{x}}_{L,i}^{g,u}$ in Eq. (4.31) for detecting the APM symbols based on the i-th tested CS matrix candidate $\mathbf{\Omega}_{g,i}^u$ during the first iteration and this process is represented as

$$\vec{\mathcal{X}}_{L,i}^{g,u}(n) = \arg\min_{\mathcal{A}} \|\hat{\mathbf{x}}_{L,i}^{g,u}(n) - \mathcal{A}_L\|^2, \tag{4.32}$$

where $n = 1, 2, \ldots, KN_t^a$, $\mathcal{A}_L \in \mathcal{A}$ represents the library of $\mathcal{L}$-ary APM symbols and $\vec{\mathcal{X}}_{L,i}^{g,u}(n)$ is the n-th estimated APM symbol.

Then we have the group-equivalent matrix candidate $\mathbf{\Omega}_{g,i}^u$, the corresponding estimated symbols vector $\vec{\mathcal{X}}_{L,i}^{g,u}$, and the received signal $\hat{\mathbf{y}}_g^u$ in Eq. (4.29). Now we can calculate the residual error value $\mathcal{R}_{g,i}^u$ by testing the i-th matrix candidate during

[4] If the testing candidate $\mathbf{\Omega}_{g,i}^u = \mathbf{\Omega}_g^u$, the residual error vector $\mathbf{r}_{g,i}^u$ should be all zeros.

the first iteration, yielding

$$\mathcal{R}^u_{g,i} = \|\hat{\mathbf{y}}^u_g - \mathbf{\Omega}^u_{g,i}\vec{\mathcal{X}}^{g,u}_{L,i}\|^2. \tag{4.33}$$

Additionally, Z^1_u residual error values $\{\mathcal{R}^u_{g,1}, \mathcal{R}^u_{g,2}, \cdots, \mathcal{R}^u_{g,i}, \cdots, \mathcal{R}^u_{g,Z^1_u}\}$ are collected during the first iteration and the specific candidate resulting in the minimum residual error is the output of the first iteration, yielding

$$\mathbf{\Omega}^u_{g,best}|_1 = \arg\min_{Z^1_u}\{\mathcal{R}^u_{g,i}\}, \tag{4.34}$$

where $\mathbf{\Omega}^u_{g,best}|_1$ is the most reliable group-equivalent matrix candidate giving the minimum residual error $\{\mathcal{R}^u_{g,min}\}_1$ during the first iteration.

Then the same process is repeated for the further iterations according to the ordered magnitudes shown in Eq. (4.27).

- Step 3:
  During the third step, we make the final decision concerning the best candidate by comparing the minimal residual errors $\{\mathcal{R}^u_{g,min}\}$ from the different iterations, where for example, if the minimal residual error during the first iteration $\{\mathcal{R}^u_{g,min}\}_1$ is the minimum value among the different iterations, then the best candidate matrix of the u-th user is determined as $\mathbf{\Omega}^u_{g,best}|_1$.

Additionally, in order to implement the SD-aided detection presented in Section 4.3.1, the extrinsic LLRs are calculated using the so-called Approx-Log-MAP algorithm formulated in Eq. (4.23). Based on the received signal model of the g-th subcarrier group in Eq. (4.29) and the uplink transmission of U users presented in Section 4.2.1, the received signal $\mathbf{y}_g$ carries $\mathbf{b}_g = [\mathbf{b}_{1,g}\, \mathbf{b}_{2,g}\, \ldots\, \mathbf{b}_{u,g}\, \ldots \mathbf{b}_{U,g}]$ $(u = 1, 2, \ldots, U)$ channel-coded bits, where each user carries $\frac{B}{G}$ channel-coded bits and $b_{u,g}(i)$ $(i = 1, 2, \ldots, \frac{B}{G})$ denotes the channel coded bits of the u-th user in the g-th subcarrier group. Specifically, the extrinsic LLR value of $b_{u,g}(i) \in \mathbf{b}_g$ is expressed by

$$L_{M,e}\left(b_{u,g}(i)\right) = \mathrm{jac}_{n^\alpha \in n^\alpha_{b_{u,g}(i)=1}}\{d\} - \mathrm{jac}_{n^\alpha \in n^\alpha_{b_{u,g}(i)=0}}\{d\}, \tag{4.35}$$

where $n^\alpha_{b_{u,g}(i)=1}$ and $n^\alpha_{b_{u,g}(i)=0}$ denote the index of the CS matrix candidate during the α-th iteration for $\mathbf{\Omega}^u_g$ and $\mathbf{x}^{g,u}_L$ of Eq. (4.29), when the i-th bit is fixed to 1 and 0, respectively. Furthermore, d in Eq. (4.35) denotes the *a posteriori* symbol probability,

which is represented as

$$d = -\frac{\|\hat{\mathbf{y}}_g^u - \mathbf{\Omega}_{g,n^\alpha}^u \vec{\mathcal{X}}_{L,n^\alpha}^{g,u}\|^2}{N_0} + \sum_{j \neq i} b_{u,g}(j) L_{M,a}\left[b_{u,g}(j)\right]. \tag{4.36}$$

4.3.3 Computational Complexity

In this subsection, the complexity orders of the ML, MMSE and the proposed RSS-IMP detectors are analysed based on the size of their search space. As discussed in Section 4.2, for every subcarrier group of each user, we have N_{SI} possible active subcarrier index combinations, N_{AC}^K possible active TA index realisations and $\mathcal{L}^{K \cdot N_t^a}$ possible classical APM symbols combinations.

- *ML Detector:*
  In terms of the detection model $\|\mathbf{y}_g - \mathbf{H}_g \bar{\mathbf{A}} (\mathbf{I}_{SI}^g)_{i_g} (\mathbf{I}_{AC}^g)_{j_g} (\mathbf{x}_L^g)_{l_g}\|^2$ of Eq. (4.11), the detector will have a complexity order of $\mathcal{O}_{ML}\left[(N_{SI} N_{AC}^K \mathcal{L}^{K \cdot N_t^a})^U\right]$, which may be excessive.

- *MMSE Detector:*
  The MMSE detector is presented as a bench-marker of the proposed RSS-IMP detector based on the operation of $\left(\mathbf{H}_g^H \mathbf{H}_g + \frac{1}{\gamma}\mathbf{I}\right)^{-1} \mathbf{H}_g^H \mathbf{y}_g$, where the complexity order is $\mathcal{O}_{MMSE}\left[U \cdot (N_{SI} N_{AC}^K \mathcal{L}^{K \cdot N_t^a})\right]$.

- *RSS-IMP Detector:*
  According to the introduction of the proposed RSS-IMP detector of Section 4.3.2, the computational complexity of the RSS-IMP detector mainly depends on the number of iterations applied. The complexity of the proposed RSS-IMP detector associated with detecting U users in terms of the search space can be expressed as

$$\mathcal{O}_{RSS-IMP}\left[\mathcal{L} \cdot N_t^a \cdot K(N_1 + N_2 + \cdots + N_i)\right], \tag{4.37}$$

  where i $(1 \leq i \leq N_v)$ represents the iteration index and N_i indicates the number of joint realisations, including the active TAs and the active subcarriers of U users during the i-th iteration.

In Table 4.2, the average complexity orders of the ML, the MMSE and of the proposed RSS-IMP detector associated with detecting all users of the CS-(G)SFIM scheme proposed for LS-MU-MIMO are compared upon varying the value of N_t^a, where the bandwidth efficiency is improved upon increasing the values of N_t^a. Specifically, if $N_t^a = 1$, the

N_t^a	Average complexity orders of the ML detection, the MMSE detection and the RSS-IMP detection for detecting all users of the proposed CS-(G)SFIM with $U = 12, N_t = 4, N_r = 64, N_c = 128, N_{cp} = 8, N_v = 16, N_f = 8, K = 2$, 8QAM			
	bits/s/Hz/user	ML $\mathcal{O}(\cdot)$	MMSE $\mathcal{O}(\cdot)$	RSS-IMP (All Iters) $\mathcal{O}(\cdot)$
1	1.88	$(6.6 \times 10^4)^{12}$	7.86×10^5	1.96×10^5
2	2.59	$(4.2 \times 10^6)^{12}$	5.03×10^7	3.93×10^5
3	3.29	$(2.7 \times 10^8)^{12}$	4.03×10^8	5.88×10^5
4	3.53	$(1.1 \times 10^9)^{12}$	2.01×10^8	4.92×10^5

Table 4.2: Comparison between average complexity orders of three detectors for the proposed CS-(G)SFIM system with $U = 12, N_t = 4, N_r = 64, N_c = 128, N_{cp} = 8, N_v = 16, N_f = 8, K = 2$, 8QAM

system becomes the proposed CS-SFIM scheme and if $N_t^a > 1$, the system become the proposed generalised scheme. More specifically, in the scenario of $N_t^a = N_t = 4$ shown in the table, the system becomes a special case of the proposed CS-(G)SFIM scheme, where all TAs are used for transmission and only frequency-domain IM is applied. We explore the full search[5] based operation of the proposed RSS-IMP detector, which has the worst-case complexity orders and we have $(N_1 + N_2 + \cdots + N_i) = U \cdot N_{SI} \cdot N_{AC}^K$ in terms of Eq. (4.37). Note that we do not consider the complexity order of the LMMSE operations in the MMSE detector and in the proposed RSS-IMP detector of Table 4.2, since it is negligible compared to the excessive complexity of the ML detector. The MMSE and the RSS-IMP detector impose much lower complexities compared to the ML detector as shown in Table 4.2. Specifically, according to Table 4.2, the proposed RSS-IMP detector is capable of significantly reducing the complexity compared to the MMSE detector. Additionally, the average complexity orders of the proposed RSS-IMP

[5] "Full search" means that all possible joint realisations of active TAs and active subcarriers are explored, which is the worst-case complexity of the RSS-IMP detector and it is only used as a complexity bench-marker here. Indeed, it is unnecessary to explore full search in practice for achieving an attractive trade-off between the performance and the complexity order.

detector increase more slowly with the improved bandwidth efficiency instead of the exponential trend of the MMSE detector.

4.4 Performance Results and Comparisons

In this section, we present our theoretical as well as simulation results characterising the proposed CS-(G)SFIM system in LS-MU-MIMO uplink scenarios using both the ML detector of Section 4.3.1 and the proposed RSS-IMP detector of Section 4.3.2 and compare them to the conventional MU-MIMO-OFDM systems, to the MU CS-aided multi-dimensional IM schemes of Section 3.2 and to the MU CS-aided frequency-domain IM schemes of Section 2.3. Specifically, we also characterise the maximum achievable rate of the proposed system with the aid of EXIT charts. Furthermore, the coded BER performance of the proposed system is presented, demonstrating that a near-capacity performance is achieved. The simulation parameters are summarised in Table 4.3.

	N_c	N_{cp}	$\mathcal{L}$-PSK/QAM	N_v	N_f	K	U	N_r	N_t	N_t^a
Scheme 1	128	8	4QAM	–	–	–	2	12	1	1
Scheme 2	128	8	4QAM	–	–	–	2	24	1	1
Scheme 3	128	8	8QAM	16	8	2	2	12	4	1
Scheme 4	128	8	8QAM	16	8	2	2	24	4	1
Scheme 5	128	8	BPSK	16	8	2	2	12	4	3
Scheme 6	128	8	BPSK	16	8	2	2	24	4	3
Scheme 7	128	8	8QAM	16	8	2	12	64	4	1
Scheme 8	128	8	8QAM	16	8	2	12	128	4	1
Scheme 9	128	8	BPSK	16	8	2	12	64	4	3
Scheme 10	128	8	BPSK	16	8	2	12	128	4	3
Scheme 11	128	8	4QAM	–	–	–	4	32	1	1
Scheme 12	128	8	8QAM	16	8	2	4	32	4	1
Scheme 13	128	8	BPSK	16	8	2	4	32	4	3
Scheme 14	128	8	8QAM	16	8	2	2	12	4	2
Scheme 15	128	8	32QAM	16	8	4	2	12	4	1
Scheme 16	128	8	8QAM	16	8	2	12	64	4	2
Scheme 17	128	8	32QAM	16	8	4	12	64	4	1
Scheme 18	128	8	8QAM	16	8	2	12	varying	4	1
Scheme 19	128	8	BPSK	16	8	2	12	varying	4	3
Scheme 20	128	8	32QAM	16	8	2	2	12	1	1
Scheme 21	128	8	16QAM	16	8	2	2	12	4	1
Scheme 22	128	8	4QAM	16	8	2	2	12	4	2
Scheme 23	128	8	16QAM	20	8	2	3	36	8	1
Scheme 24	128	8	32QAM	24	8	2	3	36	8	1
Scheme 25	128	8	128QAM	20	8	2	3	36	1	1

Table 4.3: System parameters in simulations of Chapter 4.

4.4.1 Uncoded Performances

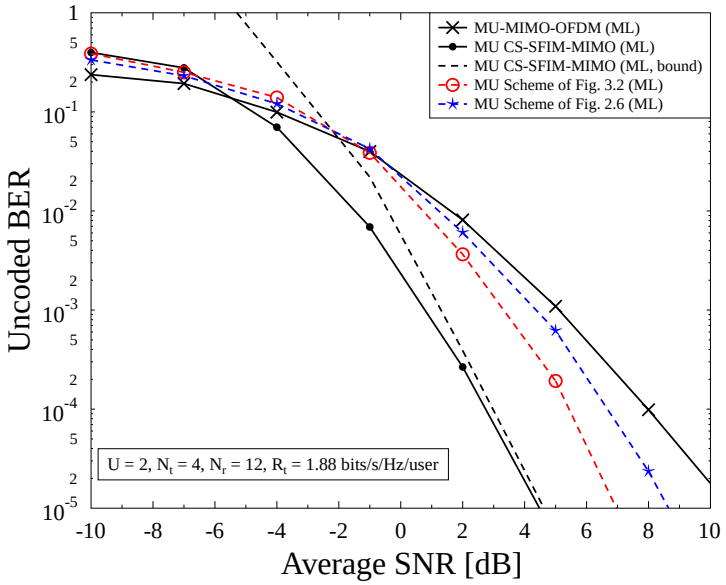

Figure 4.4: Comparison between uncoded BER performances of **Scheme 1**, **Scheme 3** of Fig. 4.2, **Scheme 20** of Fig. 2.6, and **Scheme 21** of Fig. 3.2 shown in Table 4.3 using the ML detector, at the same transmission rate of $R_t = 1.88$ bits/s/Hz/user.

In Fig. 4.4, we compare the uncoded BER performances of **Scheme 1**, **Scheme 3** of Fig. 4.2, **Scheme 20**[6] of Fig. 2.6, and **Scheme 21**[7] of Fig. 3.2 associated with the parameters of Table 4.3 at the same transmission rate of $R_t = 1.88$ bits/s/Hz/user. Observe in Fig. 4.4 that the MU CS-SFIM-MIMO system using the ML detector outperforms the conventional MU-MIMO-OFDM system by about 6 dB at the BER value of 10^{-5} at the same transmission rate. Specifically, the upper bound performance of the proposed system characterised by Eq. (4.19) is presented in Fig. 4.4, where it is observed that the upper bound is tight at moderate-to-high SNR values. In particular, we apply **Scheme 20** of Fig. 2.6 and **Scheme 21** of Fig. 3.2 in Fig. 4.4 as benchmarks. Explicitly, the proposed MU CS-SFIM-MIMO system achieves about 2.5 dB and 4 dB better performances than **Scheme 21** of Fig. 3.2 and **Scheme 20** of Fig. 2.6, respectively.

[6] **Scheme 20** is applied here to represent the CS-aided frequency-domain IM system of Fig. 2.6 and is a special instantiation of the scheme designed in Section 2.3

[7] **Scheme 21** is a special instantiation of the CS-aided multi-dimensional IM scheme of Fig. 3.2, where the same activated TAs are applied to each subcarrier group.

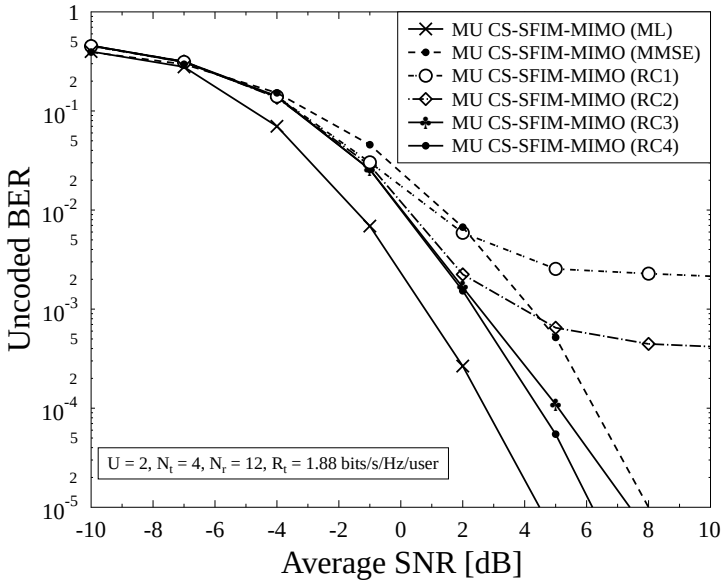

Figure 4.5: Comparison between uncoded BER performances of **Scheme 3** of Fig. 4.2 shown in Table 4.3 using both the MMSE detector and the proposed RSS-IMP detector with $I = 1$ to 4 iterations applied, at the same transmission rate of $R_t = 1.88$ bits/s/Hz/user.

Additionally, in Fig. 4.5, we portray the uncoded BER performances of the proposed system in conjunction with the parameters of **Scheme 3** of Fig. 4.2, using the reduced-complexity RSS-IMP detector of Section 4.3.2 by invoking one to four iterations, where we use the acronyms of RC1, RC2, RC3 and RC4 in Fig. 4.5 to denote one to four iterations. It can be observed that the RSS-IMP detector has the potential of approaching the optimal performance of the proposed system using the ML detector. More specifically, it is also shown in Fig. 4.5 that the RSS-IMP detector using RC3 or RC4 is capable of providing a better performance than the MMSE detector, even though the average complexity order $\mathcal{O}_{RSS-IMP}(1.6 \times 10^4)$ of the RSS-IMP detector using RC4 is much lower than the complexity $\mathcal{O}_{MMSE}(1.3 \times 10^5)$ of the MMSE detector.

In Fig. 4.6, we compare the uncoded BER performances of **Scheme 2** using the ML detector, of **Scheme 4** using both the ML detector, as well as the MMSE detector and the RSS-IMP detector associated with $I = 1$ to 4 iterations, while serving the same number of $U = 2$ users, employing the same number of $N_r = 24$ RAs and the same bandwidth efficiency of $R_t = 1.88$ bits/s/Hz/user. Observe in Fig. 4.6 that similar conclusions to those inferred from Fig. 4.4 and Fig. 4.5 can be obtained. More explicitly, **Scheme 4** of Table 4.3 using the ML detector imposes about 5.7 dB better BER performance than **Scheme 2** using the ML detector at the BER target of 10^{-5}, but the detection

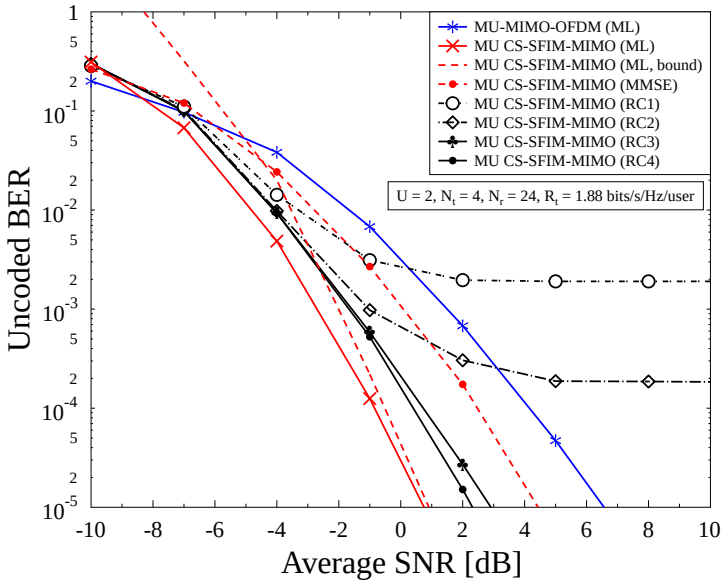

Figure 4.6: Comparison between uncoded BER performances of **Scheme 2** using ML detector, **Scheme 4** using the ML detector, MMSE detector and the proposed RSS-IMP detector with $I = 1$ to 4 iterations applied, while supporting the same number of $U = 2$ users, the same number of RAs $N_r = 24$ and the same rate of $R_t = 1.88$ bits/s/Hz/user.

complexity of **Scheme 4** of Table 4.3 using the ML detector is about $\mathcal{O}_{ML}(4.3 \times 10^9)$, which is much higher than the complexity order $\mathcal{O}(1.3 \times 10^2)$ of the conventional MU-OFDM-MIMO scheme. For the sake of reducing the excessive complexity of the ML detector, the RSS-IMP detector is proposed. As shown in Fig. 4.6, **Scheme 4** of Table 4.3 using the RSS-IMP detector associated with $I = 4$ iterations (RC4) is capable of achieving about 4.3 dB and 2.3 dB better BER performances than the conventional MU-OFDM-MIMO scheme and than **Scheme 4** using the MMSE detector at the BER target of 10^{-5}, respectively. This has to be viewed bearing in mind that the RSS-IMP detector (RC4) has a detection complexity order of $\mathcal{O}_{RSS-IMP}(1.64 \times 10^4)$, which is lower than the MMSE detector's complexity order of $\mathcal{O}_{MMSE}(1.3 \times 10^5)$. Specifically, it is also observed in Fig. 4.4 - 4.6 that, as expected, both our analysis and the simulation results predict that the BER performance improves, as the number of RAs N_r at the BS is increased.

In Fig. 4.7, we compare the uncoded BER performances of **Scheme 1**, **Scheme 5** of Fig. 4.2, **Scheme 20** of Fig. 2.6, and **Scheme 22**[8] of Fig. 3.2, where the number of

[8] **Scheme 22** is the generalised scheme of **Scheme 21**, which is also a special is a special instantiation of the scheme designed in Section 3.2, whilst the same activated TAs being applied to each subcarrier group.

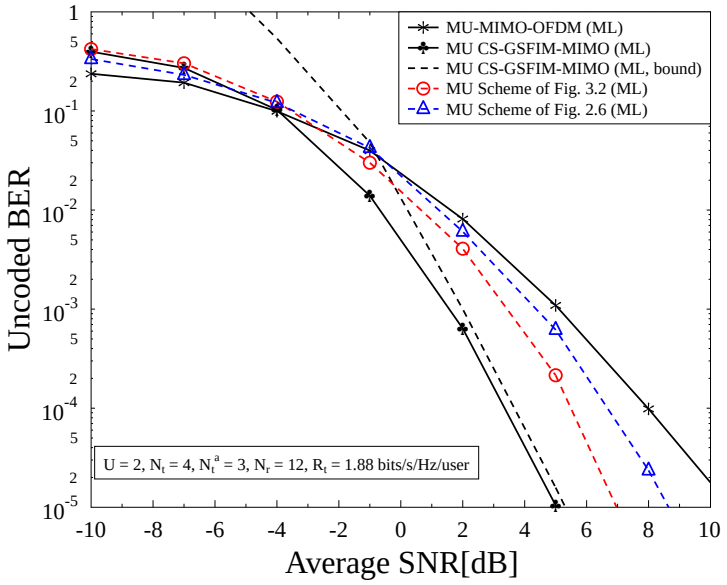

Figure 4.7: Comparison between uncoded BER performances of **Scheme 1**, **Scheme 5** of Fig. 4.2, **Scheme 20** of Fig. 2.6, and **Scheme 22** of Fig. 3.2 shown in Table 4.3 using ML detectors, at the same rate of $R_t = 1.88$ bits/s/Hz/user.

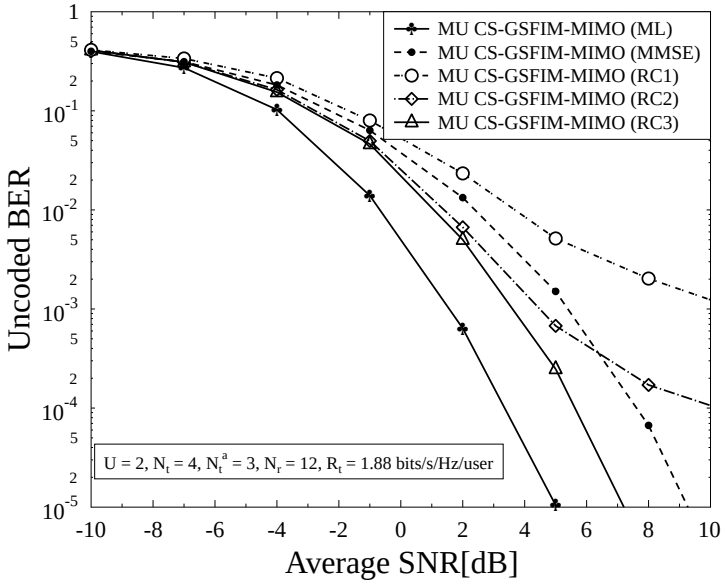

Figure 4.8: Comparison between uncoded BER performances of **Scheme 5** shown in Table 4.3 using both the MMSE detector and the proposed RSS-IMP detector with $I = 1$ to 3 iterations applied, at the same bandwidth efficiency of $R_t = 1.88$ bits/s/Hz/user.

active TAs N_t^a is generalised in **Scheme 5**, while supporting the same number of $U = 2$ users, employing the same number of $N_r = 12$ RAs and the same rate of $R_t = 1.88$ bits/s/Hz/user. Observe in Fig. 4.7 that the MU CS-GSFIM-MIMO system using the ML detector outperforms the conventional MU-MIMO-OFDM system by about 5.5 dB at the BER value of 10^{-5} and at the same transmission rate. Specifically, the upper bound performance of the proposed system obtained by Eq. (4.19) is presented in Fig. 4.7, where it is observed that the upper bound is tight at moderate-to-high SNR values. Furthermore, **Scheme 5** of Table 4.3 attains about 2 dB and 3.5 dB SNR-gains over **Scheme 22** of Fig. 3.2 and **Scheme 20** of Fig. 2.6, respectively, again at the BER value of 10^{-5}.

Additionally, in Fig. 4.8, we portray the uncoded BER performances of the proposed system in conjunction with the parameters of **Scheme 5** using the reduced-complexity RSS-IMP detector by using one to three iterations. More specifically, it is also shown in Fig. 4.8 that the RSS-IMP detector has the potential of approaching the optimal performance of the proposed generalised system using the ML detector. Observe furthermore that the RSS-IMP detector using only 3 iterations is capable of providing a better performance than the MMSE detector, even though the average complexity order $\mathcal{O}_{RSS-IMP}(8.2 \times 10^3)$ of the RSS-IMP detector using $I = 3$ iterations is much lower than the complexity $\mathcal{O}_{MMSE}(1.3 \times 10^5)$ of the MMSE detector.

In Fig. 4.9, we portray the uncoded BER performances of **Scheme 2** using the ML detector, as well as **Scheme 6** using both the ML detector, as well as the MMSE detector and the proposed RSS-IMP detector with $I = 1$ to 3 iterations applied, while supporting the same number of $U = 2$ users, employing the same number of $N_r = 24$ RAs at the same bandwidth efficiency of $R_t = 1.88$ bits/s/Hz/user. Observe in Figs. 4.7 - 4.9 that the upper bound is tight at moderate-to-high SNR values as confirmed by the simulation result. Both the analytical and the simulation results demonstrate that the BER performance is improved upon increasing the number of RAs as a benefit of the increased receive diversity gain. More explicitly, **Scheme 6** using the ML detector attains 5.2 dB SNR-gain over the conventional MU-OFDM-MIMO scheme at the cost of $\mathcal{O}_{ML}(4.3 \times 10^9)$ detection complexity, at the BER value of 10^{-5}. According to Fig. 4.9, the reduced-complexity RSS-IMP multi-user detector of Section 4.3.2 relying on as few as $I = 3$ iterations is capable of achieving 3.8 dB and 1.6 dB better BER performances than the conventional MU-OFDM-MIMO scheme and **Scheme 6** using the MMSE detector at the BER value of 10^{-5}, respectively. This is achieved at the cost of $\mathcal{O}_{RSS-IMP}(9.1 \times 10^3)$ detection complexity, where the complexity is much lower than $\mathcal{O}_{MMSE}(1.3 \times 10^5)$ of the MMSE detector and $\mathcal{O}_{ML}(4.3 \times 10^9)$ of the ML detector.

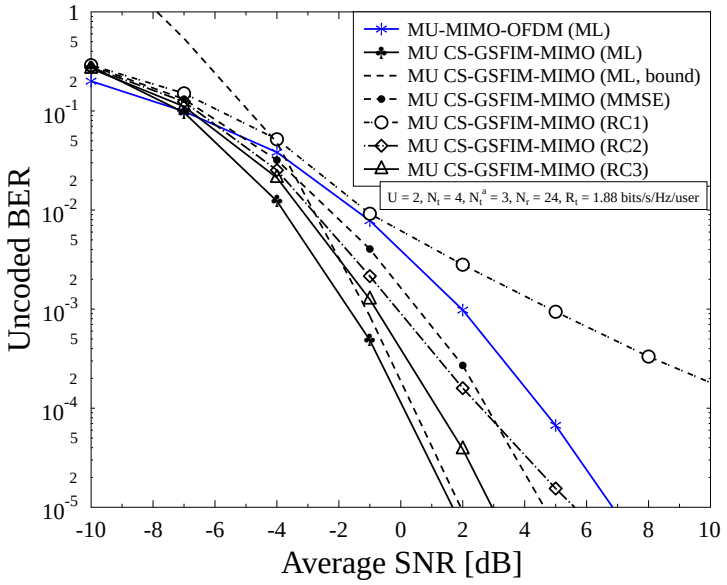

Figure 4.9: Comparison between uncoded BER performances of **Scheme 2** using the ML detector, **Scheme 6** using the ML detector, the MMSE detector and the proposed RSS-IMP detector with $I = 1$ to 3 iterations applied, while supporting the same number of $U = 2$ users, the same number of RAs $N_r = 24$ and the same transmission rate of $R_t = 1.88$ bits/s/Hz/user.

In Fig. 4.10, we compare the uncoded BER performances of **Scheme 23** of Fig. 4.2, **Scheme 24**[9], and **Scheme 25**[10] of Fig. 2.6 associated with the parameters listed in Table 4.3 at the same transmission rate of $R_t = 2.5$ bits/s/Hz/user. It is shown in Fig. 4.10 that the proposed CS-SFIM scheme (**Scheme 23**) using the ML detector achieves about 3.2 dB SNR-gain over **Scheme 24** of Fig. 3.2 and far outperforms **Scheme 25** of Fig. 2.6 at the BER value of 10^{-5}. Specifically, the RSS-IMP detector associated with $I = 4$ iterations of **Scheme 23** of Fig. 4.2 imposes better performances than both **Scheme 24** of Fig. 3.2 and **Scheme 25** of Fig. 2.6 as well, at a cost of $\mathcal{O}_{RSS-IMP}(6.9 \times 10^5)$ detection complexity, which is much lower than the $\mathcal{O}_{ML}(9.2 \times 10^{18})$ complexity of the ML detector.

Then in Fig. 4.11 and Fig. 4.12, we compare the uncoded BER performance of the proposed RSS-IMP detector to that of the MMSE detector incorporated in **Scheme 7**, **Scheme 8**, **Scheme 9** and **Scheme 10**, where the MMSE detector is used as the benchmarker, where we have $U = 12$ uplink users communicating with the aid of $N_r = 64$

[9]**Scheme 24** is a special instantiation of the CS-aided multi-dimensional IM scheme of Fig. 3.2 designed in Chapter 3, where the same activated TAs are applied for each subcarrier group.

[10]**Scheme 25** is applied here to represent the CS-aided frequency-domain IM system of Fig. 2.6 and is a special instantiation of the scheme designed in Chapter 2.

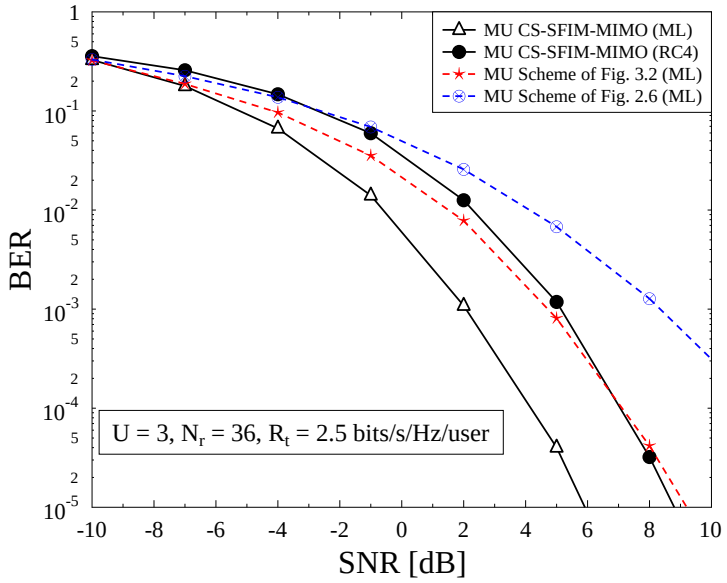

Figure 4.10: Comparison between the uncoded BER performances of **Scheme 23** of Fig. 4.2 using both the ML detector and the proposed RSS-IMP detector with $I = 4$ iterations applied, of **Scheme 24** of Fig. 3.2 using the ML detector, and of **Scheme 25** of Fig. 2.6 using the ML detector, while supporting the same number of $U = 3$ users, the same number of RAs $N_r = 36$ and the same transmission rate of $R_t = 2.5$ bits/s/Hz/user.

RAs and $N_r = 128$ RAs, at the same transmission rate of $R_t = 1.88$ bits/s/Hz/user. Note that the optimal ML detector of Section 4.3.1 has an excessive complexity for this LS-MU scenario. Hence, we are unable to include the performance of the ML detector in both Fig. 4.11 and Fig. 4.12. It can be observed both in Fig. 4.11 and Fig. 4.12 that the performance of the RSS-IMP detector is improved upon increasing the number of RAs due to the increased receive diversity and only a few iterations are required for achieving a better performance than that of the MMSE detector. More explicitly, in Fig. 4.11, the RSS-IMP detector using $I = 4$ iterations achieves about 3 dB and 3.43 dB SNR-gains over the MMSE detector relying on 64 RAs and 128 RAs, respectively, at the BER value of 10^{-5}. Furthermore, in Fig. 4.12, the RSS-IMP detector using $I = 3$ iterations achieves about 2 dB and 2.45 dB SNR-gains over the MMSE detector when communicating with 64 RAs and 128 RAs, respectively, at the BER value of 10^{-5}. In Table 4.2, we compare the complexity orders of the RSS-IMP detector using exhaustive full-search based iterations and the MMSE detector, where the RSS-IMP detector using all iterations has the best performance at the cost of the highest complexity order. Hence the RSS-IMP detector using $I = 3$ or 4 iterations presented in Fig. 4.11 and Fig. 4.12 has much lower complexity orders than that of the MMSE detector. It can be concluded

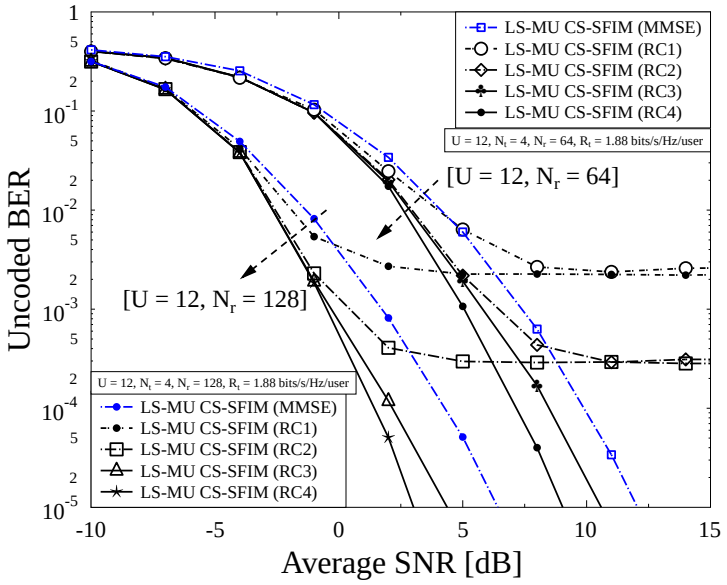

Figure 4.11: Comparison between the uncoded BER performances of **Scheme 7** and **Scheme 8** for LS-MIMO uplink scenario using both the MMSE detector and the proposed RSS-IMP detector with $I = 1$ to 4 iterations applied, at the same transmission rate of $R_t = 1.88$ bits/s/Hz/user.

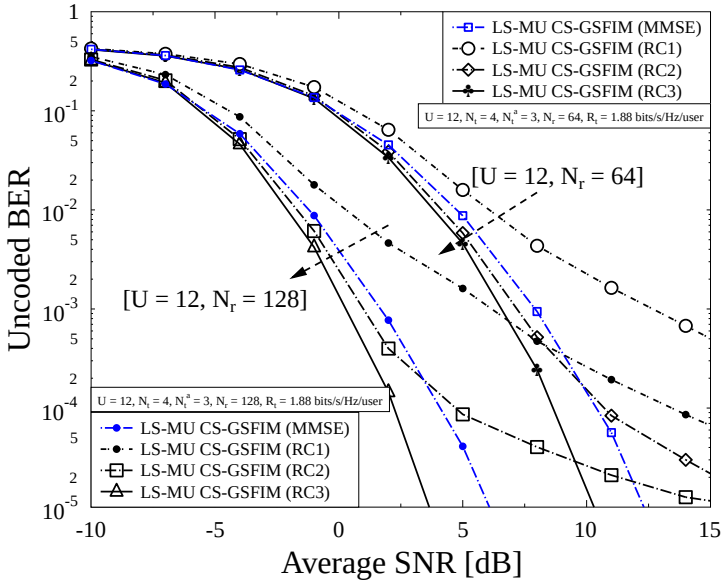

Figure 4.12: Comparison between the uncoded BER performances of **Scheme 9** and **Scheme 10** for LS-MIMO uplink scenario using both the MMSE detector and the proposed RSS-IMP detector with $I = 1$ to 3 iterations applied, at the same transmission rate of $R_t = 1.88$ bits/s/Hz/user.

that the RSS-IMP detector attains a near-optimal performance at a significantly lower complexity, which makes the proposed CS-(G)SFIM system attractive in LS-MU-MIMO scenarios.

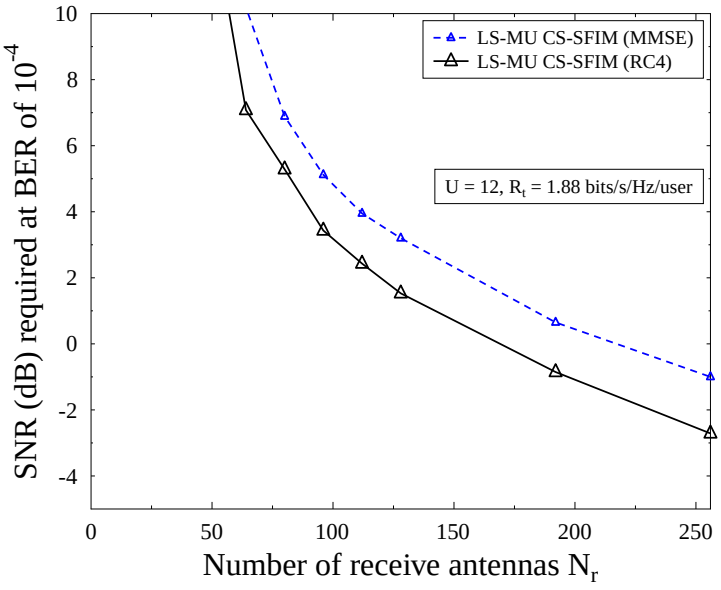

Figure 4.13: Comparison of the SNRs required at the BER target of 10^{-4} with varying values of the RAs at the BS for **Scheme 18** using both the MMSE detector and the RSS-IMP detector with $I = 4$ iterations applied.

In Fig. 4.13 and Fig. 4.14, we compare the SNRs required at the specific BER target of 10^{-4} for **Scheme 18** of Table 4.3 using both the MMSE detector and the RSS-IMP detector associated with $I = 4$ iterations, as well as for **Scheme 19** using both the MMSE detector and the RSS-IMP detector associated with $I = 3$ iterations, where **Scheme 19** is the generalised version of **Scheme 18**, while supporting the same number of $U = 12$ users, and the same transmission rate of $R_t = 1.88$ bits/s/Hz/user as well as a varying number of RAs at the BS. Note that the optimal ML detector of Section 4.3.1 has an excessive complexity for the LS-MU scenario. Hence, we are unable to evaluate the performance of the ML detector in both Fig. 4.13 and Fig. 4.14. Observe from Fig. 4.13 and Fig. 4.14 that the SNRs required by all these schemes are reduced upon increasing the number of RAs as a benefit of the improved receive diversity order. More specifically, according to Fig. 4.13 and Fig. 4.14, if the condition of $(U \cdot N_t \geq N_r)$ is satisfied, we can conclude that the proposed system using the RSS-IMP detector is capable of outperforming the proposed systems using the MMSE detector.

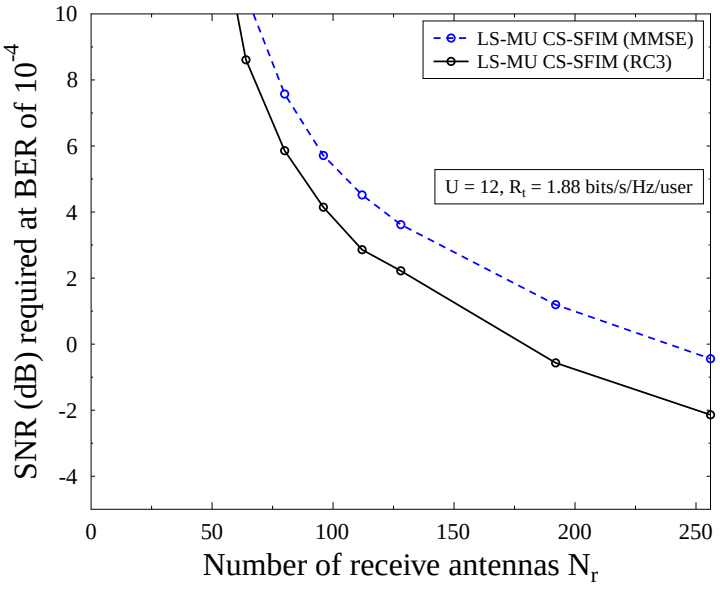

Figure 4.14: Comparison of the SNRs required at the BER target of 10^{-4} with varying values of the RAs at the BS for **Scheme 19** using both the MMSE detector and the RSS-IMP detector with $I = 3$ iterations applied.

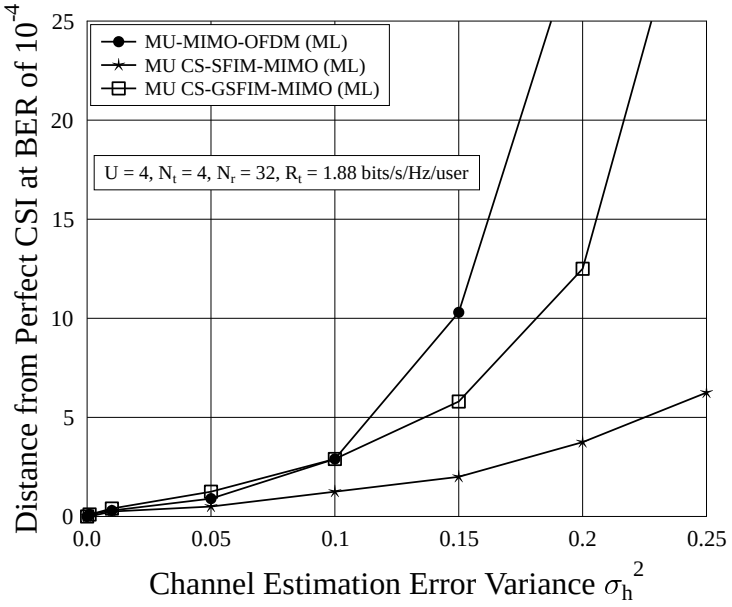

Figure 4.15: SNR-penalty wrt the perfect CSI scenario at the BER target of 10^{-4}, where **Scheme 11**, **Scheme 12** and **Scheme 13** shown in Table 4.3 are employed and we have varying values of channel estimation error variance σ_h^2.

In Fig. 4.15, the performances of the proposed systems in the presence of channel estimation errors are characterised, where the channel estimation errors at the receiver are assumed to obey the distribution of $\mathcal{CN}(0, \sigma_h^2)$ [224]. Three schemes (**Scheme 11**, **Scheme 12**, **Scheme 13**) are investigated in Fig. 4.15, while supporting the same number of $U = 4$ users, employing the same number of $N_r = 32$ RAs, at the same transmission rate of $R_t = 1.88$ bits/s/Hz/user and at varying values of channel estimation error variance δ_h^2. In Fig. 4.15, the SNR-distances between the SNR values of these three schemes having perfect CSI and the SNR values of these schemes relying on realistic imperfect CSI re compared, at the specific target BER value of 10^{-4}. Observe from Fig. 4.15 that the proposed CS-(G)SFIM systems are more robust to channel estimation errors than the classical MU-MIMO-OFDM scheme.

4.4.2 Maximum Achievable Rates

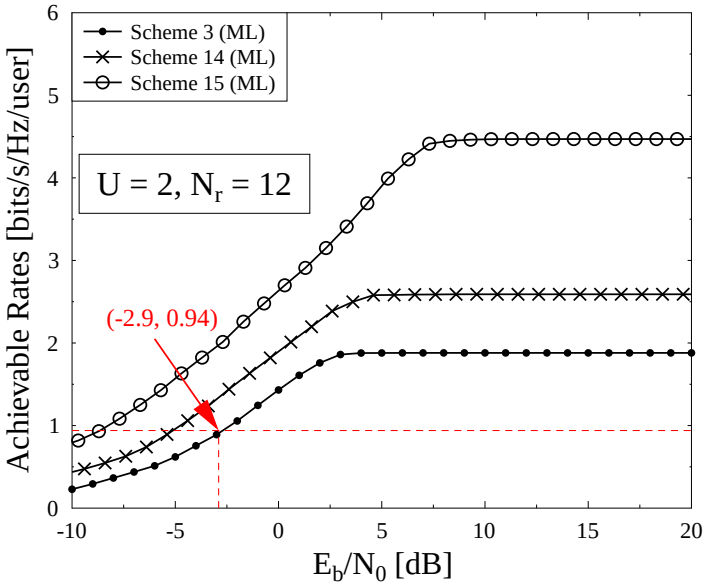

Figure 4.16: Maximum achievable rates of **Scheme 3**, **Scheme 14** and **Scheme 15** applying the ML detector.

In Fig. 4.16 and Fig. 4.17, we analyse the achievable rates per user for different E_b/N_0 values of the CS-(G)SFIM in LS-MU-MIMO uplink scenarios in conjunction with different system parameters by exploring the semi-analytical EXIT chart tool, where the maximum achievable rate of a system is equal to the area under the EXIT curve of the inner soft decoder [110, 199]. Explicitly, in Fig. 4.16, we portray the maximum achievable rate of **Scheme 3**, **Scheme 14** and **Scheme 15** of Table 4.3 applying the ML

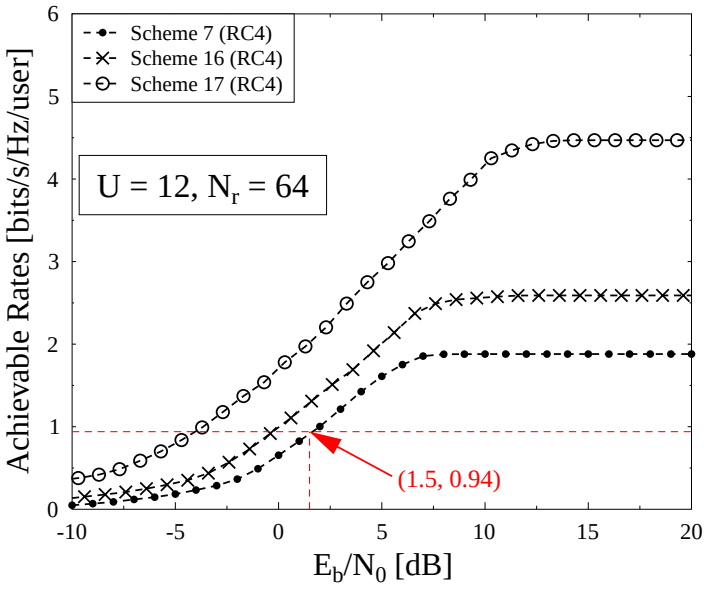

Figure 4.17: Maximum achievable rates of **Scheme 7**, **Scheme 16** and **Scheme 17** applying the RSS-IMP detector with $I = 4$ iterations involved.

detector, while having $U = 2$ users and $N_r = 12$ RAs. Furthermore, in Fig. 4.17 we also investigate the maximum achievable rate of **Scheme 7**, **Scheme 16** and **Scheme 17** applying the RSS-IMP detector of Section 4.3.2 associated with $I = 4$ iterations for efficiently reducing the complexity, while supporting $U = 12$ users and $N_r = 64$ RAs. Specifically, the proposed system's maximum achievable rate can be improved by increasing the number of active TAs N_t^a as well as by increasing the number of active subcarriers K or by increasing the size of the APM symbol alphabet. It is also shown in Fig. 4.16 and Fig. 4.17 that the proposed CS-GSFIM scheme is capable of achieving a higher rate than the CS-SFIM scheme advocated. In particular, when using a half-rate RSC channel encoder, the maximum achievable rate becomes 0.94 bits/s/Hz/user for the proposed coded **Scheme 7** applying both the ML detector and the RSS-IMP detector ($I = 4$ iterations) at $E_b/N_0 = -2.9$ dB and $E_b/N_0 = 1.5$ dB, respectively, as indicated in both Fig. 4.16 and Fig. 4.17.

4.4.3 Coded Performances

In Fig. 4.18 and Fig. 4.19, we characterise the BER performances of both the half-rate RSC-coded MU CS-(G)SFIM-MIMO scheme (**Scheme 3**) applying the ML detector

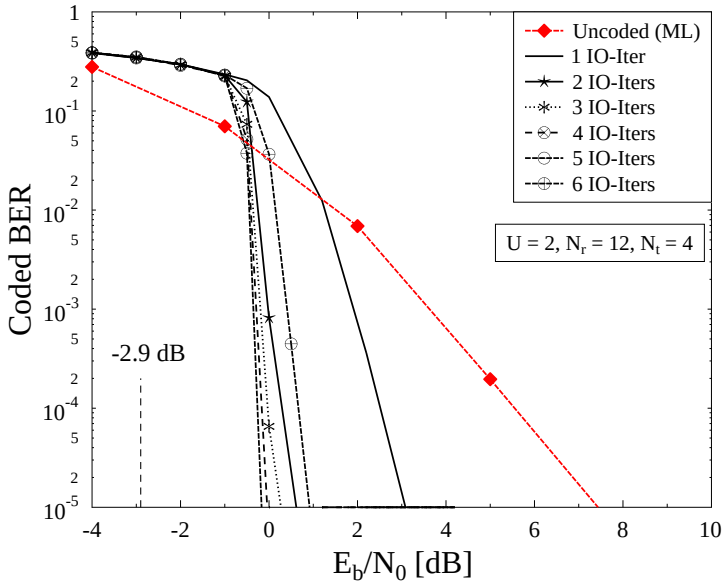

Figure 4.18: The average BER performance of the iteratively detected half-rate RSC-coded system shown in Fig. 4.2 based on the detection scheme of Eq. (4.23) in conjunction with the parameters of **Scheme 3** shown in Table 4.3 and an interleaver depth of 300,000 bits while using $I_{IO} = 1$ to 6 iterations.

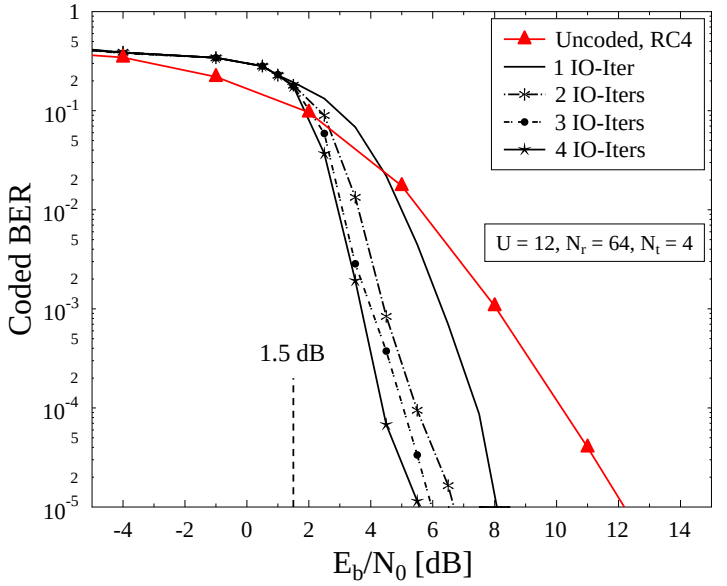

Figure 4.19: The average BER performance of the iteratively detected half-rate RSC-coded system shown in Fig. 4.2 based on the detection scheme of Eq. (4.35) applying $I = 4$ iterations in conjunction with the parameters of **Scheme 7** shown in Table 4.3 and an interleaver depth of 300,000 bits while using $I_{IO} = 1$ to 4 iterations.

and the half-rate RSC-coded CS-(G)SFIM scheme (**Scheme 7**) applying the reduced-complexity RSS-IMP detector ($I = 4$ iterations). An interleaver depth of $300,000$ bits is applied for each user, where $I_{IO} = 1$ to 6 inner-outer(IO) iterations and $I_{IO} = 1$ to 4 iterations are applied in Fig. 4.18 and Fig. 4.19, respectively. Observe in Fig. 4.18 and Fig. 4.19 that the coded BER performances approach the maximum achievable rate limits at both $E_b/N_0 = -2.9$ dB and $E_b/N_0 = 1.5$ dB with the aid of the IO iterative detection structure shown in Fig. 4.2. Explicitly, the performances of the coded systems approach the maximum achievable rate limit in both Fig. 4.18 and Fig. 4.19 upon increasing the number of IO iterations, where the performances of the coded system ($I_{IO} = 6$ IO iterations) using the ML detector in Fig. 4.18 and of the coded system ($I_{IO} = 4$ IO iterations) using the reduced-complexity detector in Fig. 4.19 are about 2.8 dB and 4 dB away from the maximum achievable rate limits at the BER value of 10^{-5}, respectively.

4.5 Chapter Conclusions

A novel CS-(G)SFIM system relying on flexible index separation strategy has been proposed for LS-MU-MIMO uplink communication. In contrast to the joint space-frequency indexing strategy of [157], the TAs and the subcarriers have been indexed separately for the case of supporting a high design flexibility. Additionally, in order to attain improved diversity gains in contrast to Chapter 3, different TA activation patterns have been employed for different transmitted symbols instead of fixing the active TAs for the whole OFDM frame or for each subcarrier group. Due to the excessive complexity of the ML detector, a reduced-complexity RSS-IMP detector based on both the classic greedy principle and on the iterative detection philosophy has been proposed, where the RSS-IMP detector has struck an attractive BER vs complexity trade-off as shown in Table 4.4.

More explicitly, in Table 4.4 we conclude with a brief summary of Fig. 4.4 and Fig. 4.5, where we show that the system proposed in this chapter achieves better BER performances than the multi-dimensional **Scheme 21** of Table 4.3 using the same activated TAs for each subcarrier group as detailed in Chapter 3. Furthermore, the scheme proposed in this chapter also outperforms the CS-OFDM-IM **Scheme 20**, which is a special instantiation of the scheme designed in Chapter 2, and the conventional MU-OFDM-MIMO **Scheme 1** of Table 4.3. Specifically, the proposed RSS-IMP detector associated with $I = 4$ iterations attained a better performance than **Scheme 21**, **Scheme 20** and **Scheme 1**, despite its significantly lower complexity order. The low-complexity

	Fig. 4.4 and Fig. 4.5					
Scenario	$U = 2$, $R_t = 1.88$ bits/s/Hz/user					
Schemes	Scheme 3 (ML)	Scheme 3 (RC4)	Scheme 3 (MMSE)	Scheme 20 (Chapter 2)	Scheme 21 (Chapter 3)	Scheme 1
SNR (at BER=10^{-5})	4.5 dB	6.2 dB	8 dB	8.5 dB	7 dB	10.5 dB
Complexity Order	$\mathcal{O}(4.3 \times 10^9)$	$\mathcal{O}(1.64 \times 10^4)$	$\mathcal{O}(1.3 \times 10^5)$	$\mathcal{O}(4.3 \times 10^9)$	$\mathcal{O}(4.3 \times 10^9)$	$\mathcal{O}(1.3 \times 10^2)$
	Fig. 4.11					
Scenario	Large-scale, $U = 12$, $N_r = 64/128$, $R_t = 1.88$ bits/s/Hz/user					
Schemes	Scheme 7 (RC4)	Scheme 7 (RC3)	Scheme 7 (MMSE)	Scheme 8 (RC4)	Scheme 8 (RC3)	Scheme 8 (MMSE)
SNR (at BER=10^{-5})	9.1 dB	10.6 dB	12.1 dB	3.1 dB	4.4 dB	6.5 dB
Complexity Order	$\mathcal{O}(9.8 \times 10^4)$	$\mathcal{O}(7.4 \times 10^4)$	$\mathcal{O}(7.86 \times 10^5)$	$\mathcal{O}(1.1 \times 10^5)$	$\mathcal{O}(8.6 \times 10^4)$	$\mathcal{O}(7.86 \times 10^5)$
	Fig. 4.16			**Fig. 4.17**		
Scenario	$U = 2$, $N_r = 12$			Large-scale, $U = 12$, $N_r = 64$		
R_t (bits/s/Hz/user)	1.88	2.59	4.47	1.88	2.59	4.47
Schemes	Scheme 3 (ML)	Scheme 14 (ML)	Scheme 15 (ML)	Scheme 7 (RC4)	Scheme 16 (RC4)	Scheme 17 (RC4)
E_b/N_0 (at achievable rate)	4 dB	6 dB	8.5 dB	8.8 dB	11.5 dB	13.5 dB
Complexity Order	$\mathcal{O}(4.3 \times 10^9)$	$\mathcal{O}(1.8 \times 10^{13})$	$\mathcal{O}(7.6 \times 10^{22})$	$\mathcal{O}(9.8 \times 10^4)$	$\mathcal{O}(1.2 \times 10^6)$	$\mathcal{O}(5.1 \times 10^7)$

Table 4.4: Summary of the multi-dimensional IM scheme of Fig. 3.2 for LS-MU-MIMO uplink scenarios, employing the system parameters of Table 4.3.

design of the RSS-IMP detector has made the CS-(G)SFIM system an attractive one for LS-MU scenarios. Our simulation results characterising **Scheme 1**-**Scheme 25** of Table 4.3 have demonstrated that the RSS-IMP detector using the most appropriate number of iterations in LS-MU scenarios outperforms both the classical MU-OFDM-MIMO system using the ML detector and the CS-(G)SFIM system using the MMSE detector at the same transmission rate. In particular, observe from the brief summary of Fig. 4.11 provided in Table 4.4 that the RSS-IMP detector using as few as $I = 3$ or 4 iterations is capable of providing a better performance than the MMSE detector, despite the lower complexity of the former. Additionally, we can conclude from the summary of Fig. 4.16 and Fig. 4.17 seen in Table 4.4 that the proposed system strikes a flexible trade-off among the transmission rate, BER performance and the complexity by beneficially configuring the different components for satisfying the designer's specific requirements.

Chapter 5

Conclusions and Future Research

In this concluding chapter, we will provide our overall summary and conclusions in Section 5.1, which is then followed by design guidelines in Section 5.2. Then several research topics concerning potential future studies will be presented in Section 5.3.

5.1 Summary and Conclusions

In this thesis, we have provided detailed CS-aided transceiver designs for enhancing BER vs throughput trade-off. More specifically, we proposed a novel CS-aided frequency-domain IM scheme (CS-OFDM-STSK-IM) in Chapter 2. In order to attain both an improved BER as well as throughput, a CS-aided multi-dimensional IM system was then proposed in Chapter 3 by amalgamating a group-level spatial-domain IM technique with the CS-OFDM-STSK-IM system of Chapter 2. Furthermore, for the sake of improving both the design flexibility and the BER performance, in Chapter 4 an enhanced multi-dimensional IM technique was proposed for large-scale multi-user scenarios, where in contrast to Chapter 3 different activated TAs are applied to different transmitted APM symbols instead of fixing the same TAs for each subcarrier group. The summaries of Chapter 1 - Chapter 4 are provided below:

- **Chapter 1:** Chapter 1 constitutes the background of our research throughout this thesis. More specifically, a rudimentary overview of spatial-domain IM techniques was provided in Section 1.2.1. Then, the family of space-time-domain IM techniques and the frequency-domain IM techniques were reviewed in Section 1.2.2 and Section 1.2.3, respectively. In Section 1.2.4, multi-dimensional IM techniques were

introduced, where multiple transmission entities, namely antennas, subcarriers, time slots and RF mirrors are indexed simultaneously for attaining performance gains. More particularly, the overview of the application of IM techniques to LS-MIMO-MU scenarios was provided in Section 1.2.5. Additionally, an overview of CS, which is applied as our pervasive tool, was presented in Section 1.3. Finally, the organisation as well as the main contributions of this thesis were detailed in Section 1.4.

- **Chapter 2 [97]:** In Chapter 2, we proposed a novel CS-aided frequency-domain IM, namely CS-OFDM-STSK-IM, where the information bits are mapped both to the space-time codewords and to the frequency-domain indices for striking a trade-off among design factors, such as the bandwidth efficiency, BER performance and complexity. More particularly, the CS-aided indexing strategy was utilised at the transmitter for transmitting more information bits at no extra cost in terms of either power or bandwidth.

  Explicitly, in Section 2.2, we briefly reviewed the background of STSK in Section 2.2.1, of the OFDM-IM scheme in Section 2.2.2 and of the CS-OFDM-IM scheme in Section 2.2.3. Section 2.3 presented our novel CS-OFDM-STSK-IM scheme in the context of both uncoded and FEC-coded scenarios. More specifically, in Section 2.3.1, the CS-OFDM-STSK-IM transmitter's bit-to-space-time-symbol mapping scheme was portrayed in Fig. 2.6. In Section 2.3.2.1, the optimal ML detector was invoked. In order to mitigate the excessive complexity of the ML detector, we then proposed a pair of reduced-complexity detection algorithms in Section 2.3.2.2. Specifically, in order to achieve a near-capacity performance, the soft-decision-aided demodulator of the CS-OFDM-STSK-IM scheme was conceived in Section 2.3.2.3.

  Then in Section 2.4 we characterised the performance of both the uncoded and FEC-coded CS-OFDM-STSK-IM schemes invoked for transmission over Rayleigh fading channels, as well as analysed the DCMC capacity of the CS-OFDM-STSK-IM schemes using different configurations. It was demonstrated in Fig. 2.9 that the beneficial flexibility can be achieved by appropriately adjusting the different parameters of the STSK encoder and the different values of N_f, N_v and K, for meeting the specific capacity requirements. Our investigations demonstrated that the proposed CS-OFDM-STSK-IM scheme is capable of achieving a better BER performance than the classic OFDM-STSK scheme.

Chapter 2				
Scheme a	**Scheme b**	**Rate (bit-s/s/Hz)**	**SNR (dB) gain at BER of 10^{-5} (a-b)**	**Complexity Ratio (a/b)**
CS-OFDM-STSK-IM (ML)	OFDM-STSK (ML)	1.1111	7.92	32
CS-OFDM-STSK-IM (ML)	CS-OFDM-STSK-IM (Algorithm 1, 4 candidates)	1.1111	4.875	1.6
CS-OFDM-STSK-IM (ML)	CS-OFDM-STSK-IM (Algorithm 2, 16 candidates)	1.1111	3.125	2
CS-OFDM-STSK-IM (Algorithm 1, 4 candidates)	CS-OFDM-STSK-IM (ML)	2	-1	0.625
CS-OFDM-STSK-IM (Algorithm 2, 16 candidates)	CS-OFDM-STSK-IM (ML)	2	-0.5	0.0625

Table 5.1: Summary of System Trade-offs for the Solutions of Chapter 2.

In particular, as summarised in Table 5.1, at the BER value of 10^{-5} and at the rate of 1.1111 bits/s/Hz, the proposed CS-OFDM-STSK-IM scheme using the ML detector achieves about 7.92 dB SNR-gain at the cost of a 32-fold increase in the order of complexity, in comparison to the classic OFDM-STSK scheme using the ML detector. Additionally, it was also found that the proposed reduced-complexity algorithms of Section 2.3.2.2 are capable of approaching the BER performance of the optimal ML detector, despite having a significantly lower complexity. Specifically, as summarised in Table 5.1, at the BER value of 10^{-5} and at a throughput of 2 bits/s/Hz, the CS-OFDM-STSK-IM scheme using the reduced-complexity **Algorithm 1** relying on 4 candidates imposes about 1 dB SNR performance loss at about 0.625 lower complexity in comparison to the proposed scheme using the ML detector. Furthermore, it was also found that the system using the reduced-complexity **Algorithm 2** having 16 candidates imposes a modest 0.5 dB SNR loss whilst having a factor of 0.0625 reduced complexity in comparison to the optimal ML detector, again at the BER value of 10^{-5} and a rate of 2 bits/s/Hz. Then, it was demonstrated in Fig. 2.16 that the 1/2-rate RSC-coded system using 6 inner-outer decoding iterations attained an infinitesimally low BER at around $E_b/N_0 = -5.5\,dB$, which is only about 1.8 dB away from the system's capacity line.

- **Chapter 3 [117]:** In Chapter 2 we investigated CS-aided OFDM-STSK relying on frequency-domain IM systems. In order to attain a better BER performance as well as a higher capacity than both the classical OFDM-STSK system and the CS-OFDM-STSK-IM scheme of Fig. 2.6, we proposed the novel CS-aided multi-dimensional IM scheme of Fig. 3.2 relying on both frequency- and spatial-domain IM techniques.

  In Section 3.2, we proposed the transceiver architecture of the CS-aided multi-dimensional IM system, which is illustrated in Fig. 3.2. In Section 3.3, we first presented the optimal ML detector for characterising the best-case bound of the proposed system's performance, where an upper bound was also derived for the ABEP. Then the novel CS-aided reduced-complexity detector, namely S-MP, was proposed for mitigating the excessive computational complexity of the optimal ML detector. Additionally, the soft-input soft-output decoders relying on both the optimal ML and on the S-MP detectors were specifically proposed in Section 3.3.2 for attaining near-capacity performances, which was illustrated in Fig. 3.7.

Chapter 3				
Scheme a	**Scheme b**	**Rate (bit-s/s/Hz)**	**SNR (dB) gain at BER of 10^{-5} (a-b)**	**Complexity Ratio (a/b)**
CS-aided multi-dimensional IM (ML)	CS-OFDM-STSK-IM (ML)	1.3333	4.3	1.4
CS-aided multi-dimensional IM (ML)	CS-aided multi-dimensional IM (S-MP)	1.3333	4.3	52
CS-aided multi-dimensional IM (S-MP)	CS-OFDM-STSK-IM (ML)	1.3333	0	0.03
CS-aided multi-dimensional IM (ML)	CS-OFDM-STSK-IM (ML)	1.89	3.4	6
CS-aided multi-dimensional IM (S-MP)	CS-aided multi-dimensional IM (ML)	1.89	-3	0.00006
CS-aided multi-dimensional IM (S-MP)	CS-OFDM-STSK-IM (ML)	1.89	0.4	0.0003

Table 5.2: Summary of System Trade-offs for the Solutions of Chapter 3.

In Section 3.4, we provided further performance analysis for characterising the overall system performance. Our investigations demonstrated that the proposed CS-aided multi-dimensional IM scheme of Fig. 3.2 is capable of achieving a better BER performance than than the classic OFDM-STSK system and the CS-OFDM-STSK-IM system of Fig. 2.6. In particular, as summarised in Table 5.2 as a glance, at the BER value of 10^{-5} and the rate of 1.3333 bits/s/Hz, the CS-aided multi-dimensional IM scheme of Fig. 3.2 achieves about 4.3 dB SNR performance gain at the cost of requiring about 1.4 higher complexity. Then, in comparison both to the classic OFDM-STSK scheme and to the CS-OFDM-STSK-IM scheme of of Fig. 2.6, the CS-aided multi-dimensional scheme of of Fig. 3.2 strikes more appealing trade-offs between the bandwidth efficiency, BER performance and the complexity. The novel S-MP detector was invoked for significantly reducing the complexity of the CS-aided multi-dimensional IM scheme, where an even lower complexity is imposed by the CS-aided multi-dimensional IM scheme using the S-MP detector, albeit a modest performance loss. As seen in Table 5.2 at a glance, in comparison to the ML detector, our S-MP detector reduces the complexity by about a factor of 0.00006 at the cost of 3 dB SNR loss at the BER value of 10^{-5} and at the rate of 1.89 bits/s/Hz. Additionally, it was also found that our S-MP detector is capable of achieving about 0.4 dB SNR gain at a factor of 0.0003 lower complexity than the CS-OFDM-STSK-IM scheme of of Fig. 2.6, at the BER value of 10^{-5} and at the rate of 1.89 bits/s/Hz.

Furthermore, in Section 3.4.2, the exchange of extrinsic information was visualised by plotting the EXIT characteristics of the inner demodulator and the outer RSC decoder. Explicitly, we presented the EXIT curves of the proposed CS-aided multi-dimensional IM scheme using ML-based soft-detection, where it was found that the iterative decoding process is expected to converge at around $E_b/N_0 = -4.75$ dB, where at least 3 iterations are required for reaching the mutual information point $(1.0, 1.0)$. Additionally, we showed the EXIT charts of the proposed CS-aided multi-dimensional IM system relying on the S-MP-based soft-detection after the LLR postprocessing, where it was found that the iterative decoding process is expected to converge around $E_b/N_0 = 3.25$ dB and at least 3 iterations are required for approaching the mutual information point $(1.0, 1.0)$. Then, we utilised the EXIT charts for determining the maximum achievable rates of different systems at given E_b/N_0 values. In particular, we then characterised the maximum achievable rates of several proposed CS-aided multi-dimensional IM schemes associated with different configurations, while using both ML-based and S-MP-based detectors. It was demonstrated that the maximum achievable rate of the system tends to

increase, when either the number of TAs N_t or the number of ACs N_{AC} increases. Specifically, it was also found that the maximum achievable rate of the CS-aided frequency-domain IM scheme of of Fig. 2.6 is lower than that of the CS-aided multi-dimensional IM scheme of Fig. 3.2. Finally, we characterised the coded BER performances of both ML-based soft-detection and the S-MP-based soft-detection, where it was shown by the simulation result of the ML-based soft-detection that the system attains an infinitesimally low BER at around $E_b/N_0 = -4.75$ dB and is within about 2.5 dB of the maximum achievable rate. Furthermore, it was found in Fig. 3.17 characterising the S-MP-based soft-detection that the system has no substantial performance gain beyond $E_b/N_0 = 3.25$ dB and its BER vs SNR curve is within about 2.0 dB from the maximum achievable rate.

- **Chapter 4 [128]:** In Chapter 3 we investigated the CS-aided multi-dimensional IM scheme of Fig. 3.2 by invoking both frequency- and spatial-domain IM for OFDM-STSK, where a better BER performance and a higher capacity was achieved in comparison to the CS-OFDM-STSK-IM scheme of Fig. 2.6. In Fig. 4.2 we proposed both uncoded and FEC-coded CS-aided CS-GSFIM IM schemes for large-scale multi-user uplink scenarios combining the benefits of LS-MU-MIMO, SM/GSM, OFDM-IM and CS for UL transmission. Specifically, in order to attain further performance gains over our solutions in Chapter 3, we employed different TA activation patterns for different transmitted APM symbols instead of using the same active TAs pattern for the whole subcarrier group, as shown in the CS-aided multi-dimensional IM scheme of Fig. 3.2.

  In Section 4.2 we introduced the CS-GSFIM scheme's transceiver architecture conceived for large-scale multi-user uplink scenarios. Then, in Section 4.3.1, we proposed both the hard-decision and soft-decision based ML multi-user detectors, where the ABEP analysis was presented as well. Additionally, in Section 4.3.2 we proposed the novel CS-aided reduced-complexity RSS-IMP multi-user detector. Then in Section 4.3.3 we analysed the complexity orders of the ML multi-user detector, of the MMSE multi-user detector and of the new RSS-IMP multi-user detector designed for the CS-GSFIM scheme of Fig. 4.3 operating in large-scale multi-user scenarios.

Chapter 4				
Scheme a	**Scheme b**	**Rate (bit-s/s/Hz/user)**	**SNR (dB) gain at BER of 10^{-5} (a-b)**	**Complexity Ratio (a/b)**
MU CS-GSFIM (ML)	MU Scheme of Fig. 3.2 (ML)	1.88	2.5	10^0
MU CS-GSFIM (ML)	MU Scheme of Fig. 2.6 (ML)	1.88	4	10^0
MU CS-GSFIM (ML)	MU CS-GSFIM (RC4)	1.88	1.7	2.6×10^5
MU CS-GSFIM (RC4)	MU Scheme of Fig. 3.2 (ML)	1.88	0.8	4×10^{-6}
MU CS-GSFIM (RC4)	MU Scheme of Fig. 2.6 (ML)	1.88	2.3	4×10^{-6}
MU CS-GSFIM (ML)	MU Scheme of Fig. 3.2 (ML)	2.5	3.2	10^0
MU CS-GSFIM (ML)	MU Scheme of Fig. 2.6 (ML)	2.5	9	10^0
MU CS-GSFIM (RC4)	MU CS-GSFIM (ML)	2.5	-2.8	8×10^{-14}
MU CS-GSFIM (RC4)	MU Scheme of Fig. 3.2 (ML)	2.5	0.4	7.5×10^{-14}
MU CS-GSFIM (RC4)	MU Scheme of Fig. 2.6 (ML)	2.5	6.2	7.5×10^{-14}
LS-MU CS-GSFIM (RC3)	LS-MU CS-GSFIM (MMSE)	1.88	2.1	1.1×10^{-1}
LS-MU CS-GSFIM (RC4)	LS-MU CS-GSFIM (MMSE)	1.88	3.4	1.4×10^{-1}

Table 5.3: Summary of System Trade-offs for the Solutions of Chapter 4.

In Section 4.4, we characterised our CS-GSFIM system in LS-MU scenarios using the ML, the MMSE and the proposed RSS-IMP multi-user detectors, compared to the conventional MU-MIMO-OFDM system, to the CS-aided frequency-domain IM scheme proposed in Chapter 2, and to the CS-aided multi-dimensional IM scheme associated with group-level selection of the activated TAs, as proposed in Chapter 3. Explicitly, we investigated all the 25 uncoded schemes listed in Table 4.3 having different system configurations. More specifically, as summarised in Table 5.3 at a glance, at the BER value of 10^{-5} and the bandwidth efficiency of 1.88 bits/s/Hz/user, the MU CS-GSFIM scheme of Fig. 4.2 using the ML multi-user detector achieves about 2.5 dB and 4 dB SNR gains, in comparison to the MU scheme of Fig. 3.2 and to the MU scheme of Fig. 2.6, respectively. Additionally, the RSS-IMP detector was invoked for significantly reducing the complexity compared to that of the optimal ML multi-user detector at the cost of a slight BER vs SNR performance loss. Explicitly, as summarised in Table 5.3 at a glance, at the BER value of 10^{-5} and at the bandwidth efficiency of 2.5 bits/s/Hz/user, our RSS-IMP multi-user detector using only 4 iterations imposes about a factor of 8×10^{-14} dramatically reduced complexity at the cost of about 2.8 dB SNR loss in comparison to the optimal ML multi-user detector. In particular, it was also found that our RSS-IMP multi-user detector using 4 iterations is capable of achieving about 0.4 dB and 6.2 dB better SNR performance at a significantly lower complexity, in comparison both to the MU scheme of Fig. 3.2 and to the MU scheme of Fig. 2.6 using the ML multi-user detectors, respectively, again at the BER value of 10^{-5} and at the bandwidth efficiency of 2.5 bits/s/Hz/user. Specifically, our RSS-IMP multi-user detector was shown to make the proposed system appealing for employment in LS-MU scenarios, where it is capable of outperforming the MMSE multi-user detector at a significantly lower complexity in LS-MU scenarios. As summarised in Table 5.3 at a glance, in LS-MU scenarios, our RSS-IMP multi-user detector using only 4 iterations is capable of attaining about 3.4 dB SNR gain at a factor of 0.14 reduced complexity, in comparison to the MMSE multi-user detector, at the BER value of 10^{-5} and at the bandwidth efficiency of 1.88 bits/s/Hz/user.

More particularly, our investigations seen in Fig. 4.16 and Fig. 4.17 also demonstrated that our CS-GSFIM system's achievable rate can be improved by either increasing the number active TAs, or the number of active subcarriers, or the size of constellations. Then, it was shown that the performances of the coded systems are capable of approaching the maximum achievable rate limits upon increasing the number of IO iterations, where the performances of the coded system (6 IO

iterations) using the ML detector and of the coded system (4 IO iterations) using the reduced-complexity detector are about 2.8 dB and 4 dB away from the maximum achievable rate limits at the BER value of 10^{-5}, respectively.

5.2 Design Guidelines

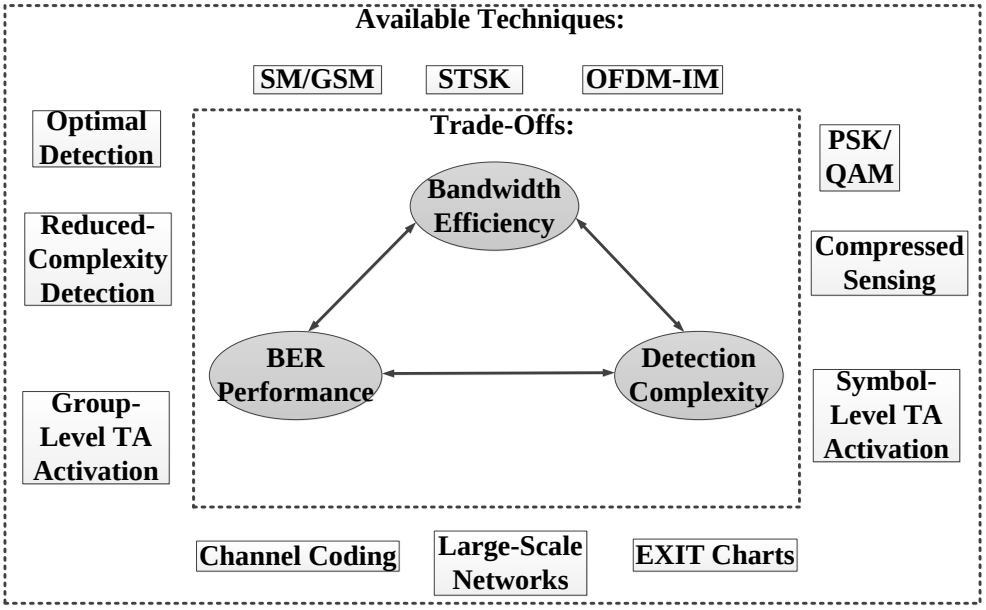

Figure 5.1: Relationship of the diverse system components affecting the different design trade-offs.

Based on our conclusions and summary provided in Section 5.1, as well as in Table 2.5, Table 3.5, Table 3.6 and Table 4.4, our suite of CS-aided IM schemes is capable of striking flexible trade-offs among the bandwidth efficiency, BER performance and the detection complexity as a benefit of the diverse system components portrayed in Fig. 5.1.

In this section, we provide explicit design guidelines for our proposed schemes, where the designers can strike the most desirable trade-off upon appropriately configuring the different components in the design.

- The values of (M, N, T) for the STSK encoder of Fig. 2.6 and of Fig. 3.2, which specify the number of TA elements, the number of RA elements and the number of symbol intervals over which spreading takes place, should be appropriately chosen in order to satisfy the required performance.

- Different combinations of $(Q, \mathcal{L})$ in the STSK encoder of Fig. 2.6 and of Fig. 3.2 may result in different bandwidth efficiencies, which impose different complexity and exhibit a different BER performance.
  - In Chapter 2, the increased value of $\mathcal{L}$ results in a higher bandwidth efficiency at the cost of a certain BER performance loss and at an increased complexity. However, the proposed pair of reduced-complexity detection algorithms of Chapter 2 is capable of operating at a much lower complexity whilst imposing a modest performance loss in comparison to the scheme using the ML detector.
  - In Chapter 3, the increased values of $(Q\mathcal{L})$ result in an increased throughput and degraded BER performance, when using the ML detector despite its and complexity. Specifically, the reduced-complexity S-MP detector is capable of eliminating the influence of the varying values of $(Q\mathcal{L})$ on the complexity.
- The values of N_v and K determine the size of the virtual domain and the sparsity level of the IM vector, which influence the number of information bits carried by the frequency index selector.
  - In Chapter 2, the increased value of K results in an increased bandwidth efficiency and complexity, but attains a BER performance gain as a benefit of the extra diversity gain achieved by increasing the values of (M, T).
  - In Chapter 3, the increased values of N_v result in a higher achievable rate, degraded performance and increased complexity for the scheme using the ML detector, while the complexity of the proposed system using the S-MP detector increases only moderately upon increasing the achievable rate in comparison to the exponentially increased complexity of the system using the ML detector.
- The values of N_t in Chapter 3 and Chapter 4, as well as of N_t^a in Chapter 4 specify the number of available TAs and the number of activated TAs involved for transmitting each symbol, respectively, which influence the trade-off between the the bandwidth efficiency, the BER performance and the complexity.
  - In Chapter 3, we considered a pair of system configurations: 1) $N_v = 16$, $N_f = 8$, $K = 2$, $N_t = 8$, STSK$(2, 2, 2, 8, 2)$, 16 bits/group, $\mathcal{O}_{S-MP} = 1.64 \times 10^5$ and 2) $N_v = 16$, $N_f = 8$, $K = 2$, $N_t = 2$, STSK$(2, 2, 2, 2, 2)$, 10 bits/group, $\mathcal{O}_{S-MP} = 4.1 \times 10^4$, where System 1) has a higher achievable rate than System 2), but the complexity of System 1) is higher than that of System 2),

and the BER performance of System 1) may be worse than that of System 2).

– In Chapter 4, an increased bandwidth efficiency can be obtained upon increasing the value of N_t^a at the cost of a BER performance degradation and increased complexity, while the RSS-IMP detector is capable of significantly reducing the excessive complexity of the ML detector at the cost of a modest BER performance loss.

5.3 Future Research

In this section, we briefly discuss a number of future research ideas.

- **Deep Neural Network Based Detector Design:** In Chapter 3, we proposed the CS-aided multi-dimensional IM system relying both on frequency- and spatial-domain IM, where despite having a better performance than both the classical OFDM-MIMO systems and the CS-aided single-dimensional IM system, this was achieved at a high detection complexity. Hence we proposed a reduced-complexity S-MP detector based on the greedy algorithm for striking a trade-off between the BER performance attained and the complexity imposed. However, as seen in Fig. 3.8, the S-MP detector still suffered from a notable performance loss in comparison to the ML detector. To deal with this issue, inspired by [225], deep neural network (DNN) based detectors can be potentially exploited for the CS-aided multi-dimensional IM for significantly reducing the complexity over existing S-MP and ML detectors, while maintaining a near-optimal performance. This idea is particularly promising in joint channel estimation and data detection, when the joint search-space becomes excessive. Our goal is to find their joint optimum despite only searching through a fraction of the entire search-space, as alluded to below.

- **Reduced-Complexity Joint Channel Estimation and Data Detector:** In our proposed systems, we assumed perfect channel state information at the receiver. For the sake of eliminating this constraint, an efficient channel estimation technique can be invoked. Additionally, in order to strike an attractive trade-off between the BER performance and the complexity, it will be necessary to apply reduced-complexity joint channel estimation and data detection [226] in our systems.

- **An Adaptive Multi-User Scheme Designed for Downlink Transmission:** In Chapter 4, we proposed a multi-dimensional IM scheme for the LS-MU-MIMO uplink communicating over Rayleigh fading channels, where we concluded that a high design flexibility can be achieved by appropriately configuring the components in the design. It is promising to apply our multi-dimensional IM scheme to multi-user downlink scenarios, where the joint design of the compressive matrix and of multi-user transmit precoding will be necessary for eliminating the multi-user interference and for guaranteeing an accurate recovery of transmitted signals. Specifically, attracted by the various components in our multi-dimensional IM scheme, we can potentially design an adaptive multi-user scheme by near-instantaneously re-configuring the different components of the scheme for maximising the system's achievable rate [227, 228]. Additionally, machine learning techniques can also be applied for determining the adaptation. Hence we can conceive an adaptive CS-aided multi-dimensional IM scheme for the multi-user downlink, which is capable of maximising the system's achievable rate, while maintaining the target BER.

References

[1] E. Basar, "Index modulation techniques for 5G wireless networks," *IEEE Communications Magazine*, vol. 54, no. 7, pp. 168–175, July 2016.

[2] C. Wang, F. Haider, X. Gao, X. You, Y. Yang, D. Yuan, H. M. Aggoune, H. Haas, S. Fletcher, and E. Hepsaydir, "Cellular architecture and key technologies for 5G wireless communication networks," *IEEE Communications Magazine*, vol. 52, no. 2, pp. 122–130, February 2014.

[3] A. Gupta and R. K. Jha, "A survey of 5G network: architecture and emerging technologies," *IEEE Access*, vol. 3, pp. 1206–1232, 2015.

[4] J. G. Andrews, S. Buzzi, W. Choi, S. V. Hanly, A. Lozano, A. C. K. Soong, and J. C. Zhang, "What will 5G be?" *IEEE Journal on Selected Areas in Communications*, vol. 32, no. 6, pp. 1065–1082, June 2014.

[5] E. Basar, "Index modulation: a promising technique for 5G and beyond wireless networks," in *Networks of the Future*. Chapman and Hall/CRC, 2017, pp. 145–166.

[6] M. Wen, X. Cheng, and L. Yang, *Index modulation for 5G wireless communications*. Springer, 2017.

[7] E. Basar, M. Wen, R. Mesleh, M. Di Renzo, Y. Xiao, and H. Haas, "Index modulation techniques for next-generation wireless networks," *IEEE Access*, vol. 5, pp. 16 693–16 746, 2017.

[8] R. Y. Mesleh, H. Haas, S. Sinanovic, C. W. Ahn, and S. Yun, "Spatial modulation," *IEEE Transactions on Vehicular Technology*, vol. 57, no. 4, pp. 2228–2241, July 2008.

[9] P. W. Wolniansky, G. J. Foschini, G. D. Golden, and R. A. Valenzuela, "V-BLAST: an architecture for realizing very high data rates over the rich-scattering wireless channel," in *1998 URSI International Symposium on Signals, Systems, and Electronics. Conference Proceedings (Cat. No.98EX167)*, Oct 1998, pp. 295–300.

[10] S. M. Alamouti, "A simple transmit diversity technique for wireless communications," *IEEE Journal on Selected Areas in Communications*, vol. 16, no. 8, pp. 1451–1458, Oct 1998.

[11] V. Tarokh, H. Jafarkhani, and A. R. Calderbank, "Space-time block codes from orthogonal designs," *IEEE Transactions on Information Theory*, vol. 45, no. 5, pp. 1456–1467, July 1999.

[12] P. Yang, M. D. Renzo, Y. Xiao, S. Li, and L. Hanzo, "Design guidelines for spatial modulation," *IEEE Communications Surveys Tutorials*, vol. 17, no. 1, pp. 6–26, Firstquarter 2015.

[13] N. Ishikawa, S. Sugiura, and L. Hanzo, "50 years of permutation, spatial and index modulation: from classic RF to visible light communications and data storage," *IEEE Communications Surveys Tutorials*, vol. 20, no. 3, pp. 1905–1938, thirdquarter 2018.

[14] N. Serafimovski, A. Younis, R. Mesleh, P. Chambers, M. D. Renzo, C. X. Wang, P. M. Grant, M. A. Beach, and H. Haas, "Practical implementation of spatial modulation," *IEEE Transactions on Vehicular Technology*, vol. 62, no. 9, pp. 4511–4523, Nov 2013.

[15] S. Ganesan, R. Mesleh, H. Ho, C. W. Ahn, and S. Yun, "On the performance of spatial modulation OFDM," in *2006 Fortieth Asilomar Conference on Signals, Systems and Computers*, Oct 2006, pp. 1825–1829.

[16] M. D. Renzo, H. Haas, and P. M. Grant, "Spatial modulation for multiple-antenna wireless systems: a survey," *IEEE Communications Magazine*, vol. 49, no. 12, pp. 182–191, December 2011.

[17] M. Di Renzo, H. Haas, A. Ghrayeb, S. Sugiura, and L. Hanzo, "Spatial modulation for generalized MIMO: challenges, opportunities, and implementation," *Proceedings of the IEEE*, vol. 102, no. 1, pp. 56–103, Jan 2014.

[18] T. Mao, Q. Wang, Z. Wang, and S. Chen, "Novel index modulation techniques: a survey," *IEEE Communications Surveys Tutorials*, vol. 21, no. 1, pp. 315–348, Firstquarter 2019.

[19] J. Jeganathan, A. Ghrayeb, and L. Szczecinski, "Spatial modulation: optimal detection and performance analysis," *IEEE Communications Letters*, vol. 12, no. 8, pp. 545–547, Aug 2008.

[20] J. Jeganathan, A. Ghrayeb, L. Szczecinski, and A. Ceron, "Space shift keying modulation for MIMO channels," *IEEE Transactions on Wireless Communications*, vol. 8, no. 7, pp. 3692–3703, July 2009.

[21] A. Younis, N. Serafimovski, R. Mesleh, and H. Haas, "Generalised spatial modulation," in *2010 Conference Record of the Forty Fourth Asilomar Conference on Signals, Systems and Computers*, Nov 2010, pp. 1498–1502.

[22] J. Wang, S. Jia, and J. Song, "Generalised spatial modulation system with multiple active transmit antennas and low complexity detection scheme," *IEEE Transactions on Wireless Communications*, vol. 11, no. 4, pp. 1605–1615, April 2012.

[23] Y. Xiao, Z. Yang, L. Dan, P. Yang, L. Yin, and W. Xiang, "Low-complexity signal detection for generalized spatial modulation," *IEEE Communications Letters*, vol. 18, no. 3, pp. 403–406, March 2014.

[24] R. Mesleh, S. S. Ikki, and H. M. Aggoune, "Quadrature spatial modulation," *IEEE Transactions on Vehicular Technology*, vol. 64, no. 6, pp. 2738–2742, June 2015.

[25] C. Cheng, H. Sari, S. Sezginer, and Y. T. Su, "Enhanced spatial modulation with multiple signal constellations," *IEEE Transactions on Communications*, vol. 63, no. 6, pp. 2237–2248, June 2015.

[26] J. Fu, C. Hou, W. Xiang, L. Yan, and Y. Hou, "Generalised spatial modulation with multiple active transmit antennas," in *2010 IEEE Globecom Workshops*, Dec 2010, pp. 839–844.

[27] A. Younis, D. A. Basnayaka, and H. Haas, "Performance analysis for generalised spatial modulation," in *European Wireless 2014; 20th European Wireless Conference*, May 2014, pp. 1–6.

[28] W. Liu, N. Wang, M. Jin, and H. Xu, "Denoising detection for the generalized spatial modulation system using sparse property," *IEEE Communications Letters*, vol. 18, no. 1, pp. 22–25, January 2014.

[29] L. Xiao, P. Yang, Y. Xiao, S. Fan, M. Di Renzo, W. Xiang, and S. Li, "Efficient compressive sensing detectors for generalized spatial modulation systems," *IEEE Transactions on Vehicular Technology*, vol. 66, no. 2, pp. 1284–1298, Feb 2017.

[30] T. L. Narasimhan, P. Raviteja, and A. Chockalingam, "Generalized spatial modulation for large-scale MIMO systems: Analysis and detection," in *2014 48th Asilomar Conference on Signals, Systems and Computers*, Nov 2014, pp. 1071–1075.

[31] B. Zheng, X. Wang, M. Wen, and F. Chen, "Soft demodulation algorithms for generalized spatial modulation using deterministic sequential Monte Carlo," *IEEE Transactions on Wireless Communications*, vol. 16, no. 6, pp. 3953–3967, June 2017.

[32] Z. Yigit and E. Basar, "Low-complexity detection of quadrature spatial modulation," *Electronics Letters*, vol. 52, no. 20, pp. 1729–1731, 2016.

[33] R. Mesleh, S. S. Ikki, and F. S. Almehmadi, "Impact of IQ imbalance on the performance of QSM multiple-inputmultiple-output system," *IET Communications*, vol. 10, no. 17, pp. 2391–2395, 2016.

[34] R. Mesleh, S. S. Ikki, and O. S. Badarneh, "Impact of cochannel interference on the performance of quadrature spatial modulation MIMO systems," *IEEE Communications Letters*, vol. 20, no. 10, pp. 1927–1930, Oct 2016.

[35] A. Younis, N. Abuzgaia, R. Mesleh, and H. Haas, "Quadrature spatial modulation for 5G outdoor millimeterwave communications: capacity analysis," *IEEE Transactions on Wireless Communications*, vol. 16, no. 5, pp. 2882–2890, May 2017.

[36] L. Xiao, P. Yang, S. Fan, S. Li, L. Song, and Y. Xiao, "Low-complexity signal detection for large-scale quadrature spatial modulation systems," *IEEE Communications Letters*, vol. 20, no. 11, pp. 2173–2176, Nov 2016.

[37] G. Jaiswal and V. B. Kumaravelu, "A low complexity receiver design for quadrature spatial modulation," in *2018 International Conference on Communication and Signal Processing (ICCSP)*, April 2018, pp. 0100–0104.

[38] M. Carosino and J. A. Ritcey, "Performance of MIMO enhanced spatial modulation under imperfect channel information," in *2015 49th Asilomar Conference on Signals, Systems and Computers*, Nov 2015, pp. 1415–1419.

[39] C. Cheng, H. Sari, S. Sezginer, and Y. T. Su, "New signal designs for enhanced spatial modulation," *IEEE Transactions on Wireless Communications*, vol. 15, no. 11, pp. 7766–7777, Nov 2016.

[40] ——, "Enhanced spatial multiplexing A novel approach to MIMO signal design," in *2016 IEEE International Conference on Communications (ICC)*, May 2016, pp. 1–6.

[41] S. Sugiura, S. Chen, and L. Hanzo, "Coherent and differential space-time shift keying: a dispersion matrix approach," *IEEE Transactions on Communications*, vol. 58, no. 11, pp. 3219–3230, November 2010.

[42] R. Mesleh, M. D. Renzo, H. Haas, and P. M. Grant, "Trellis coded spatial modulation," *IEEE Transactions on Wireless Communications*, vol. 9, no. 7, pp. 2349–2361, July 2010.

[43] E. Basar, U. Aygolu, E. Panayirci, and H. V. Poor, "Space-time block coded spatial modulation," *IEEE Transactions on Communications*, vol. 59, no. 3, pp. 823–832, March 2011.

[44] Y. Bian, X. Cheng, M. Wen, L. Yang, H. V. Poor, and B. Jiao, "Differential spatial modulation," *IEEE Transactions on Vehicular Technology*, vol. 64, no. 7, pp. 3262–3268, July 2015.

[45] G. Ungerboeck, "Channel coding with multilevel/phase signals," *IEEE Transactions on Information Theory*, vol. 28, no. 1, pp. 55–67, January 1982.

[46] S. Sugiura, S. Chen, and L. Hanzo, "Generalized space-time shift keying designed for flexible diversity-, multiplexing- and complexity-tradeoffs," *IEEE Transactions on Wireless Communications*, vol. 10, no. 4, pp. 1144–1153, April 2011.

[47] S. Sugiura, C. Xu, S. X. Ng, and L. Hanzo, "Reduced-complexity coherent versus non-coherent QAM-aided space-time shift keying," *IEEE Transactions on Communications*, vol. 59, no. 11, pp. 3090–3101, November 2011.

[48] ——, "Reduced-complexity iterative-detection-aided generalized space-time shift keying," *IEEE Transactions on Vehicular Technology*, vol. 61, no. 8, pp. 3656–3664, Oct 2012.

[49] M. Driusso, F. Babich, M. I. Kadir, and L. Hanzo, "OFDM aided space-time shift keying for dispersive downlink channels," in *2012 IEEE Vehicular Technology Conference (VTC Fall)*, Sept 2012, pp. 1–5.

[50] M. I. Kadir, S. Sugiura, S. Chen, and L. Hanzo, "Unified MIMO-multicarrier designs: a space-time shift keying approach," *IEEE Communications Surveys Tutorials*, vol. 17, no. 2, pp. 550–579, November 2015.

[51] I. A. Hemadeh, M. El-Hajjar, S. Won, and L. Hanzo, "Multi-set space-time shift-keying with reduced detection complexity," *IEEE Access*, vol. 4, pp. 4234–4246, 2016.

[52] ——, "Multi-set space-time shift keying and space- frequency space-time shift keying for millimeter-wave communications," *IEEE Access*, vol. 5, pp. 8324–8342, December 2016.

[53] B. Hassibi and B. Hochwald, "Linear dispersion codes," in *Proceedings. 2001 IEEE International Symposium on Information Theory (IEEE Cat. No.01CH37252)*, June 2001, pp. 325–.

[54] S. Sugiura, S. Chen, and L. Hanzo, "A universal space-time architecture for multiple-antenna aided systems," *IEEE Communications Surveys Tutorials*, vol. 14, no. 2, pp. 401–420, Second 2012.

[55] C. Xu, S. Sugiura, S. X. Ng, and L. Hanzo, "Reduced-complexity soft-decision aided space-time shift keying," *IEEE Signal Processing Letters*, vol. 18, no. 10, pp. 547–550, Oct 2011.

[56] P. Yang, Y. Xiao, L. Li, Q. Tang, and S. Li, "An improved matched-filter based detection algorithm for space-time shift keying systems," *IEEE Signal Processing Letters*, vol. 19, no. 5, pp. 271–274, May 2012.

[57] M. I. Kadir, S. Chen, K. Hari, K. Giridhar, and L. Hanzo, "OFDM-aided differential space-time shift keying using iterative soft multiple-symbol differential sphere decoding," *IEEE Transactions on Vehicular Technology*, vol. 63, no. 8, pp. 4102–4108, Oct 2014.

[58] M. I. Kadir, S. Sugiura, J. Zhang, S. Chen, and L. Hanzo, "OFDMA/SC-FDMA aided spacetime shift keying for dispersive multiuser scenarios," *IEEE Transactions on Vehicular Technology*, vol. 62, no. 1, pp. 408–414, Jan 2013.

[59] M. I. Kadir, S. Chen, and L. Hanzo, "A reduced-complexity detector for OFDMA/SC-FDMA-aided space-time shift keying," in *2013 IEEE 78th Vehicular Technology Conference (VTC Fall)*, Sep. 2013, pp. 1–5.

[60] I. A. Hemadeh, M. El-Hajjar, S. Won, and L. Hanzo, "Multiuser steered multiset space-time shift keying for millimeter-wave communications," *IEEE Transactions on Vehicular Technology*, vol. 66, no. 6, pp. 5491–5495, June 2017.

[61] R. Abu-alhiga and H. Haas, "Subcarrier-index modulation OFDM," in *2009 IEEE 20th International Symposium on Personal, Indoor and Mobile Radio Communications*, Sep. 2009, pp. 177–181.

[62] E. Basar, U. Aygolu, E. Panayirci, and H. V. Poor, "Orthogonal frequency division multiplexing with index modulation," *IEEE Transactions on Signal Processing*, vol. 61, no. 22, pp. 5536–5549, Nov 2013.

[63] N. Ishikawa, S. Sugiura, and L. Hanzo, "Subcarrier-index modulation aided OFDM - will it work?" *IEEE Access*, vol. 4, pp. 2580–2593, May 2016.

[64] M. Wen, B. Ye, E. Basar, Q. Li, and F. Ji, "Enhanced orthogonal frequency division multiplexing with index modulation," *IEEE Transactions on Wireless Communications*, vol. 16, no. 7, pp. 4786–4801, July 2017.

[65] D. Tsonev, S. Sinanovic, and H. Haas, "Enhanced subcarrier index modulation (SIM) OFDM," in *2011 IEEE GLOBECOM Workshops (GC Wkshps)*, Dec 2011, pp. 728–732.

[66] L. Hanzo, M. Munster, B. J. Choi, and T. Keller. IEEE, 2003, pp. 21–21.

[67] L. Hanzo, S. X. Ng, T. Keller, and W. Webb, *Introduction to orthogonal frequency division multiplexing.* IEEE, 2004.

[68] M. Wen, X. Cheng, M. Ma, B. Jiao, and H. V. Poor, "On the achievable rate of OFDM with index modulation," *IEEE Transactions on Signal Processing*, vol. 64, no. 8, pp. 1919–1932, April 2016.

[69] Y. Ko, "A tight upper bound on bit error rate of joint OFDM and multi-carrier index keying," *IEEE Communications Letters*, vol. 18, no. 10, pp. 1763–1766, Oct 2014.

[70] M. Wen, X. Cheng, and L. Yang, "Optimizing the energy efficiency of OFDM with index modulation," in *2014 IEEE International Conference on Communication Systems*, Nov 2014, pp. 31–35.

[71] W. Li, H. Zhao, C. Zhang, L. Zhao, and R. Wang, "Generalized selecting subcarrier modulation scheme in OFDM system," in *2014 IEEE International Conference on Communications Workshops (ICC)*, June 2014, pp. 907–911.

[72] Q. Ma, P. Yang, Y. Xiao, H. Bai, and S. Li, "Error probability analysis of OFDM-IM with carrier frequency offset," *IEEE Communications Letters*, vol. 20, no. 12, pp. 2434–2437, Dec 2016.

[73] Y. Xiao, S. Wang, L. Dan, X. Lei, P. Yang, and W. Xiang, "OFDM with interleaved subcarrier-index modulation," *IEEE Communications Letters*, vol. 18, no. 8, pp. 1447–1450, Aug 2014.

[74] X. Cheng, M. Wen, L. Yang, and Y. Li, "Index modulated OFDM with interleaved grouping for V2X communications," in *17th International IEEE Conference on Intelligent Transportation Systems (ITSC)*, Oct 2014, pp. 1097–1104.

[75] E. Basar, "OFDM with index modulation using coordinate interleaving," *IEEE Wireless Communications Letters*, vol. 4, no. 4, pp. 381–384, Aug 2015.

[76] R. Fan, Y. J. Yu, and Y. L. Guan, "Generalization of orthogonal frequency division multiplexing with index modulation," *IEEE Transactions on Wireless Communications*, vol. 14, no. 10, pp. 5350–5359, Oct 2015.

[77] B. Zheng, F. Chen, M. Wen, F. Ji, H. Yu, and Y. Liu, "Low-complexity ML detector and performance analysis for OFDM with in-phase/quadrature index modulation," *IEEE Communications Letters*, vol. 19, no. 11, pp. 1893–1896, Nov 2015.

[78] R. Fan, Y. J. Yu, and Y. L. Guan, "Improved orthogonal frequency division multiplexing with generalised index modulation," *IET Communications*, vol. 10, no. 8, pp. 969–974, 2016.

[79] M. Wen, Y. Zhang, J. Li, E. Basar, and F. Chen, "Equiprobable subcarrier activation method for OFDM with index modulation," *IEEE Communications Letters*, vol. 20, no. 12, pp. 2386–2389, Dec 2016.

[80] T. Mao, Z. Wang, Q. Wang, S. Chen, and L. Hanzo, "Dual-Mode Index Modulation Aided OFDM," *IEEE Access*, vol. 5, pp. 50–60, 2017.

[81] T. Mao, Q. Wang, and Z. Wang, "Generalized dual-mode index modulation aided OFDM," *IEEE Communications Letters*, vol. 21, no. 4, pp. 761–764, April 2017.

[82] H. Zhang, L. L. Yang, and L. Hanzo, "Compressed sensing improves the performance of subcarrier index-modulation-assisted OFDM," *IEEE Access*, vol. 4, pp. 7859–7873, October 2016.

[83] M. I. Kadir, H. Zhang, S. Chen, and L. Hanzo, "Entropy coding aided adaptive subcarrier-index modulated OFDM," *IEEE Access*, vol. 6, pp. 7739–7752, 2018.

[84] H. Zhang, C. Jiang, L. Yang, E. Basar, and L. Hanzo, "Linear precoded index modulation," *IEEE Transactions on Communications*, vol. 67, no. 1, pp. 350–363, Jan 2019.

[85] M. Wen, E. Basar, Q. Li, B. Zheng, and M. Zhang, "Multiple-mode orthogonal frequency division multiplexing with index modulation," *IEEE Transactions on Communications*, vol. 65, no. 9, pp. 3892–3906, Sept 2017.

[86] J. Crawford and Y. Ko, "Low complexity greedy detection method with generalized multicarrier index keying OFDM," in *2015 IEEE 26th Annual International Symposium on Personal, Indoor, and Mobile Radio Communications (PIMRC)*, Aug 2015, pp. 688–693.

[87] J. Crawford, E. Chatziantoniou, and Y. Ko, "On the SEP analysis of OFDM index modulation With hybrid low complexity greedy detection and diversity reception," *IEEE Transactions on Vehicular Technology*, vol. 66, no. 9, pp. 8103–8118, Sep. 2017.

[88] A. I. Siddiq, "Low complexity OFDM-IM detector by encoding all possible subcarrier activation patterns," *IEEE Communications Letters*, vol. 20, no. 3, pp. 446–449, March 2016.

[89] S. A. Altalib, B. M. Ali, and A. I. Siddiq, "BER performance improvement of V2I communication by using OFDM IM exploiting all subcarrier activation patternser," in *2017 International Conference on Communication, Control, Computing and Electronics Engineering (ICCCCEE)*, Jan 2017, pp. 1–4.

[90] Y. Li, M. Wen, X. Cheng, and L. Yang, "Index modulated OFDM with ICI self-cancellation for V2X communications," in *2016 International Conference on Computing, Networking and Communications (ICNC)*, Feb 2016, pp. 1–5.

[91] M. Wen, Y. Li, X. Cheng, and L. Yang, "Index modulated OFDM with ICI self-cancellation in underwater acoustic communications," in *2014 48th Asilomar Conference on Signals, Systems and Computers*, Nov 2014, pp. 338–342.

[92] M. Wen, X. Cheng, L. Yang, Y. Li, X. Cheng, and F. Ji, "Index modulated OFDM for underwater acoustic communications," *IEEE Communications Magazine*, vol. 54, no. 5, pp. 132–137, May 2016.

[93] P. Kuo and H. T. Kung, "Subcarrier index coordinate expression (SICE): An ultra-low-power OFDM-compatible wireless communications scheme tailored for internet of things," in *2014 International Conference on the Internet of Things (IOT)*, Oct 2014, pp. 97–102.

[94] E. Basar and E. Panayirci, "Optical OFDM with index modulation for visible light communications," in *2015 4th International Workshop on Optical Wireless Communications (IWOW)*, Sep. 2015, pp. 11–15.

[95] E. Basar, "Multiple-input multiple-output OFDM with index modulation," *IEEE Signal Processing Letters*, vol. 22, no. 12, pp. 2259–2263, Dec 2015.

[96] B. Zheng, M. Wen, E. Basar, and F. Chen, "Multiple-input multiple-output OFDM with index modulation: low-complexity detector design," *IEEE Transactions on Signal Processing*, vol. 65, no. 11, pp. 2758–2772, June 2017.

[97] S. Lu, I. A. Hemadeh, M. El-Hajjar, and L. Hanzo, "Compressed-sensing-aided space-time frequency index modulation," *IEEE Transactions on Vehicular Technology*, vol. 67, no. 7, pp. 6259–6271, July 2018.

[98] I. A. Hemadeh, S. Lu, M. El-Hajjar, and L. Hanzo, "Compressed sensing-aided index modulation improves space-time shift keying assisted millimeter-wave communications," *IEEE Access*, pp. 1–1, 2018.

[99] M. I. Kadir, "Subcarrier-index modulated multicarrier space-time shift keying: achievable rate, performance, and design guidelines," *IEEE Transactions on Vehicular Technology*, vol. 68, no. 3, pp. 2260–2269, March 2019.

[100] E. Basar, "On multiple-input multiple-output OFDM with index modulation for next generation wireless networks," *IEEE Transactions on Signal Processing*, vol. 64, no. 15, pp. 3868–3878, Aug 2016.

[101] S. Wang, B. Xu and H. Bai, Y. Xiao, and L. Dan, "MIMO-OFDM with interleaved subcarrier-index modulation," in *10th International Conference on Wireless Communications, Networking and Mobile Computing (WiCOM 2014)*, Sep. 2014, pp. 35–37.

[102] B. Zheng, M. Wen, E. Basar, and F. Chen, "Low-complexity near-optimal detector for multiple-input multiple-output OFDM with index modulation," in *2017 IEEE International Conference on Communications (ICC)*, May 2017, pp. 1–6.

[103] L. Wang, Z. Chen, Z. Gong, and M. Wu, "Space-frequency coded index modulation with linear-complexity maximum likelihood receiver in the MIMO-OFDM system," *IEEE Signal Processing Letters*, vol. 23, no. 10, pp. 1439–1443, Oct 2016.

[104] F. Yao, J. Zheng, and Z. Li, "MIMO OFDM index modulation with circular-shift-based activation pattern for rapidly time-varying channels," in *2016 IEEE 83rd Vehicular Technology Conference (VTC Spring)*, May 2016, pp. 1–4.

[105] Z. Hu, S. Lin, B. Zheng, F. Chen, Q. Wang, and Y. Wei, "Low-complexity subcarrier-wise detection for MIMO-OFDM with index modulation," *IEEE Access*, vol. 5, pp. 23 822–23 832, 2017.

[106] S. Chen and X. Ma, "MIMO-OFDM-IM system for high mobility communications with block Markov superposition transmission," in *2018 IEEE 87th Vehicular Technology Conference (VTC Spring)*, June 2018, pp. 1–5.

[107] A. Vora and K. Kang, "Index modulation with PAPR and beamforming for 5G MIMO-OFDM," in *2018 IEEE 5G World Forum (5GWF)*, July 2018, pp. 389–394.

[108] D. L. Donoho, "Compressed sensing," *IEEE Transactions on Information Theory*, vol. 52, no. 4, pp. 1289–1306, April 2006.

[109] C. E. Shannon, "A mathematical theory of communication," *Bell Systems Technical Journal*, vol. 27, pp. 623–656, October 1948.

[110] M. El-Hajjar and L. Hanzo, "EXIT charts for system design and analysis," *IEEE Communications Surveys Tutorials*, vol. 16, no. 1, pp. 127–153, First 2014.

[111] T. Datta, H. S. Eshwaraiah, and A. Chockalingam, "Generalized space-and-frequency index modulation," *IEEE Transactions on Vehicular Technology*, vol. 65, no. 7, pp. 4911–4924, July 2016.

[112] S. Jacob, T. L. Narasimhan, and A. Chockalingam, "Space-time index modulation," in *2017 IEEE Wireless Communications and Networking Conference (WCNC)*, March 2017, pp. 1–6.

[113] Z. Yigit and E. Basar, "Space-time media-based modulation," *IEEE Transactions on Signal Processing*, pp. 1–1, 2019.

[114] B. Shamasundar, S. Jacob, and A. Chockalingam, "Time-indexed media-based modulation," in *2017 IEEE 85th Vehicular Technology Conference (VTC Spring)*, June 2017, pp. 1–5.

[115] B. Shamasundar, S. Jacob, S. Bhat, and A. Chockalingam, "Multidimensional index modulation in wireless communications," in *2017 Information Theory and Applications Workshop (ITA)*, Feb 2017, pp. 1–10.

[116] P. Yang, Y. Xiao, Y. L. Guan, M. Di Renzo, S. Li, and L. Hanzo, "Multi-domain index modulation for vehicular communications: a survey," *IEEE Vehicular Technology Magazine*, 2018.

[117] S. Lu, I. A. Hemadeh, M. El-Hajjar, and L. Hanzo, "Compressed sensing-aided multi-dimensional index modulation," *IEEE Transactions on Communications*, pp. 1–1, March 2019.

[118] D. L. Donoho, A. Maleki, and A. Montanari, "Message passing algorithms for compressed sensing: I. motivation and construction," in *2010 IEEE Information Theory Workshop on Information Theory (ITW 2010, Cairo)*, Jan 2010, pp. 1–5.

[119] A. K. Khandani, "Media-based modulation: a new approach to wireless transmission," in *2013 IEEE International Symposium on Information Theory*, July 2013, pp. 3050–3054.

[120] M. Di Renzo and H. Haas, "Bit error probability of space-shift keying MIMO over multiple-access independent fading channels," *IEEE Transactions on Vehicular Technology*, vol. 60, no. 8, pp. 3694–3711, Oct 2011.

[121] N. Serafimovski, S. Sinanovic, A. Younis, M. Di Renzo, and H. Haas, "2-User multiple access spatial modulation," in *2011 IEEE GLOBECOM Workshops (GC Wkshps)*, Dec 2011, pp. 343–347.

[122] T. L. Narasimhan, P. Raviteja, and A. Chockalingam, "Large-scale multiuser SM-MIMO versus massive MIMO," in *2014 Information Theory and Applications Workshop (ITA)*, Feb 2014, pp. 1–9.

[123] ——, "Generalized spatial modulation in large-scale multiuser MIMO systems," *IEEE Transactions on Wireless Communications*, vol. 14, no. 7, pp. 3764–3779, July 2015.

[124] A. Garcia-Rodriguez and C. Masouros, "Low-complexity compressive sensing detection for spatial modulation in large-scale multiple access channels," *IEEE Transactions on Communications*, vol. 63, no. 7, pp. 2565–2579, July 2015.

[125] Z. Gao, L. Dai, Z. Wang, S. Chen, and L. Hanzo, "Compressive-sensing-based multiuser detector for the large-scale SM-MIMO uplink," *IEEE Transactions on Vehicular Technology*, vol. 65, no. 10, pp. 8725–8730, Oct 2016.

[126] H. Zhu, W. Wang, Q. Huang, and X. Gao, "Subcarrier index modulation OFDM for multiuser MIMO systems with iterative detection," in *2016 IEEE 27th Annual International Symposium on Personal, Indoor, and Mobile Radio Communications (PIMRC)*, Sep. 2016, pp. 1–6.

[127] I. A. Hemadeh, M. El-Hajjar, S. Won, and L. Hanzo, "Multiuser steered multiset space-time shift keying for millimeter-wave communications," *IEEE Transactions on Vehicular Technology*, vol. 66, no. 6, pp. 5491–5495, June 2017.

[128] S. Lu, M. El-Hajjar, and L. Hanzo, "Two-dimensional index modulation for the large-scale multiuser MIMO uplink," *IEEE Transactions on Vehicular Technology (Submitted)*, 2019.

[129] S. Yang and L. Hanzo, "Fifty years of MIMO detection: the road to large-scale MIMOs," *IEEE Communications Surveys Tutorials*, vol. 17, no. 4, pp. 1941–1988, Fourthquarter 2015.

[130] T. L. Marzetta, "Noncooperative cellular wireless with unlimited numbers of base station antennas," *IEEE Transactions on Wireless Communications*, vol. 9, no. 11, pp. 3590–3600, November 2010.

[131] K. Zheng, L. Zhao, J. Mei, B. Shao, W. Xiang, and L. Hanzo, "Survey of large-scale MIMO systems," *IEEE Communications Surveys Tutorials*, vol. 17, no. 3, pp. 1738–1760, thirdquarter 2015.

[132] F. Rusek, D. Persson, B. K. Lau, E. G. Larsson, T. L. Marzetta, O. Edfors, and F. Tufvesson, "Scaling up MIMO: opportunities and challenges with very large arrays," *IEEE Signal Processing Magazine*, vol. 30, no. 1, pp. 40–60, Jan 2013.

[133] E. G. Larsson, O. Edfors, F. Tufvesson, and T. L. Marzetta, "Massive MIMO for next generation wireless systems," *IEEE Communications Magazine*, vol. 52, no. 2, pp. 186–195, February 2014.

[134] S. Wang, Y. Li, M. Zhao, and J. Wang, "Energy-efficient and low-complexity uplink transceiver for massive spatial modulation MIMO," *IEEE Transactions on Vehicular Technology*, vol. 64, no. 10, pp. 4617–4632, Oct 2015.

[135] S. Wang, Y. Li, and J. Wang, "Multiuser detection in massive spatial modulation MIMO with low-resolution ADCs," *IEEE Transactions on Wireless Communications*, vol. 14, no. 4, pp. 2156–2168, April 2015.

[136] S. Wang, Y. Li, J. Wang, and M. Zhao, "Low-complexity multiuser detection in massive spatial modulation MIMO," in *2014 IEEE Globecom Workshops (GC Wkshps)*, Dec 2014, pp. 784–789.

[137] P. Raviteja, T. L. Narasimhan, and A. Chockalingam, "Detection in large-scale multiuser SM-MIMO systems: algorithms and performance," in *2014 IEEE 79th Vehicular Technology Conference (VTC Spring)*, May 2014, pp. 1–5.

[138] T. L. Narasimhan and A. Chockalingam, "CHEMP receiver for large-scale multiuser MIMO systems using spatial modulation," in *2014 22nd European Signal Processing Conference (EUSIPCO)*, Sep. 2014, pp. 86–90.

[139] J. Zheng, "Low-complexity detector for spatial modulation multiple access channels with a large number of receive antennas," *IEEE Communications Letters*, vol. 18, no. 11, pp. 2055–2058, Nov 2014.

[140] A. Garcia-Rodriguez and C. Masouros, "Energy-efficient spatial modulation in massive MIMO systems by means of compressive sensing," in *2015 IEEE International Conference on Communications (ICC)*, June 2015, pp. 4541–4546.

[141] W. Zhang, "SAGE based data detection for multiuser spatial modulation with large number of receive antennas," *IEEE Communications Letters*, vol. 19, no. 9, pp. 1520–1523, Sep. 2015.

[142] X. Meng, S. Wu, L. Kuang, D. Huang, and J. Lu, "Multi-user detection for spatial modulation via structured approximate message passing," *IEEE Communications Letters*, vol. 20, no. 8, pp. 1527–1530, Aug 2016.

[143] S. Bhat and A. Chockalingam, "Sparsity-exploiting detection of large-scale multiuser GSM-MIMO signals using FOCUSS," in *2016 IEEE 83rd Vehicular Technology Conference (VTC Spring)*, May 2016, pp. 1–5.

[144] J. Park and B. C. Jung, "Signal detection with parallel orthogonal matching pursuit in multi-user spatial modulation systems," in *2016 Eighth International Conference on Ubiquitous and Future Networks (ICUFN)*, July 2016, pp. 371–373.

[145] E. Zhou and L. Hao, "On the detection of multiple-access spatial modulations," *Chinese Journal of Electronics*, vol. 26, no. 1, pp. 172–178, 2017.

[146] L. He, J. Wang, J. Song, and L. Hanzo, "On the multi-user multi-cell massive spatial modulation uplink: how many antennas for each user?" *IEEE Transactions on Wireless Communications*, vol. 16, no. 3, pp. 1437–1451, March 2017.

[147] J. Wang, Y. Xiao, S. Li, L. Li, and J. Zhang, "Performance evaluation of precoding in spatial modulation OFDM on a LTE channel," in *2012 IEEE 14th International Conference on Communication Technology*, Nov 2012, pp. 1188–1192.

[148] S. Narayanan, M. J. Chaudhry, A. Stavridis, M. D. Renzo, F. Graziosi, and H. Haas, "Multi-user spatial modulation MIMO," in *2014 IEEE Wireless Communications and Networking Conference (WCNC)*, April 2014, pp. 671–676.

[149] X. Li, Y. Zhang, L. Xiao, X. Xu, and J. Wang, "A novel precoding scheme for downlink multi-user spatial modulation system," in *2013 IEEE 24th Annual International Symposium on Personal, Indoor, and Mobile Radio Communications (PIMRC)*, Sep. 2013, pp. 1361–1365.

[150] X. Wu, M. Di Renzoy, and H. Haas, "A novel multiple access scheme based on spatial modulation MIMO," in *2014 IEEE 19th International Workshop on Computer Aided Modeling and Design of Communication Links and Networks (CAMAD)*, Dec 2014, pp. 285–289.

[151] A. Stavridis, M. Di Renzo, and H. Haas, "On the performance of multi-stream receive spatial modulation in the MIMO broadcast channel," in *2015 IEEE Global Communications Conference (GLOBECOM)*, Dec 2015, pp. 1–6.

[152] A. Stavridis, M. D. Renzo, and H. Haas, "Performance analysis of multistream receive spatial modulation in the MIMO broadcast channel," *IEEE Transactions on Wireless Communications*, vol. 15, no. 3, pp. 1808–1820, March 2016.

[153] R. Pizzio, B. F. Uchoa-Filho, M. Di Renzo, and D. Le Ruyet, "Generalized spatial modulation for downlink multiuser MIMO systems with multicast," in *2016 IEEE 27th Annual International Symposium on Personal, Indoor, and Mobile Radio Communications (PIMRC)*, Sep. 2016, pp. 1–6.

[154] Y. Chen, L. Wang, Z. Zhao, M. Ma, and B. Jiao, "Secure multiuser MIMO downlink transmission via precoding-aided spatial modulation," *IEEE Communications Letters*, vol. 20, no. 6, pp. 1116–1119, June 2016.

[155] M. Maleki, H. R. Bahrami, and A. Alizadeh, "Layered spatial modulation for multiuser communications," *IEEE Transactions on Wireless Communications*, vol. 15, no. 10, pp. 7143–7159, Oct 2016.

[156] H. Zhu, W. Wang, Q. Huang, and X. Gao, "Uplink transceiver for subcarrier index modulation OFDM in massive MIMO systems with imperfect channel state information," in *2016 8th International Conference on Wireless Communications Signal Processing (WCSP)*, Oct 2016, pp. 1–6.

[157] R. Chen and J. Zheng, "Index-modulated MIMO-OFDM: joint space-frequency signal design and linear precoding in rapidly time-varying channels," *IEEE Transactions on Wireless Communications*, vol. 17, no. 10, pp. 7067–7079, Oct 2018.

[158] P. Patcharamaneepakorn, C. Wang, Y. Fu, E. M. Aggoune, M. M. Alwakeel, X. Tao, and X. Ge, "Quadrature space-frequency index modulation for energy-efficient 5G wireless communication systems," *IEEE Transactions on Communications*, vol. 66, no. 7, pp. 3050–3064, July 2018.

[159] E. J. Candes and M. B. Wakin, "An introduction to compressive sampling," *IEEE Signal Processing Magazine*, vol. 25, no. 2, pp. 21–30, March 2008.

[160] A. M. Bruckstein, D. L. Donoho, and M. Elad, "From sparse solutions of systems of equations to sparse modeling of signals and images," *SIAM review*, vol. 51, no. 1, pp. 34–81, 2009.

[161] M. F. Duarte and Y. C. Eldar, "Structured compressed sensing: from theory to applications," *IEEE Transactions on Signal Processing*, vol. 59, no. 9, pp. 4053–4085, Sep. 2011.

[162] D. Takhar, J. N. Laska, M. B. Wakin, M. F. Duarte, D. Baron, S. Sarvotham, K. F. Kelly, and R. G. Baraniuk, "A new compressive imaging camera architecture using optical-domain compression," in *Computational Imaging IV*, vol. 6065. International Society for Optics and Photonics, 2006, p. 606509.

[163] M. Lustig, D. L. Donoho, J. M. Santos, and J. M. Pauly, "Compressed sensing MRI," *IEEE Signal Processing Magazine*, vol. 25, no. 2, pp. 72–82, March 2008.

[164] J. Haupt, W. U. Bajwa, M. Rabbat, and R. Nowak, "Compressed sensing for networked data," *IEEE Signal Processing Magazine*, vol. 25, no. 2, pp. 92–101, March 2008.

[165] E. J. Candes, J. Romberg, and T. Tao, "Robust uncertainty principles: exact signal reconstruction from highly incomplete frequency information," *IEEE Transactions on Information Theory*, vol. 52, no. 2, pp. 489–509, Feb 2006.

[166] Y. Eldar and G. Kutyniok, *Compressed sensing: theory and applications*, ser. Compressed Sensing: Theory and Applications. Cambridge University Press, 2012.

[167] Z. Han, H. Li, and W. Yin, *Compressive sensing for wireless networks.* Cambridge University Press, 2013.

[168] C. R. Berger, Z. Wang, J. Huang, and S. Zhou, "Application of compressive sensing to sparse channel estimation," *IEEE Communications Magazine*, vol. 48, no. 11, pp. 164–174, November 2010.

[169] J. L. Paredes, G. R. Arce, and Z. Wang, "Ultra-wideband compressed sensing: channel estimation," *IEEE Journal of Selected Topics in Signal Processing*, vol. 1, no. 3, pp. 383–395, Oct 2007.

[170] A. Alkhateeb, O. El Ayach, G. Leus, and R. W. Heath, "Channel estimation and hybrid precoding for millimeter wave cellular systems," *IEEE Journal of Selected Topics in Signal Processing*, vol. 8, no. 5, pp. 831–846, Oct 2014.

[171] R. Prasad, C. R. Murthy, and B. D. Rao, "Joint channel estimation and data detection in MIMO-OFDM systems: a sparse Bayesian learning approach," *IEEE Transactions on Signal Processing*, vol. 63, no. 20, pp. 5369–5382, Oct 2015.

[172] A. Gomaa and N. Al-Dhahir, "A sparsity-aware approach for NBI estimation in MIMO-OFDM," *IEEE Transactions on Wireless Communications*, vol. 10, no. 6, pp. 1854–1862, June 2011.

[173] T. Y. Al-Naffouri, F. F. Al-Shaalan, A. A. Quadeer, and H. Hmida, "Impulsive noise estimation and cancellation in DSL using compressive sampling," in *2011 IEEE International Symposium of Circuits and Systems (ISCAS)*, May 2011, pp. 2133–2136.

[174] A. B. Ramirez, R. E. Carrillo, G. Arce, K. E. Barner, and B. Sadler, "An overview of robust compressive sensing of sparse signals in impulsive noise," in *2015 23rd European Signal Processing Conference (EUSIPCO)*, Aug 2015, pp. 2859–2863.

[175] R. W. Heath, N. Gonzalez-Prelcic, S. Rangan, W. Roh, and A. M. Sayeed, "An overview of signal processing techniques for millimeter wave MIMO systems," *IEEE Journal of Selected Topics in Signal Processing*, vol. 10, no. 3, pp. 436–453, April 2016.

[176] B. Wang and K. J. R. Liu, "Advances in cognitive radio networks: a survey," *IEEE Journal of Selected Topics in Signal Processing*, vol. 5, no. 1, pp. 5–23, Feb 2011.

[177] J. W. Choi and B. Shim, "New approach for massive MIMO detection using sparse error recovery," in *2014 IEEE Global Communications Conference*, Dec 2014, pp. 3754–3759.

[178] R. G. Baraniuk, "Compressive sensing [lecture notes]," *IEEE Signal Processing Magazine*, vol. 24, no. 4, pp. 118–121, July 2007.

[179] S. Foucart and H. Rauhut, "A mathematical introduction to compressive sensing," *Bull. Amer. Math. Soc*, vol. 54, pp. 151–165, 2017.

[180] M. Fornasier and H. Rauhut, "Compressive sensing," *Handbook of mathematical methods in imaging*, pp. 1–48, 2014.

[181] Y. C. Eldar and G. Kutyniok, *Compressed sensing: theory and applications*. Cambridge University Press, 2012.

[182] Z. Han, H. Li, and W. Yin, *Compressive sensing for wireless networks*. Cambridge University Press, 2013.

[183] K. Hayashi, M. Nagahara, and T. Tanaka, "A user's guide to compressed sensing for communications systems," *IEICE transactions on communications*, vol. 96, no. 3, pp. 685–712, 2013.

[184] J. W. Choi, B. Shim, Y. Ding, B. Rao, and D. I. Kim, "Compressed sensing for wireless communications : useful tips and tricks," *IEEE Communications Surveys Tutorials*, vol. PP, no. 99, pp. 1–1, February 2017.

[185] A. M. Tillmann and M. E. Pfetsch, "The computational complexity of the restricted isometry property, the nullspace property, and related concepts in compressed sensing," *IEEE Transactions on Information Theory*, vol. 60, no. 2, pp. 1248–1259, Feb 2014.

[186] J. A. Tropp and A. C. Gilbert, "Signal recovery from random measurements via orthogonal matching pursuit," *IEEE Transactions on Information Theory*, vol. 53, no. 12, pp. 4655–4666, December 2007.

[187] D. Needell and J. A. Tropp, "CoSaMP: iterative signal recovery from incomplete and inaccurate samples," *Applied and computational harmonic analysis*, vol. 26, no. 3, pp. 301–321, 2009.

[188] W. Dai and O. Milenkovic, "Subspace pursuit for compressive sensing signal reconstruction," *IEEE Transactions on Information Theory*, vol. 55, no. 5, pp. 2230–2249, May 2009.

[189] T. Blumensath and M. E. Davies, "Iterative hard thresholding for compressed sensing," *Applied and computational harmonic analysis*, vol. 27, no. 3, pp. 265–274, 2009.

[190] M. Bayati and A. Montanari, "The dynamics of message passing on dense graphs, with applications to compressed sensing," *IEEE Transactions on Information Theory*, vol. 57, no. 2, pp. 764–785, Feb 2011.

[191] J. Wang, S. Kwon, and B. Shim, "Generalized orthogonal matching pursuit," *IEEE Transactions on Signal Processing*, vol. 60, no. 12, pp. 6202–6216, Dec 2012.

[192] S. Kwon, J. Wang, and B. Shim, "Multipath matching pursuit," *IEEE Transactions on Information Theory*, vol. 60, no. 5, pp. 2986–3001, May 2014.

[193] J. A. Tropp and A. C. Gilbert, "Signal recovery from random measurements via orthogonal matching pursuit," *IEEE Transactions on Information Theory*, vol. 53, no. 12, pp. 4655–4666, Dec 2007.

[194] A. Maleki and D. L. Donoho, "Optimally tuned iterative reconstruction algorithms for compressed sensing," *arXiv preprint arXiv:0909.0777*, 2009.

[195] J. Jeganathan, A. Ghrayeb, L. Szczecinski, and A. Ceron, "Space shift keying modulation for MIMO channels," *IEEE Transactions on Wireless Communications*, vol. 8, no. 7, pp. 3692–3703, July 2009.

[196] R. W. Hamming, "Error detecting and error correcting codes," *Bell Systems Technical Journal*, vol. 29, pp. 41–56, 1950.

[197] P. Elias, "Coding for noisy channels," *IRE Conv. Rept.*, pp. 37–47, 1955.

[198] C. Berrou and A. Glavieux, "Near optimum error correcting coding and decoding: turbo-codes," *IEEE Trans. Commun.*, vol. 44, no. 10, pp. 1261–1271, October 1996.

[199] L. Hanzo, T. H. Liew, B. L. Yeap, R. Y. S. Tee, and S. X. Ng, *Turbo coding, turbo equalisation and space-time coding:EXIT-chart-aided near-capacity designs for wireless channels*. Wiley-IEEE Press, 2011.

[200] L. Bahl, J. Cocke, F. Jelinek, and J. Raviv, "Optimal decoding of linear codes for minimizing symbol error rate," *IEEE Transactions on Information Theory*, vol. 20, no. 2, pp. 284–287, March 1974.

[201] G. Forney, *Concatenated codes*. Cambridge: MIT Press, 1966.

[202] S. Benedetto and G. Montorsi, "Serial concatenation of block and convolutional codes," *Electronics Letters*, vol. 32, no. 10, pp. 887–888, May 1996.

[203] S. ten Brink, "Convergence behavior of iteratively decoded parallel concatenated codes," *IEEE Transactions on Communications*, vol. 49, no. 10, pp. 1727–1737, Oct 2001.

[204] A. Ashikhmin, G. Kramer, and S. ten Brink, "Extrinsic information transfer functions: model and erasure channel properties," *IEEE Transactions on Information Theory*, vol. 50, no. 11, pp. 2657–2673, Nov 2004.

[205] D. L. Donoho and X. Huo, "Uncertainty principles and ideal atomic decomposition," *IEEE Transactions on Information Theory*, vol. 47, no. 7, pp. 2845–2862, Nov 2001.

[206] E. J. Candes and T. Tao, "Decoding by linear programming," *IEEE Transactions on Information Theory*, vol. 51, no. 12, pp. 4203–4215, Dec 2005.

[207] L. Hanzo, R. G. Maunder, J. Wang, and L. Yang, *Near-capacity variable-length coding: regular and EXIT-chart-aided irregular designs.* IEEE, 2011.

[208] H. V. Nguyen, C. Xu, S. X. Ng, and L. Hanzo, "Near-capacity wireless system design principles," *IEEE Communications Surveys Tutorials*, vol. 17, no. 4, pp. 1806–1833, Fourthquarter 2015.

[209] J. Hagenauer, E. Offer, and L. Papke, "Iterative decoding of binary block and convolutional codes," *IEEE Transactions on Information Theory*, vol. 42, no. 2, pp. 429–445, March 1996.

[210] L. Hanzo, J. P. Woodard, and P. Robertson, "Turbo decoding and detection for wireless applications," *Proceedings of the IEEE*, vol. 95, no. 6, pp. 1178–1200, June 2007.

[211] P. Robertson, E. Villebrun, and P. Hoeher, "A comparison of optimal and sub-optimal MAP decoding algorithms operating in the log domain," in *Proceedings IEEE International Conference on Communications ICC '95*, vol. 2, June 1995, pp. 1009–1013 vol.2.

[212] S. X. Ng and L. Hanzo, "On the MIMO channel capacity of multidimensional signal sets," *IEEE Transactions on Vehicular Technology*, vol. 55, no. 2, pp. 528–536, March 2006.

[213] P. Aquilina and T. Ratnarajah, "Performance analysis of IA techniques in the MIMO IBC with imperfect CSI," *IEEE Transactions on Communications*, vol. 63, no. 4, pp. 1259–1270, April 2015.

[214] L. Hanzo, T. H. Liew, and B. L. Yeap, *SpaceTime block codes.* IEEE, 2002.

[215] J. D. Blanchard, M. Cermak, D. Hanle, and Y. Jing, "Greedy algorithms for joint sparse recovery," *IEEE Transactions on Signal Processing*, vol. 62, no. 7, pp. 1694–1704, April 2014.

[216] W. Koch and A. Baier, "Optimum and sub-optimum detection of coded data disturbed by time-varying intersymbol interference [applicable to digital mobile radio receivers]," in *Global Telecommunications Conference, 1990, and Exhibition. 'Communications: Connecting the Future', GLOBECOM '90., IEEE*, Dec 1990, pp. 1679–1684 vol.3.

[217] P. Robertson, E. Villebrun, and P. Hoeher, "A comparison of optimal and sub-optimal MAP decoding algorithms operating in the log domain," in *Communications, 1995. ICC '95 Seattle, 'Gateway to Globalization', 1995 IEEE International Conference on*, vol. 2, Jun 1995, pp. 1009–1013 vol.2.

[218] J. Hagenauer, "The EXIT chart - introduction to extrinsic information transfer in iterative processing," in *2004 12th European Signal Processing Conference*, Sept 2004, pp. 1541–1548.

[219] M. El-Hajjar, O. Alamri, R. G. Maunder, and L. Hanzo, "Layered steered space-time-spreading-aided generalized MC DS-CDMA," *IEEE Transactions on Vehicular Technology*, vol. 59, no. 2, pp. 999–1005, Feb 2010.

[220] C. Xu, S. Sugiura, S. X. Ng, P. Zhang, L. Wang, and L. Hanzo, "Two decades of MIMO design tradeoffs and reduced-complexity MIMO detection in near-capacity systems," *IEEE Access*, vol. 5, pp. 18 564–18 632, 2017.

[221] M. Yzgecciolu, E. Jorswieck, C. Theory, and C. Laboratory, "Uplink and downlink transceiver design for OFDM with index modulation in multi-user networks," in *2017 IEEE 28th Annual International Symposium on Personal, Indoor, and Mobile Radio Communications (PIMRC)*, Oct 2017, pp. 1–5.

[222] M. D. Renzo and H. Haas, "Bit error probability of SM-MIMO over generalized fading channels," *IEEE Transactions on Vehicular Technology*, vol. 61, no. 3, pp. 1124–1144, March 2012.

[223] A. M. Magableh and M. M. Matalgah, "Moment generating function of the generalized α - μ distribution with applications," *IEEE Communications Letters*, vol. 13, no. 6, pp. 411–413, June 2009.

[224] J. Wu and C. Xiao, "Optimal diversity combining based on linear estimation of Rician fading channels," *IEEE Transactions on Communications*, vol. 56, no. 10, pp. 1612–1615, October 2008.

[225] T. Van Luong, Y. Ko, N. A. Vien, D. H. N. Nguyen, and M. Matthaiou, "Deep learning-based detector for OFDM-IM," *IEEE Wireless Communications Letters*, pp. 1–1, 2019.

[226] M. Abuthinien, S. Chen, and L. Hanzo, "Semi-blind joint maximum likelihood channel estimation and data detection for MIMO systems," *IEEE Signal Processing Letters*, vol. 15, pp. 202–205, 2008.

[227] J. Zhang, S. Chen, R. G. Maunder, R. Zhang, and L. Hanzo, "Adaptive coding and modulation for large-scale antenna array-based aeronautical communications in the presence of co-channel interference," *IEEE Transactions on Wireless Communications*, vol. 17, no. 2, pp. 1343–1357, Feb 2018.

[228] S. Lu, I. A. Hemadeh, M. El-Hajjar, and L. Hanzo, "An adaptive multi-user MIMO scheme for the millimeter-wave downlink," in *2018 IEEE 29th Annual International Symposium on Personal, Indoor and Mobile Radio Communications (PIMRC)*, Sep. 2018, pp. 1–5.

Subject Index

Author Index